Low-Cost Electromagnetic Tagging: Design and Implementation

by

Richard Ribon Fletcher

B.S., Physics
B.S. Electrical Engineering
MIT
September 1988

S.M. Information Technology
MIT
February 1997

Submitted to the Program in Media Arts and Sciences,
School of Architecture and Planning,
in partial fulfillment of the requirements for the degree of

DOCTOR OF PHILOSOPHY
at the
Massachusetts Institute of Technology
September 2002

Signature of Author

_____

Program in Media Arts and Sciences
August 9, 2002

Certified by

_____

Neil Gershenfeld
Associate Professor of Media Arts and Sciences
Program in Media Arts and Sciences
Thesis Supervisor

Accepted by

_____

Andrew Lippman
Chairperson
Department Committee on Graduate Studies
Program in Media Arts and Sciences

Acknowledgements

It is certainly worth noting a special Thanks to several special individuals who have contributed positively to my thesis and to my years as a graduate student. Most notably, to Jim Cook, since my Air Force days, for teaching me all the electromagnetics and microwave engineering that I never learned in school; to Jeff "Champ" Silvers, for teaching me all the math I never learned in school; and to Tomas Arias and Mike Kamal for making physics look incredibly easy. Thanks for Matt Reynolds and Josh Smith -- probably the most intelligent and nicest office mates one could ever have. Thanks for Paul Yarin, Brygg Ullmer, and Amir Hasson, for helping me during the home stretch of my thesis, in addition to their friendship.

Thanks to my graduate advisor Neil Gershenfeld for his sense of humor, and for being a great role model showing what a modern-day physicist and scientist could be. Thanks to my graduate colleagues in the Physics and Media Group: Tom Z., Matt, Josh, Femi, Henry, Yael, Rehmi,, Bernd, Ravi, Pehr, Jason, Ben V., Ben R., John-Paul, and Raffi, who were both a source of education and amusement. Thanks to all the students who worked for me over the years (or did I work for them?) in support of this work, without whom much of this would not have been possible: Mukund Vengalattore, Jeremy Levitan, Joel Rosenberg, Olufemi Omojola, Esa Masood, Charles Cadieu, Glenn Tournier, Paul Oreto, Nilah Monnier, Peter Bluvas, Patricia Diaz, Andres Hernandes, and Jordan Weitz. Thanks to all the Media Lab folks (including MIT Council for the Arts), fellow students, too many to name but who have been so nice to me, taught me so much, and made me feel incredibly lucky to have the opportunity to have worked here. Thanks to all the great folks at the US Air Force Materials Lab for really opening my eyes to the amazing variety and untapped potential for advanced materials of all kinds. And a special thanks to MIT faculty from my undergrad days: "Doc" Edgerton, Charlie Miller, Jay Kirsch, and Professors George Clark and Peter Dimos for inspiration, encouragement, and long conversations outside of class beyond the call of duty, and a personal thanks to Bill Buxton, Muriel Cooper, and Doc Edgerton (again) for motivating me to come to MIT in the first place.

Finally, outside of school, no acknowledgement would be complete without a heartfelt thanks to my parents and family, for their love, their prayers, and numerous lessons of life; and most recently, a heartfelt thanks to Virginia, for enriching my life in ways that transcend technology and teaching me all the things I was supposed to have learned in kindergarten.

Low-Cost Electromagnetic Tagging: Design and Implementation

by

Richard Ribon Fletcher

Submitted to the Program in Media Arts and Sciences,
School of Architecture and Planning,
on August 9, 2002
in partial fulfillment of the requirements for the degree of

DOCTOR OF PHILOSOPHY IN MEDIA ARTS AND SCIENCES
at the
Massachusetts Institute of Technology
September 2002

Abstract

Several implementations of chipless RFID (Radio Frequency Identification) tags are presented and discussed as low-cost alternatives to chip-based RFID tags and sensors.

An overview of present-day near-field electromagnetic tagging is presented, including both chip-based and chipless technologies with associated costs. As a candidate for low-cost ID tags, a design theory and implementation is presented for multiply-resonant planar metal structures. This theory includes a circuit model, a phenomenological model, and a framework for tuning the resonant frequencies as a function of geometrical and material properties. A novel physical geometry, a tree-like spiral structure, is proposed as a design that increases the number of resonances per unit area in a planar structure relative to the present day state-of-the-art.

In addition to identification, it is shown how several chipless tags can also be designed to function as sensors. Several examples are discussed in detail, including: 1) a family of thermal sensor tags employing magnetic materials and 2) a family of sensor tags (to sense pressure, humidity, and pH) based on planar resonator structures.

The latter section of the dissertation describes the evolution of my work in developing the necessary (and low-cost) instrumentation to support these new varieties of tag technologies, ranging from a $500 frequency-agile reader to a $5 reader for toy applications. A summary of emerging technologies and promising directions for electromagnetic tagging is also presented.

Thesis Supervisor: Neil Gershenfeld, Associate Professor of Media Arts and Sciences

Low-Cost Electromagnetic Tagging: Design and Implementation

by

Richard Ribon Fletcher

Thesis Readers

Thesis Reader

_____

Robert O'Handley
Department of Materials Science and Engineering

Thesis Reader

_____

Hap Patterson
Chief Technical Advisor
Tyco-Sensormatic, Inc.

TABLE OF CONTENTS

Chapter I.

Introduction

1.1 About this thesis

1.1.1 The MIT Media Laboratory

Much of the work at the MIT Media Lab has been devoted to the goal of making information technology more useful in order to improve the environments in which we live, play, work, and learn. Much of the research has been motivated by a human perspective, such as a need to sense the environment or have an embodied presence. Successful research has yielded multi-modal systems which allow computers to see, identify, and react to the people; and new forms of tangible user interfaces, robotics, and novel electronic displays have enabled new means for people to interact with computers. More recently, research thrusts into biology and nanotechnology are giving us access to worlds which were previously unattainable. Electromagnetic tagging cuts across all these disciplines, responding to a fundamental need for wireless identification and sensing.

1.1.2 What is contained in this thesis

The scope of this thesis pertains to low-cost electromagnetic tagging. In particular, research is presented in the area of chipless electromagnetic tags as an alternative to conventional RFID (Radio-Frequency Identification).

1.1.3 What is not contained in this thesis

While existing RFID (both chip-based and chip-less) technologies are summarized, this thesis does not contain a comprehensive detailed overview of RFID technologies. This topic alone is enough to fill a book.

8.2 What are electromagnetic tags?

A "tag" is something which can be attached to a person or object and thereby enables information environments to remotely identify it, to track its position, or sense its state. The approach to wireless data presented in this thesis involves the use of electromagnetic fields, as opposed to various optical means, which require line-of-sight. In general, the information acquired via the tag is then used by some sort of electronic appliance to perform its function. Since it is not economically practical to implant computers into common objects such as mail envelope, a coffee mug, or an airplane ticket, electromagnetic tags provide a means for these objects to communicate their information by proxy to more intelligent devices that are, in turn, part of a larger information network. Electromagnetic tagging thus represents a low-level wireless technology that enables communication and computation among the numerous everyday object in our world. If we consider the evolution of different information technologies over the past decades, one can think of electromagnetic tags as the lowest level on the information "food chain," as illustrated in Figure 1. This thesis discusses the technology involved to create this bottom layer.

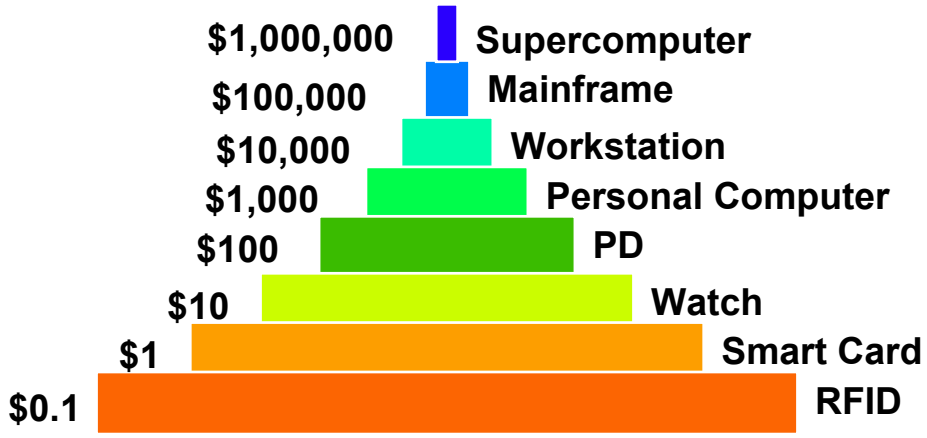

Figure 1. Illustration of "information food chain." As we move down the food chain, the potential number of devices increases dramatically, but lower cost per device is required.

Also illustrated in Figure 1 is the cost associated with each form of information technology. If these technological innovations are viewed as a function of time, it is important to note how the smaller and cheaper technologies have evolved last. There are several obvious and not-so-obvious reasons for this, some of which are mentioned in this thesis. In general, doing more with less is difficult, and as we strive for simpler and cheaper ways to communicate and store information, we are forced to invent new ways to represent and manipulate information based on increasingly fundamental physical parameters, such as resonant frequency or domain-wall kinetics.

8.3 Short history of electromagnetic tagging

Tags in the form of radio transponders have existed for at least fifty years. The simplest example is a radio beacon that emits a unique signal that can be detected with a radio receiver at some distance (many meters or more). These are commonly used on all types of commercial aircraft and military aircraft IFF ("Identification Friend or Foe") systems to identify aircraft to each other. Other radio tags function as transponders by responding only to a unique signal from a distant transmitter. Over the years, various derivative forms of tagging and identifications systems have been used in a wide variety of applications ranging from wild-animal tracking to military surveillance to stolen-car retrieval (e.g. Lo-Jack system). Such tags are comprised of a radio transmitter powered by some type of battery. If sufficient power is available, some tag systems are designed to communicate to a surveillance airplane or low-earth-orbit satellite flying overhead.

Until the 1960's, most of the interest in tagging was in far-field devices, which means that the sensing distance is long compared to the wavelength and to the size of the antennas involved. Interestingly, some of these tag designs were also chipless. Early far-field tags were simple harmonic-diode tags, such as those used to tag and track butterflies today. Other early work in far-field RFID included work in SAW (Surface Acoustic Wave) reflectors – a research field that has recently re-emerged as a viable technology for low-cost tagging. The most direct descendent, however, of modern-day far-field chip-based RFID tags originated in Los Alamos National Laboratory and the Department of Energy in the early 1970's as a means of tracking radioactive materials. These tags were battery powered, and functioned by scattering back a radio signal emitted by the tag reader. Since the battery is used only for modulating the radio signal and not to generate the radio signal itself, such tags are often termed semi-passive. This technology went on to be developed by Identronix in the 1980's and later Micron, Amtech, and (IBM) Intermec. Over the years, advances in the semi-conductor industry has enabled very low power IC's operating at UHF frequencies and today don't require the use of a battery if the tag to reader distance is sufficiently short (couple meters or so) to power the tag. This technology is most commonly found today in automatic toll collection systems for vehicles.

Inspired by the invention of the optical barcode in 1949, it was not until the mid-1960's that commercial interest began in the field of short-range RFID technology for shipping, inventory, retail and industrial applications. Short-range RFID (predominantly near-field and inductively-coupled) was developed independently of long-range far-field RFID, although some companies such as Westinghouse – that supports both military and industrial applications – worked in both technologies. In 1967, the first commercial barcode scanning systems were installed in supermarkets in Ohio (USA); and in the early 1970's the first low-cost electromagnetic tagging systems began appearing in libraries and some retail stores, led by companies such as Sensormatic and Checkpoint, which today dominate the global EAS (Electronic Article

Surveillance) market. In the late 1970's Schlage Lock company started experimenting with electronic alternatives to the standard key. Schlage explored a chipless multiple-resonance swept-frequency approach (storing information in the frequency domain), while other companies explored chip-modulated fixed-frequency approach (encoding information in the time domain) for both electronic door locks as well as automotive transportation applications. The swept-frequency approach went on to be developed by Westinghouse for security access applications, and the chip-modulated technology went on to become what we know today as short-range RFID (Radio Frequency Identification) technology. The earliest applications of this technology included tagging cattle, horses, and laboratory animals, developed by Texas Instruments, Destron, and ID systems in the early 1980's. Commercial and industrial access control systems went of to be developed by Indala Corporation in the mid-1980's, which was later bought then sold by Motorola. Hughes Corporation bought parts of the Destron technology and others to form Hughes ID systems (HID) in the early 1990's, and although no longer owned by Hughes, HID has now emerged as the market leader for access control systems in the US.

Over the years, RFID tags have appeared in a variety of form factors. On the large scale, RFID tags are used to tag freight train cars and commercial garbage dumpsters for bautomated tracking and billing. On the smaller scale, RF-ID tags have also been embedded into clothing buttons and are used by commercial laundry companies to automatically sort clothing according to each clothing item's ID code. Other tags have been embedded in roadways and walkways as location beacons to aid in navigation for vehicles or for the visually-impaired. Several companies manufacture RFID tags smaller than a grain of rice that can be injected under the skin with a syringe for tagging laboratory animals and pets. Hitachi makes a tiny RFID tag with an integrated antenna-on-chip that can be embedded in a business card or paper currency.

Despite continuing technological improvements since the mid-1980's to reduce size and power-consumption, RFID technology has not changed significantly over the years. The RFID market has remained very fragmented due to the wide variety of existing wireless standards and proprietary protocols; and the size of the RFID market has remained small due to the excessive cost of RFID labels and the lack of infrastructure to support it. Although the cost of tags and readers has been slowly decreasing, these still exists a need for very low-cost identification and sensing. While a general discussion of the RFID market is a topic that extends far beyond the scope of this thesis, it is clear that cost is a key factor for enabling new applications and markets. Thus, it is the intention of the author that this thesis can help provide some solutions, alternatives, and opportunities for low-cost tagging that can help lead the evolution of RFID in general.

Chapter II.

Fundamentals of Electromagnetic Tags

2.1 Functional description

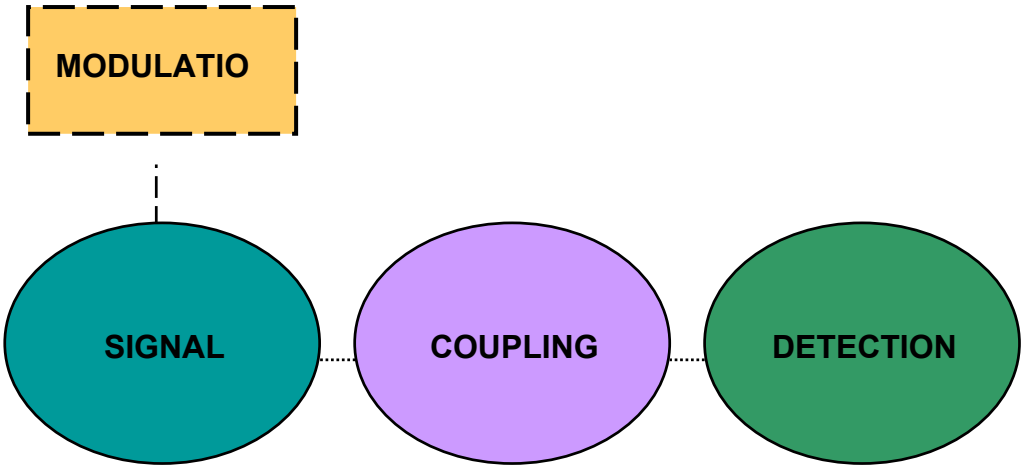

Figure 2. Basic tag model.

In order to discuss the cost of electromagnetic tagging technologies, it is important to describe the elements of an electromagnetic tag in more detail. Although many varieties of electromagnetic tags exist, all forms of electromagnetic tags can be functionally described by three basic parts: signal, coupling, and detection, as shown in Figure 2. The fundamental signal inherent to the tag can be a resonance peak, a reflection, or a generated harmonic. In a short-range near-field RFID system, the distance between the tag and the receiver (known more appropriately as the *tag reader*) is sufficiently small (<1 meter) such that their electromagnetic behavior is best characterized by the electromagnetic *coupling* between the tag antenna and the tag reader antenna. In fact, the term *antenna* is somewhat of a misnomer for common RFID tags because no far-field transmission is employed as its connotation implies. Parts of the tag and parts of the tag reader are simply coupled together in a manner similar to transformer windings (*inductive coupling*) or as opposing plates in a capacitor (*capacitive coupling*).

The near-field coupling between the RFID tag and the reader serves two important functions. First, the coupling is commonly used as a means of supplying power to the tag, if needed. If all the necessary electronics inside the tag can be powered remotely from the reader, then the tag requires no local battery. Secondly, since the tag functions as an electrical load on the tag reader, the tag can communicate information to the reader simply by changing the value of its own impedance, which does not require the tag to transmit any power to the reader.

2.2 The tag IC

The primary distinction between chip-less and chip-based tags is the physical mechanism used to store and transmit the tag's information. A common chip-less tag, such as an anti-theft label from a store, produces a single electromagnetic signal, and thus contains only a single bit of information (tag ON, tag OFF). By adding a small electronic chip, the tag IC, the tag gains the ability to *modulate* the electromagnetic signal (see Figure 3) as well as the means of storing information, thus greatly increasing the functionality of the tag.

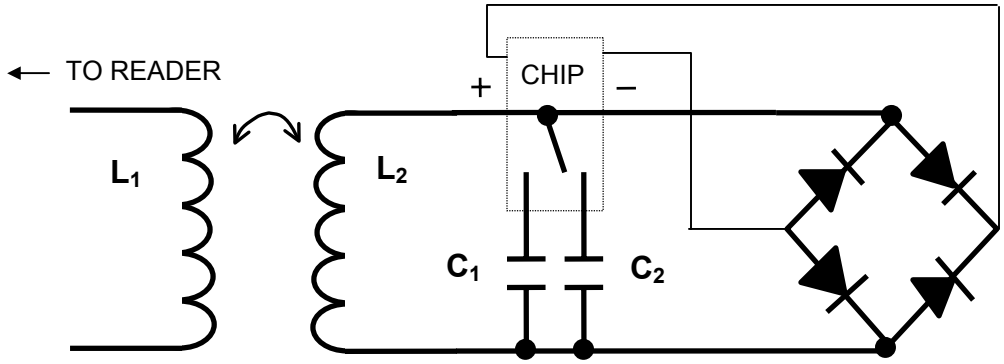

Figure 4. Simple schematic circuit diagram of a battery-less RFID tag inductively-coupled to a tag reader antenna.

The basic elements of an RFID tag and the role of the tag IC is shown schematically in Figure 2. This is not the only way RFID tags can function, but it serves as a sample implementation. The tag IC, externally powered by the field of the reader, acts as an active switch that toggles the tag's impedance in a recognizable pattern in order to transmit its information. Various forms of modulation are possible and common types include ASK, FSK, and BPSK. Since the electromagnetic field supplied by the reader is employed both for powering the chip and transferring data, careful design of the power regulation circuitry and the communication protocol is critical.

Although the integration of the electronic chip onto an RFID tag is functionally desirable, it adds significant cost relative to the total cost of the label. Unfortunately, any amount of circuitry will always be much more expensive than the most common type of short-distance wireless tagging technology, namely the optical barcode. Since barcodes can be easily printed on a variety of surfaces, optical barcode technology is extremely cost-effective. However, since reading barcodes requires line-of-sight and some degree of alignment between the barcode and the reader, there are practical limits to the applications and uses of bar codes. As a result, there exists a general desire for the invention of an "electromagnetic barcode" technology that would thus enable a greater degree of automation. Such electronic labels would, for example, allow the tag reader to be hidden behind a wall panel or under a table-top. In addition, the electromagnetic transfer of information is generally not affected by operation in dirty environments; and since line-of-sight is not required, tagged objects could be "scanned in" at a faster rate without the need to find the location of the barcode and orient it towards the reader.

2.3 Why low-cost is so difficult

RF-ID tags can be relatively cheap (~$.25) but optical barcodes are far cheaper (<$.001). So why don't we just make a cheaper tag? If tags are really to become as ubiquitous as a barcode (UPC label) and manufactured in quantities of tens of billion per year, then won't the natural economies of scale lead to very low cost tags?

2.3.1 Making a tag

The hard reality is that given the traditional means for manufacturing electronics chips and labels, there is a lower limit to how cheaply an electronic tag can be made, regardless of the number produced. The semiconductor industry simply does not know how to make a very small, very low-cost chip, because there was never a need. RFID is a very special case for silicon manufacturing. In addition, much of the cost of an RF-ID tag is not only due to the electronic chip but – more importantly – to the manufacturing complexity of the entire tag, which involves handling the tiny electronic chip and assembling the entire electronic label.

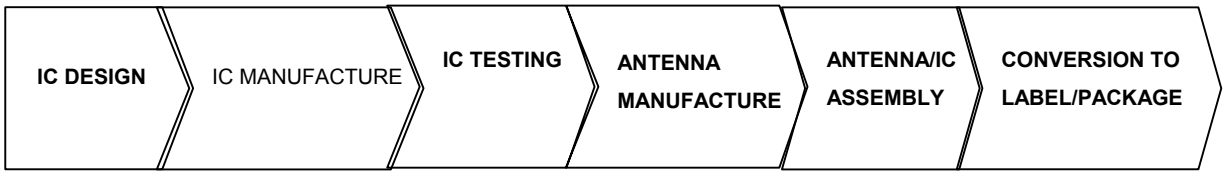

Figure 5. The basic steps required for manufacturing an electronic RFID label.

A simplified illustration of the manufacturing process for an RFID label is shown in Figure 4. The functions shown can be divided into two broad categories: the cost of silicon die, and the cost of die handling/assembly. Since the ICs being manufactured here are not of the complexity of Pentium chips, for example, the step of testing each individual die is not necessary or feasible; thus the die testing step is obviated.

2.3.2 The Cost of Silicon

Semiconductor device structures and photolithograhic processing for semiconductor integrated circuits has been standardized for thirty years, and the cost of building a modern silicon fabrication plat is on the order of tens of billions of US$ dollars. Although certain hybrid or non-planar device topologies have been invented, the predominant process for modern-day high-volume consumer electronics is CMOS.

The basic elements of an electronic semiconductor transistor have not changed since its invention in 1947. All electronic chips require the same basic semiconductor layers with N- or P-type doping, as well as several metallization layers for the interconnects, and several dielectric layers for isolation and charge storage. The only reason that we have been able to achieve the Moore's Law scaling is that over the past thirty years, we have learned to make semiconductor structures much smaller; this has enabled faster propagations speeds and switching times, but most importantly, it has enabled many more transistors to fit within a unit area.

Since electronic chips are fabricated on a wafer-by-wafer basis, there is roughly a fixed cost per wafer. This fixed cost depends on the resolution and complexity of the photolithographic process used, and this cost has been increasing as we push the limits of resolution and feature size. At present, typical cost is US$ 1000 per wafer. A more detailed cost dependence is shown in Figure 6. Although the cost per wafer has been increasing linearly, there has been a quadratic increase in the number of devices that we can fit per wafer. As a result, the overall cost and performance of electronic chips have improved over the years.

Given that the cost per wafer is roughly independent of the IC design, the cost for making an RFID chip can be estimated simply by knowing the required silicon area for the RFID chip. In comparison to a Pentium IV chip that has nearly 50 million transistors, a typical RFID chip has only 80,000 transistors or roughly 20,000 gate equivalents. In addition to transistors, the EEPROM memory cells which store the tag's data consume a considerable amount of area, since EEPROM requires a larger linewidths of 10um or so to support the higher programming voltage of 15 Volts. Depending on the tag's operating frequency, tuning and filtering capacitors can also require a significant amount of area in the 10's of square microns. As a result, a conventional RFID die area is typically 1-3 square millimeters. Assuming a typical modern-day fabrication plant with a 0.25um CMOS process and assuming a 10-inch (diameter) wafer, this translates to between 10 to 40 thousand die per wafer, bringing the cost of each die to 3-10 cents each.

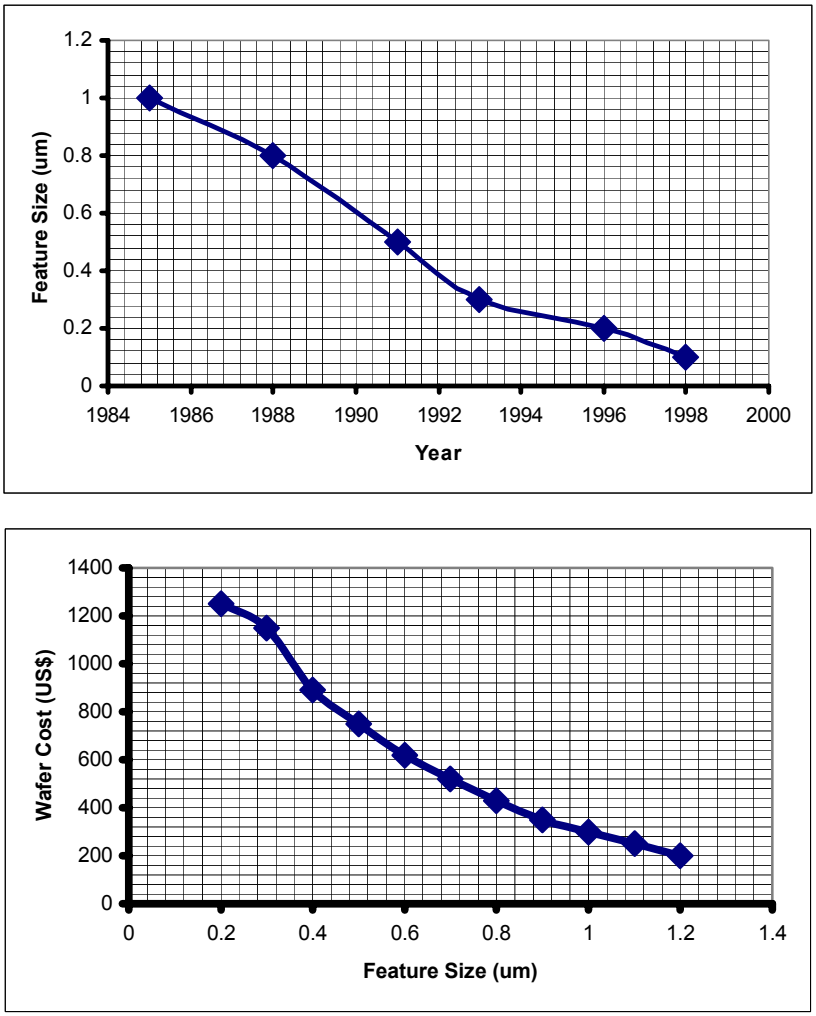

Figure 6. Wafer cost and feature size data for the past 20 years [Maly].

As a result, in order to reduce the cost of an RFID chip, great effort is being taken to reduce the size – and consequently the functionality – of an RFID chip. Several research centers, such as the MIT AutoID Center, are presently trying to create a simplified (typically 64-bit) data standard for an RFID IC that can be achieved with less than 8,000 transistors. As a bonus, smaller die size and fewer transistors also reduced the overall power consumption of the chip, which in turn greatly increases its read range. Unfortunately, these reduced die sizes are, in turn, posing new challenges, as mentioned below.

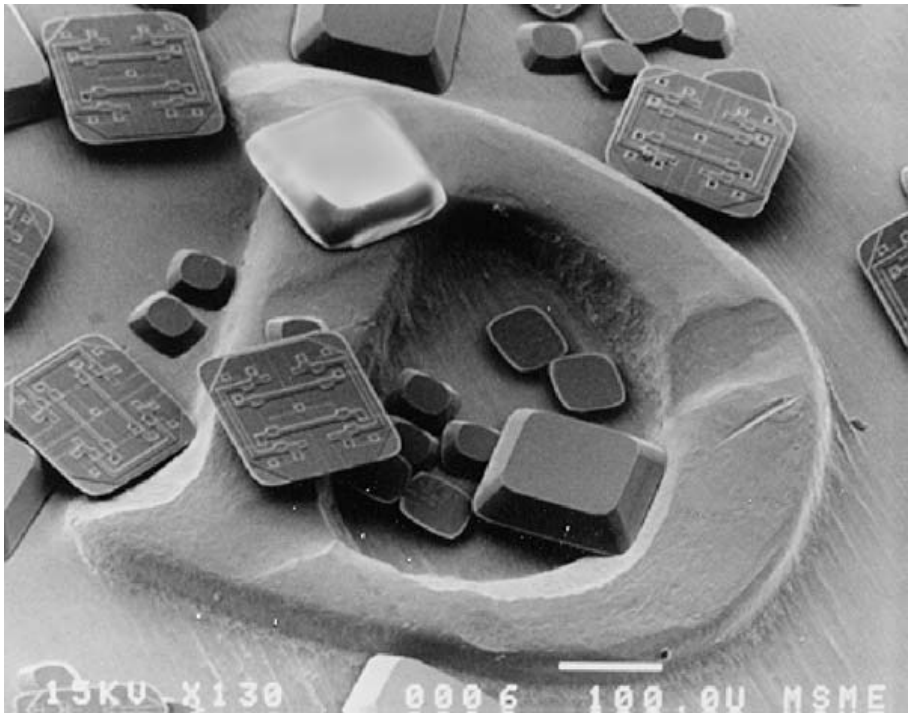

Figure 7. Scanning Electron Micrograph of two sizes of semiconductor die, having dimensions of 400um X 400um and 180umX180um respectively, resting on the surface of a penny [Alien Technology].

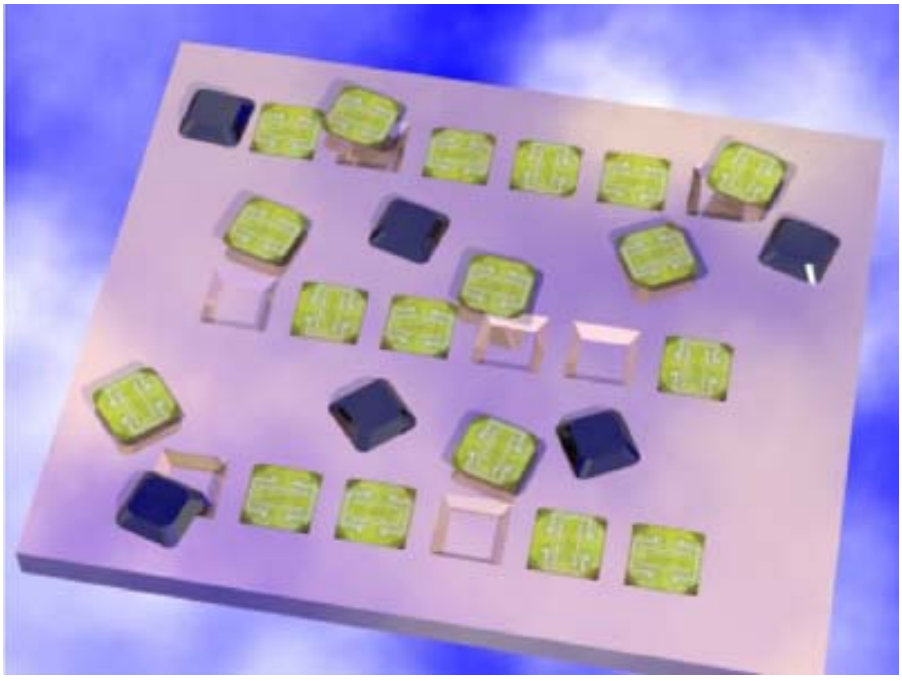

Figure 8. Illustration of fluidic self-assembly technique used for automatic placement of very small semiconductor die.

2.3.3 The Cost of Assembly

Even if it cost nothing to make a silicon IC chip, the cost of dividing the wafer, handling all the die and placing them onto a label is still significant. Although the cost per die is lower as the die size is reduced, the cost of handling the die increases, simply because the semiconductor electronics industry is not accustomed to handling such small chips. Optimized pick-and-place robotics is generally the most cost-effective means for placing the die onto carriers called *lead frames* or *interposers*; this can be done at a cost of 2 cents per die. However, if even smaller die are used completely new means of die handling and placement have been invented that enable the die to essentially place themselves. By performing the assembly process in a liquid environment, it is possible to wash large numbers of die over a prepared embossed surface such that the die can be made to fall into place. Figure 6 illustrates one of these techniques known as Fluidic Self-Assembly.

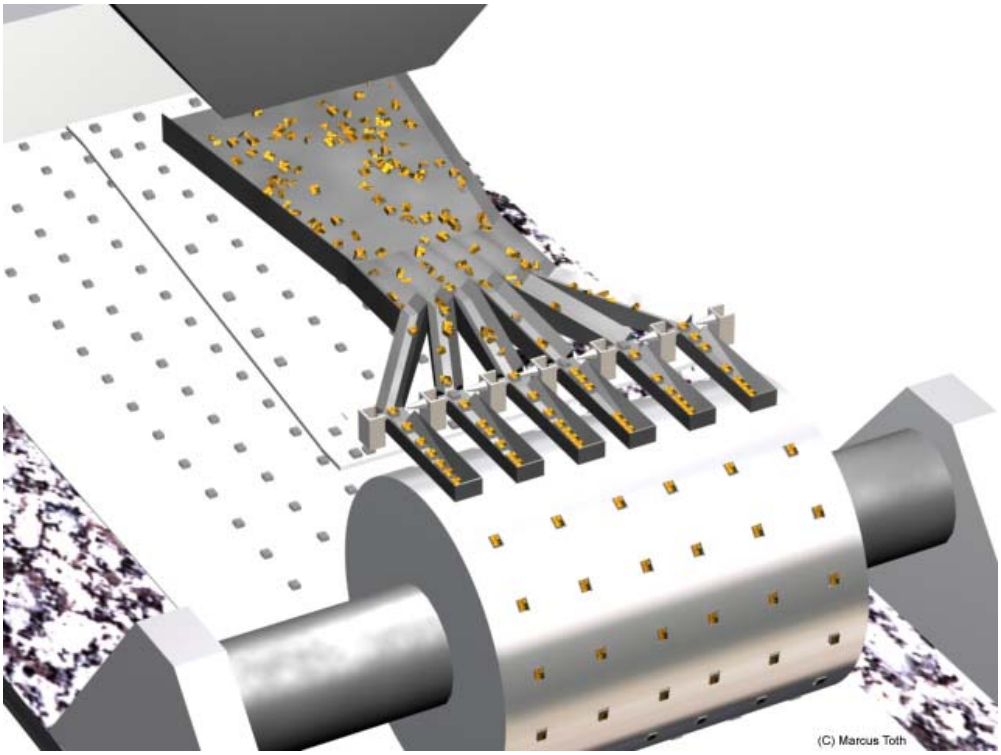

Figure 9. Illustration of fluidic self-assembly technique used for automatic placement of very small semiconductor die.

Another mechanical self-assembly technique being explored by Sanjay Sarma's group at MIT and others, is known as Vibratory Self-Assembly. In this case, the individual die are guided down mechanical chutes that vibrate over a moving vacuum roll that pulls each die off the chute and places it onto a substrate material below. This process is illustrated in Figure 7.

Once the die has been placed onto a substrate or holder, it then needs to be attached to an antenna and converted into a label. Depending on what type of electromagnetic coupling is used, (inductive, capacitive, or backscatter), the fabrication of the antenna can be as simple as printing with carbon-ink or some type of metallic screen printing, metal etching, electro-deposition, or electroforming. This process costs a couple cents at minimum, not counting the cost of the antenna (1-20 cents).

As a result of all these steps, the most optimistic estimate for the cost of a chip-based RFID tag is 5 cents in volumes of one billion tags or more per year. However, achieving this cost figure will require very aggressive and creative redesign of the tag IC as well as successful implementation of new die-handling technologies.

2.4 Low-cost alternatives

Given the intrinsic cost limitations of silicon manufacture and tag assembly, it is useful to consider an approach to creating a low-cost electromagnetic tagging technology that does not require traditional semiconductor manufacturing, and can achieve a label cost below 5 cents. In this regard, two general approaches have emerged to this problem: printed electronic circuits and chipless material structures. While printed electronic circuits, based on electronic polymer materials or inorganics, do hold great promise for the long-term future and have been demonstrated in the laboratory as early as 1998 [Philips Research], many serious problems still need to be overcome, including device stability and electronic performance. As a result, it is not likely that printed electronics for this application will be feasible within the next 5 years.

The challenge and research presented in this thesis is thus the design and manufacture of RFID tags using materials alone, hereafter termed *chipless RFID tags*. The two primary issues considered here are: 1) the detection and interpretation of electromagnetic material signals and 2) the storage and coding of information using the electromagnetic response of materials.

Since the development of the multiply-resonant chipless tags in the early 1980's, relatively less work has been done in developing chipless RF-ID solutions. While detecting specific materials electromagnetically is not uncommon – as demonstrated by metal detectors, shoplifting security systems, and medical Magnetic Resonance Imaging systems – it would be useful to create a unified, quantitative and general approach to this topic. By identifying the electromagnetic response of materials, we can view materials as physical representations of information. Furthermore, by knowing how this electromagnetic response depends on the local material environment, materials can also be viewed as remote sensors. The notion that any material structure or object around us can function as a sensor or repository of information can fundamentally change the way we manufacture and package all kinds of products, ranging from military airplanes to pizza boxes to sport shoes.

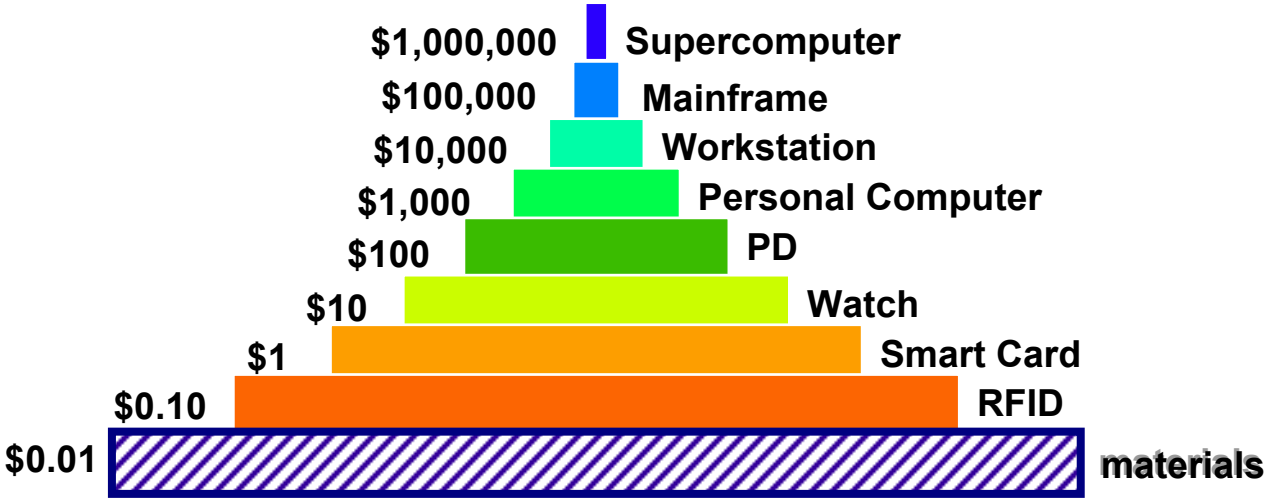

Figure 10. Illustration of "information food chain" similar to Figure 1, with the addition of new information technology layer comprised solely of materials.

In this thesis, I explore a new layer in the information technology food chain – a layer comprised of material structures alone. This is illustrated in Figure 3. In terms of cost, material structures thus form a separate class of tagging technology that lies somewhere between RF-ID, magnetic stripe cards, and the optical barcode. Naturally, the cost of a particular tag would depend on the choice of materials and the design of the tag. A description of various materials tag concepts and their corresponding physical description are presented in the following chapters. Whether the future RFID market uses material structures or printed electronic circuitry, it is clear that traditional silicon fabrication is not the solution to low-cost high-volume applications such as RFID or paintable computing. As nanotechnology, molecular computers, and biological materials continue to be at the forefront of research in the physical sciences, Feynman's dictum *"There's plenty of room at the bottom"* continues to hold true today more than ever.

Chapter III.

Analog Information

Thousands of years ago, it is unlikely that somebody sat down one day and created hieroglyphics from scratch, or instantly created any form of written language that exists today. The written characters of language, Eastern or Western, have evolved – and presumably improved – over many hundreds of years. Perhaps one day the same will be said for information encoded in electromagnetic signals.

3.1 Analog to Digital to Analog

Electromagnetic information encoding is not new. Since the invention of Morse code, we have seen the invention of the telephone, radio, TV, and now many portable electronic communication devices exist, each introducing new flavors of information encoding.

Throughout the 20th Century, scientists and engineers have invented a variety of digital and analog representations of information as a means for automation and computation. Physical implementations have ranged from mechanical switches to vacuum tubes to op-amps and pulses of light. As late as the 1970's, following the demise of the slide rule, there was significant interest in using analog circuits to solve mathematical equations, with the numbers represented by various voltage and current values in the circuit.

After the late 1970's, digital representations of information quickly grew in popularity, fueled by the advent of the integrated circuit, the convenience of digital algorithms and the noise immunity provided by digitization. As we continue to push the limits of technology further, however, the need for analog circuitry and analog representations of information have resurfaced. In trying to build higher frequency software radios, it has become apparent that all-digital approaches are far too power-hungry compared to their analog counterparts; and in trying to build smaller or cheaper information devices, we are now discovering new ways to use natural materials and learning how natural mechanisms of physics, biology, and chemistry can be used to store and compute information. In summary, present-day information technology requires the presence of both digital and analog.

In most electronic communications devices, there must be some point where analog signals are converted into digital data or vice versa. At a basic level, analog to digital conversion can be simply digitizing an analog waveform and playing it back, as we see everyday in digital cell

phones. At an intermediate level, the digital information is actually coded in the frequency and time signals of the analog waveform, such as we see in DTMF codes or telephone data modems. At a higher level of complexity, it is also possible to extract meaning as well as information from the analog waveform, as is done in speech recognition systems for machine understanding.

For the purpose of electromagnetic tagging, we are interested in coding the information such that it can be stored and retrieved using material structures having analog representations. However, in order to form a proper coding method, we must first explore and understand the electromagnetic signals that are available and accessible within these electromagnetic material structures. This is discussed in the next section.

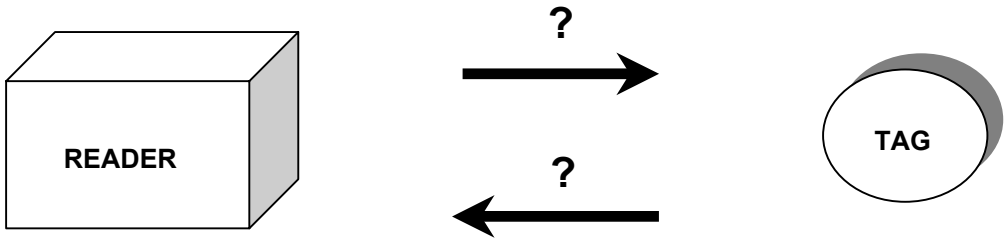

Figure 11. Illustration of "information food chain" similar to Figure 1, with the addition of new information technology layer comprised solely of materials.

3.2 The Electromagnetic Response

In the case of a chipless tag, the electromagnetic response is created by the material structures within the tag arising from fundamental physical interactions. By definition, the electromagnetic response of a tag must be easily distinguishable from that of the surrounding environment. Through materials processing, design, and manufacture, the electromagnetic response of the tag can be engineered to be constant and repeatable, unless the tag is purposely designed to be random, or to respond to its local conditions (e.g. light, heat, pressure) thus functioning as a type of sensor. The tag can be interrogated in various ways by the tag reader, and the electromagnetic response of the tag is ultimately detected as voltages or currents induced in the tag reader antenna. For the purpose of discussion,there are two basic representations in which these signals can be observed and processed: time-domain and frequency-domain. These are described below.

3.2.1 Time Domain

One approach to interrogating a chipless tag is to stimulate the tag with an electromagnetic field and observe the response as a function of time. If tags could be designed to have distinctly different transient responses, then each tag could be uniquely identified.

For a chipless tag that contains no electronic circuitry or internal source of energy, it is challenging to design a tag that can be interrogated as a function of time. However, several physical mechanisms exist that can alter the storage and propagation of energy within the tag. For example, it might be possible to build up energy within a material structure that could be release slowly over time. It may also be possible to create internal dynamics in a tag that can appear as amplitude modulations of multiple resonant frequencies or harmonic spectra. Alternatively, if frequency or phase can be viewed as a function of time, it would also be possible to observe the evolution of energy modes among a given number of resonators.

Some examples of time-domain mechanisms are given below.

3.2.1.1 Surface Acoustic Wave Reflectors

The most well-known – and perhaps the oldest – time-domain method for electromagnetic tagging are surface acoustic wave (SAW) tags, illustrated in Figure 7 below. A radio pulse (typically in the high UHF frequency) from the reader is received by the tag antenna and converted via a transducer structure to a surface acoustic wave that propagates along the piezoelectric substrate. A series of reflectors along the length of the tag can be employed to produce a reflection or phase shift in the traveling wave. The reflected signals are transmitted back out through the tag antenna and are received by the tag reader as pulse echoes. These received pulses are then processed and interpreted as data. A variety of sensor elements can also be attached to these substrates as well, thus allowing the SAW tags to function as wireless sensors.

Commercially, SAW tags have been developed by Seimens research in the mid-1990's and are currently being developed by start-up companies such as i-Ray in Israel and RF-Saw in the USA. However, although SAW tags can have very impressive read range (hundreds of meters or so, depending on the reader power), the process of fabricating the tag die (usually comprised of silver or gold lines on Lithium Niobate substrates), carefully packaging the die, and attaching the antenna, is not significantly cheaper than traditional semiconductor RFID chips. This example shows that all chipless tags are not necessarily low-cost, and underscores the importance of manufacturing and packaging costs as well as raw materials cost.

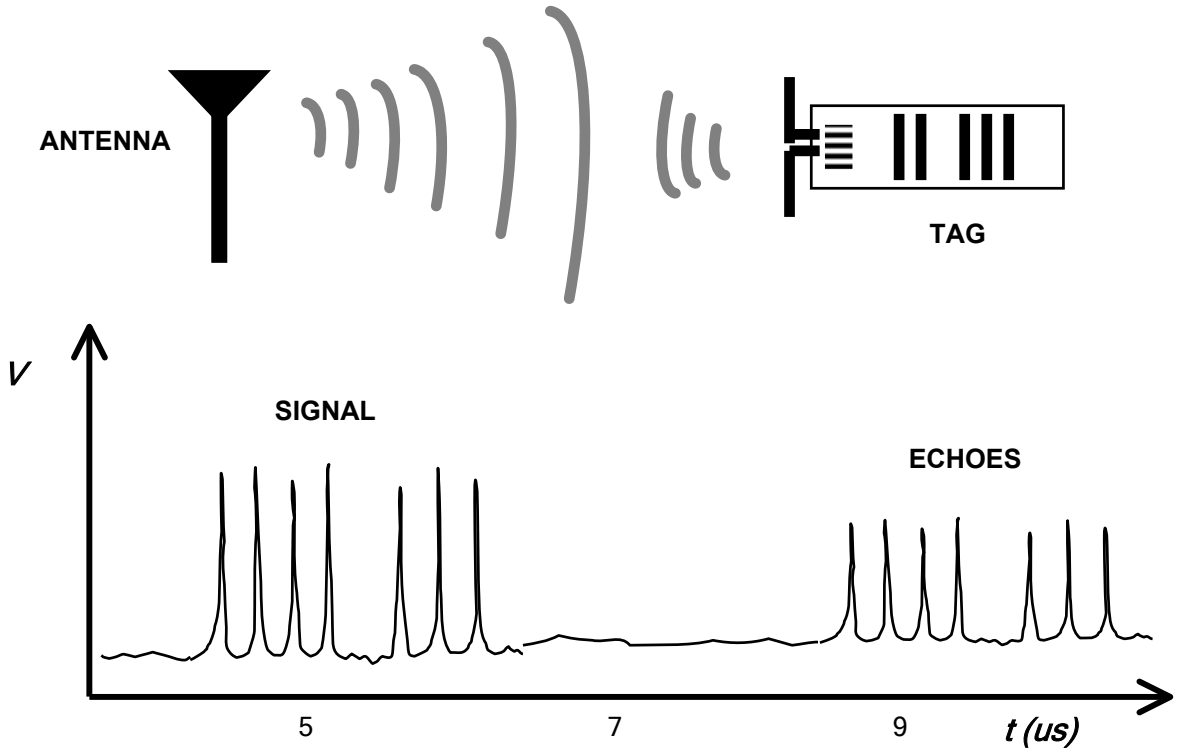

Figure 12. Schematic illustrating the basic operational concept (left); idealized M vs H loop for this structure (right).

3.2.1.2 Domain-Wall Kinetics

Another type of dynamic physical mechanism can be found in the motion of domain walls in magnetic materials. When a magnetic material is exposed to a time-varying magnetic field, the microscopic magnetic domains (with their associated magnetic spins) are induced to rotate. As the applied magnetic field is increased (or decreased) the transition region between differently-aligned domains, known as *domain walls*, are induced to move transversely. As more spins are aligned with the field, the changing magnetization of the material can be measured wirelessly (such as with a magnetic pick-up coil). The magnitude of the detected signal is proportional to the change in the materials magnetization, which depends on several factors including the speed of the domain walls and the shape of the material.

The domain wall motion and their resulting measured magnetization, however, is not a simple continuous function. Local stochiometric or physical defects in the material can act to temporarily pin the moving domain walls until sufficient energy builds up to free it. As a result, the movement of the domain walls, and the measured magnetization of the material, has jagged features known as Barkhausen jumps, indicating the jerky motion of the domain walls.

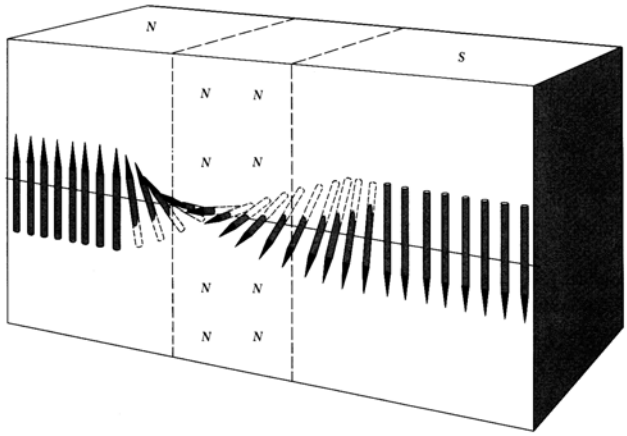

Figure 13. Schematic illustrating the basic operational concept (left); idealized M vs H loop for this structure (right).

In the mid-20th Century, scientists invented a simple method to identify and characterize different magnetic materials by literally listening to sounds induced by the Barkhausen flux jumps, as shown in Figure 19 below. Similarly, for electromagnetic tagging applications, it is interesting to explore the design of material structures that can be interrogated and identified wirelessly by a tag reader.

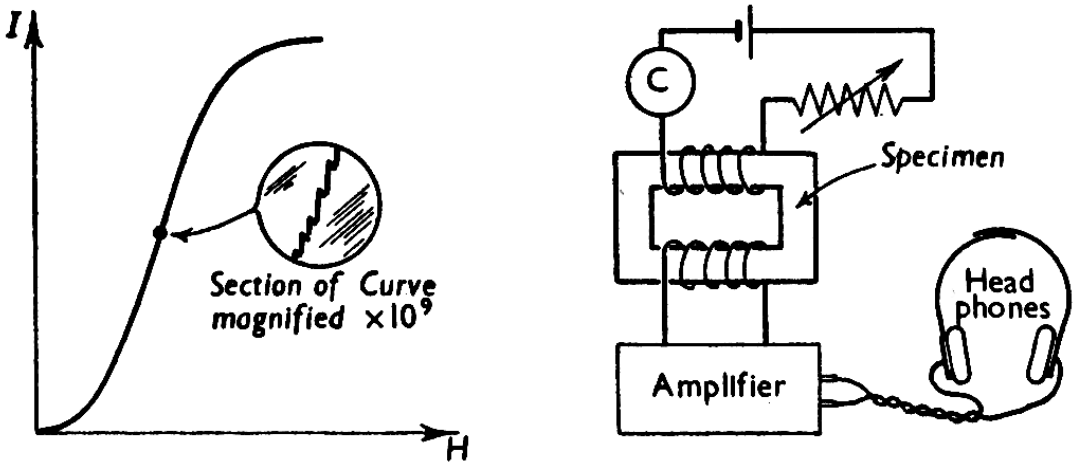

Figure 14. Schematic illustrating the basic operational concept (left); idealized M vs H loop for this structure (right).

3.2.2 Frequency Domain

As an alternative to time-domain methods, perhaps the most effective way to differentiate the electromagnetic response of a material structure from its surrounding environment is to employ the frequency domain. Thus, by designing material structures that respond to particular frequencies, it is possible to discriminate a tag signal from background noise.

3.2.2.1 LC Resonators

Structures that exhibit electromagnetic resonance are of particular interest to the field of electromagnetic tagging. One reason is that capturing a frequency response of a material structure can be accomplished with very little transmitted energy. Secondly, in the frequency-domain representation, resonances appear as peaks in the spectrum, and are thus easy to interpret and process even in the presence of environmental noise.

More specifically, resonance is a frequency-dependent stimulated response characterized by a large amplitude response at a specific frequency (or very narrow frequency band). This amplitude response is an indication that a resonant system has the ability to store energy at a particular resonant frequency. Energy storage in a passive material structure is sustained by a continuous exchange between one form of energy and another. This transfer of energy is sometimes called the circulating power. Energies can be in the form of kinetic energy and potential energy, or expressed in terms of electric fields and magnetic fields, currents and voltages, mechanical stresses and strains, pressure and displacement, or a mixture of these. In order to exhibit a large amplitude response, low internal losses and weak coupling to the external environment are also required. The ratio of total *stored* energy to the *dissipated* energy per unit cycle defines the quality factor, Q, of the resonator:

$$Q = \frac{W_{TOTAL}}{P / \omega} = \frac{\omega W_{TOTAL}}{P} \qquad \text{(Eq. 3)}$$

where W = total stored energy, P = the average dissipated power, and ω_0 is the resonant frequency. Qualitatively, the Q-factor is generally interpreted as an indication of the sharpness of the resonance peak.

Resonances are commonly created by constraining the flow of energy out of a physical system as defined by the physical boundary conditions. These constraints can give rise to reflected waves that constructively interfere to produce an enhanced amplitude. For example, constraining the ends of a taut violin string gives rise to a discrete set of frequencies that can exist; if the string is excited acoustically by a signal that is an integer fraction of half-wavelengths then the string will exhibit a resonance.

In an electromagnetic system, the boundary conditions are determined by the spatial dependence of the electromagnetic material properties. In structures having physical dimensions

that are on the scale of the electromagnetic wavelength or larger, it is customary to describe resonators as transmission lines with additional boundary conditions added along the direction of propagation. For example, the transverse 2D boundary conditions of a transmission line define a band of frequencies which can propagate, and adding a third boundary condition in the direction of propagation (e.g. by adding metal plates to either end of a metal waveguide segment) will give rise to a discrete set of resonant frequencies.

a) b)

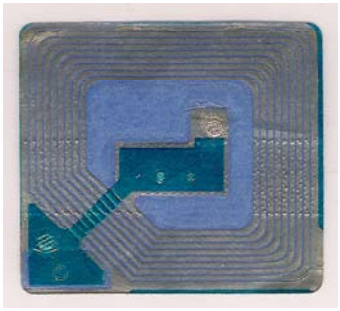

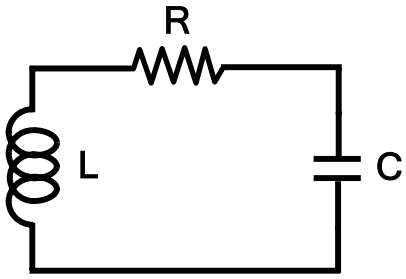

Figure 15. Schematic illustrating the basic operational concept (left); idealized M vs H loop for this structure (right).

In electromagnetic tagging, the most common type of resonator is planar LC resonator, which appears as a flat spiral coil structure and is commonly used as an anti-theft tag. This structure can be modeled as a series RLC (resistor-inductor-capacitor) circuit (Figure 7b), also known as a tank circuit. The inductor is the magnetic energy storage element, and the capacitor is the electric energy storage element. By considering the flow of current as a function of time, it is easy to see that the magnetic energy is maximum when the electric energy is minimum, and vice versa. Assuming that the resistance in negligible, the current flowing in the resonator (I=V/Z) is maximum when the total impedance, $Z=R+jX \approx jX$, around the circuit is minimum. This occurs when the total reactance $X=X_m+X_e$ is zero, where $X_m = L\omega$ and $X_e = -1/C\omega$. By inspection, this implies that the resonant frequency occurs at $\omega_0 = 1/\sqrt{LC}$. Of course, the resonance frequency can also be found by solving the differential equations for the circuit with R=0.

By understanding the nature of resonance and Q-factor is possible to design material structures that have a predictable frequency response, and by creating structures with multiple selectively-tuned resonances, it is possible to create LC tags with a capacity for information storage.

3.2.2.2 Magnetoelastic Resonators

Magneto-mechanical resonators is another type of resonant material structure that is commonly found in anti-theft labels, and generally exist in the form of metallic strips or wires. Unlike the resonators mentioned in the previous sections, this type of resonator employs a *mechanical* resonance that can be excited with a *magnetic* field and is best described in terms of basic physics and materials mechanisms.

Figure 16. Electronic Article Surveillance label (Ultramax™ label by Sensormatic, Inc.) containing magnetoelastic strip and trapezoidal bias magnet.

For the purpose of electromagnetic tagging, resonators can be made from magnetoelastic materials by incorporating them into a *mechanically*-resonant structure, which can then be remotely excited and detected *magnetically*. However, unlike a standard LC resonator, the observed amplitude vs frequency of a magnetoelastic resonator is dispersive in nature, while the phase vs frequency signal exhibits a single peak (Figure 11). A lumped-element equivalent circuit model explaining the qualitative behavior of a magnetoelastic resonator can be found in the literature [Butterworth]. Also, the magnetomechanical coupling coefficient depends on the absolute value of the magnetic field and is zero if the applied bias field is zero, so a finite bias field is required for operation. In commercial EAS labels, this DC bias field is provided by a thin permanent magnet layer that can be de-magnetized at the point of sale to deactivate the tag.

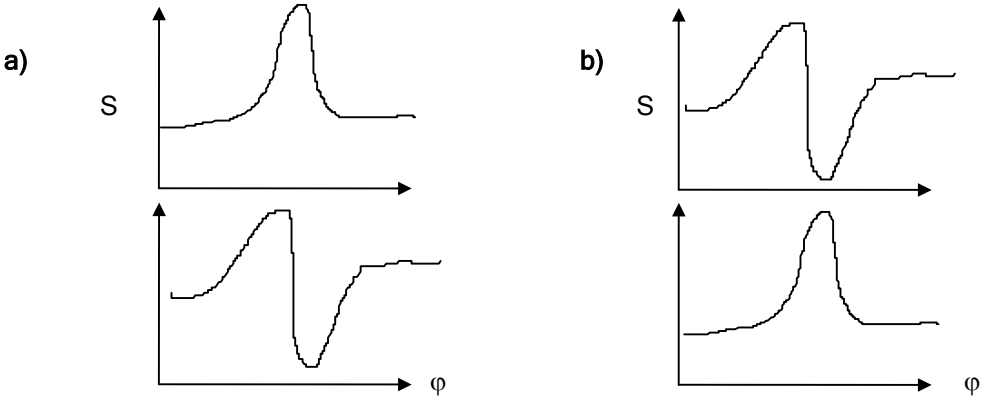

Figure 18. Amplitude S and phase φ as a function of frequency for a) an LC resonator and b) a magnetoelastic resonator.

3.2.2.3 Harmonic Generation

Some materials generate harmonics when placed in an electromagnetic field having a particular frequency and amplitude. Harmonic generation is a general term often discussed in a variety of contexts that span the entire electromagnetic spectrum and have a variety of physical origins. For example, materials can exhibit harmonics in their magnetic properties, transport properties, or optical properties. Such materials can be used in applications analogous to those employing non-linear semiconductor electronic devices. Perhaps the most rapidly growing application of such properties can be found in non-linear optical materials that are used to make optical parametric oscillators, phase-conjugate mirrors, and optical computing elements. However, at low frequencies, harmonic generation has been perhaps most widely studied in magnetic materials and magnetic devices, such as transformers.

In the electromagnetic tagging of objects, harmonics generated by a soft magnetic material can be used as a means of discriminating the response of the object from the surrounding environment. Some anti-theft tags used for electronic article surveillance have employed this mechanism for at least two decades, and are known as *harmonic* tags. The earliest form of harmonic tag employed a diode as the non-linear element to produce the harmonics. If the tag antenna is tuned to the propagation frequencies, such a tag can be detected at great distances (~ 100 meters). At lower RF frequencies (~100 KHz) such tags have been used to locate people buried in an avalanche. At much higher frequencies (2.4 GHz) such tags are used commercially to tag and track butterflies.

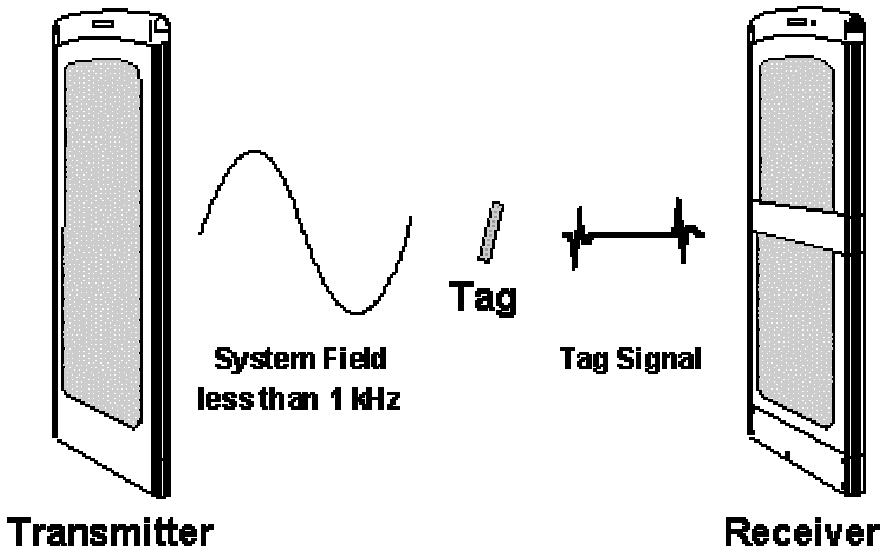

Figure 19. Diagram depicting a harmonic tag between the transmit and receive antennas. Generally, one of the antennas functions as the exciter and the other functions as the pick-up coil.

Most commonly, however, harmonic tags are used in the retail market for electronic article surveillance, manufactured by companies such as 3M and Sensormatic. In its simplest form, a harmonic tag is comprised of a thin strip of magnetic material a few centimeters long. The basic elements of a detection system for such tags is shown in the figure below. The exciter antenna generates magnetic field of a fixed frequency (typically less than 100 Hz) and the receive antenna detects the higher-order harmonics (1-20 KHz) produced by the tag material.

3.3 Information Coding

Once the physical mechanisms and physical constraints of a particular tag design is known, it is then possible to choose an appropriate representation for the information stored in the tag and define an appropriate coding algorithm to convert the analog signals into digital information.

From the perspective of the tag reader, the overall data decoding process can be divided into three basic steps illustrated in Figure 19.

Figure 11. Data decoding process employed by a chipless reader.

Each of these steps can be described as follows:

- **Waveform detection:** the RF front end of the tag reader must have the necessary resolution and dynamic range to detect particular features in the analog waveform without excessive clipping or filtering. Also, it is often useful to preserve phase information as well as magnitude. In the case of a SAW tag, for example, the RF front end must have sufficient gain and bandwidth to detect and resolve the individual reflected pulses from the tag.
- **Feature extraction:** the reader must apply the necessary analog signal processing to detect and measure specific features in the analog waveform. These features can be the reflected pulses of a SAW tag, resonant peaks from an LC array, flux jumps from a magnetic materials tag, or the length of the transient ringdown in a resonant structure, for example.
- **Feature decoding:** Once the specific features are measured and digitized, an algorithm is applied to convert this set of features into digital data. This decoding algorithm must

represent a consistent mapping between the analog features and the digital bits. In addition, this algorithm must be robust against signal variations due to manufacturing tolerances of the tag.

Although the tag communicates its information to the reader using signals that are dynamic in both time and frequency, in most cases it is possible to choose one representation or the other. For simplicity, time and frequency encoding methods are discussed separately in the following sections.

3.3.1 Time-Domain Data Coding

As with Morse code, semaphore or smoke signals, the most common – and perhaps the oldest – means of coding information is to modulate a signal over time, thus transmitting a series of tones, patterns or symbols.

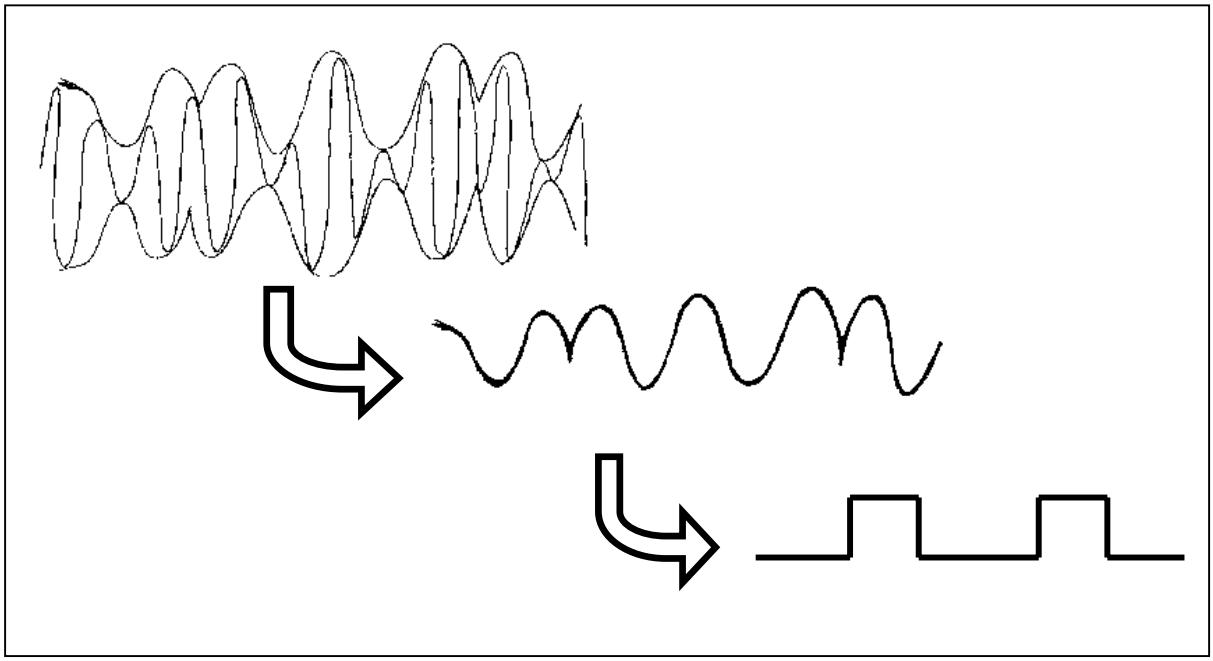

Figure 23. Data decoding process employed by a conventional RFID reader..

Chip-based RFID tags employ time-domain signaling almost exclusively, and is illustrated in Figure 15. By internally varying its input impedance, the RFID chip is able to create a tiny modulation in the reader field via the tag antenna. The amplitude-modulated signal transmitted back from the RFID tag is then stripped of the carrier and demodulated to recover the digital waveform. The digital bits are then read sequentially as a digital bit stream.

For the purpose of time-domain signaling and coding, chipless RFID suffers from several disadvantages compared to chip-based technologies. A lack of a time base and lack of control circuitry restricts the ability to code the tag ID information as a conventional digitally-modulated

waveform. In a magstripe, as can be found on the reverse side of any credit card, the digital bits are spatially encoded sequentially with interspersed clocking bits that set the data timing regardless of the speed with which the car is scanned over the magnetic read head. However, in the chipless case, the timing of the tag response is completely determined by the characteristic time scales of the electromagnetic interactions. It is not possible, for example, to slow down the tag data rate in order to increase the signal to noise ratio at the reader. Perhaps some day it may be possible to efficiently interrogate a tag with an encoded sequence of pulses and wait for the tag to echo its response. We are not quite there yet.

Without a clock signal to tell the reader when to sample a data bit and without a useful threshold level to use for bit comparisons, the chipless tag reader requires some degree of analog signal processing in order to do its own feature extraction and data capture. Two general types of features that a reader may detect are the following:

- Periodic pulses, zero-crossings, or sharp features in the *steady-state* response of the tag when excited by a continuous-time (CW) waveform of the reader
- *Transient* response waveform of the tag following a discontinuous change in the reader waveform, such as an RF pulse or a change in the DC-level of electric or magnetic field.

Once the features are found and measured by the reader, it is necessary to convert those time measurements into meaningful data. In some cases, such as SAW tags, the relationship between digital ID bits and the tag's electromagnetic response is relatively straightforward. However, in other cases, such as in magnetic materials or quantifying the ring-down modulations in an LC array, the conversion from time measurements to digital bits is somewhat arbitrary, and it is best to chose a coding algorithm that matches the particular physical mechanism employed.

For a given set of time measurements, the following are two possible approaches to bit coding algorithms:

- **Fourier Transform (FFT):** the time measurements or time wave from can be placed into an array and the digital ID code can be derived from the fourier coefficients.

- **Statistical fitting:** the time data can be fitted to a particular model, such as a Poisson process, and the statistical parameters extracted from the data can be used to create a digital ID code.

As with other time-domain techniques, external noise and interference can be a problem, but it is possible to improve the signal-to-noise ratio with standard techniques such as averaging and synchronous sampling.

While time-domain signaling and coding is the adopted standard for chip-based RFID applications, finding useful and controllable time signatures in chipless systems is still very much an active research field.

3.3.2 Frequency-Domain Data Coding

The frequency domain is commonly used for detecting and analyzing various classes of chipless RFID tags. However, there is no standard universal approach for converting an arbitrary frequency spectra into an ID code. However, if we really want to consider storing digital information in materials and in their electromagnetic signature, it may be possible to create an approach that would be valid for specific classes of physical phenomena. Three basic categories are discussed below.

3.3.2.1 Frequency Response

The most general type of frequency-domain data is the frequency response of a material which can be collected using a magnetic or capacitive type of probe. Both the magnitude and phase of the electromagnetic response can be collected examples include complex permittivity measurements or magnetic susceptibility measurements. Electromagnetic materials measurements such as these are commonly done for materials characterization and materials development. For example, microwave cake batter is measured in order to characterize it's ability to cook in a microwave oven. For sensors, looking at the dielectric frequency response of motor oil, for example, provides an indication of when the oil is contaminated and needs to be changed. A sample dielectric spectrum of whole milk is shown in Figure 21.

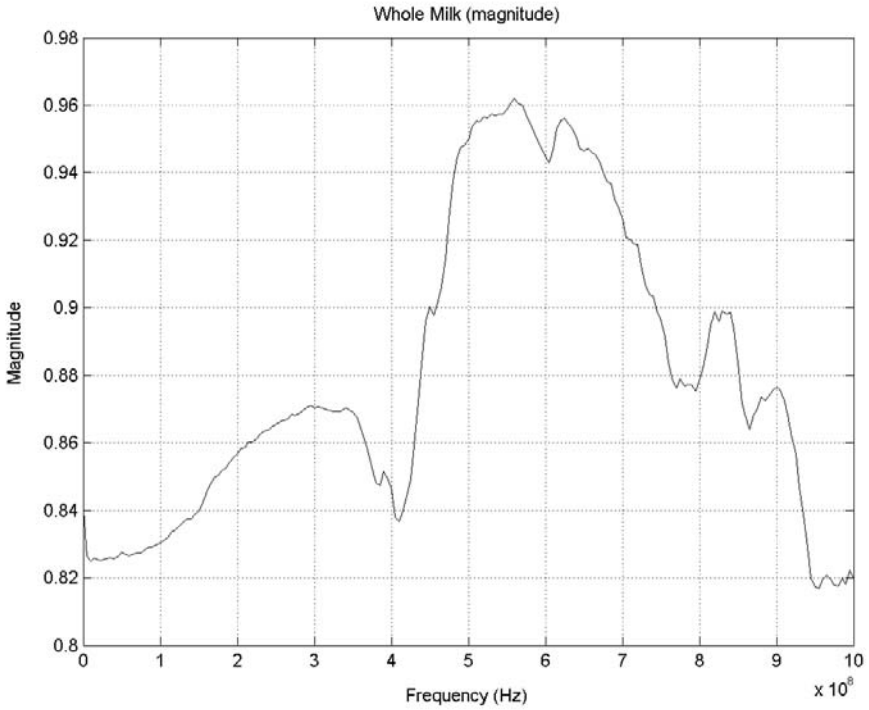

Figure 24. Sample frequency response data taken from whole milk.

Although the frequency response of different materials and material structures can vary greatly, these spectra do not in general exhibit any specific features that are simple to identify. Therefore, unless the background environment is known, it is of little value to use this type of data for electromagnetic tagging. If there was an interest in doing so, the only standard approach to numerically characterizing a particular spectrum is to perform a Fourier decomposition, using a standard set of basis functions, which can be sinusoidal or wavelets.

3.3.2.2 Harmonic Spectra

The frequency spectrum of harmonic generator materials is easily distinguishable from the background environment, making them useful for tagging purposes. Frequency spectra derived from harmonic phenomena contain a considerable amount of periodicity on many scales, as shown in Figure 21 and Figure 22.

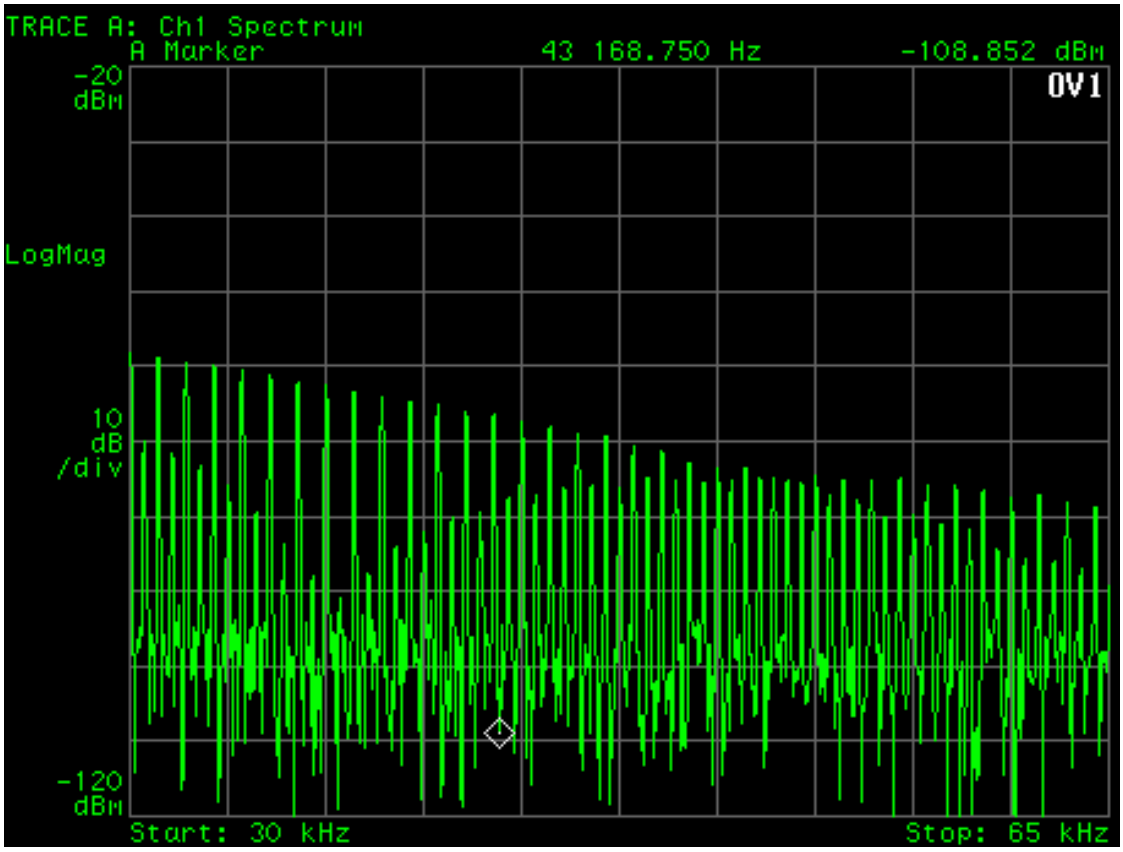

Figure 25. Section of harmonic spectrum of magnetic wire harmonic tag with fundamental excitation of 500 KHz.

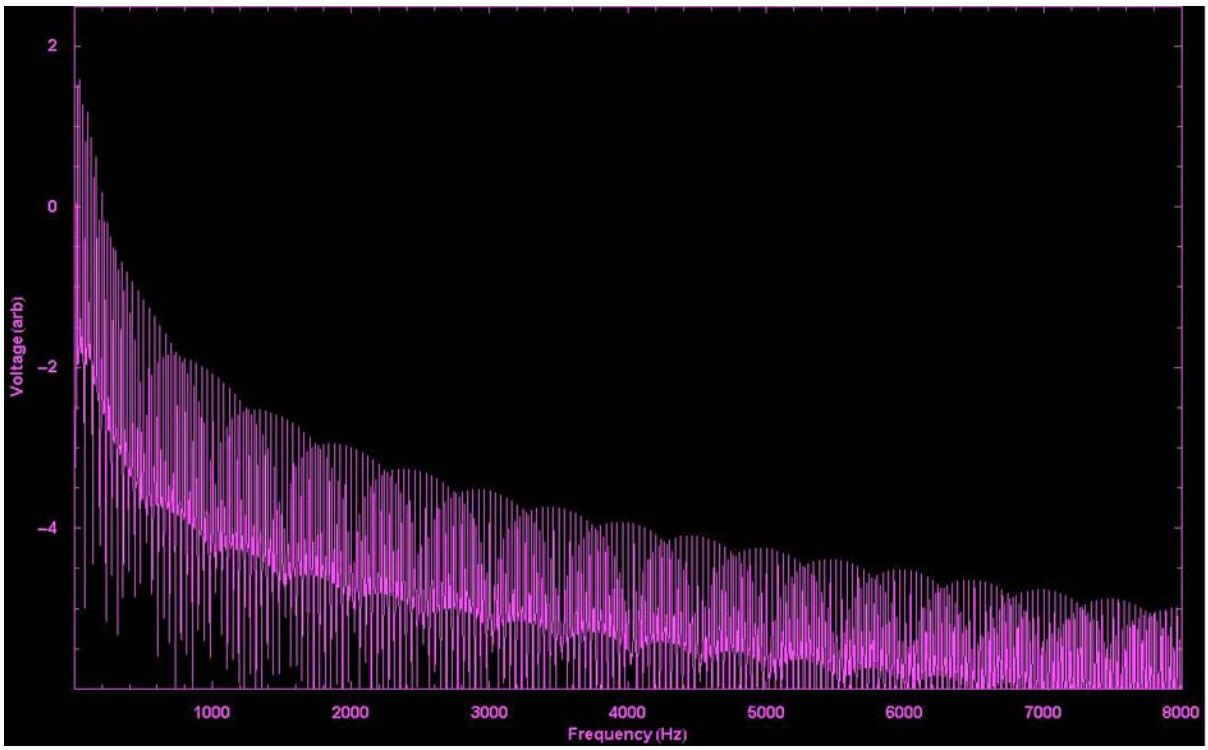

Figure 26. Simulated harmonic spectrum of harmonic tag with DC magnetic bias.

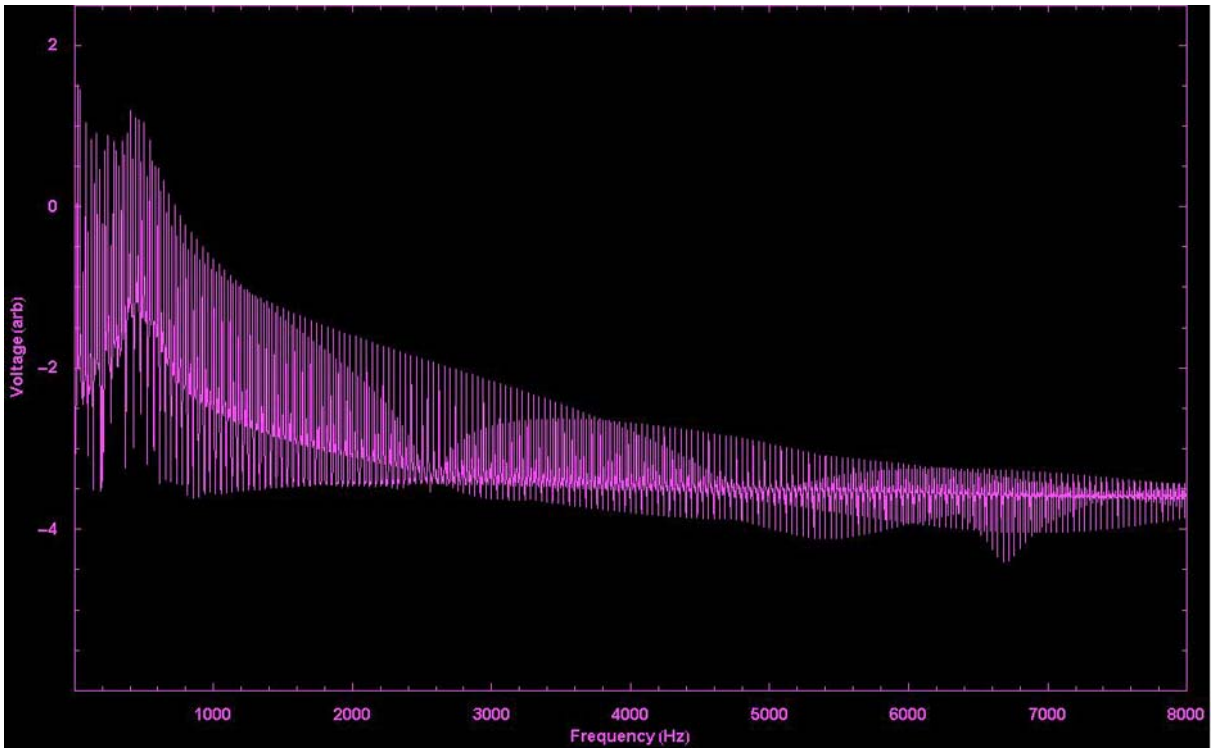

Figure 27. Simulated harmonic spectrum of harmonic tag with DC magnetic bias.

Although the spectra of harmonic tags can have many complex features (and even aesthetic beauty), the information content is relatively low, due to the strong and predictable periodicity. For most measurements, the magnitude of the tag signal is commonly used; however, the phase spectrum can also be of interest. In general, for the process of feature extraction, the relevant parameters to record are the following:

- **Total harmonic power:** this is a measure of the integrated power present in all the harmonics. This value depends on the materials properties of the tag but also depends on the strength of the excitation field; therefore some calibration is necessary.
- **Harmonic cut-off frequency:** This is the frequency of the highest-order harmonics. This property is strongly-dependent on the material properties and tag design. In order to standardize this measurement, it should be specified at some amplitude threshold relative to the excitation field strength. For an excitation frequency of 500 Hz, a good harmonic generator can have a harmonic cut-off frequency over 150 KHz.
- **Period of amplitude modulations:** As evident in the figures, the amplitude of the harmonics are not constant or monotonic but have a periodic frequency dependence. This "period," or frequency spacing, is a function of the applied DC bias field among other

factors. Odd and even harmonics should be measured separately, since they may have different periods. If a harmonics strip is subjected to a non-homogeneous DC bias field, then the observed amplitude variations may not be periodic (Figure 23) and will need to be characterized more specifically.

- **Baseline frequency response:** In addition to the amplitude variations of the harmonics, the non-harmonics baseline has a frequency response of its own. This frequency response can reveal certain resonant effects due to the macroscopic geometric structure of the tag itself. As an example, we can see the observed peak in the baseline of the spectrum shown in Figure 23.

After extracting the features listed above, a corresponding digital code can be created. In the case of magnetic materials, it is also common to probe the materials structure as a function of the applied DC magnetic field, so it is difficult to devise a universal coding method that would apply in all cases. For the case of magnetic materials, further iinformation can be found in Chapter IV.

3.3.2.3 Resonant Spectra

The use of resonant structures is perhaps the most practical method for encoding data in chipless tags. The frequency response of a material structure contains features that are relatively easy to extract and can be collected by a variety of simple electronic hardware.

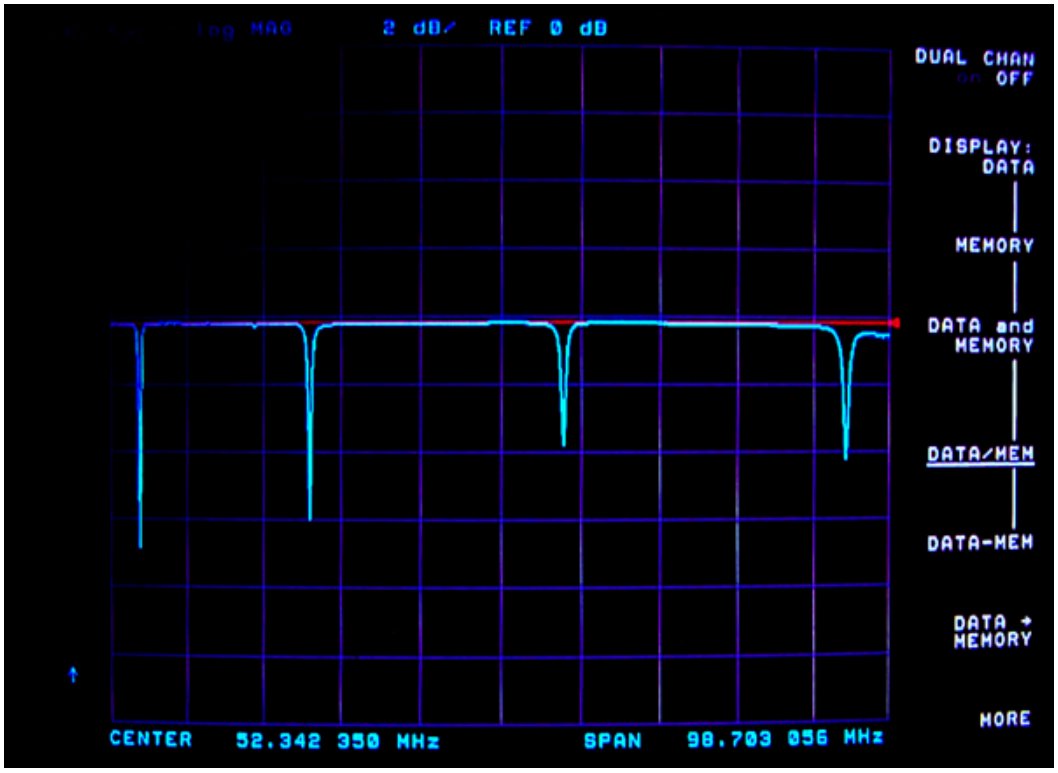

Figure 28. Sample frequency response of a multi-resonant LC tag.

A sample frequency response of a resonant tag is shown in Figure 28; although the magnitude data is shown in the figure, the plot of phase vs. frequency can also be useful for certain applications. The physical design of such structures is discussed in more detail in Chapter V. Comparing this figure to the frequency spectra of a harmonic tag, it is easy to see the advantage of resonant structures for decoding data.

.3.2.3.1 Feature Extraction

Given the simplicity of the raw data from a resonant tag, the step of feature extraction is thus essentially reduced to simple peak-finding, which can be executed relative to a particular threshold signal value. The basic parameters that are of interest here are the following:

- **Peak position:** The center frequency, F_0, of every peak above a specified threshold amplitude is recorded. In order to utilize the full precision of the tag, the frequency resolution of the tag reader should be a least $F_0/4Q$ to ensure adequate measurement of the peak position.
- **Peak Q-factor:** Without calibration of the coupling between the tag and the reader antenna, the observed Q is actually defined as the *loaded* Q, which is always lower than the actual *unloaded* Q of the tag. Precise determination of the observed Q-factor for each peak is done by measuring the center frequency of the peak as well as the width of the peak at half-maximum, ΔF, (also defined as the 3db-points if log scale is used) and applying the formula $Q = F_0/\Delta F$. For simple measurements, it is not necessary to measure the peak width at exactly half-maximum. For any reasonably low-loss resonator with Q>50, it is adequate to simply measure the peak width at a fixed pre-set threshold amplitude value and for weak coupling the loaded Q and unloaded Q are roughly equal.
- **Peak amplitude:** Peak amplitude is generally measured with relative to the transmitted power signal level. By convention, logarithmic units (**db**) are often used; absolute levels can be specified in terms of **dbm**, which are decibel units relative to 1 mW of power (for example, 20 dbm = 100 mW).
- **Relative measurements:** Each of the parameters listed above can also be measured relative to the values for other peaks. In some cases, for example, we may want to monitor the spacing between two or more peaks, even when all the peaks have shifted higher in frequency. Relative measurements are particularly useful for the amplitude and Q measurements, since the loaded Q and the amplitude are highly dependent on the coupling between the tag and the reader. For senor tags, in particular, it is often useful to design a “control” peak that remains fixed, while the other peaks are variable; thus the control peak can be used as a relative calibration for measurements of the other peaks.

For the purpose of feature extraction and data coding, it is most practical to work with the resonant frequency values alone, since these remain invariant under most operating conditions. Given a set of frequency values, we must then devise an appropriate algorithm for translating a set of frequency points to a single numeric value or to a string of digital bits.

.3.2.3.2 Feature Decoding Algorithm

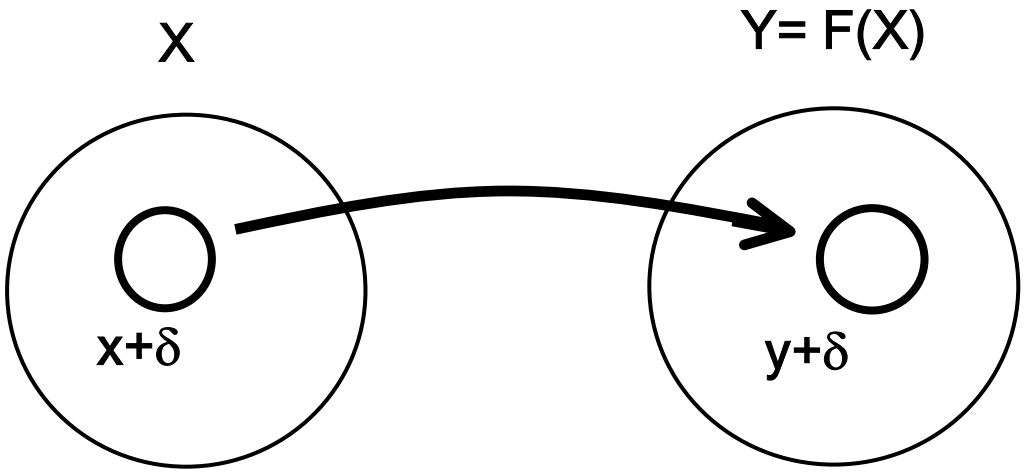

Figure 29. Graphical representation of desired encoding function.

In designing a coding algorithm, it is necessary to consider the desired properties of the algorithm. In the ideal case, we require the algorithm to meet the following requirements:

- **Uniqueness:** The algorithm should perform a mapping between the extracted feature parameters and an ID number, such that this ID number is unique to this particular set of feature parameters.
- **Continuity:** The algorithm should have a crude measure of continuity, such that similar sets of feature parameters will map to similar ID numbers. Since the notion of similarity is somewhat subjective, various criteria can be chosen. This continuity requirement is desired not simply for the purpose of comparing one tag to another, but is necessary for **resistance to noise**. Due to manufacturing tolerances and operating conditions, it is not possible to produce truly identical tags; therefore, if the continuity condition is met, then two tags that are nearly identical will not produce wildly different numerical values.
- **Compactness:** For practical reasons, it is desirable that the ID number associated with each tag be as short as possible. It is faster and less resource-intensive to work with 100-digit binary numbers rather than 1000-digit numbers, for example.

- **Computational simplicity:** Since there is interest in implementing this algorithm in a low-cost tag reader, the algorithm must be sufficiently simple to run on a simple 8- or 16-bit microcontroller with a minimum of memory resources.

For the case of multi-resonant tags, a simple attempt at such an algorithm is to discretize the frequency axis into frequency bins with a bin-width approximately equal to the average peak width. A digital bit string can then be constructed, point-by-point, by comparing the signal value at each frequency point to a particular threshold level, and thus assigning to that point a digital "1" or digital "0." Thus, by doing a frequency sweep, a sequence of digital "1's" and"0's" would be generated by the presence or absence of a resonance peak. This is illustrated in Figure 24.

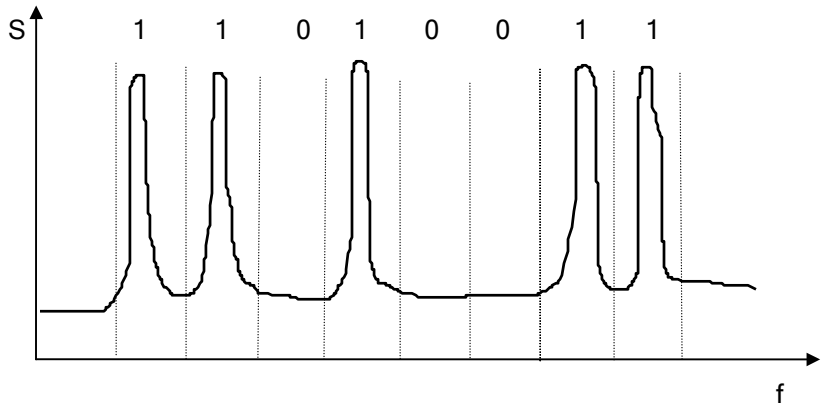

Figure 30. Sample response from a tag containing five resonators of different frequencies.

The main disadvantage of the simple coding in Figure 24 is that the continuity condition is not met. If the peak positions are perturbed slightly, all of the bits in the ID string are equally likely to change. If the ID string is interpreted numerically in a conventional manner, as right-to-left or left-to-right, then even a small shift in one of the peak positions can produce a large change in the numerical result.

In order to design a better coding algorithm, it is necessary to use a method of generating digital bits that are not affected by small changes in the peak positions. A viable approach to this problem is to make use of simple convolution. A proposed approach is illustrated in Figure 25. If we start with the raw digital ID string, collected as mentioned previously (Figure 24), it is possible to apply successive convolutions in order to generate higher-order bits that are less sensitive to changes in peak position. A simple way to understand this approach is to consider each convolution step as a successive blurring of the data. We can then define the property of similarity as follows: *Two tags are considered similar, if after successive blurring steps, the two tags produce identical bit strings; the less number of blurring steps that are required to achieve identical bit strings, the greater the similarity.* Thus, two tags with identical peak positions will require no blurring and be the most similar; and tags with very different distributions of peak positions will require many blurring steps to produce identical bit strings and thus be the least similar.

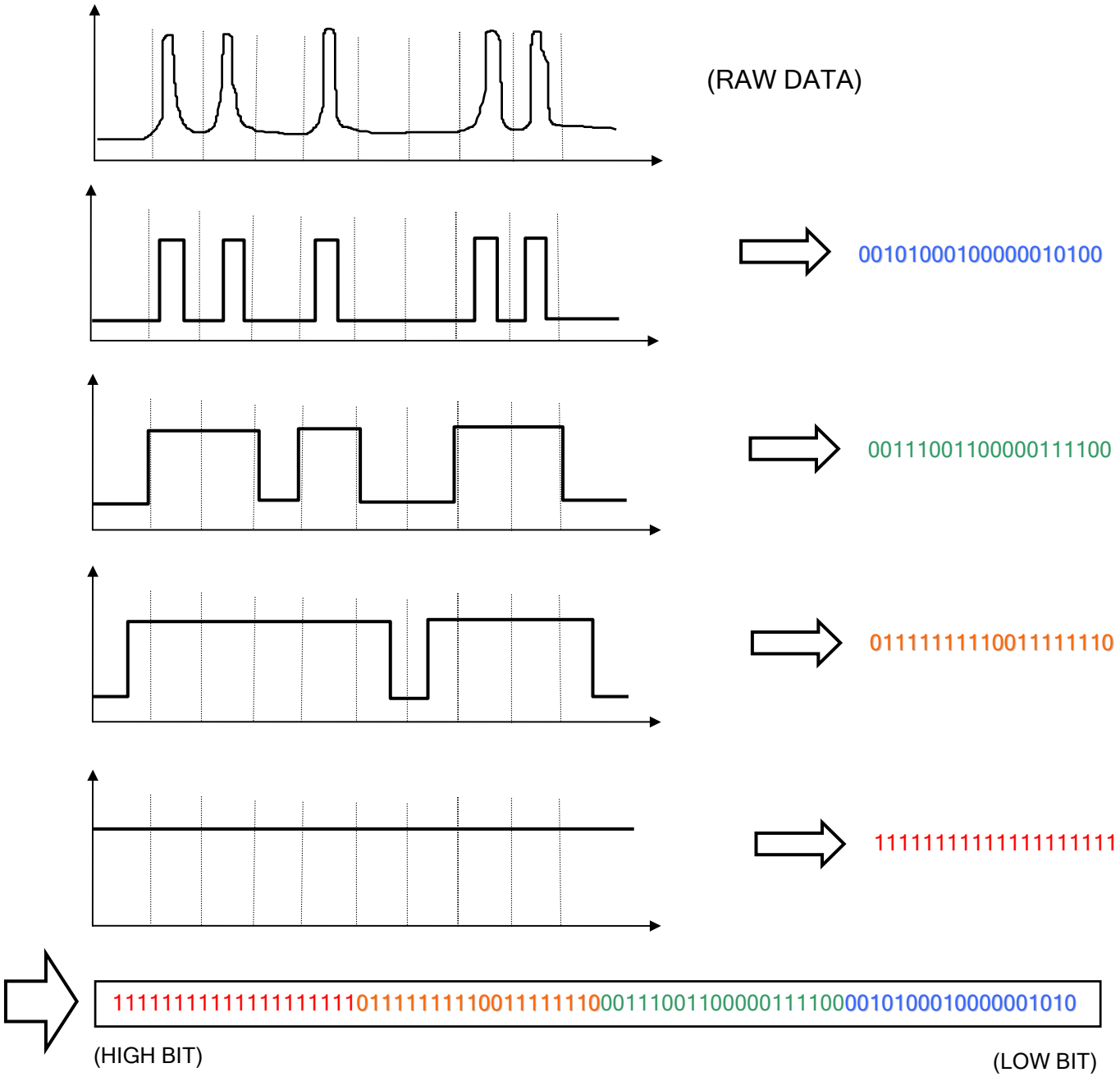

Figure 31. Sample response from a tag containing five resonators of different frequencies.

Once the convolution steps have been executed on the raw data string, all of the bit strings resulting from each of the convolution steps can be concatenated together to form a full ID string for the tag. The length of the ID string then depends on the length of the original raw data string, **N**, and the number of convolutions steps, **I**. At worst case, if we assume no data compression, the length of the total ID string is **NI**. Given the fact that a typical value for **N** is 100 or so, and **I** is on the order of $\log_2 N$, we see that the length **NI** of the ID string can be undesirably long.

By observing the result of each convolution step, it is clear that a significant amount of redundancy can be eliminated. I propose an iterative algorithm, where each iteration is comprised of two steps, a *convolutions step* and a *compression step*. In the *convolution step*, a logical OR is performed between neighboring bits that simulates the blurring effect of convolution. Then, in the *compression step*, the length of the bit string is halved by performing a logical OR between pairs of adjacent bits. A subtle but very important rule of this algorithm is that the pairs of bits used in the convolution step are *interleaved* with the pairs of bits used in the compression step. Without this interleaving, the performance of the algorithm will be poor, since it is possible for a small bit shift in the raw data to propagate up the binary tree and still produce changes in the higher-order bits. We can thus view the interleaving rule as a means of ensuring that blurring will occur *across* branches of the binary tree, and thus produce higher order bits that are less susceptible to small changes in the original peak positions. The basic algorithm is illustrated in Figure 32.

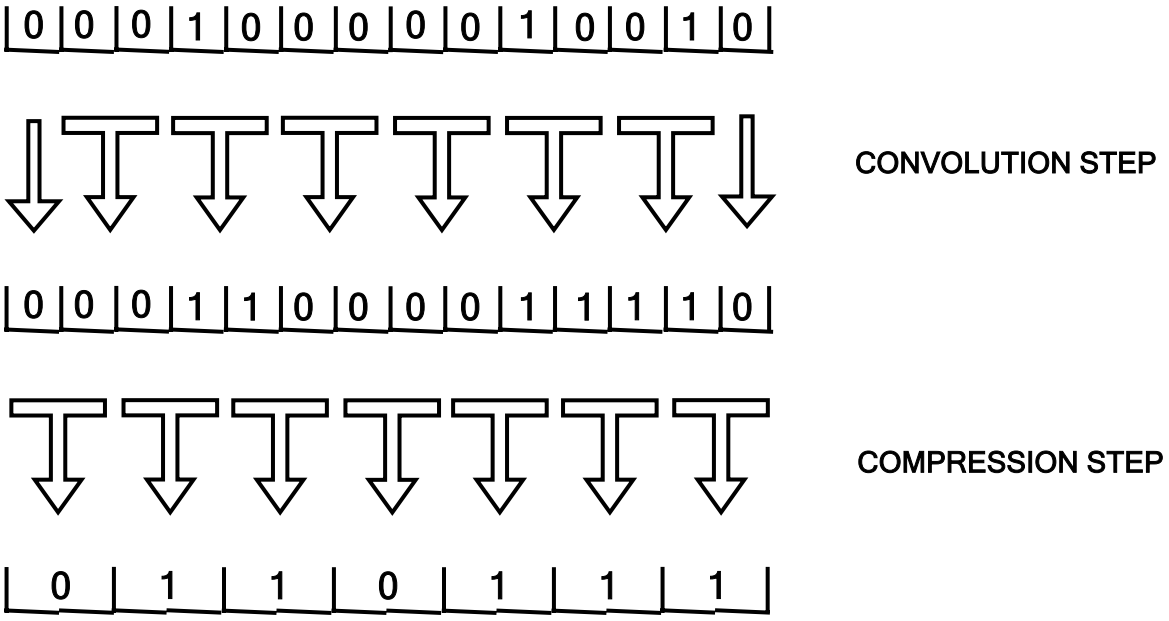

Figure 32. Illustration of single iteration of coding algorithm.

Using the improved iterative algorithm to an **N**-bit raw data string, the length of the tag ID string can be reduced considerably, from $N \log_2 N$ to **2N.** In terms of computation time, we can also easily determine the number of computation steps required. Given the fact that each iteration contains two separate computation steps, the total number of computation steps required is $2N \log_2 N$, which is comparable in speed to an FFT (Fast Fourier Transform) calculation.

As an example, the algorithm was applied to 2 different sets of resonant data, using a raw data string length of **N**=128 containing 5 resonant peaks. The variance of the peak positions was set to 2%, producing similar but distinct raw data. The results are shown in Figure 33.

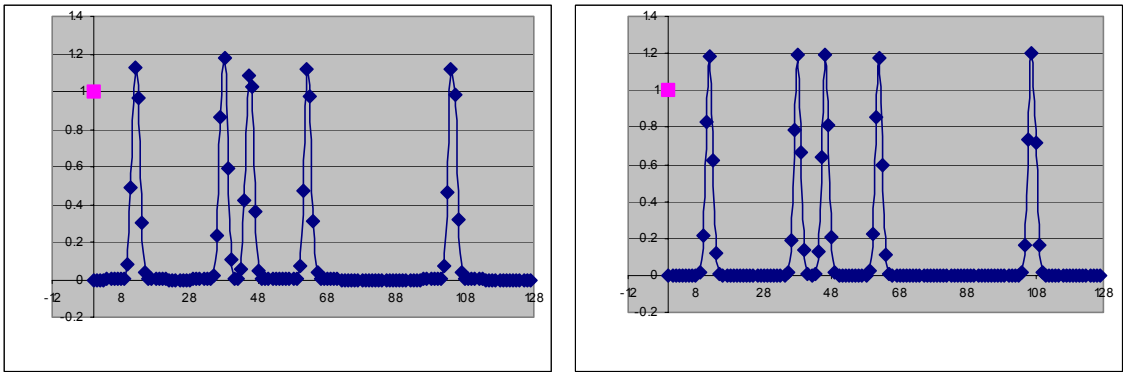

0	0	1	1	1	1	1	1	1	1
0	1	1	1	1	1	1	1	1	
1	1	1	1	1	1	1	1		
1	1	1	1	1	1	1	1		
0	1	1	1	1	1				
0	0	1	1	1	1				
0	0	1	1	1	1				
0	1	1	1	1	1				
1	1	1	1						
1	1	0	0						
1	1	0	0						
1	1	0	1						
1	1	1	1						
0	1	1	1						
1	1	0	1						
1	1	0	0						
1	1								
0	0								
0	0								
0	0								
0	0								
0	0								
0	0								
0	0								
0	0								
1	1								
1	1								
0	0								
0	0								
0	0								
0	0								
0	0								

0	0	1	1	1	1	1	1	1	1
0	1	1	1	1	1	1	1	1	
1	1	1	1	1	1	1	1		
1	1	1	1	1	1	1	1		
0	1	1	1	1	1				
0	0	1	1	1	1				
0	0	1	1	1	1				
0	1	1	1	1	1				
1	1	1	1						
1	1	0	0						
1	1	0	0						
1	1	0	1						
1	1	1	1						
0	1	1	1						
1	1	1	1						
1	1	0	0						
1	1								
0	0								
0	0								
0	0								
0	0								
0	0								
0	0								
0	0								
0	0								
0	1								
1	1								
1	1								
0	1								
0	0								
0	0								
0	0								

Figure 33. Portions of ID code for 2 separate 128-bit data sets.

By monitoring the bit codes produced at each step in the bit code algorithm, it is also possible to estimate the potential amount of information that can be stored in a given tag design with a given manufacturing uncertainty. It is possible to test a certain number of "identical" tags and compare their data strings to see at which point in the calculation the output bit strings match; the length of that string gives an approximate measure of the amount of data that can be successfully stored using that tag design. For example, from the tag data shown in Figure 33, we can see that the ID code for the two tags do not match until the 16-bit data string. Therefore, this amount of

process variability can only support between 16 and 32 bits of data storage. If more bits of storage are desired, then the manufacturing variability needs to be reduced.

An additional property of this algorithm is that it can be easily scaled to large or small data sets, with the only restriction being that the data set length be a power of 2. This *multi-scale capability* is very important, since it enables efficient tagreader design. For example, a smart tag reader could easily adapt to a different tag design by changing its frequency resolution in real-time and change the raw data length without affecting the tag ID code. If finely-tuned tags ar used, the tag reader can increase its frequency resolution to access more bits of information; on the other hand, if the tags are very coarsely-tuned, then the tag reader can decrease its frequency resolution in order to gain speed. In addition, this algorithm can be adapted to suit the limitations of the reader itself, and can easily be adapted to both low-cost, simple readers, and high-performance readers as well.

The bit code algorithm presented here is perhaps not ideal, but it possesses several attractive properties. This algorithm meets the basic requirements of uniqueness, continuity, and computational simplicity. The compactness of the ID code can perhaps be improved further; however, this property is a trade-off with the desired multi-scale property of the code as well. This algorithm serves as a good example of the type of coding process and multi-scale properties that are desirable for systems that integrate digital information with analog physical systems.

3.3.3 Hybrid Methods

Although the approaches presented in this chapter have discussed time-domain and frequency-domain methods explicitly, there is certainly an opportunity to develop coding and decoding methods for data that spans both time and frequency. Many variations are possible.

Commercial communications technologies routinely use both time- and frequency- domain processing for coding and decoding data, particularly in applications where significant interference noise exists and digital and analog signals are present simultaneously. One good example of present-day coding techniques is the new HomePlug™ standard, which enables digital data to be transported along power lines at Ethernet-like data rates. Orthogonal-frequency-division multiplexing is used to transmit on as many as 84 carriers in the 4.5- to 21-MHz band. Viterbi and Reed-Solomon forward error-correction codes are interleaved with the data

to ensure the receiver can recover the data even if parts of the bit stream are lost. The communications module maps the encoded data onto a set of channels that the transmitter and receiver previously agree upon, then an inverse FFT processor modulates each bit stream to create each channel's waveform, converting the signals from the frequency domain to the time domain.

As we learn and invent new approaches to encoding information in physical systems, perhaps the field of chipless RFID will follow a similar evolution in complexity to that of existing communication systems.

CHAPTER IV.

Tags for Identification: Magnetic Materials

Magnetic materials play an important role in chipless RFID as well as in information technology in general. The invention of magnetic recording media and magnetic core memories were key milestones in the development of computer technology, and magnetic materials are still revolutionizing the computer industry through ever-higher capacity disk drives and other storage media. One of the simplest and most common example of magnetic information technology, however, is the magnetic stripe that is found on the reverse side of the common credit card.

Magnetic materials have been of historical significance in the electromagnetic tagging industry as well, often providing simpler and lower-cost substitutes for electronic devices such as LC resonators or harmonic diodes. The use of magnetic materials has generally been limited to Electronic Article Surveillance (EAS); however, several companies have explored approaches to using these materials to make ID tags as well.

Two broad classes of materials have served as the workhorses of magnetics-based electromagnetic tagging. These are termed soft magnetic materials and magnetostrictive materials. I have explored both of these families of materials as part of my graduate work, and some of these studies are summarized in the sections below, following an introduction.

4.1 Introduction to Magnetic Materials

Despite the importance of magnetic materials to chipless RFID, it is a topic that is rarely discussed in the chip-based RFID community. As a benefit to the reader, I have decided to include here a comprehensive summary of magnetic materials theory.

Macroscopically, the interaction of a magnetic field in matter is generally expressed as $\mathbf{B}=\mu\mathbf{H}=\mu_0\mathbf{H}(1+\chi_m)=\mu_0(\mathbf{H}+\mathbf{M})$, using the notation for the magnetic field in SI units. In order to understand the physical mechanisms used in magnetic chipless RFID, it is useful to know the microscopic origin of the magnetization $\mathbf{M}$ and susceptibility χ_m presented here.

4.1.1 Physical Origin

Twentieth century physics has introduced to us the structure of an atom and the concept of spin and magnetic moment produced by nuclei and electrons. The subtle aspects of understanding magnetic phenomena has to do with understanding how atomic particles interact with each other and react to the presence of an applied external field.

The fact that permanent magnets exist is a hint that materials are able to generate their own magnetic field. Without considering the implications of quantum mechanical spin, atoms can indeed have a magnetic moment simply due to the orbital motion of electrons about a given nucleus. In fact, the magnetic moment due to the orbital motion of a single electron about a 1-proton nucleus is defined as a unit of one Bohr magneton and given the symbol μ_B, not to be confused with the SI symbol for magnetic permeability. In CGS units, μ_B is equal to $e\hbar/2m_ec \sim 10^{-20}$ erg/gauss $\sim 10^{-19}$ amp-cm2. In order to achieve the scale of forces we usually associate with magnets, it is logical to suspect that these macroscopic forces are due to some sort of cooperative behavior between the many atoms inside a material. On the other hand, if all the atoms inside a material aligned their magnetic moment in the same direction, the magnetic field produced by a hand-sized chunk of material would be on the order of 10 kGauss (=1 Tesla), as estimated by assuming roughly 10^{29} atoms per cubic meter. Since most permanent magnets that we encounter have a much smaller field, this implies that perhaps not all atoms have magnetic moments and that only a fraction of the spins inside a material are ordered to point in a given direction.

As a first pass in explaining the physical origin of magnetic moments and ordering, a reasonable start would be to examine the electric and magnetic forces on the atomic scale and compare that to the thermal energy kT (~.025 eV) at room temperature (300K).

Consider the interaction between two atoms a distance r apart. The magnetic field of an atom is on the order of a Bohr magneton ($\mu_B = e\hbar/2m_ec$) which falls off as $1/r^3$. An estimate of the interaction energy can be calculated from the product of the atom's own magnetic moment ($\sim\mu_B$) and the local field: $E = \mu_B \cdot \mu_B/r^3$. Assuming a lattice spacing of 10 Angstroms, this gives an energy of 10^{-12} ergs, or approximately 0.1 eV/atom.

Although energies of 0.1 eV might have some small effect even at room temperature, one might recall from basic chemistry that electrostatic energies due to Coulombic attraction and repulsion are hundreds of times larger, on the order of 10 eV. Therefore, electrostatic forces are a more likely cause for interatomic spin-ordering.

Electric and magnetic interactions can also be compared by relating electric and magnetic dipole moments. In the CGS system of units, electric and magnetic dipole moments have the same units, so it is possible to calculate an electrical dipole moment ($p = qd$) for a unit charge that

is equivalent in strength to a Bohr magneton ($\mathbf{p} = \mu_B$). The dipole spacing **d** for an electric dipole of equivalent strength to a Bohr magneton is only $\hbar/2m_e c$ = 0.002A. This result is quite small compared to the scale of a molecular charge distribution and approximately 1000 times smaller than the charge displacements which occur in ferroelectrics. Therefore, we can see that electrostatic interactions are dominant on the atomic and molecular scale.

4.1.2 Diamagnetism

Knowing that materials contain moving electrons and knowing that microscopic interactions are dominant, it is easy to explain the phenomena of diamagnetism, which causes certain materials to be weakly repelled by a magnetic field.

Diamagnetism can be intuitively explained using the classical description of an orbiting electron subject to the Lorentz force $\mathbf{F} = \mathbf{ma} = \mathbf{q}\,[\,\mathbf{E}(r,t)+\mathbf{v}\times\mathbf{B}(r,t)\,]$. In this case, an applied field will cause an additional centripetal force which must be balanced by a change in the angular momentum in the plane perpendicular to the applied field. The resulting change in the electron's orbital motion will alter is orbital magnetic moment in a direction anti-parallel to the direction of the applied field. In effect, diamagnetism is simply a microscopic manifestation of Lenz's law familiar from basic electromagnetic theory.

A formal derivation of diamagnetism for a single orbiting electron can be carried out using the Hamiltonian associated with the Lorentz force equation:

$$H = \frac{1}{2m}\left[\mathbf{p} + \frac{e}{c}\mathbf{A}(r,t)\right]^2 - e\varphi(r)$$

given for a static central potential $-\nabla^2\phi(r)=4\pi\rho(r)$ using the Coulomb gauge $\nabla\cdot A(r,t)=0$.

The Schrödinger equation for this system can be written as:

$$\frac{1}{2m}\left(\frac{\hbar}{i}\nabla + \frac{e}{c}\mathbf{A}\right)^2 \psi(r,t) = [E + e\varphi(r)]\cdot\psi(r,t)$$

Assuming a constant uniform magnetic field **B**, the vector potential can be written in the form $\mathbf{A} = -[\mathbf{r}\times\mathbf{B}(r,t)]/2$ such that and consequently $\nabla\times\mathbf{A} = \mathbf{B}$.

The components of **A** are then

$$\mathbf{A} = -\frac{1}{2}\left(yB_z - zB_y, zB_z - xB_z, xB_y - yB_x\right)$$

The left side of the Schrödinger equation can then be simplified as

$$H\psi = \frac{1}{2m}\left(\frac{h}{i}\nabla + \frac{e}{c}\mathbf{A}\right)\left(\frac{h}{i}\nabla\psi + \frac{e}{c}\mathbf{A}\psi\right)$$
$$= -\frac{\hbar^2}{2m}\nabla^2\psi - \frac{ie\hbar}{mc}\mathbf{A}\bullet\nabla\psi + \frac{e^2}{2mc^2}\mathbf{A}^2\psi$$
$$= -\frac{\hbar^2}{2m}\nabla^2\psi - \frac{e}{2mc}\mathbf{B}\bullet\mathbf{L}\psi + \frac{e^2B^2}{8mc^2}\left(x^2+y^2\right)\cdot\psi$$

The last term, which is independent of angular momentum, corresponds to diamagnetism for the 2-dimensional orbital motion ($r^2=x^2+y^2$). By taking the expectation value of this term and correcting for a spherical geometry ($r^2=x^2+y^2+z^2$), the diamagnetic susceptibility χ can be derived:

$$E = \frac{e^2B^2}{12mc^2}\left\langle r^2\right\rangle$$
$$\mu = -\frac{\partial E}{\partial B} = -\frac{e^2\left\langle r^2\right\rangle}{6mc^2}B$$

$$\chi = \frac{\mu}{B} = -\frac{e^2\left\langle r^2\right\rangle}{6mc^2} \qquad SI \quad units \Rightarrow \chi = \frac{\mu_0\mu}{B} = -\frac{\mu_0 e^2\left\langle r^2\right\rangle}{6m}$$

This is the same result that would be found by using the simple classic model mentioned previously.

Diamagnetism is an intrinsic property of all materials. However, as evident from the angular momentum term in the Hamiltonian given above, there are other factors that can mask the diamagnetic effect. It is instructive to compare the relative magnitudes of the diamagnetic and angular momentum terms, approximating **r** as the Bohr radius $\mathbf{a_0}$ and approximating L as order $\hbar$ and aligned parallel to **B**:

$$\frac{diamagneti\ c\quad contributi\ on}{angular\quad momentum\quad contributi\ on} = \frac{\left(e^2/8mc^2\right)a_0^{\,2}B^2}{\left(e/2mc\right)\cdot\hbar B} \approx \frac{B}{9\times10^9\ gauss}$$

Because the magnetic fields produced in the laboratory will always be far less than 10^9 gauss, this result shows that diamagnetism will always be easily masked by the effect of angular momentum, unless the angular momentum happens to be zero.

4.1.3 Paramagnetism

A material's weak attraction to a magnet is known as paramagnetism and is more subtle to explain. As mentioned above, the presence of angular momentum in a system of electrons can have a significant effect on the magnetic response of the material, and the minus sign on the angular momentum term in the Hamiltonian implies that the associated magnetic moment would prefer to align with the field. We would like to follow these clues to derive an expression for paramagnetism in terms of the angular momentum and also find some way to determine how much angular momentum a given atom will have.

An important revelation is that angular momentum includes more than just the orbital motion of electrons. Perhaps the most significant contribution of 20th century quantum theory to magnetism, is the statement that an electron has *intrinsic* angular momentum in the form of spin, which is independent of the orbital angular momentum. This was first deduced empirically from spectroscopic measurements of atoms in a magnetic field, but later derived quantitatively from the Dirac equation in relativistic quantum field theory and quantum electrodynamics.

With the addition of *spin angular momentum*, **S**, the angular momentum term in the electron Hamiltonian is modified to

$$H' = -\frac{e}{2mc}(\mathbf{L} + g\mathbf{S}) \bullet \mathbf{B}$$

Where the *gyromagnetic ratio* g ≅2.0023192, for a bound electron. For a free electron, the expression for g takes on the more general form

$$g = 1 + \frac{J(J+1) + S(S+1) - L(L+1)}{2J(J+1)}$$

where **J** is defined as the *total angular momentum* **J**=**L**+**S**.

If it is possible to derive the total angular momentum for a given atom (this is discussed in the next section), then the magnetic properties of the atom can be calculated. The magnetic energy of an atom in a magnetic field **H** is given by

$$E = -g\mu_B \mathbf{J} \bullet \mathbf{H}$$

Where **H** is aligned in the **z** direction and, in reality, also includes small contributions from neighboring atoms.

According to quantum mechanics, the total angular momentum projected along a given direction takes on discrete values $\mathbf{m_J}\hbar$, with $\mathbf{m_J}$ ranging from -**J** to **J**. Thus an atom in state m_J has a magnetic moment equal to

$$\mu_z = g\mu_B m_J$$

With associated energy:

$$E = -g\mu_B m_J H$$

Using statistical mechanics, we can use this energy to calculate the probability that the atom will be in the given state $\mathbf{m_J}$ at a temperature **T**:

$$p(m_J) = e^{\beta g \mu_B m_J H}$$

where β = 1/**kT**.

The mean **z**-component of the magnetic moment of the atom can then be calculated by averaging over all possible $\mathbf{m_J}$ states:

$$\bar{\mu}_Z = \frac{\sum_{m=-J}^{J} e^{\beta g \mu_B m_J H} (g\mu_B m_J)}{\sum_{m=-J}^{J} e^{\beta g \mu_B m_J H}} = \frac{1}{\beta}\frac{\partial \ln Z_a}{\partial H}$$

where the partition function $\mathbf{Z_a}$ is defined as

$$Z_a = \sum_{m=-J}^{J} e^{\eta m_J} = \frac{e^{-\eta J} - e^{\eta(J+1)}}{1 - e^{\eta J}} = \frac{\sinh(J + \frac{1}{2})\eta}{\sinh\frac{\eta}{2}} \qquad \text{and } \eta = g\mu_B H / kT$$

The mean magnetic moment can then be simplified as

$$\overline{\mu}_z = g\mu_B J B_J(\eta)$$

Where the function B_J, known as the *Brillouin function*, shown in Figure 34, is given by

$$B_J(\eta) = \frac{1}{J}\left[\left(J + \tfrac{1}{2}\right)\coth\left[\eta\left(J + \tfrac{1}{2}\right)\right] - \frac{1}{2}\coth\frac{\eta}{2}\right]$$

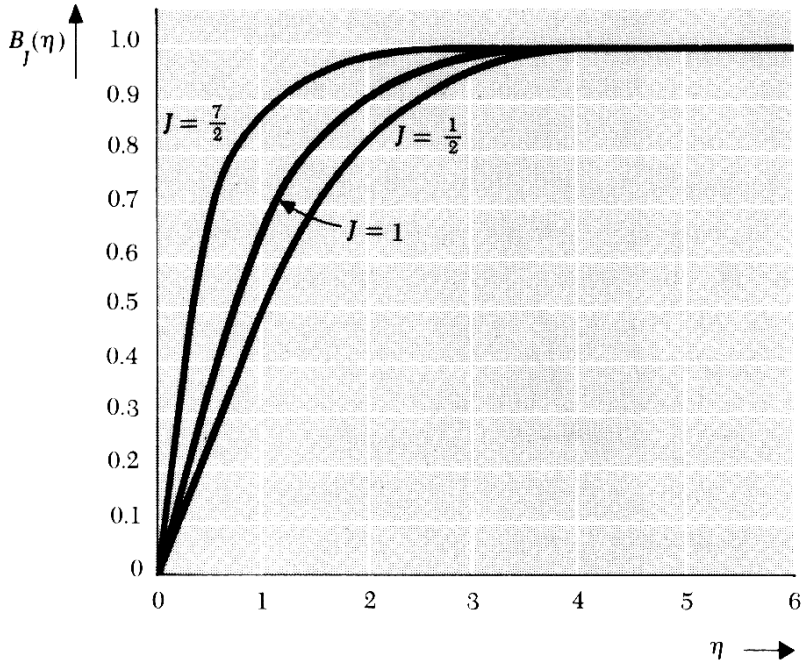

Figure 34. Brillouin function plotted as a function of parameter η for different values of spin **J**.

Although the mean magnetic moment (and thus the magnetic permeability) of a material is a complex function of the temperature and the applied magnetic field, it is customary to use approximations that are valid for certain ranges of applied field and temperature, $g\mu_B H / kT << 1$ and $g\mu_B H / kT >> 1$. Assuming a material with N_0 similar atoms per unit volume, the magnetic susceptibility χ, defined as magnetization per unit volume, can be expressed in terms of **M** and **H** as follows:

$$\chi = \frac{M_z}{H} = \frac{N_0 \mu_z}{H}$$

At room temperature, $g\mu_B H / kT \cong 4.7 \times 10^{-7} H$. Therefore, for low to moderate-size applied magnetic fields, it is valid to use the approximation $g\mu_B H / kT << 1$. In this limit, B_J can be written as

$$B_J(\eta) = \frac{J+1}{3}\eta$$

and the susceptibility is given by

$$\chi = N_0 \frac{g^2 {\mu_B}^2 J(J+1)}{3kT} \equiv \frac{C}{T}$$

The $1/T$ temperature dependence of the susceptibility is known as the Curie Law and the constant C known as the Curie constant.

At very low temperatures or very high magnetic fields, the magnetic moments in the material are much more likely to align parallel to the applied field. In this case, $g\mu_B H / kT >> 1$ and $B_J \cong 1$, which yields

$$M_z = N_0 \mu_B J$$

In this case all the moments are aligned with the field, and the magnetization is said to be *saturated*.

In the case of metals, only the thermally excited electrons near the Fermi level E_F are free to participate in the magnetization process, so the susceptibility values in the non-saturated case must be reduced by a factor of kT/E_F. In this case, the susceptibility is

$$\chi = N_0 \frac{g^2 {\mu_B}^2 J(J+1)}{3E_F}$$

This is known as Pauli paramagnetism.

4.1.4 Intra-atomic spin-ordering

As shown above, knowing the total angular momentum J for an atom allows us to calculate its magnetic properties, such as its magnetic susceptibility, χ. However, the process of determining the total angular momentum for a given atom relies heavily on the basic principles of quantum mechanics. In order to understand the reason behind the electronic configuration of a given

atom, it is necessary to understand how electrons interact with the nucleus and how they interact with themselves. The most stable state of a system is generally the state with the lowest total energy. Thus, by understanding the Hamiltonian and energy associated with each interaction it is possible to predict, albeit semi-empirically, the lowest energy configuration for a given atom.

4.1.4.1 Spin-orbit interaction

The fact that the electron has an intrinsic magnetic moment gives rise to an interaction with the charged atomic nucleus. In the electron's rest frame, the relative motion of the electron and charged nucleus gives rise to an apparent nuclear magnetic field which then interacts with the electron's own magnetic moment. (as an aside, the nucleus generally does have its own intrinsic nuclear spin and associated magnetic moment which causes *hyperfine* energy splitting of its own, but this is not relevant to this discussion) Since the apparent nuclear magnetic field is a function of the electron's orbital angular momentum, this interaction is known as the *spin-orbit interaction* and is given by

$$H' = -\frac{1}{2m^2c^2}\mathbf{L}\bullet\mathbf{S}\frac{1}{r}\frac{d\left[e\varphi(r)\right]}{dr}$$

$$H' = \frac{1}{4m^2c^2}\left[J(J+1)-L(L+1)-S(S+1)\right]\frac{1}{r}\frac{d\left[e\varphi(r)\right]}{dr}$$

The relative energy contribution of this term can be estimated by comparing the magnitude of this term to the other terms in the simple Hamiltonian given previously. For simplicity, we can choose **L**=1, **S**=1/2 for the hydrogen atom potential **e/r** and substitute the known expectation value of $<1/r^3>=1/(3a_0^3)$ for $1/r^3$:

$$\frac{spin-orbit\quad contribution}{J\bullet B\quad contribution}=\frac{\left(\hbar^2e^2/6m^2c^2a_0{}^3\right)}{\left(e/2mc\right)\cdot\hbar B}\approx\frac{25\times10^3\,gauss}{B}$$

This result implies that for low to moderate fields (**B**< 25 kG), the spin-orbit interaction will generally have a greater influence on the spin orientation than the applied external field. Since the orbital angular momentum **L** is a function of the electron orbitals, molecular bonds, and the crystal lattice geometry, we see that the spin-orbit interaction gives rise to an energy that is an anisotropic function of the crystal orientation.

4.1.4.2 Pauli exclusion

The energy contribution of the spin-orbit interaction is relatively significant with a typical value of $\hbar^2 e^2/6m^2c^2a_0^3 \cong$ 10-4 eV. Nonetheless, the energy of all the magnetic interactions discussed so far are quite small compared to Coulombic interactions which are on the order of $e^2/r \cong e^2/a_0 \cong$ few eV. All spin-dependent interactions would be inconsequential were it not for a fundamental principle of quantum mechanics, known as the Pauli exclusion, which indirectly links the strong Coulombic interactions with electron spin.

The Pauli principle states that *no two electrons can exist in the same quantum state.* This is a consequence of the fact that the electron belongs to a class of particles called fermions, as determined by experimental observation. It is a fundamental property of all fermions that they have half-integer spins, posses an antisymmetric wave function and obey Fermi-Dirac statistics. Since spin is one of the parameters which comprise an electron's quantum state, the Pauli exclusion principle creates a dramatic spin-dependent constraint on the way electrons configure themselves in a Coulomb potential.

In order to understand the implications of Pauli exclusion in many-electron atoms, it is instructive to first consider the case of 2 interacting electrons in the simplest case of a Helium atom. The wave function is:

$$H = \frac{\mathbf{p_1}^2}{2m} + \frac{\mathbf{p_2}^2}{2m} - \frac{Ze^2}{r_1} - \frac{Ze^2}{r_1} + \frac{e^2}{|\mathbf{r}_1 - \mathbf{r}_2|}$$

This Hamiltonian can be written as the sum of 2 hydrogen atoms plus the addition of the electron-electron interaction term, which can be treated as a perturbation. We expect that some linear combination of the hydrogen atom wave functions will be eigenfunctions of this system.

The hydrogen atom wave functions are well known and have the form

$$\psi_{hydrogen} = u_{nlm}(r)\sigma = R_{nlm(r)}Y_{lm}(\theta,\phi)\sigma$$

Since hydrogen has a singe electron, the spin state σ of the electron is generally not noted explicitly since it has no consequence on the functional form of the eigenfunctions. For the case of more than one electron, however, the fermion nature of the electrons require that spin be considered explicitly.

As a general rule, we expect that the spatial component of the ground state wave function for the helium atom must have no nodes and even parity. We would expect that the helium ground state wave function should be the product of the hydrogen atom ground state solutions:

$$\psi_0 = u_{100}(r_1)u_{100}(r_2)\sigma_1\sigma_2$$

The problem that becomes immediately apparent is that this wave function does not satisfy the asymmetry requirement for fermions which prevents two fermions from occupying the same state. Since we know that the wave function determines the state's probability distribution ($\propto\psi 2$), the functional form of the wave function must be such that the wave function (and thus the probability) goes to zero if both fermions are given the same set of quantum parameters (n, l, m, spin). The proper wave function must have the following form:

$$\psi = \{symmetric \quad spatial \quad function\} \times \{asymmetric \quad spin \quad function\}$$

or

$$\psi = \{asymmetric \quad spatial \quad function\} \times \{symmetric \quad spin \quad function\}$$

With this in mind, we see that the correct wave function should be

$$\psi_0 = u_{100}(r_1)u_{100}(r_2)\frac{\sigma(+)_1\sigma(-)_2 - \sigma(-)_1\sigma(+)_2}{\sqrt{2}}$$

The wave functions for the excited states allow increasingly more combinations, but must obey the same rules. For the first excited state wave function, the spatial dependence can be either symmetric or antisymmetric, so there are four possible states:

$$\psi_1 = \frac{1}{\sqrt{2}}\left(u_{100}(r_1)u_{2lm}(r_2) + u_{2lm}(r_1)u_{100}(r_2)\right)\left(\frac{\sigma(+)_1\sigma(-)_2 - \sigma(-)_1\sigma(+)_2}{\sqrt{2}}\right)$$

$$\psi_1 = \frac{1}{\sqrt{2}}\left(u_{100}(r_1)u_{2lm}(r_2) - u_{2lm}(r_1)u_{100}(r_2)\right)\sigma(-)_1\sigma(-)_2$$

$$\psi_1 = \frac{1}{\sqrt{2}}\left(u_{100}(r_1)u_{2lm}(r_2) - u_{2lm}(r_1)u_{100}(r_2)\right)\left(\frac{\sigma(+)_1\sigma(-)_2 + \sigma(-)_1\sigma(+)_2}{\sqrt{2}}\right)$$

$$\psi_1 = \frac{1}{\sqrt{2}}\left(u_{100}(r_1)u_{2lm}(r_2) - u_{2lm}(r_1)u_{100}(r_2)\right)\sigma(+)_1\sigma(+)_2$$

It is important to note that the first function has a total spin S=0, and it denoted as a "singlet." The other three wave functions have total spin (magnitude) S=1 and are denoted as "triplet" states.

We also note that symmetry rules place a constraint on the orbital angular momentum number L, since L determines whether the function $Y_{nlm}(\theta,\phi)$ has even or odd symmetry:

$$Y_{lm}(\theta,\phi) \to Y_{lm}(\pi-\theta,\phi+\pi) = (-1)^l Y_{lm}(\theta,\phi)$$

4.1.4.3 The exchange interaction

Knowing the functional form of the wave functions for a multi-electron system enables us to finally investigate how these spin interactions may affect the energy of the system. Continuing with the Helium example, we want to know how the Coulomb interaction will affect the energies of the four excited states given above.

Treating the Coulomb repulsion as a perturbation, we know from time-independent perturbation theory that the first order energy shift is given by the expectation value of the perturbation. Using the four excited state functions given above, the energy shift for the case **m**=0, is given by the following:

$$\Delta E = \left\langle \psi_1 \left| \frac{e^2}{|r_1 - r_2|} \right| \psi_1 \right\rangle = \frac{1}{2} e^2 \int d^3 r_1 \int d^3 r_2 \left(u_{100}(r_1) u_{2l0}(r_2) \pm u_{2l0}(r_1) u_{100}(r_2) \right)^*$$

$$\times \frac{1}{|r_1 - r_2|} \left(u_{100}(r_1) u_{2l0}(r_2) \pm u_{2l0}(r_1) u_{100}(r_2) \right)$$

$$= e^2 \int d^3 r_1 \int d^3 r_2 \left| u_{100}(r_1) \right|^2 \left| u_{2l0}(r_2) \right|^2 \frac{1}{|r_1 - r_2|}$$

$$\pm e^2 \int d^3 r_1 \int d^3 r_2 u^*{}_{100}(r_1) u^*{}_{2l0}(r_2) \frac{1}{|r_1 - r_2|} u_{100}(r_1) u_{100}(r_1)$$

$$\equiv E_{nl} \pm E'_{nl}$$

The first term in this result is the ground state energy shift. However, the second term is an additional energy shift that depends on the total spin of the given eigenstate. The Coulomb interaction lifts the degeneracy of the different spin states. Note that the singlet state with **S**=0 results in a higher total energy state than any of the triplet **S**=1 states. Thus, due to Pauli exclusion, electrons with parallel spins are more likely to be further apart, resulting in a lower Coulomb energy. This demonstrates that electron configurations that *maximize* the total spin are

energetically favored. Another way of saying this is that the Coulomb interaction mediates the spin ordering of the atom -- an important result. Therefore, in understanding how the electrons in an atom populate the different spin states, we can see that not only do the electrons prefer to be in different spin states (due to Coulomb repulsion) but it is also energetically favorable for the electrons to aligns themselves parallel to each other.

Exactly *how* favorable it is for electrons align themselves with parallel spins is given by the value of the energy integral presented previously. In order to show more explicitly the contribution of electron spin to the total energy, Hisenberg invented a new Hamiltonian term called the *Hisenberg Hamiltonian* and is given by

$$H_S = -2J\mathbf{S}_i \bullet \mathbf{S}_j$$

where the constant J is related to the energy difference between the singlet and triplet spin states and is given by the following, known as the "*exchange integral*":

$$E_S - E_T = 2\int dr_1 dr_2 \left[\psi_A^*(1)\psi_B^*(2)\right] \cdot V(r_1, r_2)\left[\psi_A(2)\psi_B(1)\right] \equiv 2J$$

We can, therefore, calculate quantum mechanically the degree to which a particular atom prefers to have its electrons spins aligned parallel.

4.1.4.4 Hund's rules

Although modern computers do make it possible to compute the exchange interaction for a given material, it is not a practical means of quickly assessing the magnetic properties of different materials. However, we know from our high-school chemistry course that there exist handy well-known empirical approaches to determining the spin ordering of many-electron atoms through the use of molecular orbital diagrams. The most popular set of empirical rules were invented by Hund in the early 1900's based solely on experimental observation, and are commonly used by chemists today, using the popular notation of orbitals *s, p, d, f,* etc to indicate the different angular momentum states. These rules are summarized as follows:

- *When electrons fill a subshell, every orbital in the subshell is occupied before any orbital is doubly occupied and*
- *All electrons in singly occupied orbitals have their spins aligned in the same direction*

For example, for elemental oxygen, we know it has eight electrons an its electron configuration is $1s^2 2s^2 2p^4$ which is represented by the following orbital diagram: (↑ ↓) (↑ ↓) (↑ ↓) (↑) (↑) . The unpaired spins thus produce a net total spin, and we can predict that oxygen will be *paramagnetic*.

On the other hand, the electron configuration for neon is $1s^2 2s^2 2p^6$ which has the following orbital diagram: (↑ ↓) (↑ ↓) (↑ ↓) (↑ ↓) (↑ ↓) . Since there are no unpaired spins, we expect the total spin to be zero and thus expect neon to posses only the weak intrinsic *diamagnetism*.

4.1.5 Inter-atomic spin ordering

Perhaps the most interesting category of magnetic phenomena is *ferromagnetism*, which is a cooperative alignmentn that occurs not only among electrons within the same atom, but among electrons of neighboring atoms as well. Such a material has a large magnetic permeability and, in the case of permanent magnets, the stable cooperative alignment of the atomic moments can result in a significant external magnetic field.

The fundamental physical mechanism that gives rise to inter-atomic spin ordering is a similar exchange interaction as that which gives rise to intra-atomic spin ordering. However, the case of multi-atom systems this interaction is much more complex, due to the fact that atoms can bond to each other in a variety of ways as well as the fact that, in metals, electrons in the conduction band are not localized and can also take on a variety of spin states.

4.1.5.1 Direct Exchange Model

In the years since 1926, the exchange energy description described previously for a single atom has been generalized and applied to multi-atoms system. The most basic and general model for ferromagnetism is the direct exchange model, which applies to localized weakly-coupled magnetic atoms. The more general form of the Heisenberg Hamiltonian is given by the following:

$$H_S = constant \quad -2\sum_{i>j} J\mathbf{S}_i \bullet \mathbf{S}_j$$

where J is the value of the exchange integral mentioned previously. Since it is often difficult to calculate J explicitly, there exists a mean field approximation for J which assumes that a magnetic atom interacts with z nearest neighbors:

$$J = \frac{3kT_C}{2zS(S+1)}$$

where T_c is an important parameter called the *Curie temperature*, which is the temperature above which inter-atomic spin ordering breaks down. The Curie temperature is proportional to the Curie constant presented earlier for paramagnetism:

$$\frac{T_C}{C} \equiv \lambda = \frac{2zJ}{\mu_0 N_0 g^2 \mu_B}$$

The Heisenberg Hamiltonian applied to molecular compounds thus quantifies the tendency for neighboring localized magnetic moments to align parallel (corresponds to **J** > 0) or anti-parallel (**J** < 0) to each other.

As in the case of Hund's rules for spin ordering within a single atom, there exist empirical methods that can be used to qualitatively predict the magnetic properties of multi-atom compounds. A full description of these methods is beyond the scope of this summary; however, these methods can be easily found in most college-level Chemistry text books. In these methods, it is generally necessary to consider the lattice structure of the material and the types of bonds present. For metal ion complexes bonding with ligands, orbital diagrams can be written for the metal and for the ligand using *valence bond theory*, which looks at the electron assignment in the unoccupied molecular orbitals participating in the molecular bond. For 2 atoms bonding together, bonding states favor paired anti-parallel spins (presumably one electron from each atom) and anti-bonding states favor parallel alignment.

Of particular interest are the magnetic properties of the transition metal complexes, where the d-orbitals play an important role. In this case, *crystal field theory* and *ligand field theory* are simplifications which treat the ligands in a metal complex as point charges. Further simplifications and generalizations of these methods to other types of compounds is provided by *molecular orbital theory*, which is very analogous to the orbital theory for electron assignment in single atoms and also supports de-localized bonds.

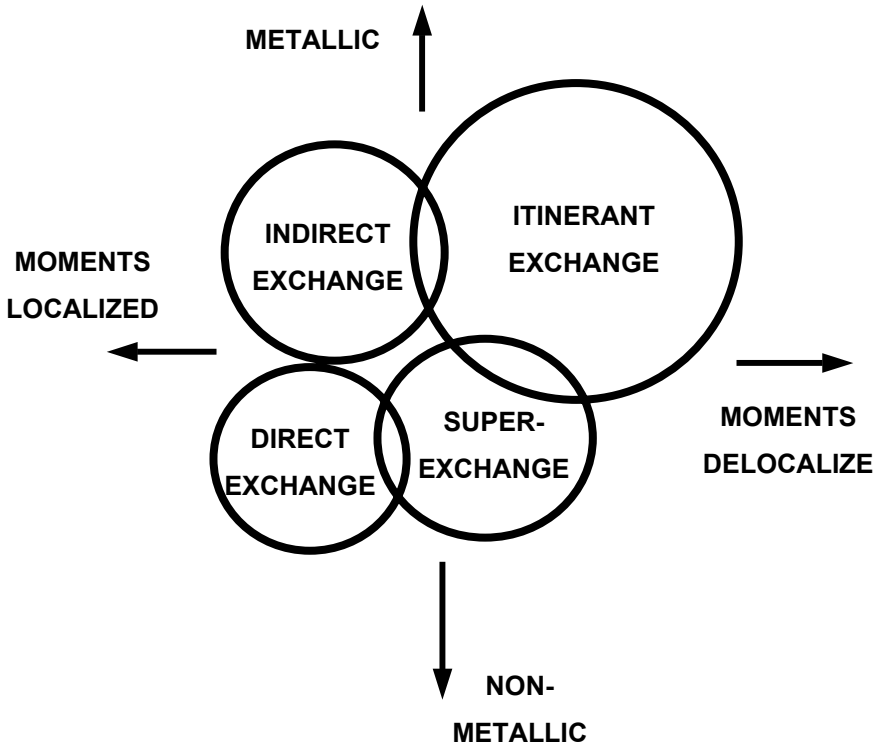

Figure 35. Photograph of sample coil test fixture.

4.1.5.2 Other Exchange Models

In addition to the direct exchange model, other spin exchange models also exists for other cases when the type of bonding is de-localized or when free conduction electrons are also present (metals). The relationship between the different exchange models is shown schematically in Figure 43.

4.1.6 Anisotropy

How a material responds to an applied magnetic field is generally dependent on the relative orientation of the material. This is true because the internal spins and magnetic moment of a material have preferred orientations -- a property generally termed *magnetic anisotropy*.

At the simplest level, part of the observed anisotropy is simply due to the shape of the material. This is true even if we model an arbitrary material as a collection of spins. As many children know from playing with magnet toys, disk magnets prefer to align themselves end-to-end rather than side-by-side; and if bar magnets are brought together, they prefer to align themselves anti-parallel rather than parallel. We can also see this behavior if we break a permanent magnet and notice the repulsion force if we attempt to re-assemble the pieces. This occurs because a magnetic field has energy, and a system will always tend to a state with minimum energy. The *magnetostatic energy* in the magnetic field is given by the following volume integral:

$$E = \int \frac{H^2}{8\pi} dv$$

Therefore, configurations that minimize the extent of the magnetic field are preferred. This is illustrated graphically in Figure 45.

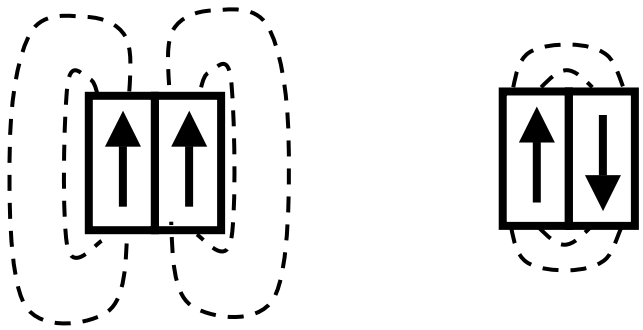

Figure 36. Possible geometric configurations for two bar magnets and their corresponding magnetic fields. The configuration on the right has a lower magnetostatic energy and is preferred.

Microscopically, however, there exists a more important source of magnetic anisotropy, which governs the alignment of the electron spins and magnetic moments on the molecular scale. As discussed previously, the spin-orbit interaction represents an energy associated with the coupling

between the electron spin and the orbital angular momentum. However, we also know from chemistry that the angular momentum (in the form of electron orbitals) plays an important role in the chemical bonds that link all the atoms together; and we also know that in a solid, these chemical bonds have a well-defined geometry electric field within the lattice, as governed by the local electric field, often called the crystal field. If there are no unpaired spins (net S=0) or if the angular momentum in the bonding orbitals is zero, or if the crystal field is rotationally symmetric, then we would not expect any magnetic anisotropy. However, in general, this is not the case, and some degree of anisotropy is observed.

Therefore, for a magnetic material (which has nonzero spin, by definition), magnetic anisotropy will be observed if:

- There exists an asymmetry in the crystal field, and
- The highest occupied electronic states (which are those that interact with neighboring atoms) have non-zero orbital angular momentum

In considering a specific material's response to an applied magnetic field, the degree of anisotropy will be depend on the relative strength of the spin-orbit coupling and the coupling between the orbital angular momentum and the lattice. If the spin-orbit coupling is weaker (as in the case of transition metals), the magnetic moment can more easily follow the applied magnetic field and a small degree of anisotropy will be observed. If, however, the spin-orbit coupling is strong (as in the case of rare-earth compounds), then a very large magnetic anisotropy will be observed. If the spin-orbit coupling is strongly dominant, the rotation of the applied field can produce a deformation of the lattice, exhibited by mechanical strains. This effect is known as *magnetosctriction*.

This microscopic origin of magnetic anisotropy is often termed crystalline anisotropy to distinguish it from the shape anisotropy mentioned earlier. For the purpose of materials characterization and making relative comparisons, the crystalline anisotropy of a material is commonly given in terms of coefficients in a power-series expansion of the uniaxial anisotropy energy density, which is the energy needed to saturate the magnetization in-plane (a-b axis basal plane) minus the energy required to saturate the material in the out-of-plane direction (c-axis):

$$U = K_1 \sin^2 \theta + K_2 \sin^4 \theta + \ldots$$

For a material that exhibits magnetic anisotropy, its internal spins and associated magnetization will thus lie in a preferred direction. The preferred axis of the magnetization is termed the *easy-axis* and the direction perpendicular to this is termed the *hard axis*.

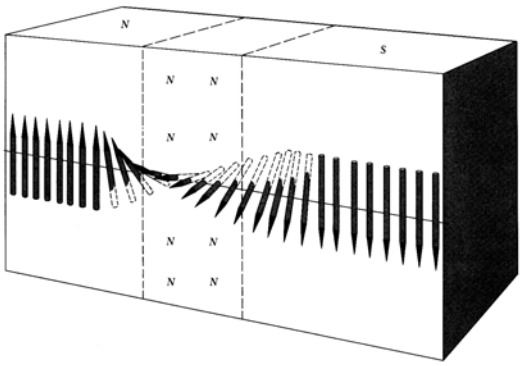

Figure 37. Illustration of a linear array of spins forming a domain wall.

4.1.7 Domain walls

Perhaps the most pertinent topic for electromagnetic tagging is an understanding of the behavior of spins inside a material when an external magnetic field is applied and how it contributed to the observed magnetization of the material. A general discussion of this topic is referred to as the *magnetization process*; however, as an introduction, it is useful to understand some of the basic contributions to this process based on the collective behavior of the spins.

Given the discussion of magnetic anisotropy, it is known that the local magnetic moments of a material have preferred directions of orientation relative to the crystal lattice. Given the previous discussion of the exchange interaction, we also know that the spins inside a magnetic (presumably ferromagnetic) material prefer to be aligned in parallel, due to Pauli exclusion and the crystal field interactions. From these two interactions alone, we would expect any ferromagnetic material to have all of its spins aligned in the same direction, and thus exhibit a very large remnant magnetic field. However, we know from observation that this is not what happens.

If we view this system in terms of energy terms, it turns out that the large ensemble of spins inside a magnetic material behave similarly to a large collection of permanent magnets: they will orient themselves to minimize the energy. Although the exchange interaction acts to maintain parallel alignment among individual spins, the magnetostatic energy prefers anti-parallel alignment (as discussed in the previous section). As a result, a magnetic material in the presence of no applied magnetic field will contain segregated regions of magnetization in one direction or the other, such that the total energy is minimized. These regions of parallel spin are called *domains*.

The transition region between regions of parallel spin are called *domain walls*. The width of these walls is a function of two opposing forces: the exchange energy acts to keep the spins parallel and thus lengthen the width of the wall, but crystalline anisotropy acts to keep the spins aligned (parallel or anti-parallel) along particular crystal orientations and thus make the domain wall as narrow as possible. Quantitatively, the width of a domain-wall has the following dependence on the exchange interaction **J**, the net spin **S** and crystalline anisotropy **K**:

$$\delta = a \cdot \sqrt{JS^2\pi^2 / Ka^3}$$, where **a** is the lattice constant.

Other, more exact, expressions for the domain wall thickness are available depending on the shape of the material and -- in the case of a planar material -- whether the domain wall lies in the plane (Neel wall) or perpendicular to the plane (Bloch wall).

4.1.8 Magnetization Process

With a basic understanding of spin ordering, magnetic anisotropy, domain walls, and the relative energies involved, it is possible to achieve a basic understanding of the observed magnetization signal of a material in response to an applied external magnetic field.

The two basic components of the magnetization process are: domain-wall motion and magnetization rotation. Which of these two components is dominant depends on the relative orientation of the applied external field. The initial slope of the magnetization **M**, as the applied field **H** is increased, is defined as the initial magnetic permeability **μ**.

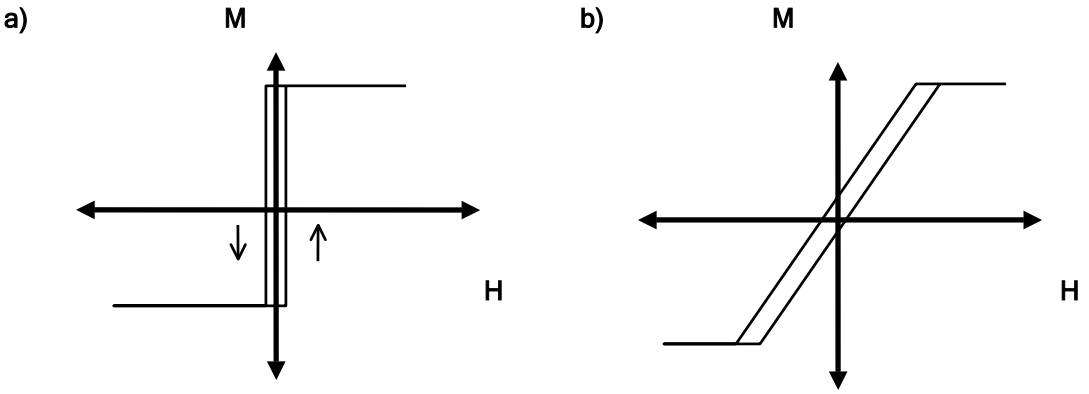

Figure 38. a) M vs H for H applied along the easy magnetic axis
b) M vs H for H appied perpendicular to the magnetic easy axis

If the external field is applied along a preferred magnetization axis of the material (easy axis), then the magnetization signal is formed predominantly through domain wall motion. As the applied field is increased from zero, the magnetic domains redistribute and coalesce in order to minimize the magnetic potential energy and to enable more spins to be aligned with the field. In doing so, the domain walls move within the material in a direction generally perpendicular to the direction of the applied field. Since the applied field is in the preferred direction of magnetization, this process can occur quite quickly even at small applied fields, and continues until effectively all spins are aligned with the applied field (termed *saturation*). This results in a relatively square magnetization curve shown in Figure 46a.

The speed of the domain walls is dependent on the strength of the applied field and is given by the following expression:

$v = H\left(2M_s / \beta\right)$, where M_s is the magnetization value at infinite applied field,

and β is the damping factor.

The domain wall velocity is limited by spin relaxation damping, given by

$\beta_r = [CM_s / \gamma](K / A)^{1/2}$, where γ is the gyromagnetic ratio. If the material is electrically conductive, there is an additional source of damping caused by the induced eddy currents in the material and is given by $\beta_e = (16M_s)^2 d / \pi\rho c^2$, where d is the thickness of the material and ρ is the resistivity.

If the external field is applied along an axis (hard axis) that is not preferred by the material's magnetic anisotropy, then it is more difficult to coerce the spins to rotate into the direction of the applied field. In this case, the external field exerts a torque on the internal magnetic moments that is proportional to the magnitude of the applied field and acts to rotate the magnetization of the domains. In contrast to the easy-axis magnetization curve, the magnetization along the hard-axis increases more gradually as a function of the applied field, producing what is often called a *sheared* magnetization loop, shown in Figure 46 b.

In practice, the movement of the domain walls may not be completely smooth due to imperfections or defects in the material that act as *pinning centers* to temporarily stop or impede the movement of the domain wall. As the applied field increases, eventually the increasing force on the domain wall will cause it o become *de-pinned*. This sudden de-pinning will produce small sudden flux jumps (called *Barkhausen jumps*) that appear as small kinks in the magnetization curve.

If the applied field is reversed, the pinning and loss mechanisms impede the domain wall motion, resulting in *hysteresis* and a non-zero *remnant field* when the applied field is zero. Permanent magnet materials are an extreme example of this effect.

4.2 Soft Magnetic Materials

Materials whose magnetization can be easily influenced by an externally applied magnetic field are termed soft magnetic materials. In terms of the magnetic properties discussed in the previous sections, these materials are engineered to have a high permeability, low crystalline anisotropy, and low-remnance, which generally produce a square magnetization curve, as shown in Figure 23 below. Because the magnetization of these materials is easy to manipulate and also produces higher-order harmonics, these materials are useful for chipless tagging.

4.2.1 Materials Properties

The sharp discontinuities exhibited by the magnetization curve of magnetically soft alloys arise from high domain-wall mobility as well as internal irreversible mechanisms, such as domain wall pinning and de-pinning. In the demagnetized (M=0) state, the magnetic domains will orient themselves along several different energetically favorable directions (usually along a local easy axis). If the material contains local regions with easy axes that are not parallel to the applied field, then the applied field must work harder to align these straggling domains during the magnetization process. This process leads to a rounded magnetization curve. Therefore, crystalline anisotropy is generally not a desired property for achieving a square M vs H loop, except for the special case of a single crystal material with a magnetic field applied along an easy axis.

Applying the excitation field along the easy axis of magnetization can be used to generate a square hysteresis loop similar to the plot shown in Figure 44a. In this configuration, the magnetization process is primarily due to domain wall motion rather than magnetization rotation. For this reason, it is desirable to eliminate all factors that can impede domain wall motion, such as magnetic defects or magnetosctriction, which can produce local strain fields which result in domain wall pinning. Although a small amount of magnetic anisotropy may help to stabilize and maintain the magnetization as the excitation field is reduced from saturation, high anisotropy is generally undesirable since it results in a high domain wall energy density, which makes the domain walls more difficult to move.

Typical soft magnetic materials used for harmonic generation have been Permalloy™, mu-metal, and similar high-permeability materials. For EAS applications, such as for library books or CD's, these materials are generally cut into thin long strips parallel to the easy axis of the material. As expected, the longer the strip, the larger the signal. The long thin geometry is not only convenient for concealment but its thin width and shape anisotropy also help to produce a very square hysteresis loop.

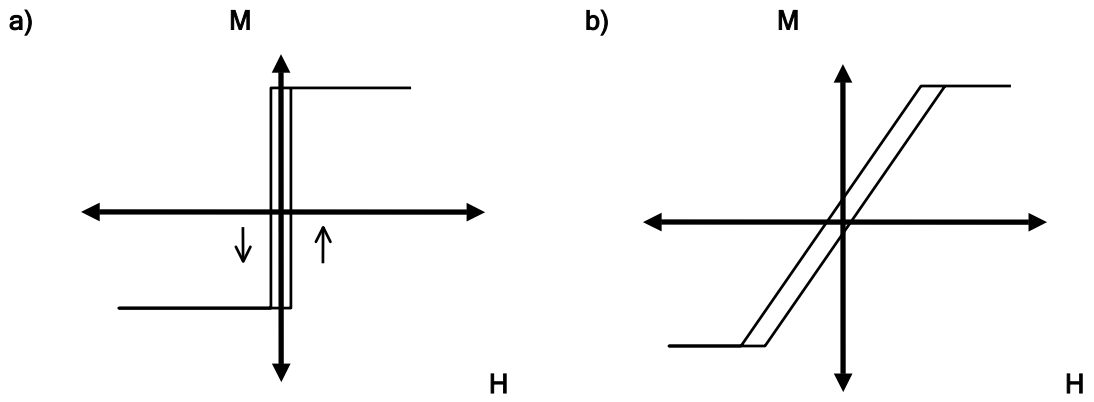

Figure 39. a) M vs H for H applied along the easy magnetic axis
b) M vs H for H appied perpendicular to the magnetic easy axis

A relatively new class of soft magnetic material are amorphous metal alloys, which were developed in the mid-1970s and are produced by very rapid cooling of the molten alloy. These materials have no crystalline grain structures which can contribute to magnetic anisotropy and domain wall pinning. Perhaps most importantly, these materials exhibit a relatively high electrical resistivity, thus diminishing eddy currents which can impede domain wall motion associated with energy loss in dynamic applications. Now that it is possible to fabricate amorphous metal alloys in thin wire form, amorphous wire has become the material of choice for harmonic tags.

In amorphous wires, the squareness of the loop can be enhanced further by several techniques. Local anisotropies can be reduced further by current-annealing the wire. In addition, if the material composition happens to be magnetostrictive, the material is also temperature-processed such that the center of the wire is in tension, thus making the magnetization along the axis of the wire even more bi-stable.

Another method of producing discontinuities in the **M** vs **H** curve of a material is to induce a sudden flux jump during the magnetization process by momentarily pinning the movement of one or more domain walls. The pinning regions are created by annealing the material in order to induce local anisotropies at the location of the domain walls present during the annealing process. These pinning regions are in the form of line defects which act as 2D potential wells. The pinning energy of these regions depends on the annealing kinetics (temperature, mobility of the species). The local anisotropies formed during the annealing process are also a function of the chirality of the domain wall, so the pinning energies of these line regions are also chirality-dependent.

The hysteresis loop of a pinned-wall type material and an illustration of its internal domain structure is shown in Figure 5. In its demagnetized state, a narrow strip of this material may have one or more domain walls. As the applied field is increased, the unusual flat sections of the

hysteresis loop are the result of domain wall pinning. As the applied field is increased further, eventually enough energy is available to overcome the pinning energy of an existing domain wall or to fully nucleate one of the budding domain walls present at the edge of the material. Once this occurs, the freed domain wall quickly moves to its equilibrium position, thus generating a burst of flux and a step in the **M** vs **H** loop.

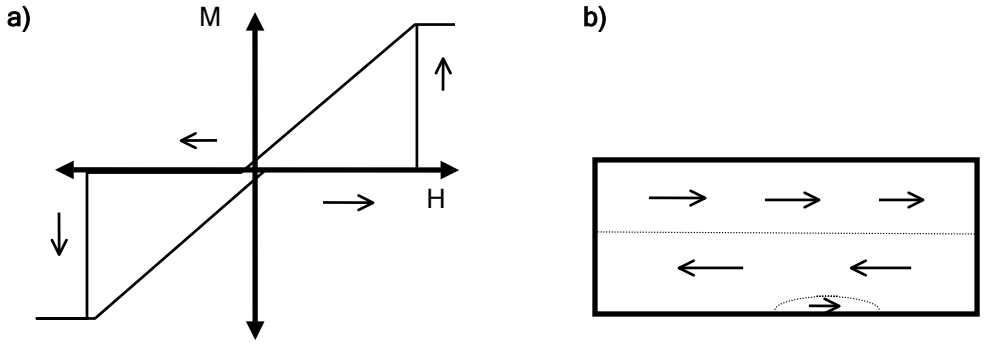

Figure 40. a) Magnetization curve for a pinned-wall material annealed in zero field. b) Diagram of a possible internal domain structure for zero applied field. Domain walls are represented by dotted lines.

If the material is annealed in the presence of a magnetic field, very asymmetric hysteresis loops can be created (Fig 50). Since the potential well regions are formed at the location of the domain walls during the annealing process, the flat sections of the resulting hysteresis loop correspond to the applied field values which reproduce the domain wall configuration during the annealing. It also follows that the value of the magnetization during pinning (the flat sections of the curve) corresponds to the magnetization value during annealing. As shown in Figure 40, this process can produce large steps in the **M** vs **H** loop which have high harmonic content. It should also be noted that this process also provides a way to create an asymmetric step in the **M** vs **H** curve without the need for an external bias magnet, which serves to safeguard against accidental activation by small environmental excitation fields.

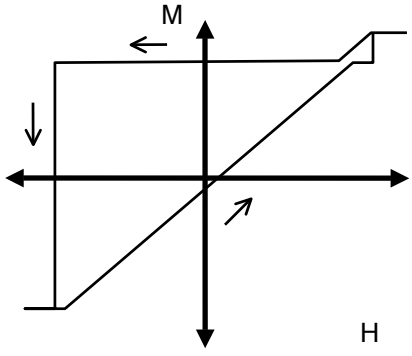

Figure 50. Example of a magnetization loop for a pinned-wall material annealed in a field. Of particular interest is the resulting large step in magnetization.

4.2.2 Harmonic Generation

The primary role of soft magnetic materials in electromagnetic tagging has been harmonic generation. In a tag reader system, the harmonics detected by the receive antenna are the result of the discontinuities in the tag materials magnetization curve. When excited by the magnetic field of the reader transmit coil, the induced voltage in the receive coil is due to the changing flux generated by the magnetic field of the transmit coil as well as the magnetization of the tag material.

In order to understand the behavior of a magnetic material in the presence of a tag reader, it is useful to relate the signal detected by the tag reader to the magnetization of the material. The voltage **V** in a receive coil with **N** turns and area **A** can be related to the material properties and to the applied field **H** as follows:

$$V = -\frac{d\Phi}{dt} = -N\frac{d}{dt}\left[\oint nB \bullet dA\right] = -\frac{d}{dt}\int (\mu_0 H + M(H)) \bullet dA$$

The amplitude of the detected signal depends on the relative orientations of both antennas as well as the tag. In terms of frequency, it is simple to see that if the magnetization in the material is purely a linear function of the applied magnetic field, then no frequency components would be present other than the frequency of the applied field **H**. Conversely, if the function **M(H)** is non-linear over the range of applied field values, then the detected voltage would have harmonic content. If we model the square loop magnetization function **M(H)** as an ideal step function $\mathbf{u_{-1}}$ of height **m** centered at the origin, then the receive signal would have an infinitely long harmonic spectrum, as can be shown by taking the Fourier transform of the induced voltage:

$$\begin{aligned}
F\{V(t)\} &= \int_{-\infty}^{\infty} -\mu_0 N\left[\int \frac{d}{dt}\left[H(r,f_0,t) + u_{-1}(H(r,f_0,t))\right]\cdot m \bullet dA\right]\cdot e^{-j2\pi ft}dt \\
&= -\mu_0 N\int_{-\infty}^{\infty}\int \frac{d}{dt}\left[e^{-j2\pi f_0 t}H(r)\bullet dA\right]\cdot e^{-j2\pi ft}dt - NA(m\bullet dA)\int_{-\infty}^{\infty}\delta(t)e^{-j2\pi ft}dt \\
&= -\mu_0 N\int_{-\infty}^{\infty}\int 2\pi f_0\left[e^{-j2\pi f_0 t}H(r)\bullet dA\right]\cdot e^{-j2\pi ft}dt - NA(m\bullet dA) \\
&= C_1 f_0\delta(f - f_0) + C_2
\end{aligned}$$

Here, the time **t** = 0 denotes the time in the **M** vs **H** curve at which the applied field **H**=0. The above result also assumes that the driving field is periodic with single frequency $\mathbf{f_0}$, so that $\mathbf{H}(r,\omega_0,t) \propto e^{j2\pi fot}$. For a perfectly vertical step with infinite slope, the there are an infinite number of

harmonics extending to infinitely high frequencies. In practice, however, the harmonics do taper off after the 100th order or so. A sample spectrum is shown in Figure 51 below for a harmonic tag excited at 500 Hz, with harmonics extending to over 150 kHz.

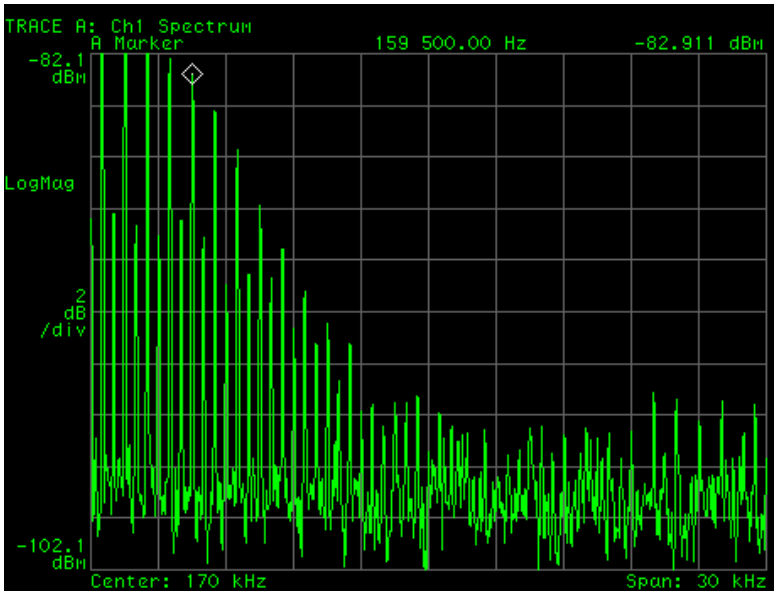

Figure 51. Section of a spectrum from a harmonic tag spanning 155 kHz-185 kHz showing the highest-order harmonics. The excitation frequency was 500 Hz.

Although it is difficult to generalize, harmonic generators generally produce a smaller signal than resonant mechanisms, since the energy of the reader is distributed among many harmonics. However, the ability to transmit at one frequency and detect at other frequencies allows for good signal separation and enables very sensitive detection methods with potentially very low noise floors.

4.2.3 Approach to Multi-Bit Tags

It is well known that the spectrum of a harmonic tag can be modified by coupling it to a planar permanent bias magnet. Such a structure is illustrated graphically in Figure 52 below. If such a bias field is present, the effective magnetization curve of the entire tag structure is shifted from the origin. If this shift is greater than the amplitude of the excitation field, then the harmonic material will remain in its single saturated magnetized state and not be affected by the excitation field. Without any change in the magnetization, no harmonics will be produced.

This method of inhibiting the harmonics has been used for many years by the EAS industry as a means of tag deactivation, commonly used in library books and videotape rental cases. In practice, however, the bias magnet is generally a periodic strip of permanent magnet segments as a means of better distributing the magnetic flux. When the permanent magnet is magnetized,

the harmonics are suppressed; and if the permanent magnet strip is de-magnetized, the tag becomes activated. Such a tag is thus a 1-bit chipless RFID tag that can be either ON or OFF.

Figure 52. Section of a spectrum from a harmonic tag spanning 155 kHz-185 kHz showing the highest-order harmonics. The excitation frequency was 500 Hz.

In order to explore multiple-bit implementations of such structures, the general approach pursued by myself as well as others has been to explore more complex patterns of bias magnets, and study the response. In terms of domain wall motion, the motivation for this approach can be explained using the illustrations in Figure 53 below. From an understanding of domain-wall motion presented previously, we know that the domain-wall velocity is dependent on the magnitude of the applied field. By coupling the magnetic material to locally-varying magnetic bias pattern, the domain wall motion will not b uniform and will result in a magnetization curve that contains features that are dependent on the applied bias pattern.

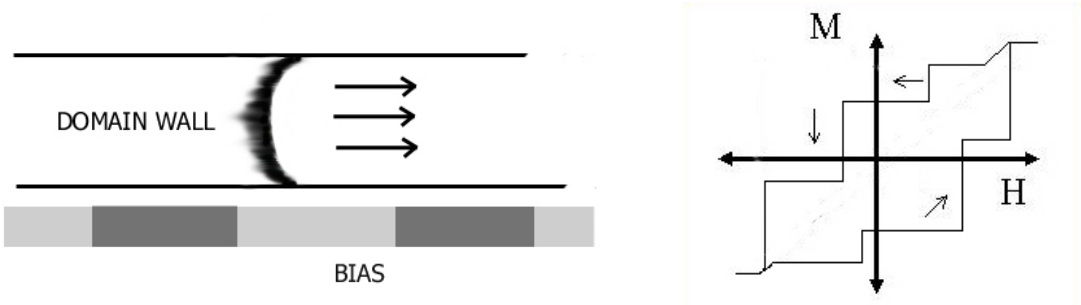

Figure 53. Schematic illustrating domain wall motion in the presence of a non-uniform magnetic field bias (left); idealized **M** vs **H** loop for this structure (right).

Although there are other physical interactions that can be used to affect domain wall velocity, the externally coupled bias pattern is attractive because it can, in principle, be re-written. Unlike most chipless technologies that are read-only or WORM (write once, read many), domain-wall tags with a patterned magnetic bias are an example of a re-write-able chipless tag. It represents a technology that combines the simplicity, re-write-ability, and low-cost of magnetic stripe label, with the wireless accessibility of an RFID label. This approach is discussed further in the following sections.

4.2.4 Magnetization Signal Model

In order to generate spectrum containing multiple bits of information, it is necessary to study how the magnetization curve of the composite material structure relates to the observed harmonic spectrum and time-domain signal. I first considered a multi-step magnetization curve such as that illustrated in Figure 48 that could be produced by a soft magnetic strip coupled to a segmented bias magnet strip. For a thin strip or wire with a single domain present, the domain would speed up and slow down according to the local magnetic field at that point. If such a motion were sufficiently discontinuous, a multi-step magnetization curve would be produced by the intermittent generated flux jumps.

I created a simple model in Mathematica to simulate the frequency response of a harmonic tag in the presence of a bias field. In order to create a more realistic response with a finite number of harmonic terms, the magnetization curves as a function of **H** were modeled as piece-wise continuous sinusoidal segments.

From Maxwell's equations, the voltage induced in the pick-up coil is a function of the applied field **H** and the induced magnetization **M** of the tag:

$$V(t) = -\frac{\partial}{\partial t}\int \mu_0 (H + M) \bullet dA$$

In order to express the voltage **V** as a function of frequency, a Fourier transform is applied, and the result is plotted on a logarithmic scale.

4.2.4.1 Simulation Data

Several sample plots from this model are given on the following pages. In addition to the magnetization curve, the signal induced on the reader pick-up coil is plotted both as a function of time and as a function of frequency. The following are the common parameters for all the plots:

N = Number of steps in M – H curve
Excitation Frequency = 40 Hz
Excitation field amplitude = 20 (normalized units)
Applied DC Bias Field = 0, 3, 5, 5.5, 10

Single-Step Magnetization Curve

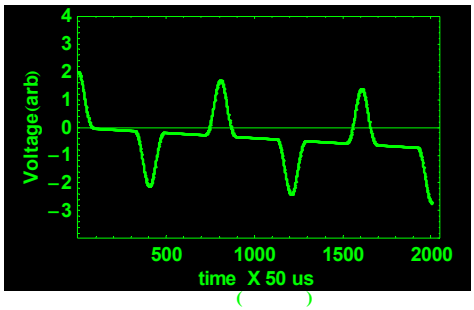

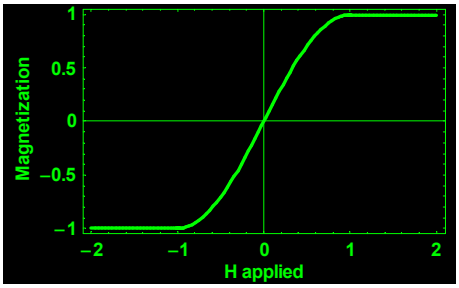

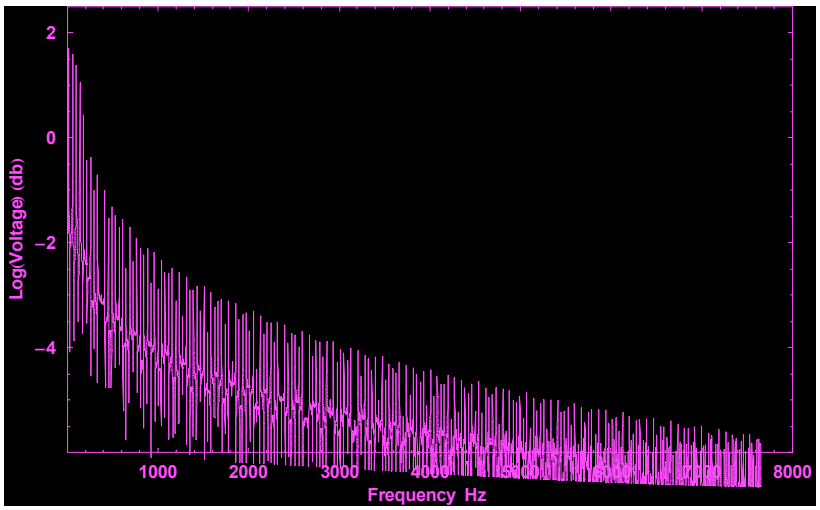

1-Step
Bias = 0

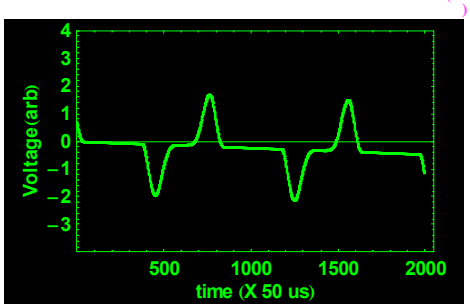

1-Step
Bias = 3

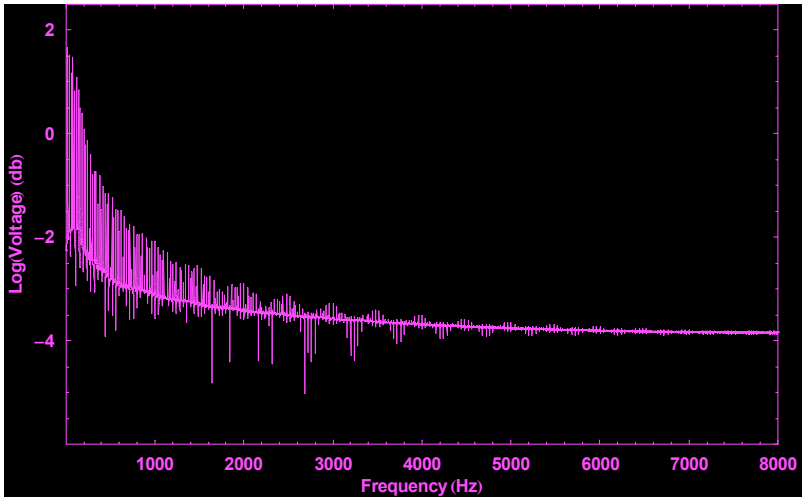

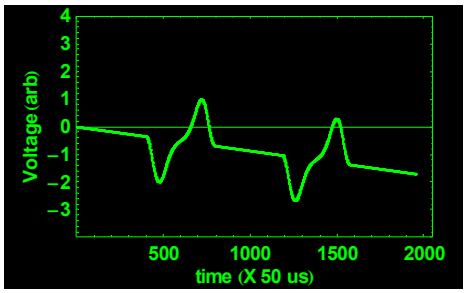

1-Step

Bias = 5

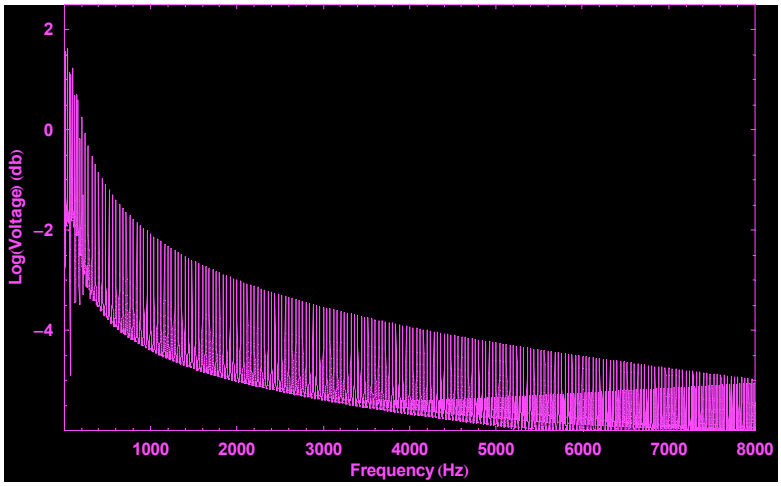

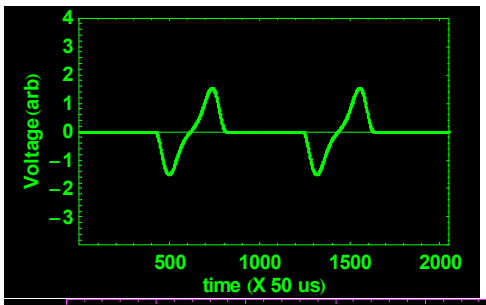

1-Step

Bias = 5.5

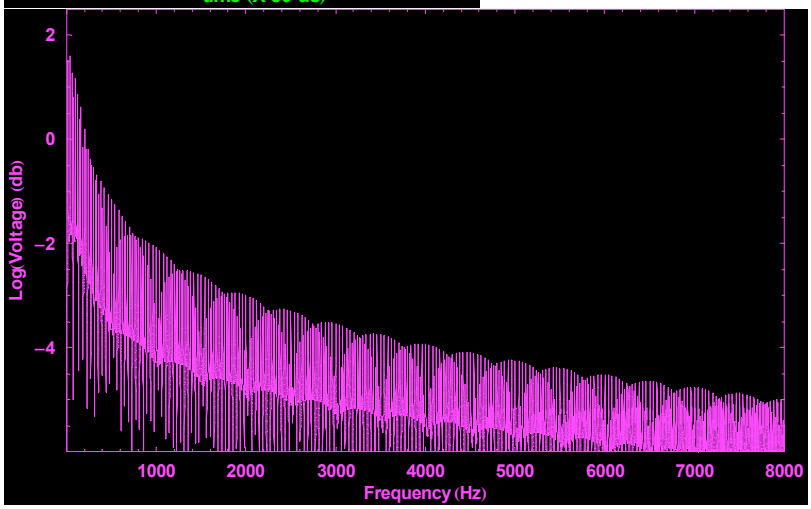

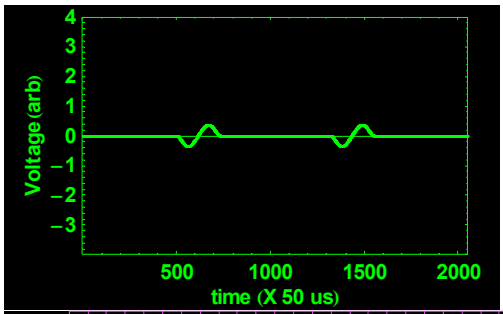

1-Step

Bias = 10

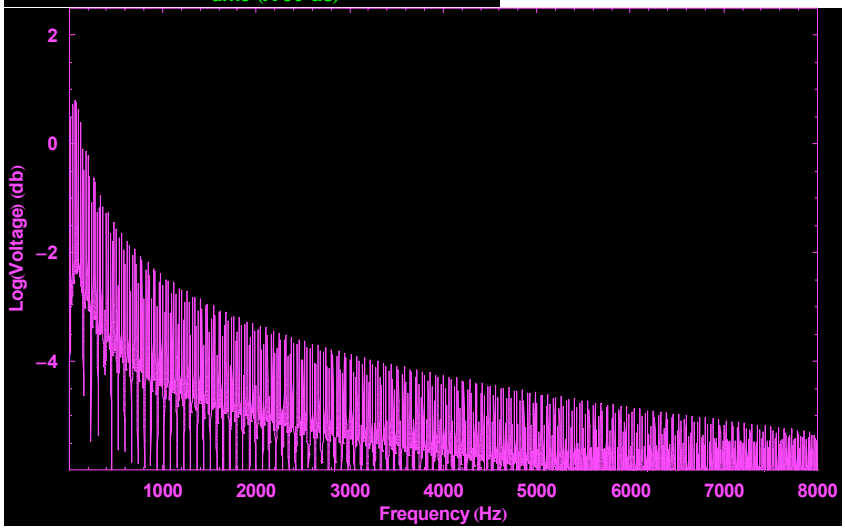

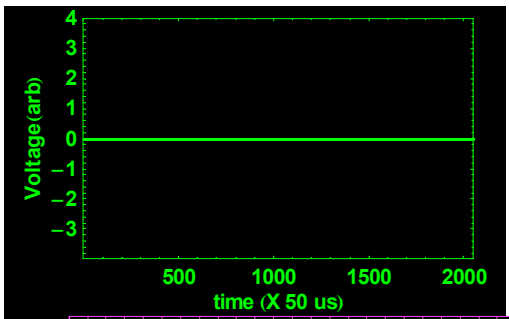

1-Step

Bias = 15

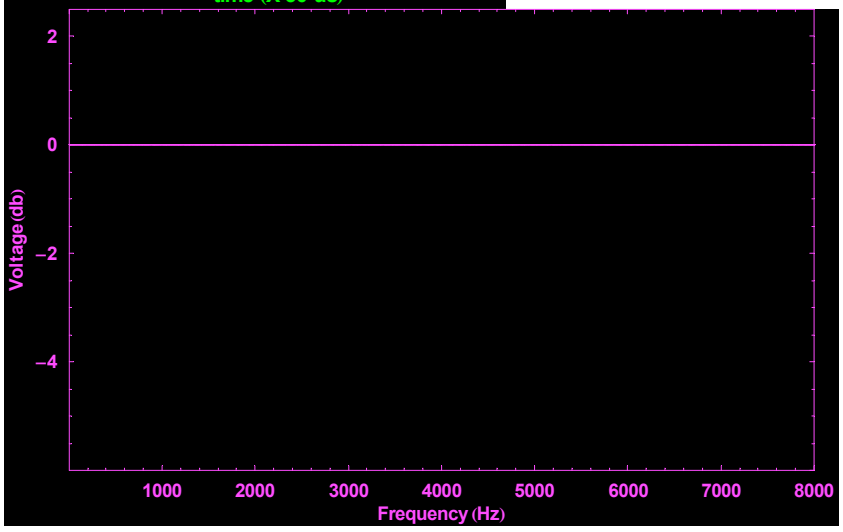

5-step Magnetizaton Curve:

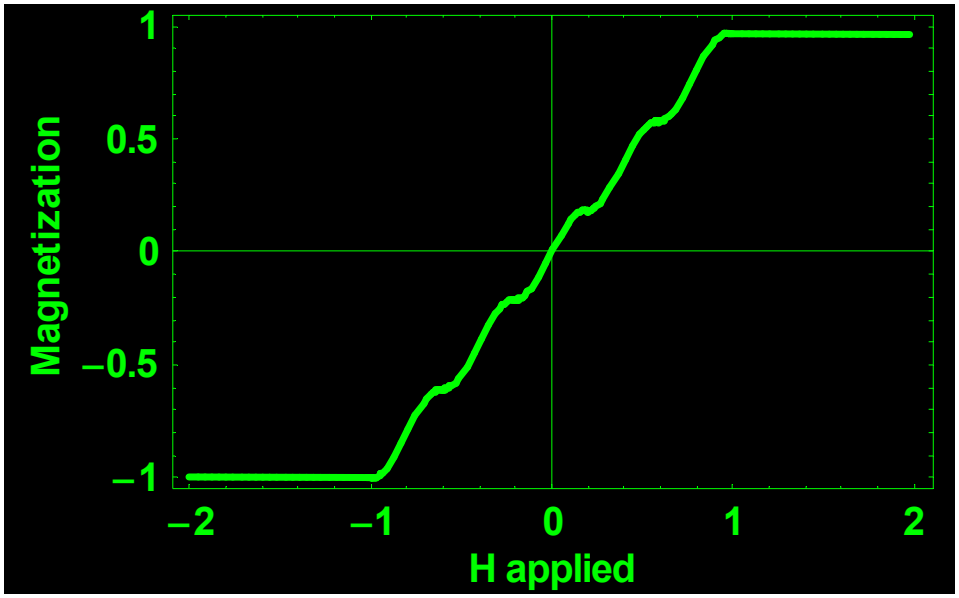

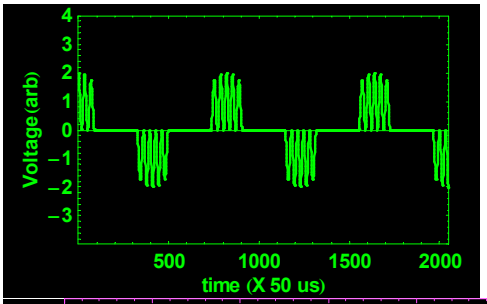

5-Step

Bias = 0

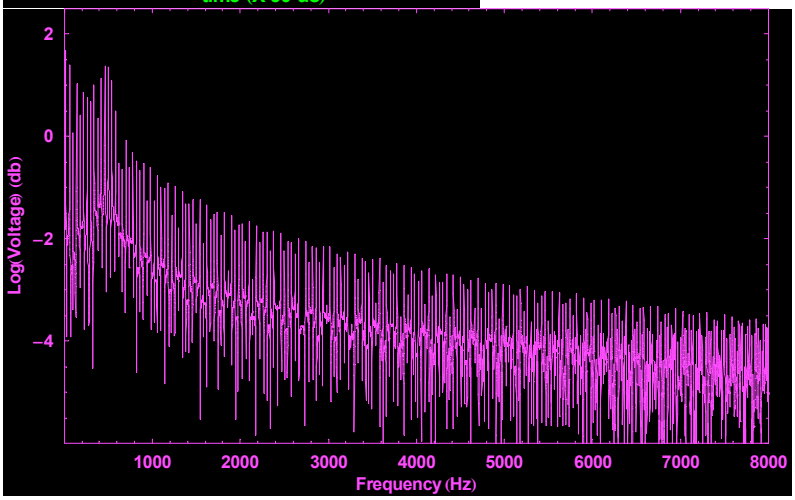

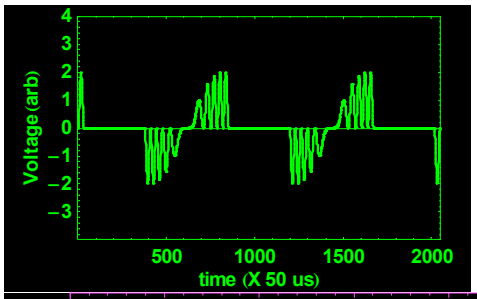

5-Step
Bias = 3

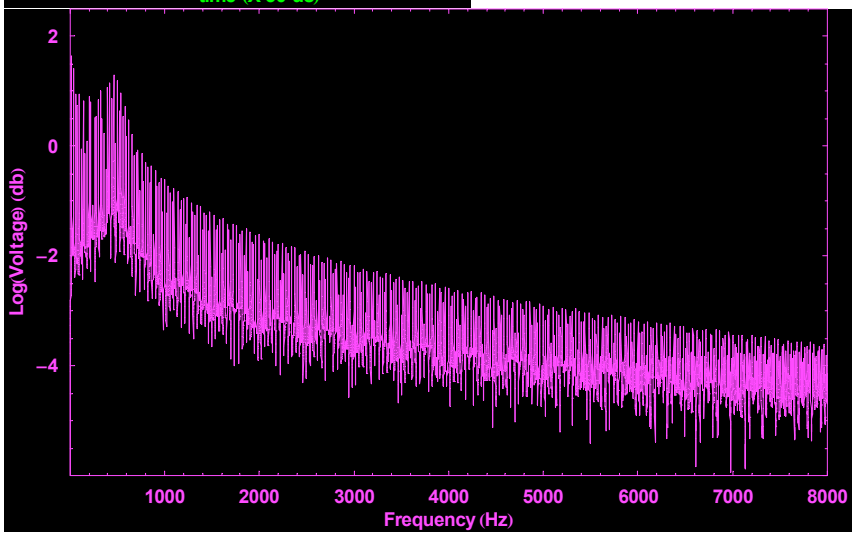

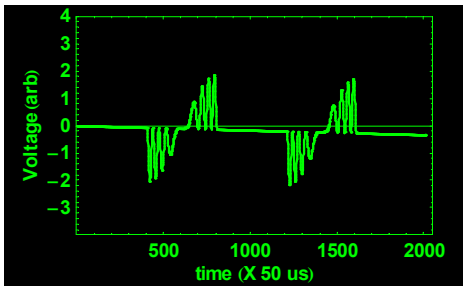

5-Step
Bias = 5

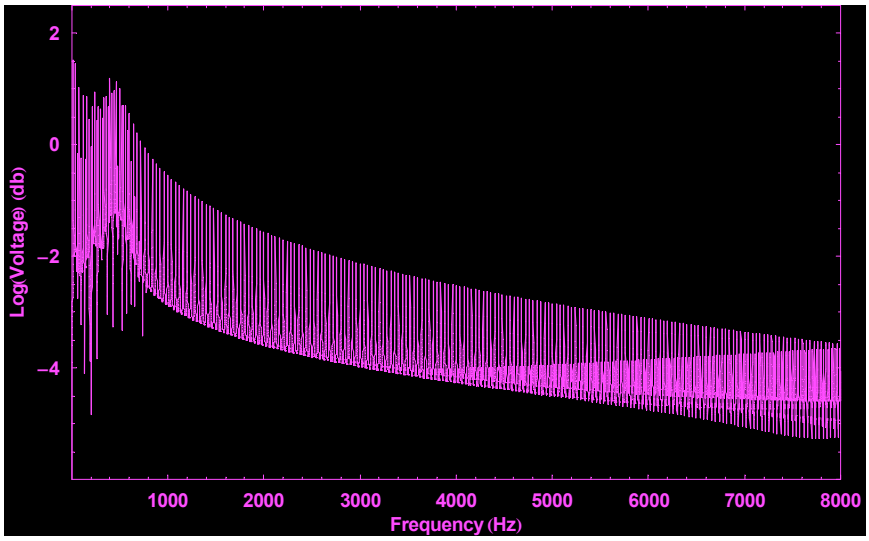

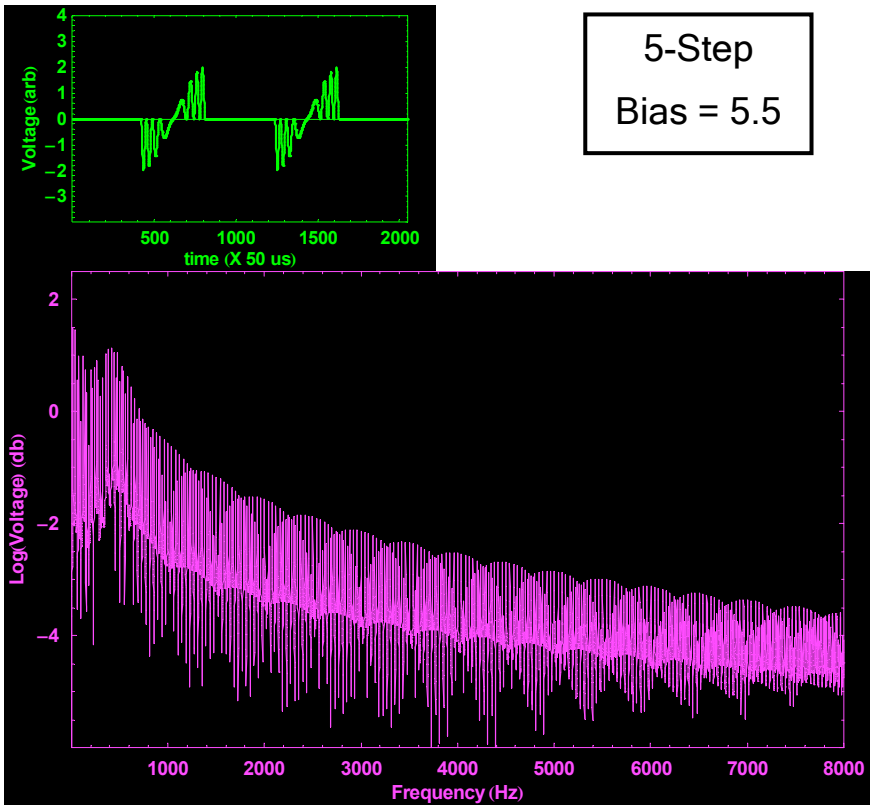

5-Step
Bias = 5.5

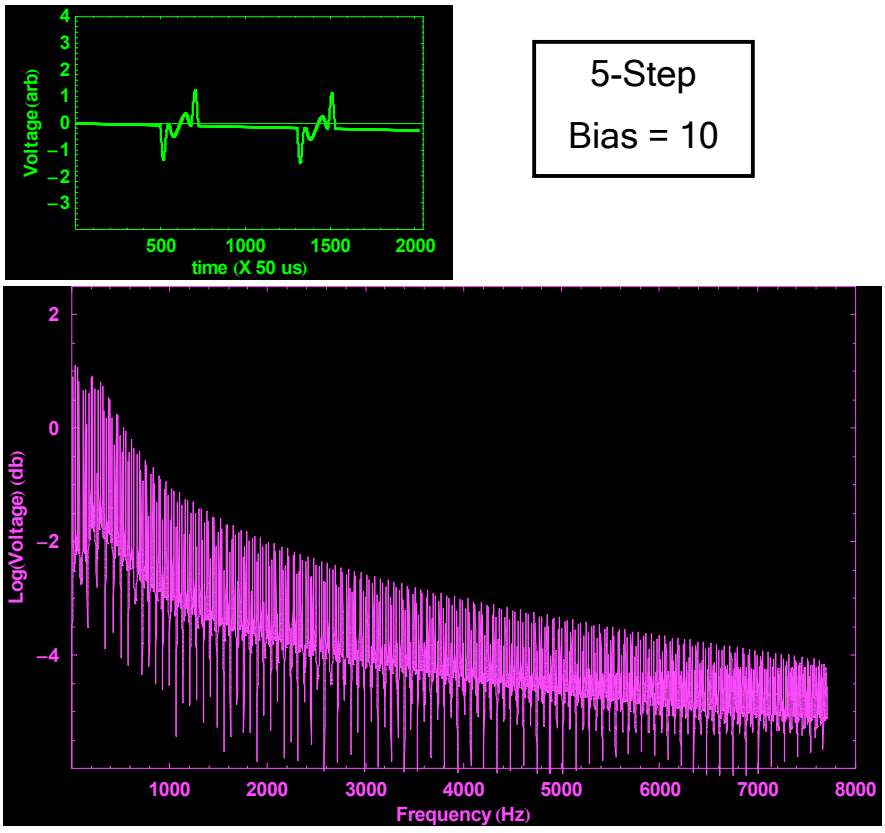

5-Step
Bias = 10

10-step Magnetization Curve:

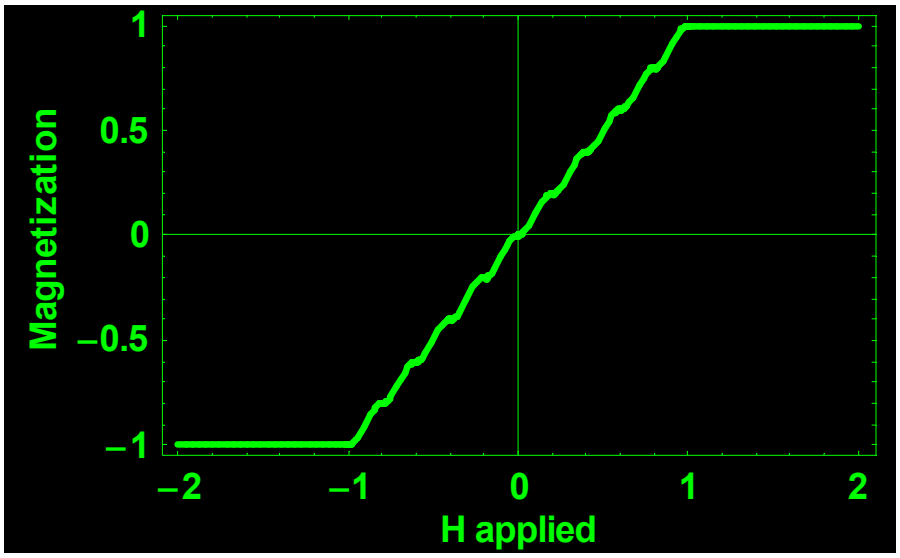

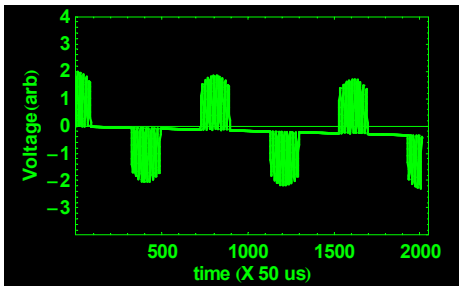

10-Step

Bias = 0

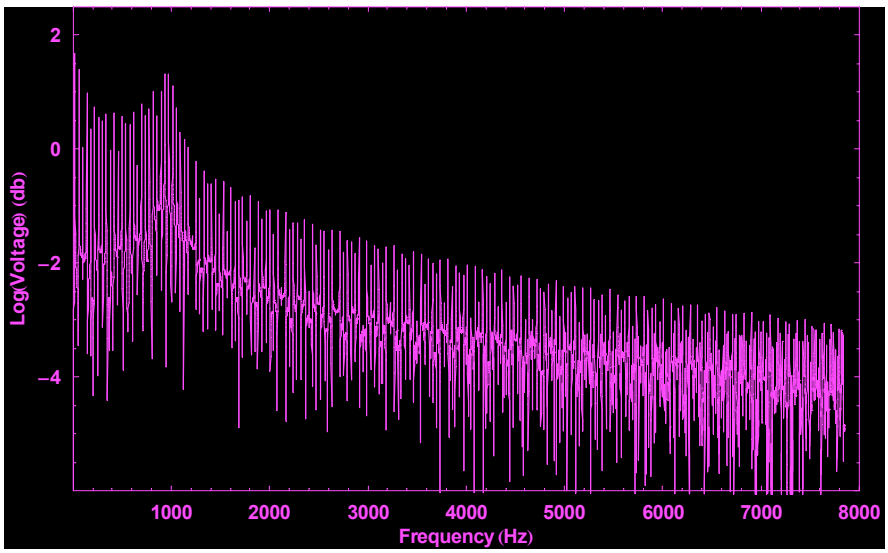

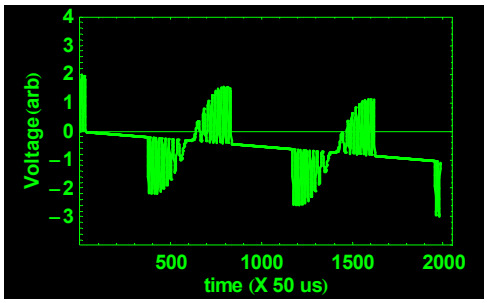

10-Step
Bias = 3

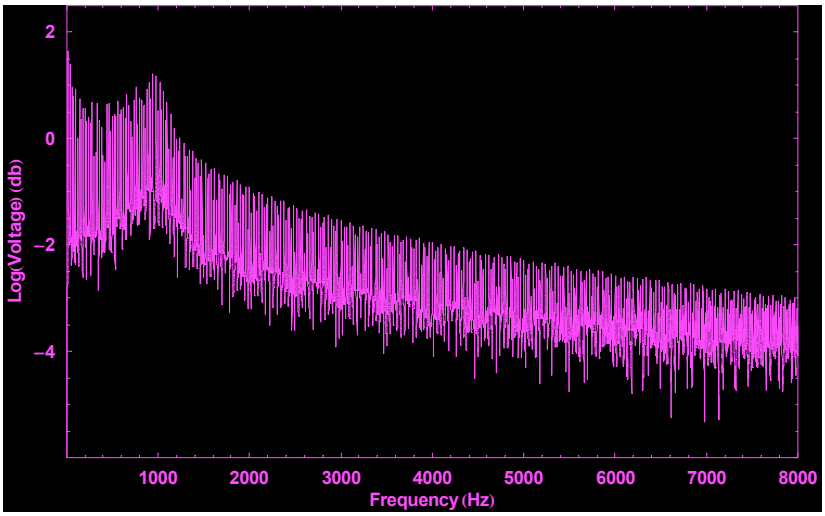

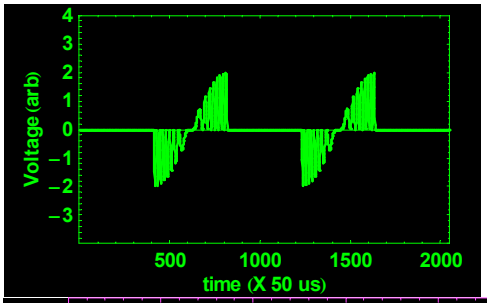

10-Step
Bias = 5

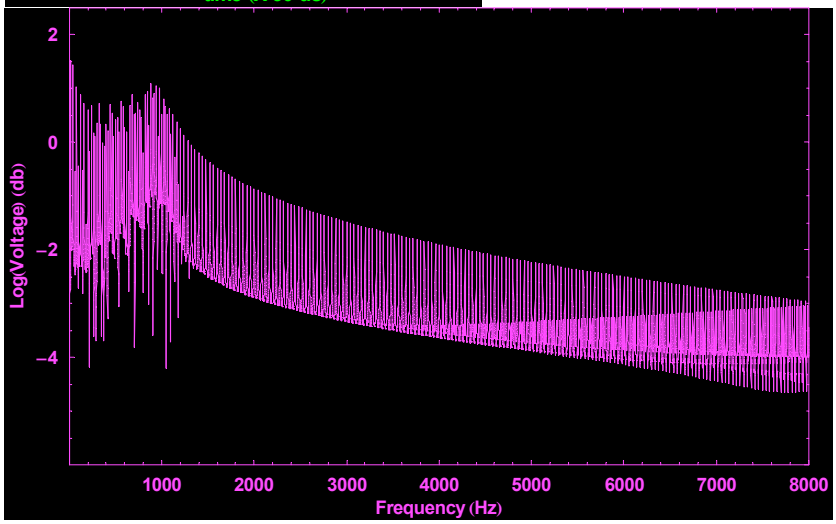

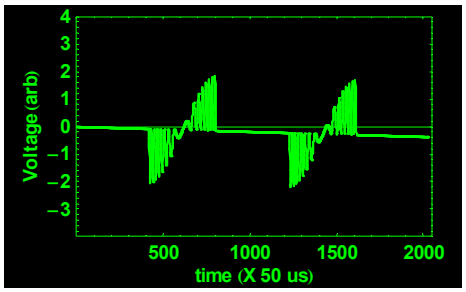

10-Step

Bias = 5.5

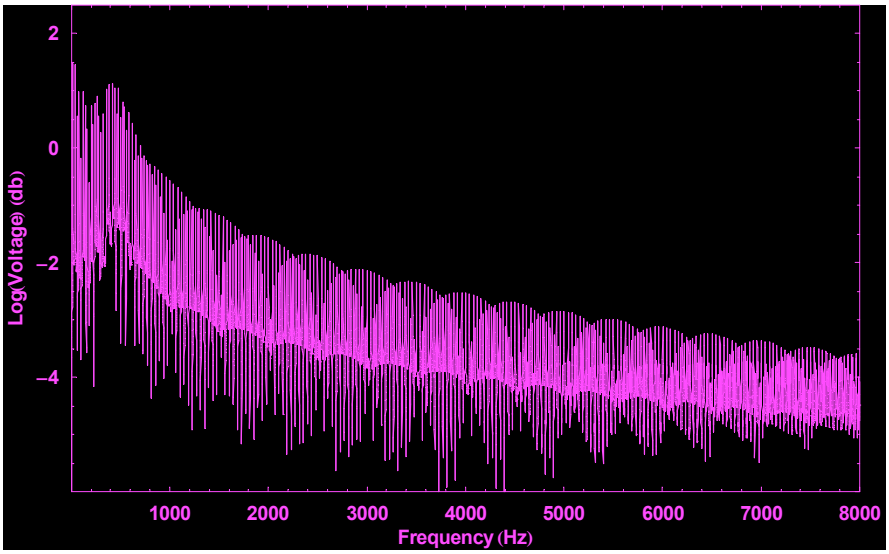

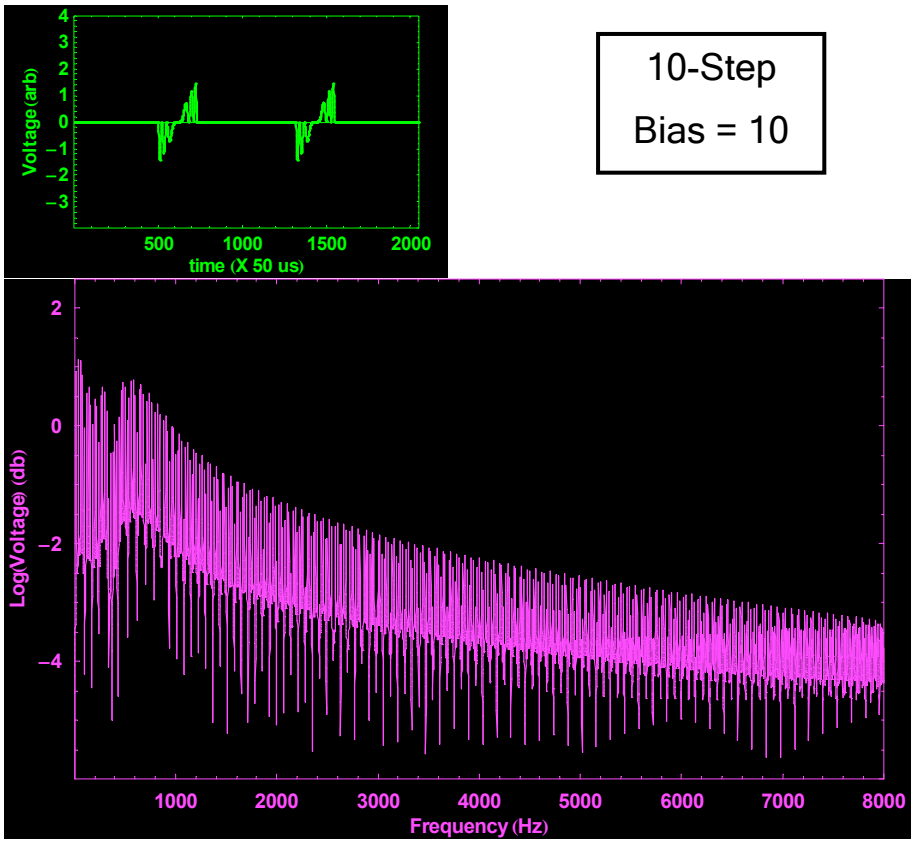

4.2.4.2 Observations

The simulations indicate a rich set of signal behaviors that are dependent on specific initial conditions, but a few general observations can be made:

- **Relative Phase** -- From the time-domain signal we can see that phase of the magnetization pulses relative to the excitation phase increases as the DC bias field is increased. We can observe this experimentally on an oscilloscope by seeing the how the position of the magnetization pulses occurs at a different point on the excitation sine-wave as the DC field is varied.
- **Harmonic Content** -- The amplitude of the odd- and even- harmonics occur with different periodicities. As can be observed from the data (for example, when Bias = 5.5), the even harmonics vanish completely. This is expected because the time-domain wave at this bias field becomes completely odd (anti-symmetric), and thus contain no even components..
- **Meta-resonance** -- In the case of a larger number of steps, the interval between magnetization pulses becomes increasingly small such that the frequency of those pulses gives rise to a frequency-peak of its own.

4.2.5 Multi-bit harmonic tag implementation

Although the features in the frequency spectrum of a harmonic tag signal are very redundant, the simplicity and low-cost of these materials have made them attractive candidates for research in low-cost chipless RFID. In the following sections, I review some of the research done in this field as part of my graduate wok as well as some of the approaches used commercially.

4.2.5.1 Test Setup

In order to test candidate structures, a custom built fixture was fabricated, shown in Figure 45. This fixture consisted of a 2-layer excitation coil made of 422 turns of copper magnet wire, with a 2000-turn pick-up coil into which the sample was inserted. The DC bias field was provided by an adjustable permanent magnet that could be positioned a specified perpendicular distance from the sample. The armature holding the permanent magnet was marked with reticules indicating specified values of the DC field in Gauss, as calibrated by an electronic Gaussmeter.

The excitation signal was generated from a Hewlett-Packard signal generator, and then amplified using a two-stage transistor amplifier I designed. The received signal required no additional amplification and was fed directly into a Hewlett-Packard Mixed Signal Analyzer for analysis.

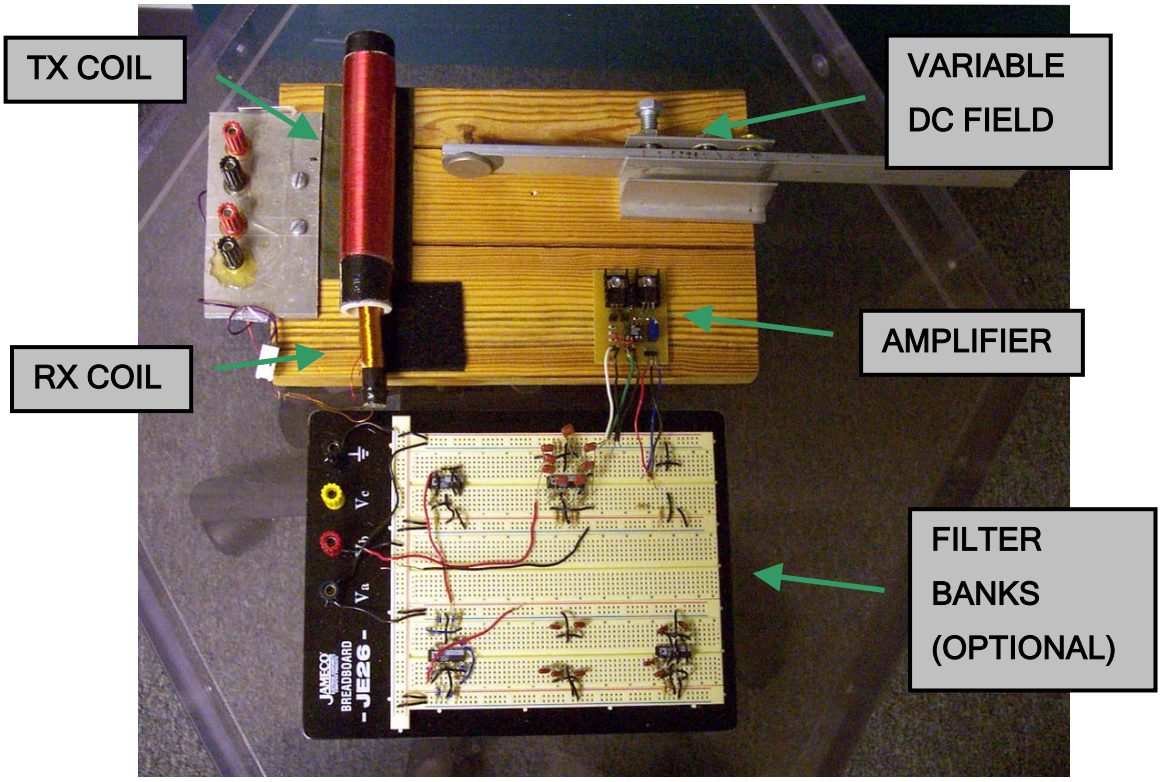

Figure 54. Photograph of sample coil test fixture.

4.2.5.2 Experimental Measurement: Tiled Bias Magnet

The initial implementation of a patterned-bias domain-wall tag was constructed from a 2mm-wide amorphous ribbon material (VCB) made by VacuumSchmelze, shown in the Figure below. This alloy is composed of Co, Fe, Si, and B, and is current-annealed to induce a transverse magnetization.

Figure 55. Photograph of amorphous ribbon material used for study.

The bias pattern was constructed from small segments of Arnochrome 3 permanent magnet material that were either magnetized using a large electromagnet or magnetized manually with a bar magnet. For each tag, four permanent magnet segments were then taped to the magnetic strip samples to form the magnetic bias pattern. In this first set of data, the magnet segments were aligned to be transverse to the long axis of the magnetic strip.

On the following pages, I show data for three different bias patterns with excitation frequency f_0=200 Hz. The bias pattern is indicated by the boxes and arrows above each spectrum.

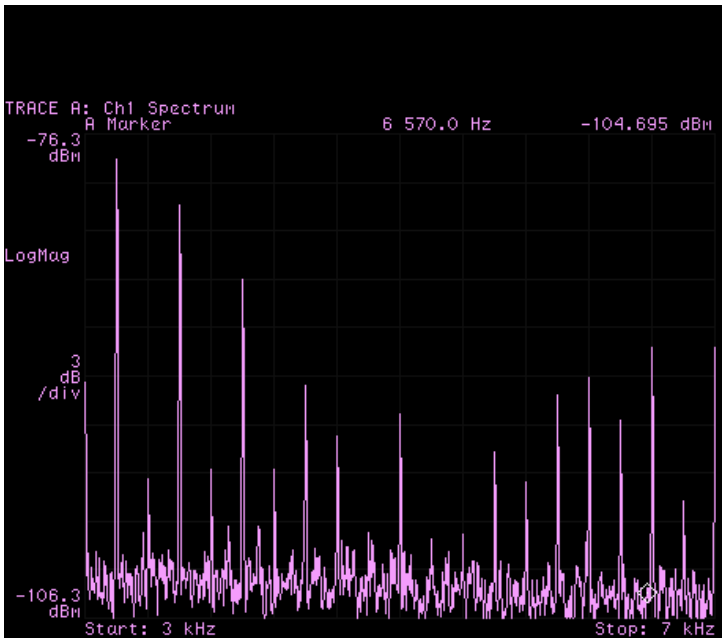

BIAS PATTERN 1

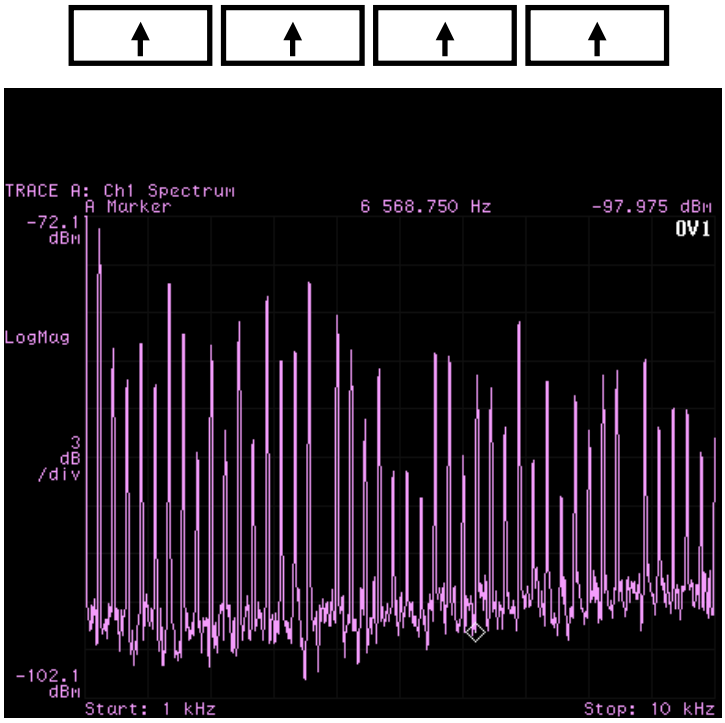

BIAS PATTERN 1
(wideband view)

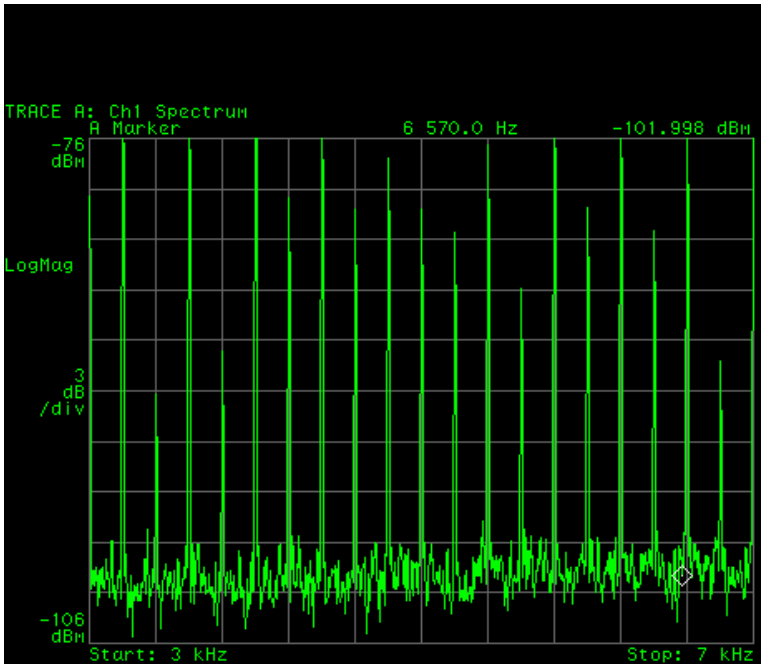

BIAS PATTERN 2

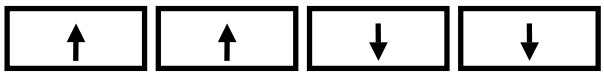

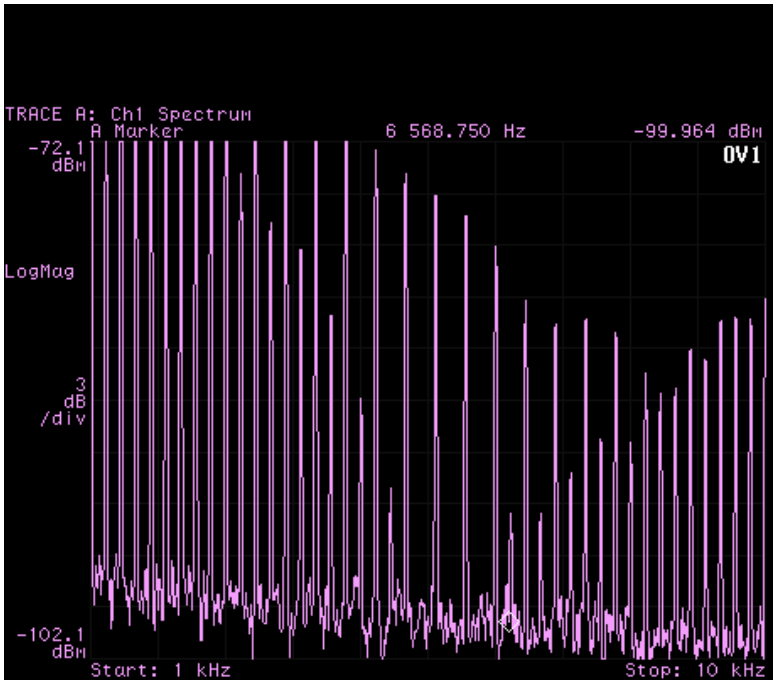

BIAS PATTERN 2
(wideband view)

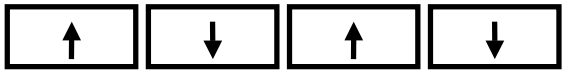

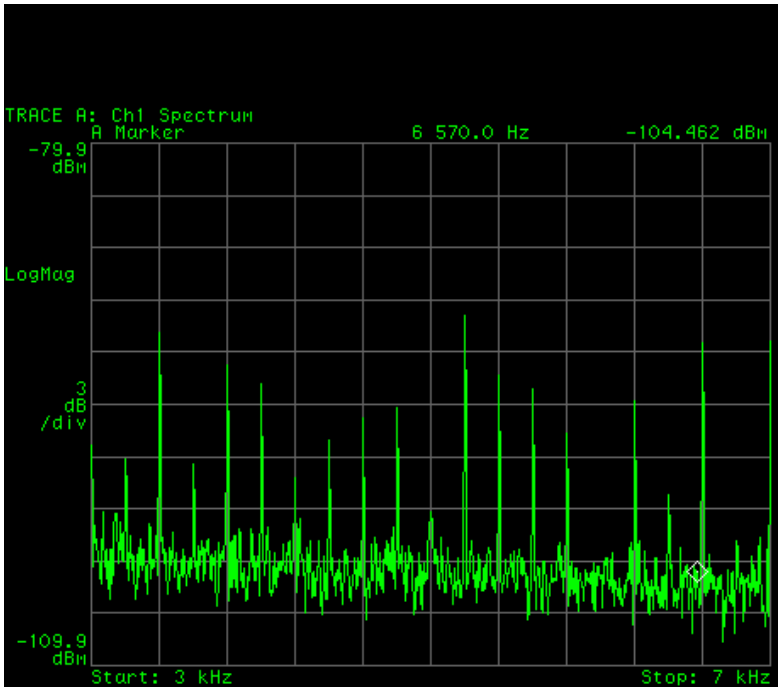

BIAS PATTERN 3

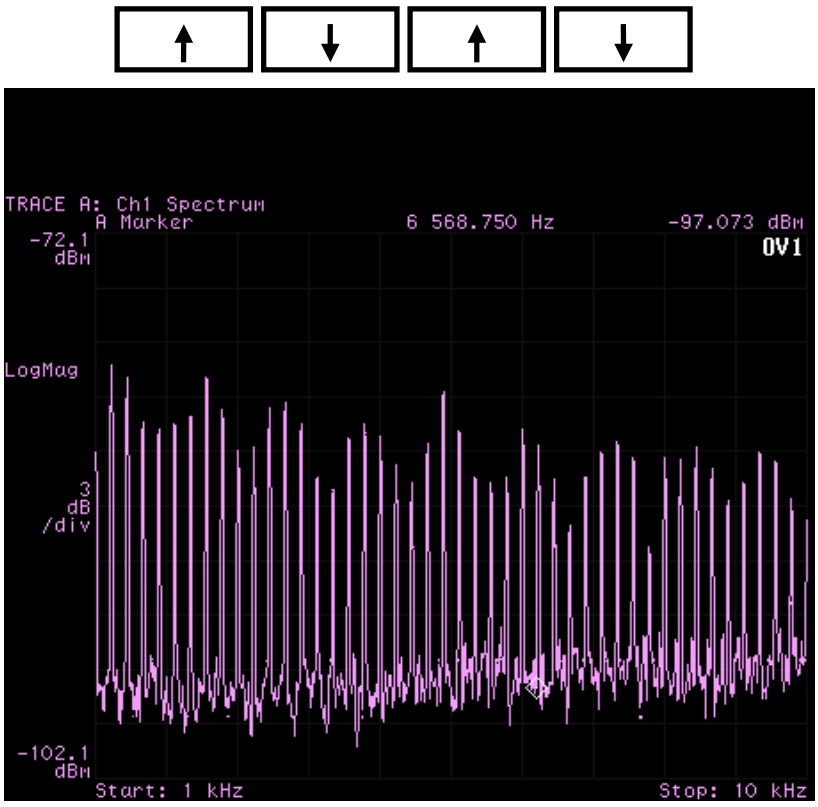

BIAS PATTERN 3
(wideband view)

This initial data demonstrated that the harmonic spectra did depend on the magnetic bias pattern. However, the bias pattern was difficult to control and reproduce without specialized equipment. Even if I magnetized a long strip of Arnochrome 3 using an electromagnet, it was not clear what how the magnetization of the individual pieces would behave after they were cut. I was concerned that the magnetization vector would wander due to shape anisotropy as well as the stress during cutting. An additional difficulty is not having the ability to properly visualize or characterize the magnetization patterns of the bias strip.

It became immediately apparent from this first implementation that a major challenge of this type of chipless design is the proper construction of the bias pattern as well as the coupling to the magnetic strip.

4.2.5.3 Measured Data: Magnetic Stripe Bias

In an attempt to create a more reproducible process for creating a magnetic bias pattern, I obtained a credit card writer machine and proceeded to try a credit card magnetic strip as a means of providing the bias pattern. Using the credit card writer, I created three distinct bias pattern strips containing large blocks of digital 1's or 0's.

For the magnetic strips, two different materials were used: one strip was the same VCB amorphous ribbon as before, and the second was an amorphous wire, made by Unitika in Japan. Using an excitation frequency of f_0 = 500 Hz, the following data was collected.

Amorphous Wire Sample

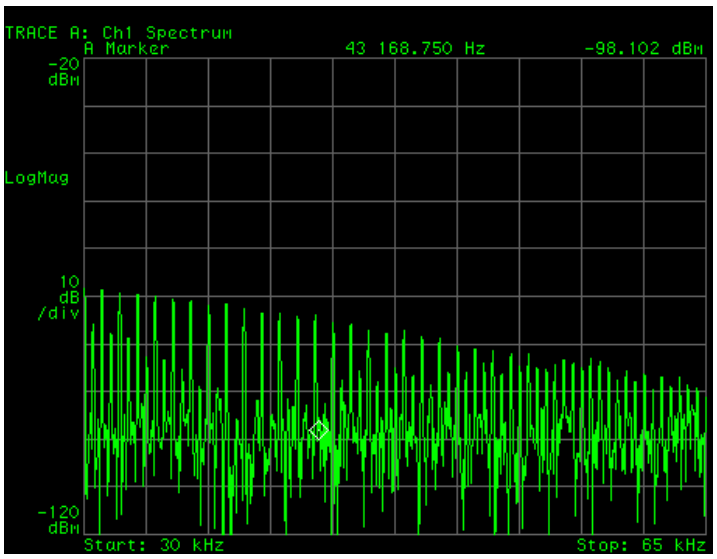

NO BIAS

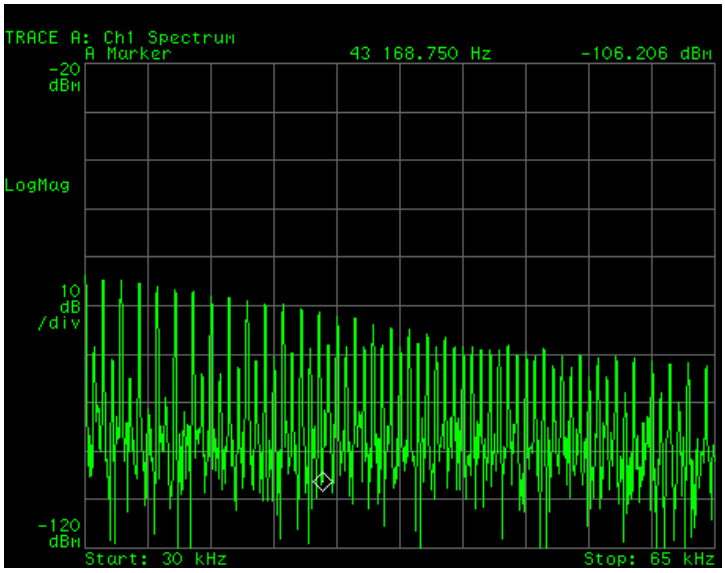

BIAS 1

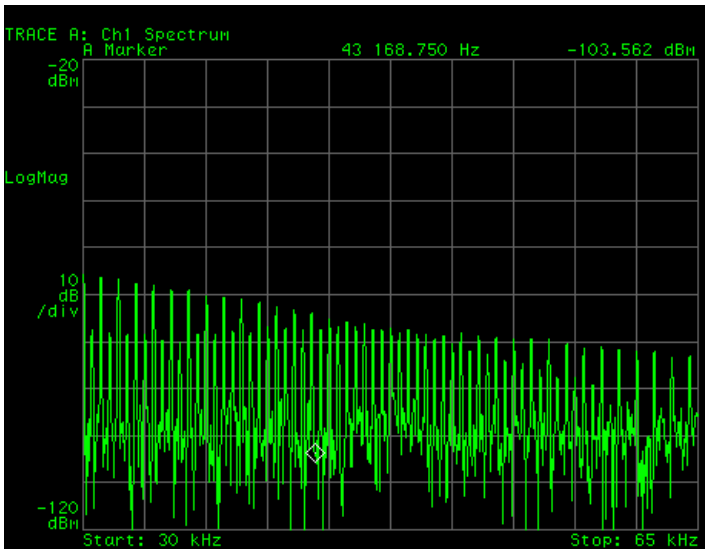
TRACE A: Ch1 Spectrum
A Marker
43 168.750 Hz
-103.562 dBm
-20
dBm
LogMag
10
dB
/div
-120
dBm
Start: 30 kHz
Stop: 65 kHz

BIAS 2

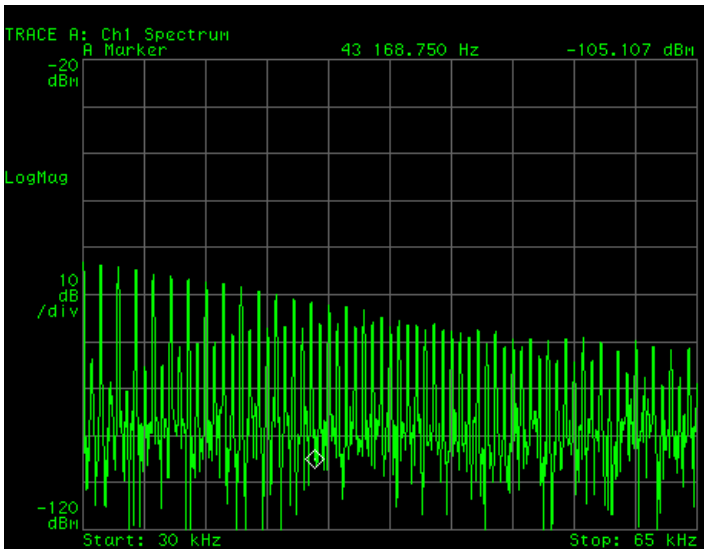
TRACE A: Ch1 Spectrum
A Marker
43 168.750 Hz
-105.107 dBm
-20
dBm
LogMag
10
dB
/div
-120
dBm
Start: 30 kHz
Stop: 65 kHz

BIAS 3

VCB Amorphous Ribbon

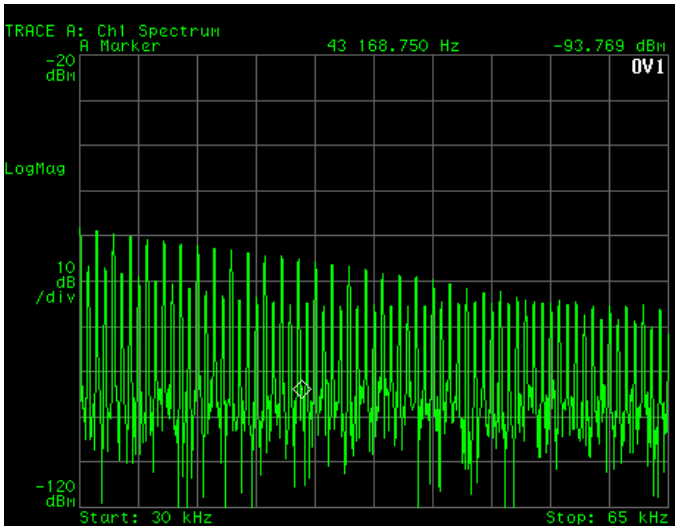

NO BIAS

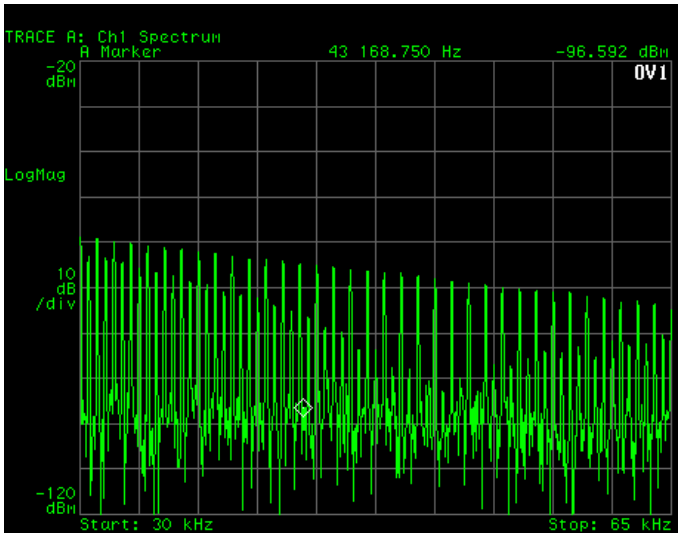

BIAS 1

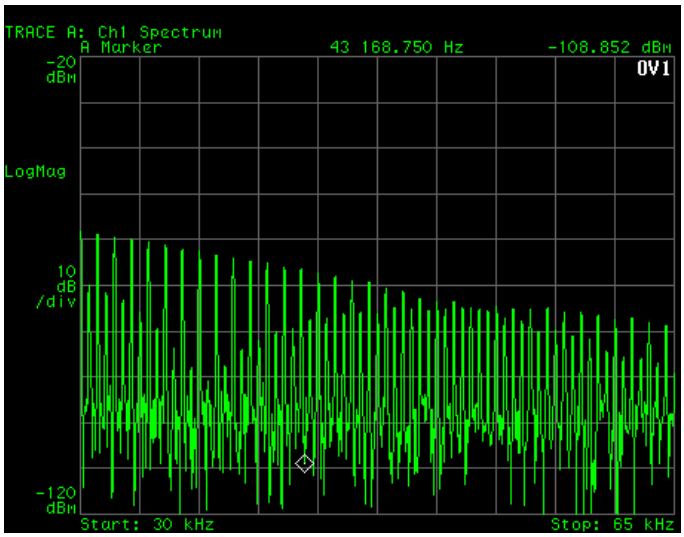

BIAS 2

4.2.5.4 Observations and Conclusions

From the measurements, we can see that the VCB material exhibits a more pronounced signal variation in response to the bias pattern. It is clear that the additional area of the ribbon material provides better coupling to the bias magnets than the amorphous wire. It is also interesting to note that in this case, only the odd harmonics exhibit a pronounced effect; even harmonics are not significantly affected by the bias.

Although this experiment demonstrated a reproducible method for creating different bias patterns, it did not provide a means for creating an arbitrary bias pattern. The credit card writer machine is restricted to writing bit patterns that correspond to alphanumeric characters; and in addition, the produced magnet stripe contains clocking bits interspersed within the data bits.

It is very difficult to correlate and predict the frequency response of a tag without knowing its magnetization curve. However, direct measurement of the magnetization curve was not possible by standard means (using a magnetometer) due to sample size limitations.

Given other promising research paths, I decided not to pursue this work further. Although the basic concept seemed feasible and promising, it is clear that a better manufacturing method would be necessary for producing samples and tags. If this work were to continue at the Media Lab, it would be necessary to build a custom magnetic head writer that would enable reproducible and arbitrary bias patterns to be written on the magnetic stripe. Nevertheless, the problem still reduces to measuring the magnetization curve that results from a given bias pattern, and learning how to predict the resulting magnetization curve.

4.2.5.5 Commercial Development

Another reason that I did not pursue this family of tags further is that I learned of several companies that began working in this area. In the late 1990's two companies, Flying Nulls and Holotag, with the support of researchers at Cambridge University, each developed tag technology based on domain-wall motion and patterned magnetic bias. Although the specific details are not known; however, the general approach employed by Flying Nulls is to slowly sweep the applied DC field and monitor the harmonics. This is a nice approach for applications that do not require a long read-range, since the probing AC field can have a relatively small amplitude and the swept DC field is used to slowly trace out the magnetization curve of the tag. This technique represents a useful approach for probing the bias magnet configuration.

As of 2002, Flying Nulls is still in business with primary support from the soft goods industry as a means of tagging and authenticating clothing items. The number of bits produced by this method is on the order of 10 bits and is dependent on the length of the strip. The read range is very short (<2 inch).

In the late 1990's, a company named Holotag created an interesting variation of the method used by Flying Nulls. Instead of using a linear geometry, Holotag proposed a circular one. In the linear case, the domain wall is driven by an axial magnetic field, and adding more bits requires lengthening the tag. However, in the case of Holotag, the domain wall was driven azimuthally in a circular tag by two coils 90° out of phase and at right angles to each other in order to produce a rotating domain wall. The bias patterns can be made in the shape of wedges or sectors, with additional bits created by making thinner slices of the "pie." Although this concept is clever, the complexity of the reader and the humble performance of the tag did not prove successful commercially.

Figure 56. Photograph of a hand-held reader used to for authenticating goods. This particular tag and reader do not provide any ID information and only indicate presence.

4.2.6 Multi-Bit Time-Domain Implementation

Although it is possible to encode data in the magnetization curve, some of this data is lost when represented in the frequency-domain. For example, the frequency-domain data can implicitly tell us the periodicity of steps in the magnetization curve but cannot easily tell us the position of those steps. As a result, it is useful to consider a time-domain measurement as more direct method of probing the magnetization curve of the tag, and ultimately, probing the bias configuration.

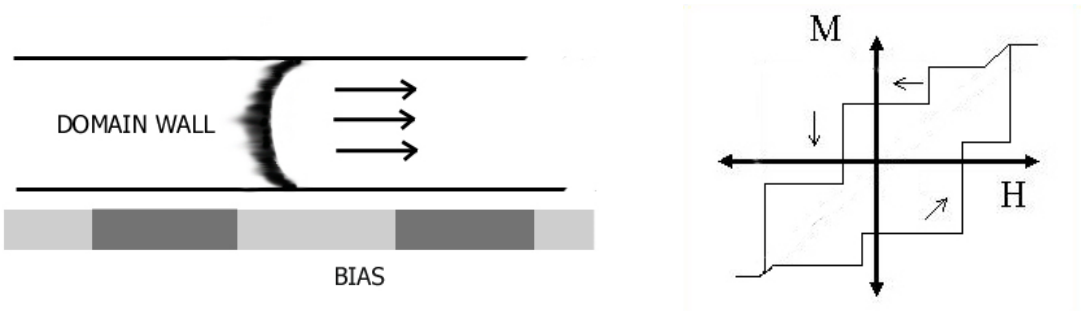

Figure 57. Schematic illustrating the basic operational concept (left); idealized **M** vs **H** loop for this structure (right).

4.2.6.1 Basic Design Considerations

Considering the domain wall motion inside a thin non-uniformly-biased material, it is most simple to consider a single domain traveling linearly along the length of the tag. In order to do so, the following main design properties to be considered:

- **Width of the strip** -- In order to increase the probability that there is a single domain-wall, it is desirable to constrain the width of the strip to 1 millimeter or so, based on the domain wall width of typical soft magnetic alloys. There is a performance trade-off in this parameter, however, because a more narrow strip reduces the amplitude of the magnetization (because there is less material present), and more importantly, reduces the amount of coupling between the strip and the planar bias magnets.
- **Domain-wall Nucleation** -- The material properties and morphology at the ends of the strip are critical to ensure that a domain wall will nucleate from the ends of the strip. The can be dome by changing the shape of the taper at the ends of the strip as well as using flux concentrators to produce a local field maximum at the ends. In addition, since it is possible for the domain wall to nucleate from both ends of the tag at once, it is useful to consider introducing an asymmetry, such as applying a flux concentrator to only one end of the strip.

4.2.6.2 Experimental Measurements

For studying domain-wall signatures in the time-domain, four separate magnetic strip were prepared and are shown in Figure 43 below. Strip #1 and Strip #2 were 2 mm-wide VCB strip of slightly different lengths approximately 4 inches long. Strip #3 was comprised of two 1mm-wide strips of VCB side by side. Strip #4 was a 4-inch length of amorphous wire.

Since such large samples cannot be measured by traditional means, such as using a VSM (Vibrating Sample Magetometer), custom designed apparatus was used for measurements. In order to observe the time-domain signatures, we employed the same test coil fixture that was used in the frequency-domain measurements, with the output of the receive coil connected directly to a digital oscilloscope. In order to attenuate the fundamental excitation signal produced by the transmit coil, a balanced pick-p coil twice as long as the samples was constructed with an equal number of turns in each direction on each half of the coil. In addition, an active 8-pole high-pass filter with a cut-off frequency of 500 Hz was employed to further attenuate the low-frequency contributions. Using configuration, the signal received by the pick-up coil appeared nearly flat when viewed on the oscilloscope at 50 us per division and 50 mV per vertical division.

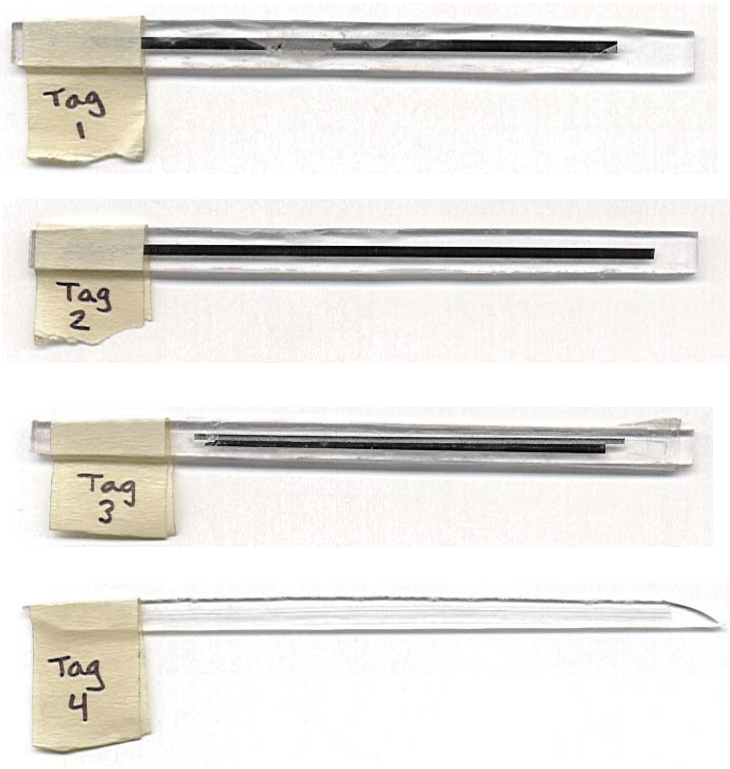

Figure 58. Photograph of VCB magnetic strips mounted on Plxiglas employed for the time-domain measurements. The strip on the bottom (#4) is an amorphous wire sample made by Unitika in Japan.

Four separate bias patterns were prepared using magnetic stripes that were cut from credit card stock. These stripes were magnetized manually using a strong bar magnet and the polarity verified using a handheld gauss meter. These bias segments were permanently glued to a thin strip of Plexiglas in four different configurations. For testing, each bias pattern strip could then be attached to each numbered magnetic strip by simply taping the two pieces of Plexiglas together

face to face. The four sample bias pattern strips used are shown in Figure 59 below applied to Strip #1.

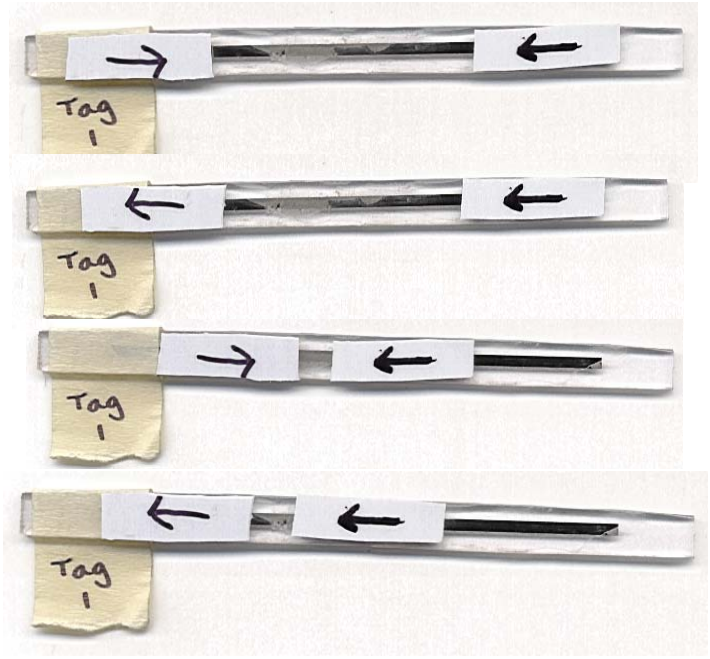

Figure 59. Photograph of magnetic strips employed for the time-domain measurements.

Measurements were then performed for all combinations of magnetic strips, bias patterns, and applied DC bias fields (0, 0.3, 0.5, 0.7, 1.0, 1.5, 1.7, and 2.0 Gauss respectively) and each waveform was recorded on a digital oscilloscope and stored in a file. A small fraction of this data is presented in the following pages.

EXPERIMENTAL PARAMETERS

4 Different Magnetic Materials Strips

4 Different Bias Patterns

Excitation Frequency = 200 Hz

Approximate TX field amplitude = 200 Oe

Applied DC Bias Field = 0, 0.3, 0.5, 0.7, 1.0, 1.5, 1.7, and 2.0 Gauss

DC Bias field = 0

VOLTAGE (50 mV/div)

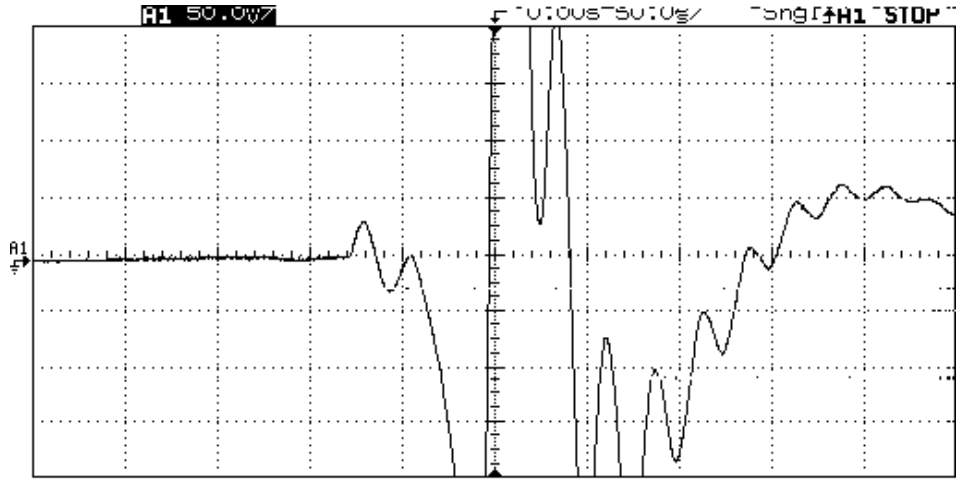

BIAS PATTERN 1

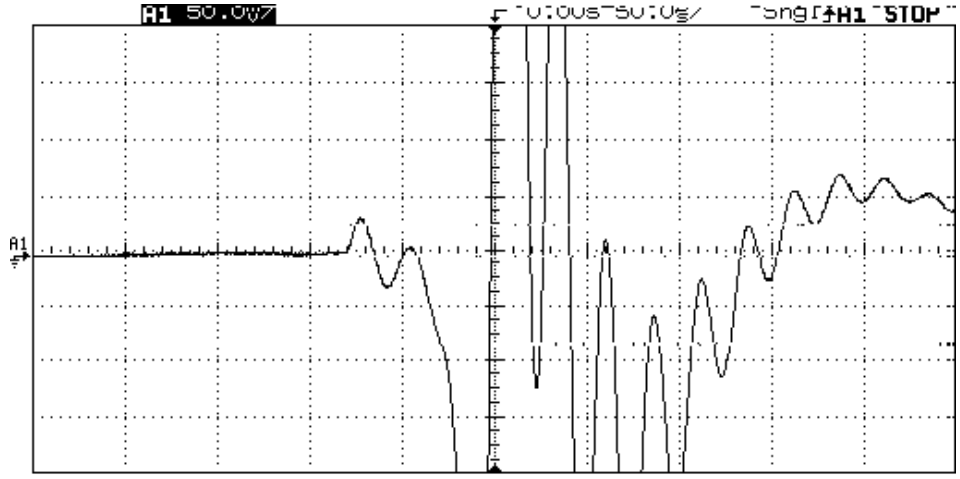

BIAS PATTERN 2

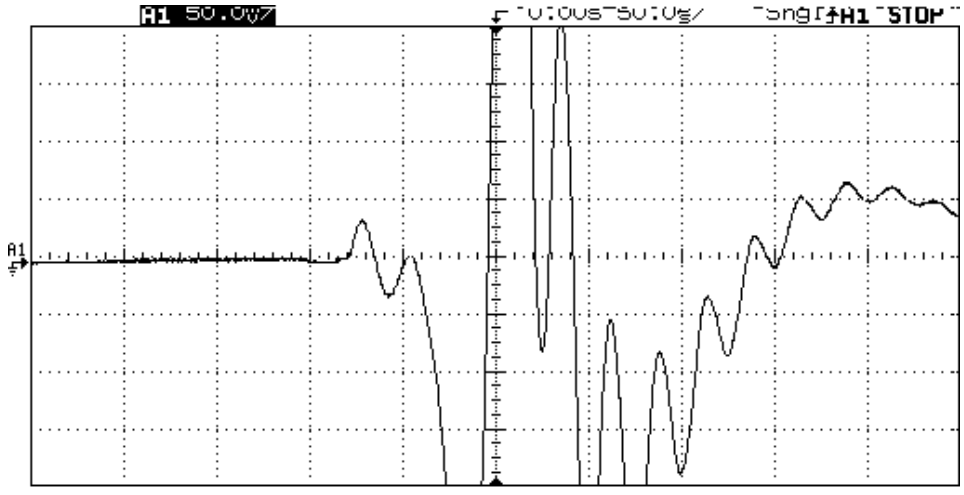

BIAS PATTERN 3

TIME (50 us/div)

DC Bias field = 0.3 Gauss

VOLTAGE (50 mV/div)

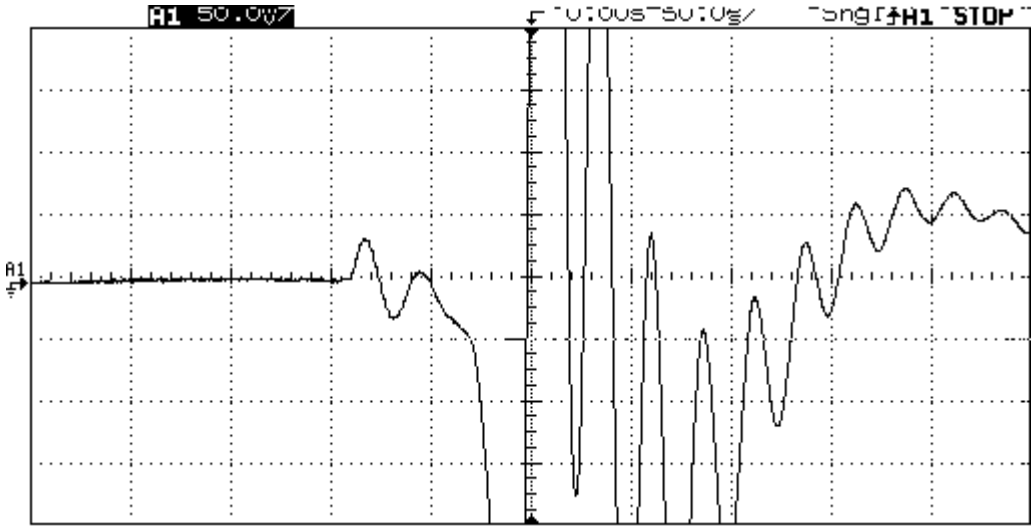

BIAS PATTERN 1

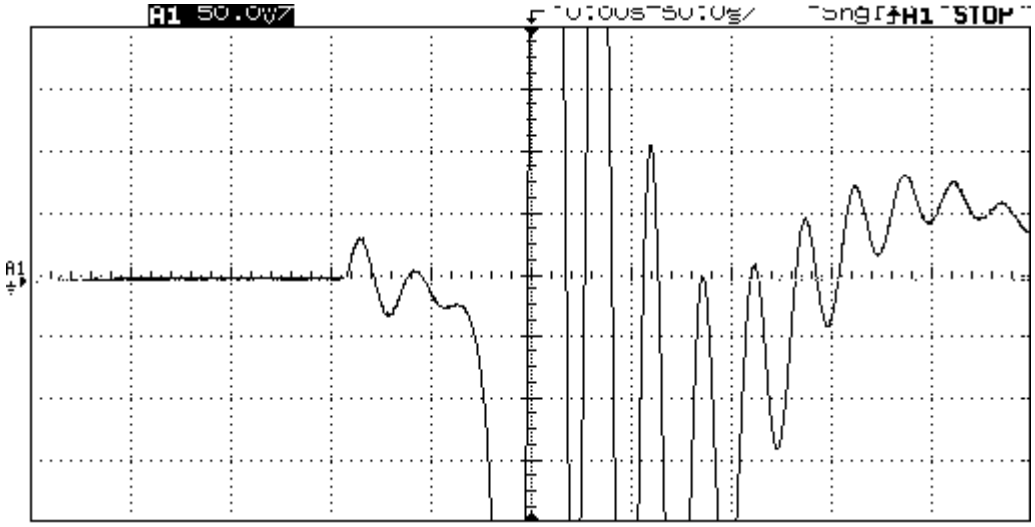

BIAS PATTERN 2

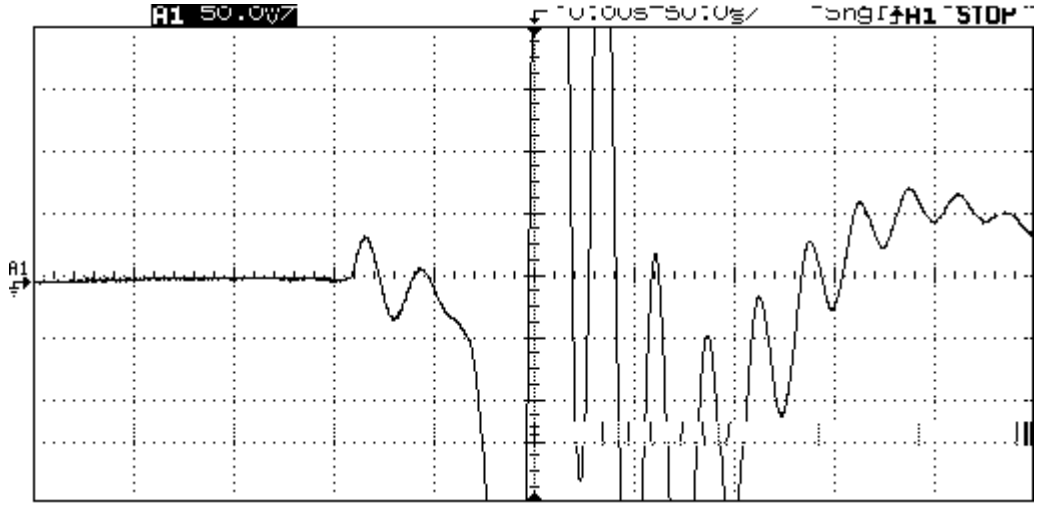

BIAS PATTERN 3

TIME (50 us/div)

DC Bias field = 1.0 Gauss

VOLTAGE (50 mV/div)

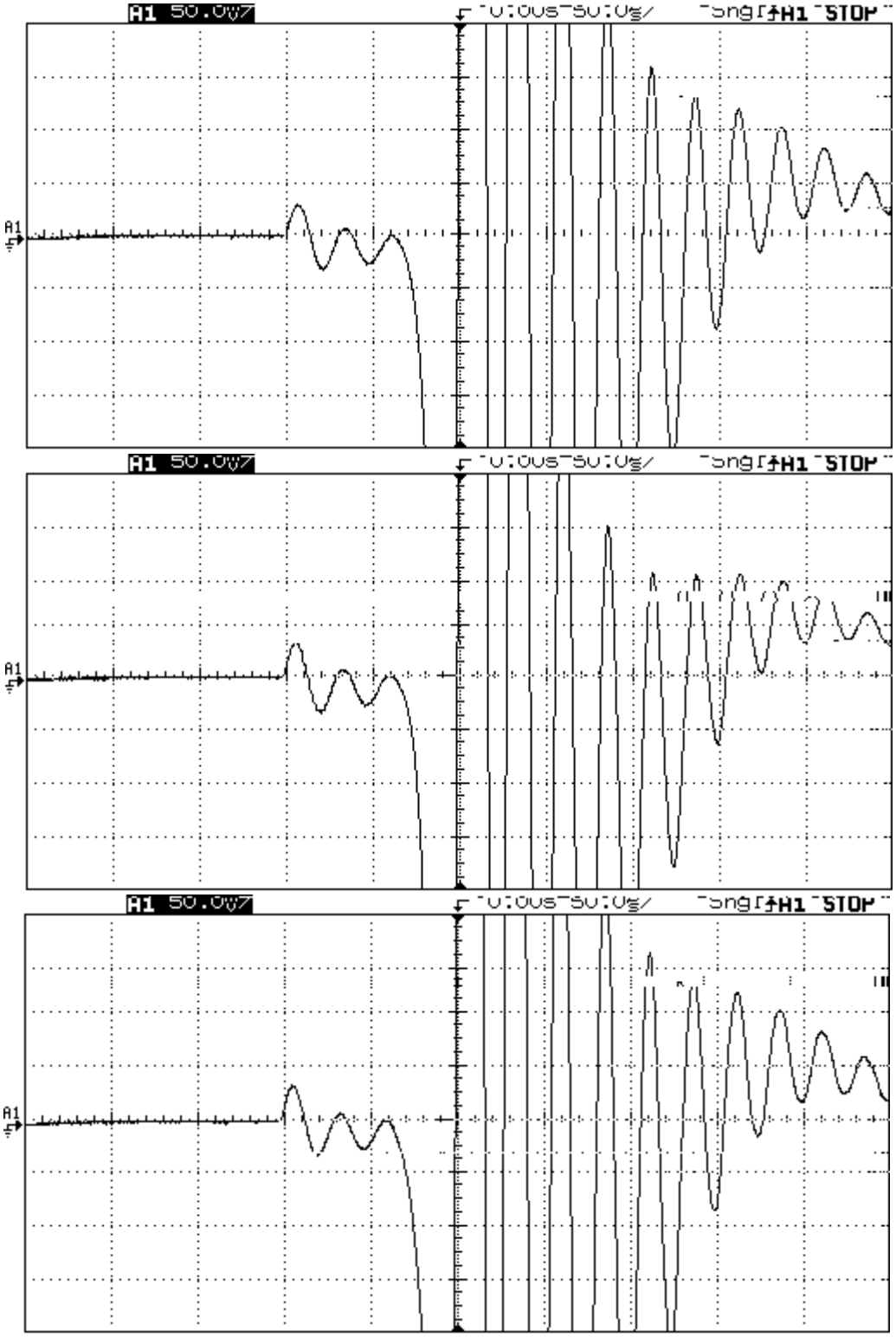

BIAS PATTERN 1

BIAS PATTERN 2

BIAS PATTERN 3

TIME (50 us/div)

DC Bias field = 1.5 Gauss

VOLTAGE (50 mV/div)

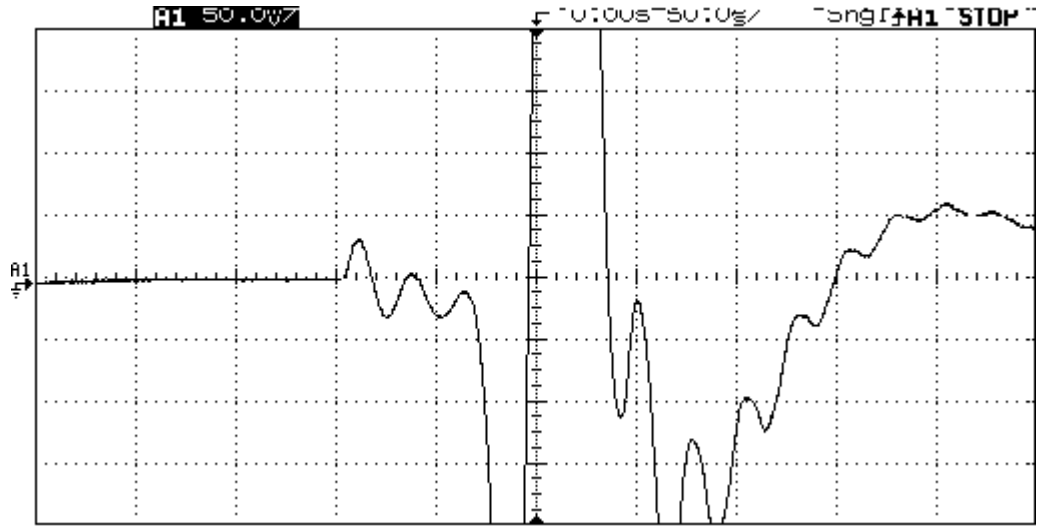

BIAS PATTERN 1

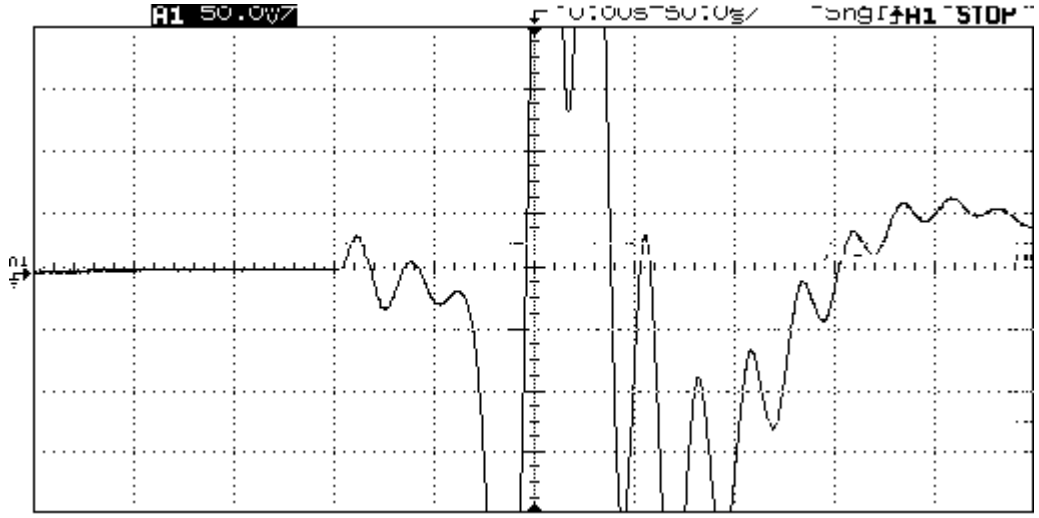

BIAS PATTERN 2

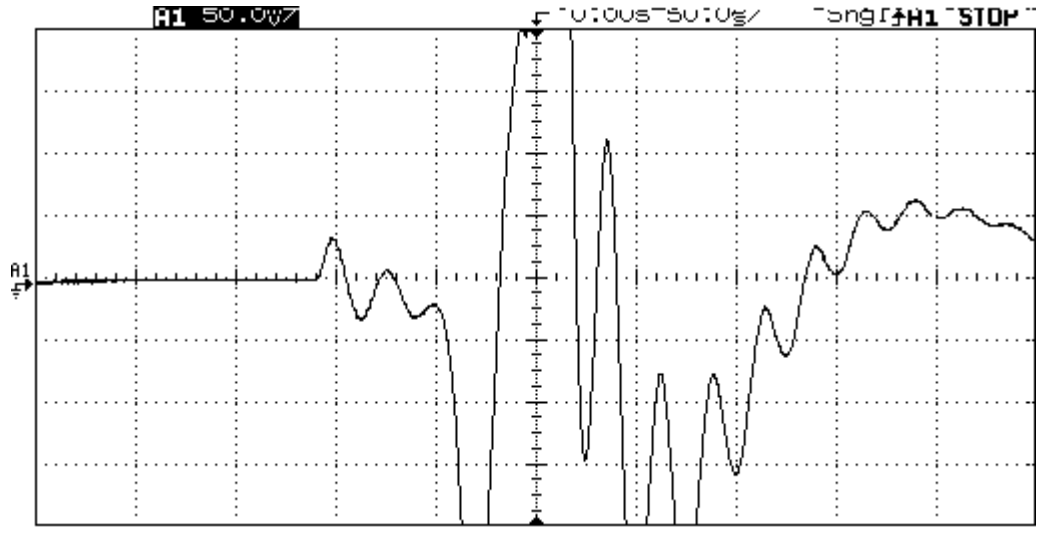

BIAS PATTERN 3

TIME (50 us/div)

DC Bias field = 2.0 Gauss

VOLTAGE (50 mV/div)

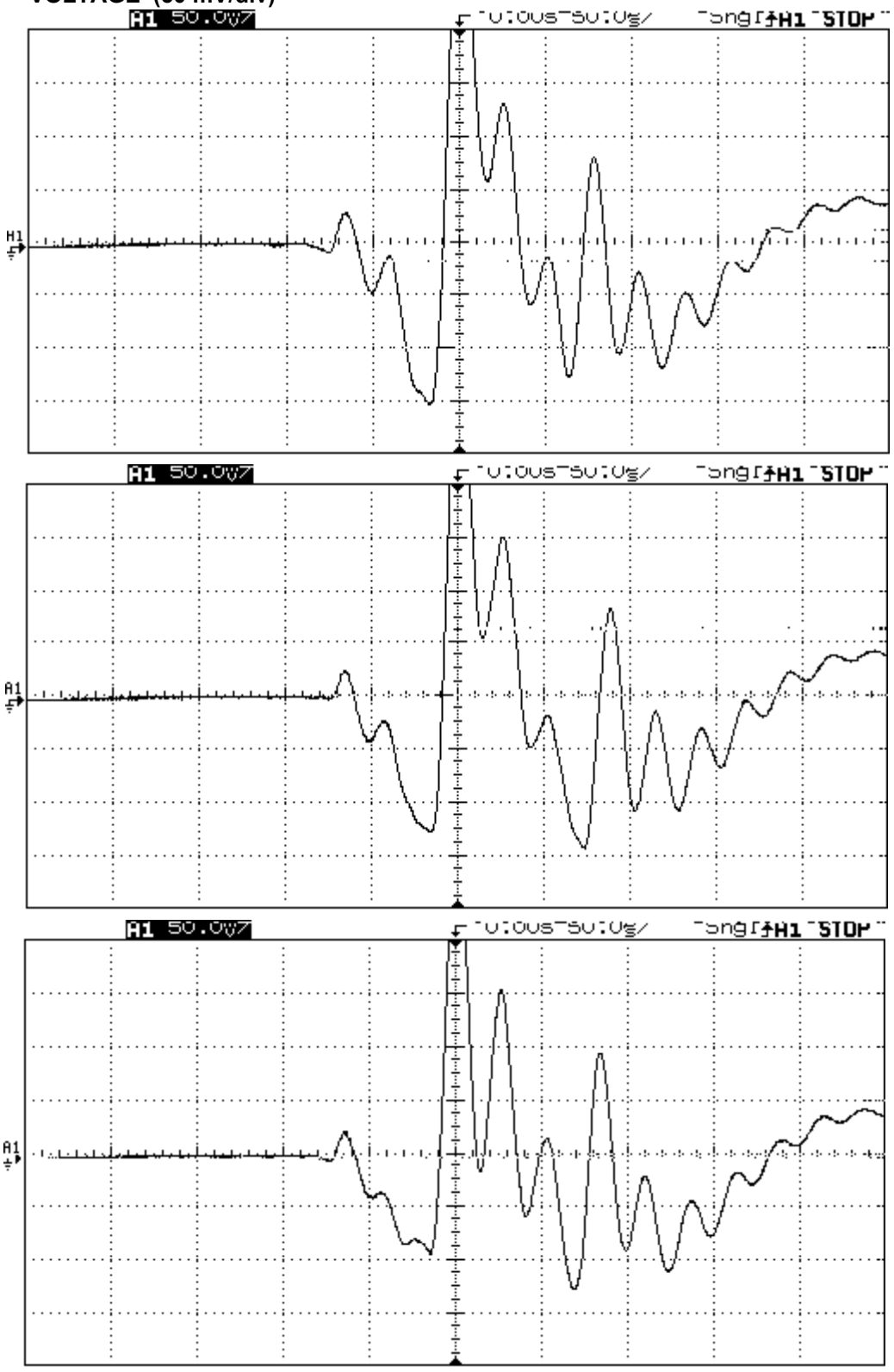

BIAS PATTERN 1

BIAS PATTERN 2

BIAS PATTERN 3

TIME (50 us/div)

4.2.6.3 Results and Conclusions

From the data, we can make some general observations. At low fields, the waveforms produced by the different bias patterns are similar, perhaps due to the fact that the magnetization pulses are spaced relatively far apart in time. As the applied DC bias field is increased, the difference between bias patterns becomes more pronounced, as the magnetization pulses move closer together and produce a larger transient signal in the pick-up coil. If the applied DC field is increased further, the signal begins to attenuate as the excitation field is not able to completely drive the domain walls through their full range of motion along the length of the magnetic strips.

The primary challenge in these time-domain measurements proved to be signal separation. Despite filtering the large transmitted signal produced by the tag reader itself, an additional source of interference came from the transient waveforms of the balanced receive coil itself. For future work it would be useful to design a new test fixture using a different coil design (perhaps a damped unbalanced coil) and relying on receiver circuitry for signal extraction.

Perhaps the biggest limitation on using the magnetization curve as a means of encoding data is that despite how many steps or features are present in the magnetization curve, the *total* magnetization of the material remains constant. Therefore, as more steps are added, the signal produced by each step becomes increasingly small and difficult to detect. This points to a need for exploring engineered material structures that have a larger total magnetization, such as hybrid materials comprised of microencapsulated permanent magnets, for example.

Ultimately, reading multi-bit chipless tags that employ domain wall kinetics requires the ability to wirelessly capture the magnetization curve of relatively large (label-size) composite structures. Although this seems like a simple task, our results demonstrate there are many parameters that can affect this measurement. Because the signal levels are small and orientation-dependent, it is difficult to achieve moderately long (couple feet) read ranges for multi-bit tags that employ domain wall kinetics. As an additional practical matter, the required power levels for this measurement are relatively high (on the order of several Watts) even for short read distances, which makes this method unattractive for some portable applications. Nonetheless, the time-domain response of material structures remains as an interesting research opportunity in the field of chipless electromagnetic tagging and can perhaps be combined with other chipless technologies to overcome inherent limitations.

4.3 Magnetostrictive materials

Magnetostrictive materials, mentioned briefly in Chapter 3, exhibit relatively large mechanical strains (~ 10^{-5}) in response to an applied AC field. Magnetostrictive materials that have low mechanical losses are particularly useful as high-Q mechanical resonators that can be excited and detected magnetically. As a result, these materials are commonly used in antitheft tags, as shown in Figure 60 below. For the purpose of chipless RFID, it is useful to understand the properties of these materials and explore how they may be used to create multi-bit RFID tags.

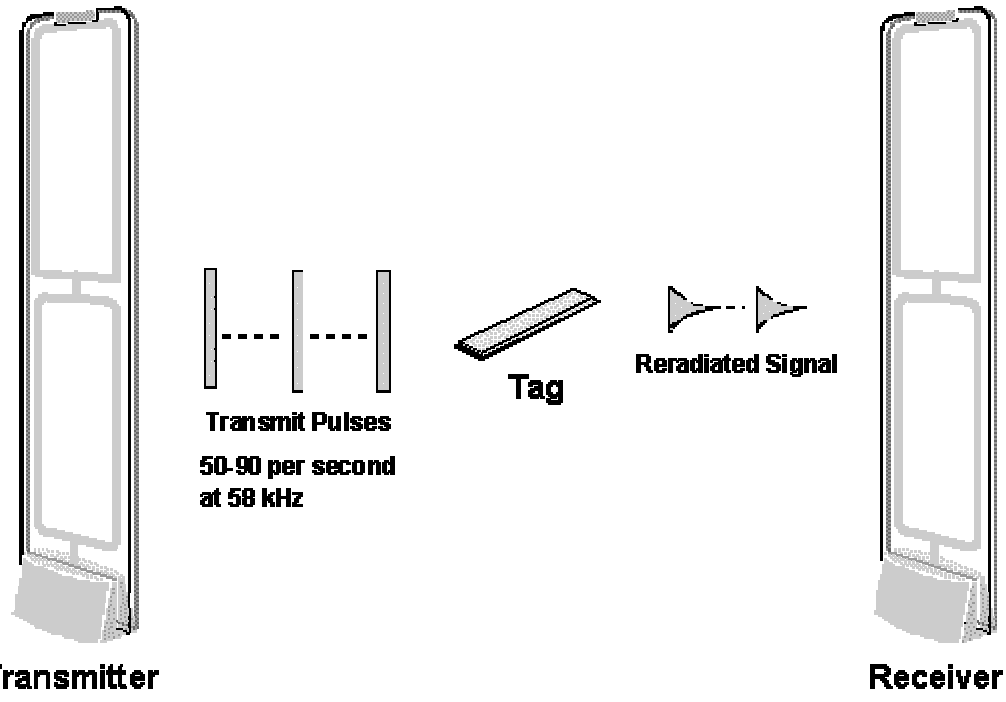

Figure 60. (Top) Electronic Article Surveillance label (Ultramax™ label by Sensormatic, Inc.) containing magnetoelastic strip and trapezoidal bias magnet. (Bottom) Antenna pedestals for EAS readers used in the retail market.

4.3.1 Materials Properties

Although magnetosctriction seems to be a rather unique phenomenon, it is actually found to some degree in most magnetic materials. Since the magnetic properties of materials are strongly dependent on their electronic structure, the magnetic and mechanical properties are necessarily coupled. In most materials, this coupling is very weak, or is overshadowed by other physical effects; however, some materials, including iron, exhibit significant coupled magnetic and mechanical properties. Creating a magnetization in a material can produce an anisotropic strain (magnetostriction) and, conversely, applying a strain on the material can produce a change in its magnetization properties (piezomagnetism). This general class of phenomena are termed *magnetoelastic* effects and coupling between the magnetic and mechanical properties of a material is most commonly characterized by the magnetosctrictivity, **d** (change in magnetization per unit strain), and the magnetomechanical coupling factor, **k** (ratio of energy coupling between magnetic modes and elastic modes). For the purpose of characterization, the saturation magnetostriction, λ_s, is defined from the measured longitudinal and transverse strains when the material is in the fully magnetized state (see Figure 61b).

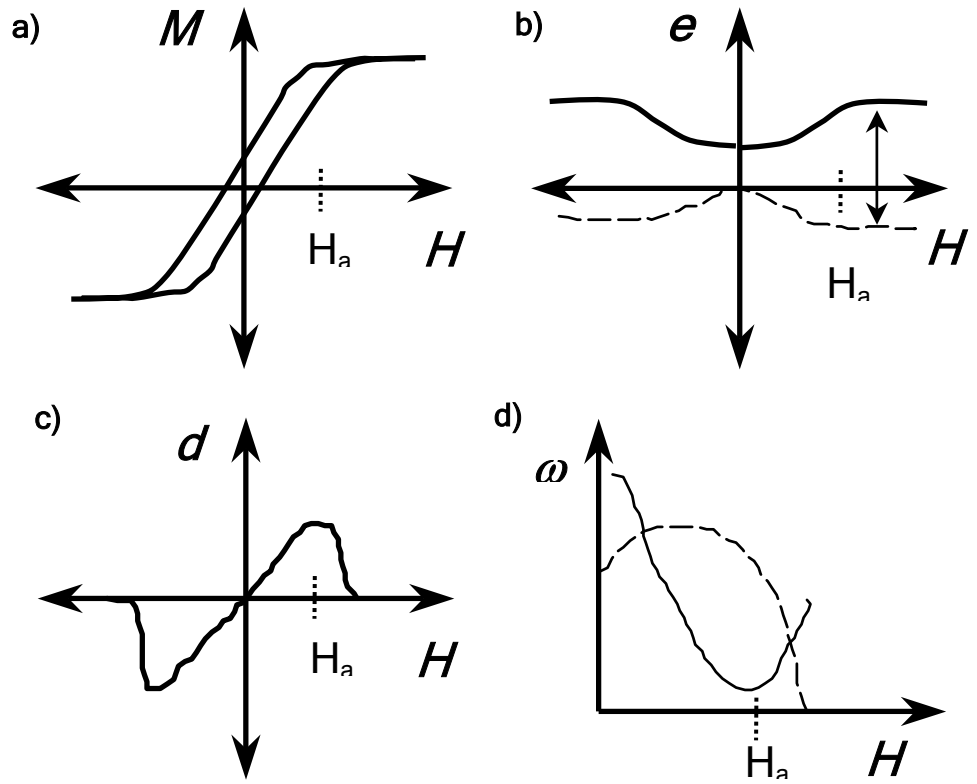

Figure 61. Diagram showing some of the fundamental properties of a strip of magnetoelastic amorphous metal alloy. a) Magnetization curve b) mechanical strain as a function of applied magnetic field; solid line is strain parallel to field, dotted line is strain perpendicular to field. c) magnetostrictivity, $d = \partial e / \partial H$ and d) resonant frequency (solid line) and amplitude (dotted line) as a function of applied magnetic field.

The physical origin of magnetoelasticity is a function of a material's macroscopic shape and microscopic electronic structure, which are in turn dependent on the composition and processing of the material. The conditions which cause magnetoelasticity are best described in terms of energy, and a deformation is said to be energetically favorable if it results in a net decrease in the total magnetic and elastic energies. For anisotropic magnetostriction, it is appropriate to consider the magnetic anisotropy energy which is the change in free energy as a function of the rotation angle of the magnetization about a given axis. The three main contributions to the magnetic anisotropy energy are: magnetostatic energy (due to shape anisotropy), magnetocrystalline anisotropy, and magnetoelastic anisotropy.

Generally, the magnetoelastic contribution to the anisotropy energy is overwhelmed by the other two factors. Some materials may have a large saturation magnetostriction, but are not easy to magnetize due to significant magnetocrystalline anisotropy. For example, relatively large strains ($\varepsilon \approx 10^{-3}$) can be induced in stressed single crystals of $Tb_{0.35}Dy_{0.65}Fe_2$,(a.k.a. Terfenol-D) through the application of a strong field (~kOe). However, in amorphous metal alloys, such as $Fe_{40}Ni_{38}Mo_4B_{18}$, the low magnetocrystalline anisotropy make these materials easy to magnetize (i.e. high permeability); and although their magnetoelastic anisotropy may not be particularly large, the absence of long-range order and small magnetocrystalline anisotropy, allow the magnetoelastic effects to dominate the response. As a result, these materials can achieve magnetoelastic strains of $e \approx 10^{-5}$ in relatively weak fields (~10 Oe). This is why amorphous metals are good candidates for electromagnetic tags and other devices where the material must respond to a weak magnetic field.

Amorphous metal ribbons are good candidates for magneto-mechanical resonators for several reasons. Their high yield strength ($>10^8$ N/m^2) makes them resistant to magnetic degradation due to plastic deformation in flexing. In addition, these materials have a relatively high electrical resistivity which limits eddy current losses, and they can be easily tuned to a particular resonant frequency by trimming a strip to the appropriate length given by $\mathbf{f} \approx (1/2\pi\, \mathbf{l})\sqrt{(\mathbf{Y}/\rho)}$, where l = length, **Y**=Young's modulus, and ρ=density. Since the magnetomechanical coupling and the effective modulus of the material can vary with applied magnetic field, the resulting resonant frequency also exhibits some bias-field dependence, with $\Delta\mathbf{f}/\mathbf{f} \approx 1\%$.

A rather powerful feature of amorphous metal resonators is the ability to control various resonator parameters through annealing of the material. As shown in Figure 12d, the amplitude of the resonance and the bias-field dependence of the resonant frequency can be related to the magnetization curve of the material. As mentioned previously for harmonic tags, the magnetization curve of amorphous materials can be easily modified by annealing in a magnetic field. In a manner similar to other soft magnetic materials, the induced magnetic anisotropy created by annealing produces a sheared **M** vs **H** loop after annealing in a transverse field, and produces a squared loop after annealing in a longitudinal field, as shown in Figure 45 for the

harmonic materials. However, in this case, we want to avoid inducing an easy axis along the length of the resonant strip, because if the domains in the **M**=0 state lie parallel to the applied field, then no domain rotation would take place to produce the desired mechanical strains (180° rotations produce no strain). Similarly, we would expect the greatest mechanical strains from a sample which was annealed in a transverse magnetic field. It should also be noted that the **Q** of this resonator is limited by the mechanical damping loss of the material (negligible), the eddy current loss, and by the amount and size of the micro-crystallites that may form during the post annealing process and produce acoustic losses.

4.3.2 Multi-Bit Implementations

Over the past thirty years since amorphous alloy ribbons have been available, a variety of methods have been used to encode multiple bits of information into a tag. In the following sections, I briefly discuss some multi-bit approaches implemented as part of my graduate work as well as methods used commercially.

4.3.2.1 Resonator Arrays

In order to encode more bits of information, it is desirable to create structures (i.e. tags) that exhibit multiple resonances. As mentioned in Chapter 3, in such a case, each resonance peak can be treated as a single bit within a multi-bit ID string, as shown in Figure 62. Certainly, other encoding schemes are also possible.

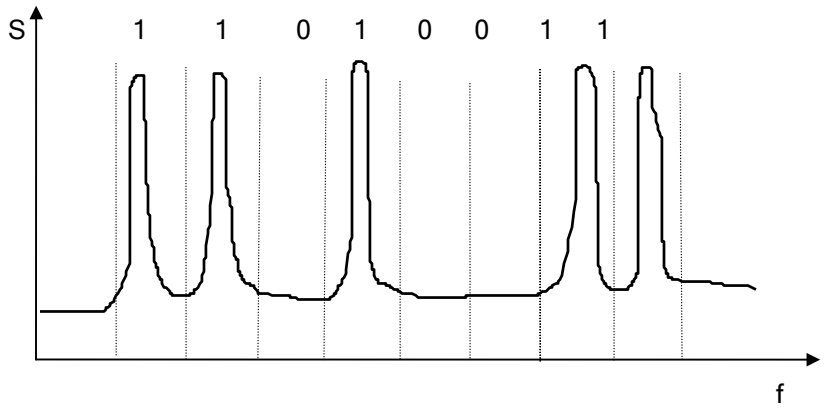

Figure 62. Sample response from a tag containing five resonators of different frequencies.

A very attractive feature of magnetostrictive amorphous metal ribbon is that the resonant frequency can be tuned very easily simply by trimming the length of the resonator. At low frequencies, the length of the resonator is limited simply by the practical length of the tag; and at the upper range of frequencies, the length of the resonator is limited by the eddy current losses, which attenuate the resonance signal. Over my years of graduate work, I have tuned many such tags for various demonstrations with resonant frequencies ranging from 42 kHz to 90 kHz. Pictured in Figure 63 is an example from a demonstration in October 1997, which demonstrated tuning and discrimination of twelve distinct resonators embedded in small colored bottles.

Figure 63. Portions of an October 1997 demonstration employing one dozen distinguishable items tagged with magnetoelastic resonators.

The simplest method of creating multiple resonators is to encase several resonators in a single package. This is not very practical, however since an array of multiple resonators can occupy a significant amount of space. As a result, several companies, such as IBM and Nashua, have developed miniature arrays of magnetosctrictive resonators. These structures can be cut in the form of a multi-pronged tuning fork (similar to the sound element inside a mechanical music box) or can be fabricated on an even smaller scale (millimeters) using thin-film deposition techniques and semiconductor processing. Although these approaches are of intellectual curiosity, the number of bits produced by such structures is not sufficiently high to justify the manufacturing cost.

4.3.2.2 Intrinsic Multiple-Resonance

Perhaps the most promising low-cost method is the possibility of producing multiple resonances from a single strip of magnetostricitve alloy. A consulting firm named Scientific Generics, working with Cambridge University developed such a structure though the use of a pattered magnetic bias strip, much like the structures discussed previously for harmonic material tags. In these tags, called PMR (Programmed Multiple Resonance), it was possible to create multiple resonances within the same structure by simply segmenting the magnetic bias. Although somewhat surprising, segmented magnetic bias can cause the magnetoelastic element to behave as two separate (but coupled) resonators.

At the MIT Media Lab, I actually created such a structure by accident in the summer of 1996, while doing annealing studies for a magnetostrictive displacement sensor (see Chapter 6). By annealing samples in a magnetic field slightly above the crystallization temperature (~450 °C) for approximately 15 minutes, portions of the amorphous alloy crystallized and became permanently magnetized. Alloys processed by this technique exhibited two very interesting properties:

- **Self-biasing** -- The permanently magnetized crystals provided sufficient bias field to the resonator such that an additional bias magnet was not necessary.
- **Multiple-resonance** -- The different magnetized regions within the tag resulted in multiple resonances produced by a single magnetoelastic strip.

Although the multiply-resonant structures I created by accident proved to be brittle and had unpredictable resonances, it points to a possible research path for creating multiply-resonant magnetostrictive structures. We can, for example, explore ways to control the formation and the placement of the microcrystallites. This can be done through techniques similar to spot welding or stressing, scribing or doping a certain region of the strip before the high-temperature anneal.

4.3.3 Magnetic Materials Conclusions

The implementation of ID tags based on magnetic materials has demonstrated several possible approaches to chipless RFID, including time-domain and frequency-domain signatures of both harmonic materials and magnetoelastic resonators. It has been shown that the electromagnetic response of these materials can be modified using an external non-uniform magnetic bias strip, producing a response that is a reproducible function of the applied bias pattern. The primary challenges to implementation, however, is the ability to reliably produce and characterize the magnetic bias strip. In recent years, some of these approaches to chipless RFID have been commercialized independently of the work done at MIT. Although commercial manufacturing process enable reliable manufacturing of the bias strip, magnetic materials approaches to chipless RFID in general still have the disadvantage of shorter read range and higher power relative to other chipless technologies.

CHAPTER V.

Tags for Identification: Planar LC Resonators

5.1 Fundamentals of LC Tags

The LC resonator is the workhorse of wireless electronic devices, dating back to the early days of radio and popularized by inventors such as Nikola Tesla. Today, the planar electromagnetic resonator is perhaps the most common structure used in electromagnetic tagging, as well as countless applications in radio antennas, filters, and oscillators. In the field of RFID, LC resonators can be found in the form of patterned metal foil spirals for anti-theft tags, or in the form of antennas and inlets for 13.56 MHz RFID tags. These structures can be fabricated quite inexpensively (less than US$0.01) using a metal foil stamping process that can be scaled up to very high volumes using a reel-to-reel or web manufacturing line. However, other manufacturing methods are also used, such as metal etching, screen-printing, or metal deposition (e.g. chemical vapor deposition or CVD).

In order to discuss the use of LC resonators in the context of chipless RFID, it is important perhaps to first review the fundamental design principles for the LC resonators in use today and then see how these structures can be combined to form multi-bit tags.

5.1.1 Elements of an LC Resonator

The physical design and equivalent circuit for the LC resonator seem very simple. However, there are several key parameters that must be calculated if we desire optimal performance. Since all resonant phenomena can generally be modeled as an LC resonator, a good understanding of LC resonators can be applied to a variety of problems.

5.1.1.1 Definition of Resonance

A general electromagnetic structure is comprised of elements that dissipate energy and store energy. Electronic components are generally optimized for one of these functions: resistive components that dissipate energy and reactive components that store energy. The stored energies give rise to a phase shift between the voltages and currents in a system. Mathematically, it is customary to employ complex variables to describe such systems, such that a measured real quantity is in phase with the excitation signal and a measured imaginary value are 90 degrees out of phase with the excitation signal. A positive value of reactance is defined as inductive and a negative value of reactance is defined as capacitive.

For any passive network, we can define the following properties at resonance:

- At resonance, the capacitive stored energy is equal to the inductive stored energy. Since these reactances are of opposite signs, they exactly cancel each other.
- Since the reactance vanishes at resonance, the observed impedance of the network is purely resistive. Mathematically, this implies that the measured impedance is thus purely real with zero phase shift.
- Provided that the losses in the network are small relative to the reactances, the magnitude of the measured voltages and currents shall exhibit a pronounced peak (or dip) in the vicinity of resonance.

5.1.1.2 Definition of Q

Although the Q-factor was defined previously in Chapter 3, it is useful to define it more carefully here in order to gain a more intuitive understanding of the physical principles involved. Perhaps the most fundamental definition of Q is the maximum energy stored in the resonator relative to the amount of energy dissipated per single period of oscillation. This is described by the following equation:

$$Q \equiv \left[\frac{Max.Stored.Energy}{Energy.Loss.per.cycle} \right] = 2\pi \left[\frac{W_{MAX}}{W_d} \right] \qquad \text{(Eq. 3)}$$

From this fundamental definition of Q, it is important to note that Q is, in effect, normalized with respect to a particular frequency (period of oscillation). Although it is often tempting to compare a high-frequency resonator with a low-frequency resonator simply by comparing the Q values, such judgment is somewhat misleading. Two nearly identical resonators can have disparate Q factors, simply due to the fact that their resonant frequencies are different.

Since it is more practical to measure time-averaged stored energies and power levels, the definition of Q can be rewritten as

$$Q \equiv 2\pi\left[\frac{W_{MAX}}{W_d}\right] = \frac{\omega W_{MAX}}{P_d} \quad \text{(Eq. 3)}$$

where P_d = *time-averaged power* dissipated in the resonator, and is interpreted as the *energy loss per second in the system*.

Although the electromagnetic fields in a resonator vary with time, the energy is being circulated back and forth between the electric and magnetic fields, which is often referred to as the *circulating power*. In the steady-state, the value of the maximum stored energy is thus constant, and is simply equal to the sum of the magnetic stored energy plus the electric stored energy. Given that the time-domain waveform is assumed to be sinusoidal for each of the stored energies (electric and magnetic), we can also use the mean value theorem from mathematics to easily express the time-averaged stored energies in terms of their maximum values, since for a sine wave, the average value is simply half the maximum value.

The Q-factor can then be expressed as follows:

$$Q = \frac{\omega W_{MAX}}{P_d} = \frac{\omega\left[w_E + w_M\right]}{P_d} = \frac{\omega\left[\frac{1}{2}\cdot w_E^{MAX} + \frac{1}{2}\cdot w_M^{MAX}\right]}{P_d} \quad \text{(Eq. 3)}$$

where $\mathbf{W_E}$ and $\mathbf{W_M}$ are the electric and magnetic stored energies, respectively.

5.1.1.3 Circuit Model

Having established a definition of Q, we can then proceed to calculate the Q-factor and input impedance for the two basic cases, series resonance and parallel resonance. A very useful fact of electromagnetics and electrical engineering (that will not be proven here) is that for any electromagnetically resonant system (e.g. microwave cavity, microstrip resonator, etc) it is always possible to define specific points on the network where the resonant system can be modeled as either a series or parallel resonant circuit.

5.1.1.3.1 Series Resonance

The case of series resonance is modeled by the circuit below:

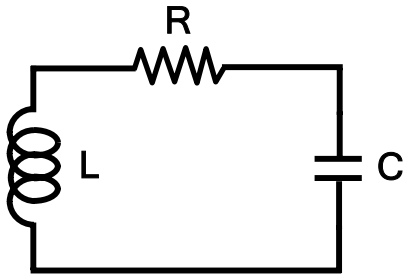

Using the fundamental definition of resonance given previously, the resonant frequency can be calculated as follows:

$$W_m = \frac{1}{2} W_{m\max} = \frac{1}{4} L I_{\max}^2$$

$$W_e = \frac{1}{2} W_{e\max} = \frac{1}{4} C V_{\max}^2 = \frac{1}{4} C \left(\frac{I_{\max}}{C\omega} \right)^2 \qquad \text{(Eq. 4)}$$

Setting the energies to be equal at resonance yields the following result

$$\boxed{W_m = W_e \Rightarrow 1/\sqrt{LC} \equiv \omega_0} \qquad \text{(Eq. 5)}$$

We can then use these energy quantities to solve for the Q-factor, using the definition given previously.

$$Q = \frac{W_{total}}{P/\omega_0} = \frac{\omega_0 (W_m + W_e)}{\frac{1}{2} I_{\max}^2 R} = \frac{\omega_0 (2W_m)}{\frac{1}{2} I_{\max}^2 R} = \frac{\omega_0 2 \frac{1}{4} L I_{\max}^2}{\frac{1}{2} I_{\max}^2 R} = \frac{\omega_0 L}{R} \qquad \text{(Eq. 6)}$$

$$\boxed{Q_0 = \frac{\omega_0 L}{R}} \qquad \text{(Eq. 6)}$$

We can also solve for the total impedance around the series loop.

$$Z = R + j\omega L - \frac{1}{j\omega C} = R + j\omega L\left[1 - \left(\frac{\omega_0}{\omega}\right)^2\right]$$

It is useful to find a simplified expression for Z at frequencies near resonance. For this, we introduce the quantity $\Delta\omega = \omega - \omega_0$ such that $\frac{\Delta\omega}{\omega} << 1$.

We can then make the following approximation:

$$1 - \left(\frac{\omega_0}{\omega}\right)^2 = \frac{(\omega - \omega_0)(\omega_0 + \omega)}{\omega^2} \approx 2\frac{\Delta\omega}{\omega}$$

using this approximation as well as the expression for Q, the impedance Z near resonance can then be written as:

$$\boxed{Z \approx R\left[1 + j2Q_0\frac{\Delta\omega}{\omega}\right]}$$

From this, we can see that the magnitude of Z is minimum at resonance.

5.1.1.3.2 Parallel Resonance

Parallel resonance is modelled by the circuit below, where the conductance $G \equiv \frac{1}{R}$.

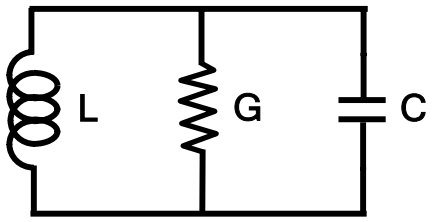

For the case of parallel resonance, the calculation of the resonant frequency is identical to that of the series resonator, yielding the same result:

$$\boxed{W_m = W_e \Rightarrow 1/\sqrt{LC} \equiv \omega_0} \qquad \text{(Eq. 5)}$$

We can then calculate the Q factor from the stored energy values as before:

$$W_E = \frac{1}{2} W_{E\max} = \frac{1}{4} C V_{\max}^2$$

$$W_M = \frac{1}{2} W_{M\max} = \frac{1}{4} L I_{\max}^2 = \frac{1}{4} L \left(\frac{V_{\max}}{L\omega} \right)^2 \qquad \text{(Eq. 4)}$$

$$Q = \frac{W_{total}}{P/\omega_0} = \frac{\omega_0 (W_m + W_e)}{\frac{1}{2} V^2 G} = \frac{\omega_0 2 \frac{1}{4} C V_{\max}^2}{\frac{1}{2} V^2 G} = \frac{\omega_0 C}{G} \qquad \text{(Eq. 6)}$$

$$\boxed{Q_0 = \frac{\omega_0 C}{G}} \qquad \text{(Eq. 6)}$$

In the parallel resonant case, it is simplest to work in terms of the admittance $Y \equiv \frac{1}{Z}$ as follows:

$$Y = G + j\omega C - \frac{1}{j\omega L} = G + j\omega C \left[1 - \left(\frac{\omega_0}{\omega} \right)^2 \right]$$

Using the expression for Q_0, the admittance Y in the vicinity of resonance can be expressed as follows:

$$\boxed{Y \approx G \left[1 + j 2 Q_0 \frac{\Delta\omega}{\omega} \right]}$$

From this, we see that the magnitude of the impedance is a maximum at resonance, and the symmetry between the parallel and series circuits is apparent.

5.1.1.4 Physical Model

In order to make use of the resonant circuit models, it is necessary to relate the physical properties of the system to equivalent circuit parameters. This step is generally not straightforward and requires a good deal of care and experience in order to make valid approximations of the materials behavior over the appropriate operating conditions.

5.1.1.4.1 Resistance

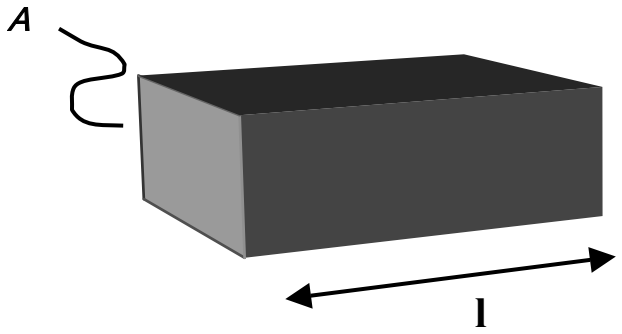

Figure 64. Diagram showing relevant sample dimensions used for resistance calculation.

The resistance, R, of a sample is a function of the bulk resistivity, ρ, or conductivity, σ, and the material dimensions:

$$R = \frac{\rho l}{A}$$

Typical resistivity values for a few materials are given in Table 2 below.

Aluminum	2.65×10^{-8}
Copper	1.67×10^{-8}
Gold	2.35×10^{-8}
Silver	1.59×10^{-8}
Aluminum Oxide	1×10^{14}

Figure 65. Sample resistivities of several metals plus an oxide at 20 °C, in units of Ohm-meters.

In metals, the electromagnetic fields, and thus the currents, are generally not uniformly distributed along the cross-section of the metal layer, but rather decay exponentially as function of depth, $\propto e^{-z/\delta}$. Therefore, the entire cross-sectional area, A, will not give good approximations to the resistance and should be reduced. The exponent, δ, that defines how fast the currents decay as a function of depth, is called the **skin-depth** and is given by the following.

$$\delta = \sqrt{\frac{2}{\omega\mu\sigma}}$$

The skin depth of common metals is on the order of several microns at microwave frequencies, and is approximately 40 um at 13.56 MHz. In order to minimize resistive loss, the metal layer thickness should be designed to be at least twice the skin depth. At very high frequencies (approaching infrared) or very high conductivities (superconductors), the fields and associated currents decay more slowly than exponentially with depth (called the *anomalous skin-effect*) and other approximations should be used for the skin-depth.

Due to the skin effect, the resistance of a wire cannot be reduced simply by increasing the wire diameter. In order to reduce the AC resistance in a coil, for example, it is common practice to use several thinner wires braided together in parallel. This braided magnet wire is known as Litz wire and is sold commercially.

5.1.1.4.2 Inductance

In the field of electromagnetic tagging, inductance is most commonly used in near-field RFID tags as a means of electromagnetically coupling the reader to the tag, as well as a means of tuning the resonant frequency of the tag.

Formally, the inductance of a coil, more specifiacally known as *self-inductance*, is defined as the amount of flux it induces on itself per unit current, as given by the following equation:

$$L = \Phi / I = \frac{1}{I}\iint_S B \bullet da$$

where B is the magnetic field generated by the coil given a current I.

One of the challenges in calculating the inductance L for an arbitrary coil is that its magnetic field is generally difficult to calculate analytically. In many cases, the best approach for calculating the magnetic field is to use the *magnetic vector potential*, defined as

$$\boldsymbol{B} = \nabla \times \boldsymbol{A}$$

where $\boldsymbol{A}(\vec{r}) = \frac{\mu_0}{4\pi} \int_V \frac{\boldsymbol{J} \cdot d\boldsymbol{V}}{r'}$,

and r' is the distance between a current element and the measurement point.

If the geometry can be defined such that r' is an independent variable, then the integral in A can usually be readily calculated. Given the expression for $\boldsymbol{A}$, the magnetic field $\boldsymbol{B}$ can then be derived.

In the following sections, the two most common types of inductor structures are discussed, wire-wound coils and planar coils.

.1.1.4.2.1 Wire Coils

Wire coils are commonly used as the reader antenna for near-field RFID tags and also commonly used as the tag antenna for lower-frequency RFID tags, in the range of a few hundred kHz or less. The practical challenge in calculating the inductance of a non-ideal coil, is that the coil wire has a finite size. In deriving the flux and magnetic field of the coil, it is thus necessary to treat separately the magnetic field outside the coil and the magnetic field inside the coil. The self-inductance of a coil is then expressed as the sum of these two contributions:

$$\boldsymbol{L} \equiv \boldsymbol{L_e} + \boldsymbol{L_i}$$

For calculating the external inductance, $\boldsymbol{L_e}$, of a single-turn coil, the current in the loop can be assumed to be concentrated along its central axis, $\mathbf{C_0}$, similar to the ideal case of an infinitely thin coil. However, in calculating the amount of flux intercepted by the coil, since the coil wire has a finite width, we use a different contour, $\mathbf{C_1}$, given by the perimeter of the coil wire, as shown in Figure 66.

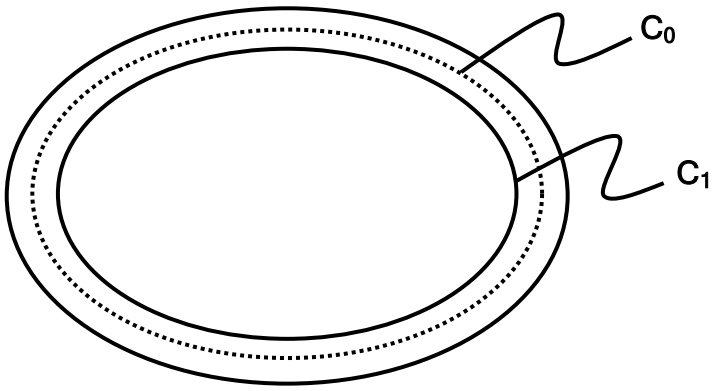

Figure 66. Diagram showing integration contours for calculating the inductance of a wire coil.

Even though this is a single wire, since separate contours are used for the current and for the flux calculation, it is convenient to treat this as a *mutual inductance* calculation. For two contours, denoted as loop 1 and loop 2, the mutual inductance between and arbitrary loop 1 and arbitrary loop 2 is given by

$$M_{21} = \Phi_{21} / I_1 = \frac{1}{I_1} \iint_S B_1 \bullet da_2$$

where Φ_{21} is the flux linking loop 1 and loop 2.

By symmetry, we can see that $M_{21} = M_{12}$. Also, we can see that the ideal self-inductance of a given loop, say L_1, can then be expressed in the following notation:

$$L_1 = M_{11} = \Phi_{11} / I_1 = \frac{1}{I_1} \iint_S B_1 \bullet da_1$$

We can use this notation of generalized inductance to show the validity of this approach by considering two separate coils as shown in Figure 67.

The flux captured by a given coil will always be less than the flux produced. So we can write, $\Phi_{12} < \Phi_{11}$ and $\Phi_{21} < \Phi_{22}$. Therefore,

$$\frac{\Phi_{12}}{I_1} \cdot \frac{\Phi_{21}}{I_2} < \frac{\Phi_{11}}{I_1} \cdot \frac{\Phi_{22}}{I_2}$$

$$M_{12}{}^2 < L_1 L_2$$

Thus due to flux leakage, the square of mutual inductance between two coils will always be less than the product of their individual inductances. However, we can also see that as the two coils are brought together, the mutual inductance M approaches the limiting value of $L_1 L_2$.

Therefore, returning to the original problem of solving for the inductance of a single loop of wire having a finite wire radius, we see that the mutual inductance formulation is valid, and that if we look at the limit as the thickness of the wire goes to zero, then as $C_1 \rightarrow C_0$, the mutual inductance between contours C_0 and C_1 approaches the inductance of an ideal wire loop C_0.

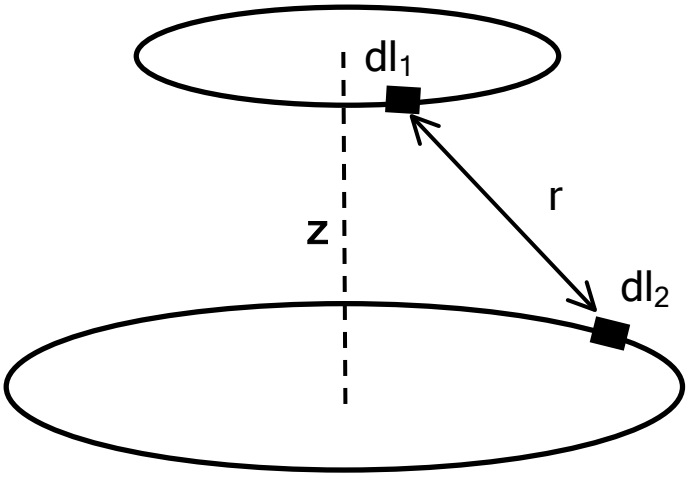

Figure 67. Diagram illustrating notation used for Neumann's formula.

The magnetic vector potential mention previously provide us with an elegant method for calculating the mutual inductance between two loops, as illustrated in Figure 67. For the case of a wire structure, where the current is confined to a filamentary path, the magnetic vector potential can be written as

$$A = \frac{\mu_0}{4\pi} \oint \frac{dl}{r}$$

where dl is the distance along the current path.

Using the vector potential, we can then write the mutual inductance M between contours C_0 and C_1 as the following, known as *Neumann's formula*:

$$M = \frac{\mu_0}{4\pi} \oint_{C_1} \oint_{C_0} \frac{dl_1 \cdot dl_2}{r}$$

For the loops in Figure 67, the mutual inductance in cylindrical coordinates is derived as follows:

$$dl_1 \cdot dl_2 = dl_2 R_1 d\theta \cos\theta$$

$$r = \sqrt{z^2 + (R_1 \sin\theta)^2 + (R_1 \cos\theta - R_2)^2}$$

Using the substitution $\theta = \pi - 2\phi$ and $k^2 = \frac{4R_1R_2}{z^2 + (R_1 + R_2)^2}$, the integral for M can be written as

$$M = \mu k \sqrt{R_1 R_2} \int_0^{\pi/2} \frac{(2\sin^2\theta - 1)\cdot d\theta}{\sqrt{1 - k^2 \sin^2\phi}}$$

This integral is a standard elliptic integral. Thus we can write the solution to M as:

$$M = \mu \sqrt{R_1 R_2} \left[\left(\frac{2}{k} - k \right) K(k) - \frac{2}{k} E(k) \right]$$

where

$$E(k) = \int_0^{\pi/2} \sqrt{1 - k^2 \sin^2\phi}\, d\phi \quad \text{and} \quad K(k) = \int_0^{\pi/2} \frac{d\phi}{\sqrt{1 - k^2 \sin^2\phi}}$$

are complete elliptic integrals of the first and second kind, respectively.

The external inductance L_e of a single-loop coil can then be found by applying Neumann's formula to two circular contours, C_0 and C_1, whose diameters differ by the radius a of the physical wire. Using $R_1 = R$, and $R_1 = R - a$, then the external inductance of the single-turn coil is

$$M = \mu \sqrt{R(R-a)} \left[\left(\frac{2}{k} - k \right) K(k) - \frac{2}{k} E(k) \right] \text{ and } k^2 = \frac{4R(R-a)}{a^2 + (2R - a)^2}$$

If the radius of the wire is much smaller than the radius of the coil ($R >> a$), which is usually the case, then

$$K(k) \cong \ln\left(\frac{4}{\sqrt{1 - k^2}} \right) \text{ and } E(k) \cong 1$$

which results in the following simplified expression for the external inductance,

$$L_e = \mu R \left(\ln\left[\frac{8R}{a} \right] - 2 \right)$$

In order to solve for the internal inductance, L_i, it is generally necessary to know the current distribution inside the wire itself. If the radius of the wire is less than the skin depth (mentioned previously), then we can neglect skin effects and assume that the current in the wire is uniformly

distributed across its cross-section. In this case, the magnetic field inside the wire can be written as

$$B = \frac{\mu I}{2a^2} r$$

Noting that the magnetic energy of an inductor is $W_M = \frac{1}{2} L_i I^2$, and noting that we can also express the magnetic stored energy in terms of the magnetic field $W_M = \frac{1}{2}\int B \bullet H dV$, the internal inductance can easily be derived from the magnetic field:

$L_i = \frac{1}{I^2}\int_0^a \frac{\mu I^2 r^2}{4\pi^2 a^4} 2\pi r l dr = \frac{\mu l}{8\pi}$, where l is the length of the wire.

For the single-turn coil, the length of the wire is simply $2\pi R$; therefore, the internal inductance is simply

$$L_i = \frac{\mu R}{4}$$

For very high frequencies or very large gauge wire, the skin-effect must be taken into account as most of the current is concentrated on the surface of the wire. In this case, the internal inductance is simply calculated from the impedance per unit length derived from Maxwell's equations and defined as

$$Z_i = \frac{E_\perp (r = a)}{\oint H \bullet dl}$$

Exact calculation of Z_i for a round wire requires the use of Bessel functions, but the high-frequency approximation is given by

$$Z_i \approx \frac{(1+j)}{2\pi a \sigma \delta}$$

where δ is the skin-depth, $\delta = \sqrt{\frac{2}{\omega\mu\sigma}}$, given previously. Taking the reactive component of Z_i, the internal impedance is then given by

$$L_i \approx \frac{1}{4\pi a}\sqrt{\frac{2\mu}{\sigma\omega}}$$

For typical wire gauges and frequencies of 500 MHz or below, the low frequency expression for Z_i is sufficient. In this case, we can thus write the total inductance of a wire coil as

$$L = L_e + L_i = \mu R\left(\ln\left[\frac{8R}{a}\right] - 2\right) + \frac{\mu R}{4}$$

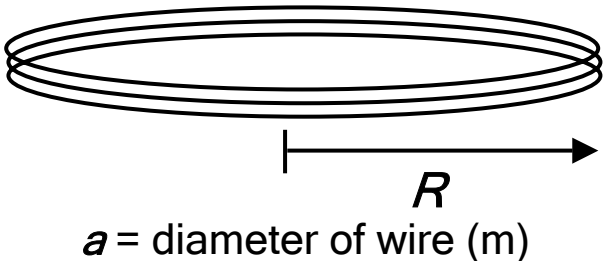

Figure 66. Diagram showing relevant coil dimensions for inductance calculation.

Finally, we can scale this expression to many turns N, thus giving the following expression for the inductance of a wire coil with N turns:

$$L = \mu R\left(\ln\left[\frac{8R}{a}\right] - 2\right) \cdot N^2 + \frac{\mu R}{4} \cdot N$$

From this expression, we can see that the internal inductance term can generally be neglected for multi-turn coils.

Although the inductance derived here is for a round coil, the same approach could be used to solve for the inductance of a square loop, starting with Neumann's formula in Cartesian coordinates. In addition, the magnetic permeability, μ, in the preceding equations is generally taken to be that of free space. However, for small low-frequency RFID tags, the coil is often loaded with a ferrite material having a relative permeability of a few hundred, which greatly reduces the required size of the tag antenna.

.1.1.4.2.2 Planar coils

Planar coils are commonly used for the purpose of tag antenna design. Since paper labels are often rectangular, the planar coil is generally also designed to be rectangular in order to maximize the flux capture area.

Creating an analytical model of a planar rectangular coil is particularly challenging for several reasons: the coils is not round, the coil is not concentric, and the coil is thin. The inductance for a single square loop can be readily calculated following the same approach presented in the previous section using Neumann's formula, $L = \frac{\mu_0}{4\pi} \oint_{C_1} \oint_{C_0} \frac{dl_1 \cdot dl_2}{r}$, in Cartesian coordinates and using the contours shown in Figure 68.

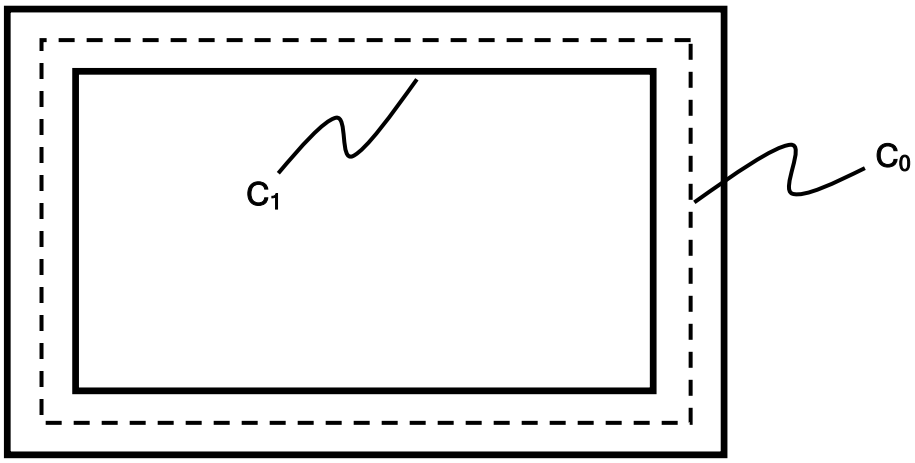

Figure 68. Diagram showing integration contours for calculating the inductance of a square coil.

In order to account for the fact that the planar coil is not concentric and flat, an effective diameter for the coil is used, as well as an effective diameter for the wire itself.

Working from the geometry outlined in Figure 69, the inductance of the coil can be computed as follows [Philips Design Note]:

We can define an effective diameter for the metal trace, $d = \frac{2 \cdot (t + w)}{\pi}$

as well as an average length and width of the tag:

$$a_{avg} = a_0 - N \cdot (g + w)$$

$$b_{avg} = b_0 - N \cdot (g + w)$$

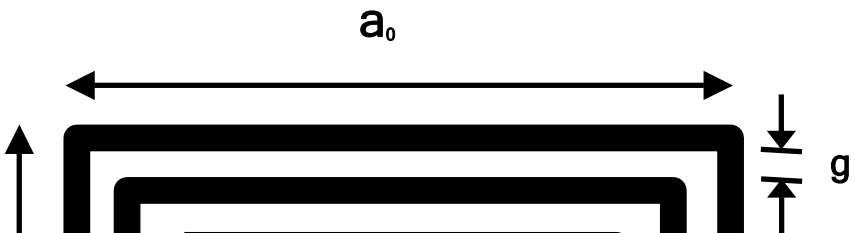

N = number of turns

t = metal thickness

Figure 67. Diagram showing planar coil geometry and dimensions.

Following the same approach as in the previous section, the inductance of the coil is then given by the following equations:

$$x_1 = a_{avg} \cdot \ln\left[\frac{2 \cdot a_{avg} \cdot b_{avg}}{d \cdot \left(a_{avg} + \sqrt{a_{avg}^2 + b_{avg}^2}\right)}\right]$$

$$x_2 = b_{avg} \cdot \ln\left[\frac{2 \cdot a_{avg} \cdot b_{avg}}{d \cdot \left(b_{avg} + \sqrt{a_{avg}^2 + b_{avg}^2}\right)}\right]$$

$$x_3 = 2 \cdot \left[a_{avg} + b_{avg} - \sqrt{a_{avg}^2 + b_{avg}^2}\right]$$

$$x_4 = \frac{a_{avg} + b_{avg}}{4}$$

$$L \approx \frac{\mu_0}{\pi} \cdot \left[x_1 + x_2 - x_3 + x_4\right] \cdot N^p$$

where the exponent p is a constant approximately equal to 1.8, that depends on the geometric cross section of the metal trace. Note that this differs from the ideal case computed from Maxwell's equations where p=2 and $L \propto N^2$.

5.1.1.4.3 Capacitance

The capacitance in a material structure is given by the distribution of charge in the structure and is generally correlated with the conductor surface area. The contributions to the total capacitance can be roughly divided onto two basic parts:

$$C = C_\sigma + C_\varepsilon$$

where C_σ is the capacitance of a single metal layer section, and C_ε is the capacitance produced by the 2-layer sections having a dielectric in between. For common tag dimensions, C_σ is on the order of a pF or tenths of pF, while C_ε is on the order of tens of pF. Unless large areas of single-layer conductors are used (as in the case of capacitively-coupled tags), it is generally valid to simply use the capacitance due to the multi-layer structures. It is then possible to tune the capacitance by adjusting the conductor overlap area as well as the properties of the dielectric layers.

The two basic approaches to capacitance design for RFID tags is discussed below.

.1.1.4.3.1 Lumped Capacitance

If the sections of the tag having overlapping conducting regions is limited to well-defined patches separate from the coil traces, then we can "lump together" the capacitance in each region and treat them as a single *lumped* capacitance. It is then possible to employ the traditional formula for a parallel-plate capacitor:

$$C = \frac{\varepsilon A}{t_\varepsilon}$$

where t_ε is the thickness of the dielectric, A is the area of the overlapping region, and ε is the dielectric permittivity.

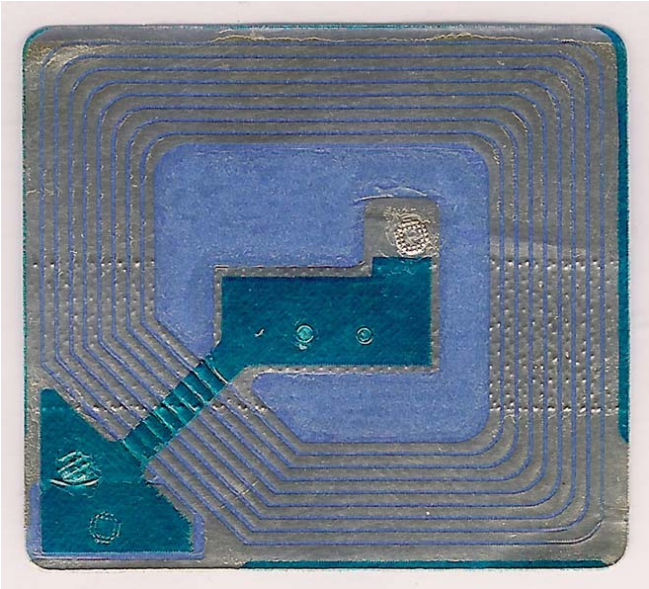

Figure 68. Photograph of planar LC tag showing lumped capacitance in center and outer corner.

This traditional parallel-plate formula is valid as long as the lateral dimensions of the overlap area are large compared to the dielectric thickness. If this is not the case, then the fringing field at the edge of the conducting layers must also be taken into account. In this case, the charge distribution across the area of the capacitor plates cannot be assumed to be uniform. For certain geometries, this charge distribution can be calculated using conformal mapping techniques. For the case of a rectangular capacitor geometry, the Schwarz-Christoffel transformation is used to derive the following formula, which gives the capacitance in terms of the lateral dimensions a,b, where $A=ab$:

$$C = \frac{\varepsilon A}{t_\varepsilon}\left[1 + \frac{\ln(\pi a / t_\varepsilon)}{\pi a / t_\varepsilon} + \frac{\ln(\pi b / t_\varepsilon)}{\pi b / t_\varepsilon}\right]$$

.1.1.4.3.2 Distributed Capacitance

Figure 69. Photograph of two different tag designs employing distributed capacitance. The tag on the left is shown unfolded and the photograph on the right shows a single layer of a tag.

If the regions of conductor overlap are not confined to a discrete section of the tag separate from the inductor coil, then the capacitance must be treated as a distributed capacitance. For the purpose of creating a constitutive model, the parallel-plate formula can be adapted such that the capacitance can still be readily calculated as the geometry of the tag is varied.

For computer simulations, it is generally useful to express the capacitance of the tag as a function of the number of turns in the planar tag coil. Although the diameter and resulting area of each turn is not uniform, we can treat them as uniform using the average dimensions of the tag that were also employed in the inductance calculations presented previously:

$$C = \frac{\varepsilon}{t_{\varepsilon}}\left[2 \cdot a_{avg} + 2 \cdot b_{avg}\right] \cdot N$$

If greater accuracy is required, the actual surface area of the tag can be computed and used to calculate the tag capacitance.

5.1.2 Coupling to a Tag Reader

Given a circuit model for the tag, and given appropriate physical models for the individual circuit parameters, it is then possible to create a model for the complete system comprised of the tag and reader. Unlike the case of far-field RFID tags, the electromagnetic fields of the tag and reader can be strongly coupled, which requires the reader-tag system to be analyzed as an integrated unit. At the heart of this calculation, is being able to characterize and model the wireless coupling between the tag and reader, which in general can be capacitive and/or inductive. After all, it is precisely this wireless coupling between tag and reader that makes RFID a novel and interesting technology.

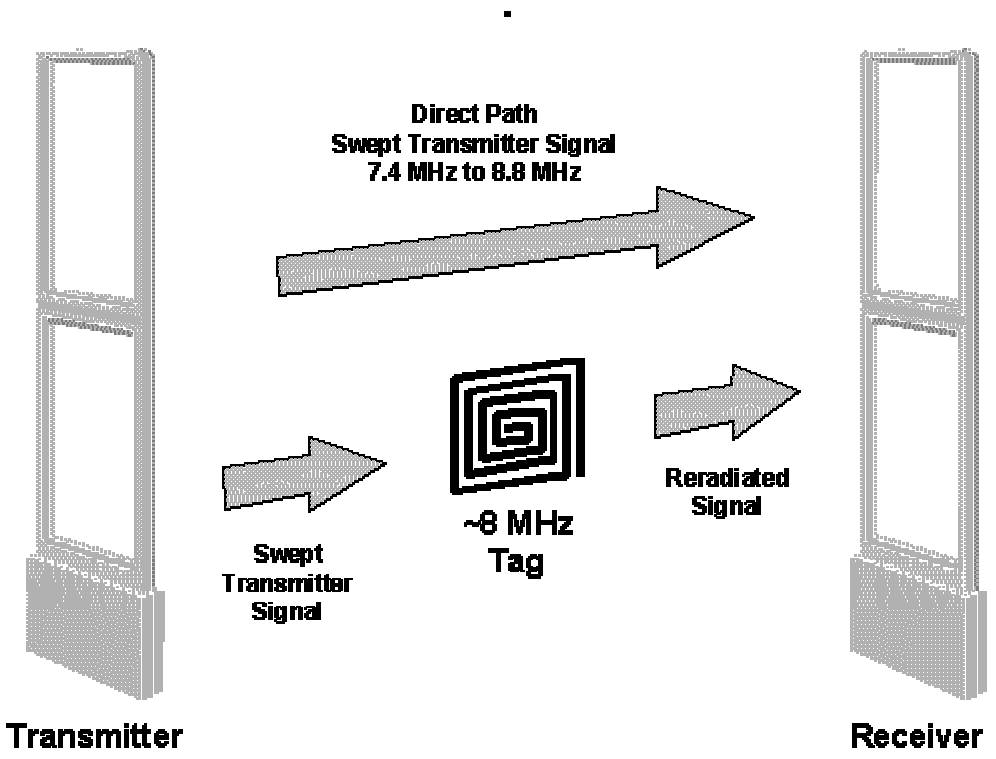

Figure 70. Illustration of reader configuration employed in a typical 8 MHz EAS system.

5.1.2.1 Reader system Configurations

There are many possible ways to detect a near-field RFID tag, employing one of more reader antennas. For the purpose of brevity, I simply list the basic configurations below:

- **Reflected power:** A single transmit/receive antenna is employed and the reader electronics detects the amount of power coupled out of the antenna into the tag, also informally referred to as *antenna loading.*
- **Pulse and Ring-down:** An RF pulse is transmitted by the reader coil to excite the tag at its resonant frequency; the reader then detects the "ring-down" power radiated by the decaying oscillations of the tag.
- **Transmitted power:** Two separate antennas are used, one for transmit and one for receive functions, set a distance apart. The reader detects the increase in transmitted power as the tag enters the zone between the transmit and receive antennas.
- **Dual-Antenna Pulse and Ring-down:** This is a two-antenna version of the pulse and ring-down method. The advantage of using two antennas is that the transmit and receive antennas can each be optimized to perform their respective functions.

In the spirit of low-cost tagging technology, the single-antenna reflected power measurement is the simplest and most inexpensive to implement for short-range operation (e.g. tabletop or handheld readers). As a result, the discussion in this chapter will focus on this method of detection. However, the other methods of detection can be modeled by very similar means. In all cases, it is necessary to model the coupling between a reader antenna and the tag antenna.

5.1.2.2 Dipole Approximations

For inductive coupling, if the distance between both coils is much larger than the diameter of the tag coil, the mutual inductance between tag and reader can be estimated by modeling one or both coils as a magnetic dipole $\mathbf{m}$, where $\mathbf{m}$ is the magnetic moment of a given coil and is equal to the total current in the coil multiplied by the area of the coil. This is shown in Figure 71. The coupling is then simply proportional to the dot product $\mathbf{m}_1 \bullet \mathbf{m}_2$. This simple approximation is very useful for lunch-time back-of-the-envelope calculations, but becomes inaccurate as the distance between the coils decreases, particularly if the reader and tag coils are not coaxial. In these cases, it is necessary to actually calculate the magnetic field distribution for at least the larger coil. If the tag coil is much smaller than the reader coil, the tag can still be modeled as a magnetic dipole but coupled to the full magnetic field distribution of the reader coil.

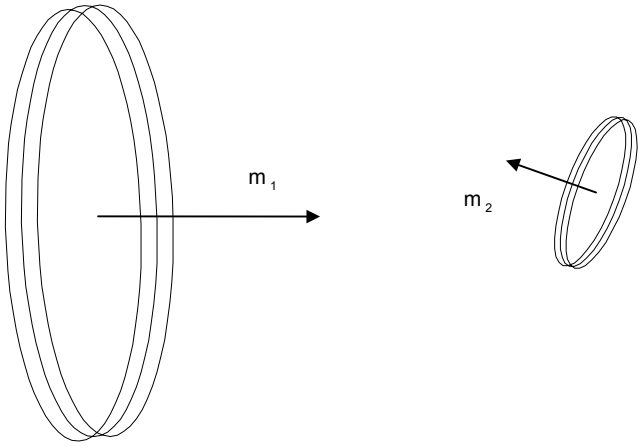

Figure 71. Diagram illustrating the dipole model for a magnetically-coupled tag system. The mutual inductance between two coils, in the far-approximation, is proportional to $\mathbf{m}_1 \bullet \mathbf{m}_2$, where $\mathbf{m}$=niA.

5.1.2.3 Mutual Inductance

More formally, the mutual inductance between the tag and reader coils can be calculated from Maxwell's equations, as mentioned previously. Denoting the reader coil as loop 1, and the tag coil as loop 2, the mutual inductance between loop 1 and loop 2 is given by

$$M_{21} = \Phi_{21} / I_1 = \frac{1}{I_1} \iint_S B_1 \bullet da_2$$

where Φ_{21} is the flux linking coil 1 and coil 2.

It is useful to recall that in general, $M_{21} = M_{12}$. This may not seem very significant, but it is very useful, because it enables the calculation of mutual inductance for cases where the field distribution cannot be easily calculated. In the case of a rectangular reader antenna, for example, it is possible to calculate the mutual inductance by using a standard circular geometry for the tag coil and then simply solve for the flux intercepted by the rectangular reader coil cross section. This is much easier than trying to calculate the magnetic field distribution of the square reader coil directly.

In calculating the mutual inductance, the quasi-static expression for the magnetic field is often used. The quasi-static field is valid at all frequencies provided that the free space wavelength of the field is significantly larger than the dimension of the reader coil and read distance. As ham radio operators know, the free-space wavelength at 13.56 MHz, for example, is approximately 30 meters, so this is not a concern. At microwave frequencies, the quasi-static approximation is only valid over distances of a couple centimeters or less.

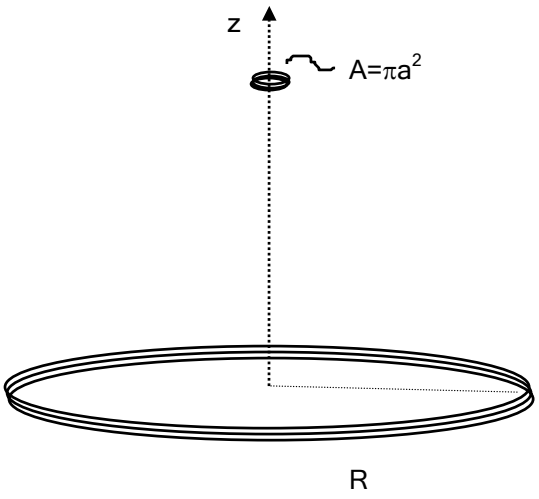

Figure 72. Example of tag and reader configuration used to estimate read range.

As mentioned previously in the derivation of self-inductance, the vector potential method and Neumann's formula are very powerful techniques for calculating the mutual inductance for many coil geometries, including rectangular coil antennas. Using Neumann's formula, the mutual inductance between two coils is given by

$$M = \mu\sqrt{aR}\left[\left(\frac{2}{k} - k\right)K(k) - \frac{2}{k}E(k)\right] \text{ with } k^2 = \frac{4aR}{z^2 + (a+R)^2}$$

where R=radius of reader coil, a=radius of tag coil, z is distance between them, and K and E are complete elliptic integrals of the first and second kind, respectively.

If the antenna coil of the tag is significantly smaller than the reader coil, then we can assume that the magnetic field is nearly constant across the area of the tag, and then use this resulting flux to calculate the mutual inductance. The basic geometry in Figure 72 can be solved for tags that lie along the axis of the reader coil, and does not require the use of elliptic integrals. As a result this geometry is very useful for modeling inductively-coupled RFID systems.

To solve for the magnetic field for a simple wire structure such as this, the vector potential method reduces to the Biot-Savart expression for the magnetic field:

$$B = \frac{\mu_0 I}{4\pi}\oint\frac{dl' \times r_1}{|r_1|^3}$$

where $\mathbf{dl}$ is a segment along the length of the coil, $\mathbf{r_1}$ is the distance from this segment to a given point along the z-axis.

Working in cylindrical coordinates and noting that $r_1^3 = \left(z^2 + R^2\right)^{3/2}$, the integral for B can be written as

$$B = \frac{\mu_0 I}{4\pi} \int_0^{2\pi} \frac{\left(\hat{x} \cdot z\cos\phi + \hat{y} \cdot z\sin\phi + R\hat{z}\right) \cdot R d\phi}{\left(z^2 + R^2\right)^{3/2}}$$

The first two terms in the integral integrate to zero, leaving the following expression for the axial magnetic field produced by the reader:

$$B = \frac{\mu_0 I R^2}{2(z^2 + R^2)^{3/2}} = \frac{B_0 R^3}{(z^2 + R^2)^{3/2}} \qquad \text{(Eq. 61)}$$

where R is the radius of the reader coil, and $B_0 = B(x = 0) = \mu_0 I / 2R$.

Given the simple analytic expression for magnetic field distribution, we can calculate the mutual inductance using the equation listed previously, yielding the following result.

$$M = \frac{\mu R_R^2 R_T^2 n_R n_T \pi}{2\left(d^2 + R_R^2\right)^{3/2}}$$

where d has been used to represent the distance from the reader to tag. Note that the mutual inductance decreases with distance as $1/d^3$ which is as expected for near-field coupling. The signal detected back at the reader is thus proportional to M^2, which results in a $1/d^6$ dependence characteristic of near-field RFID tags. For a typical EAS tag geometry and a 20 cm radius reader coil, the mutual inductance is plotted as a function of read distance in Figure 22 below.

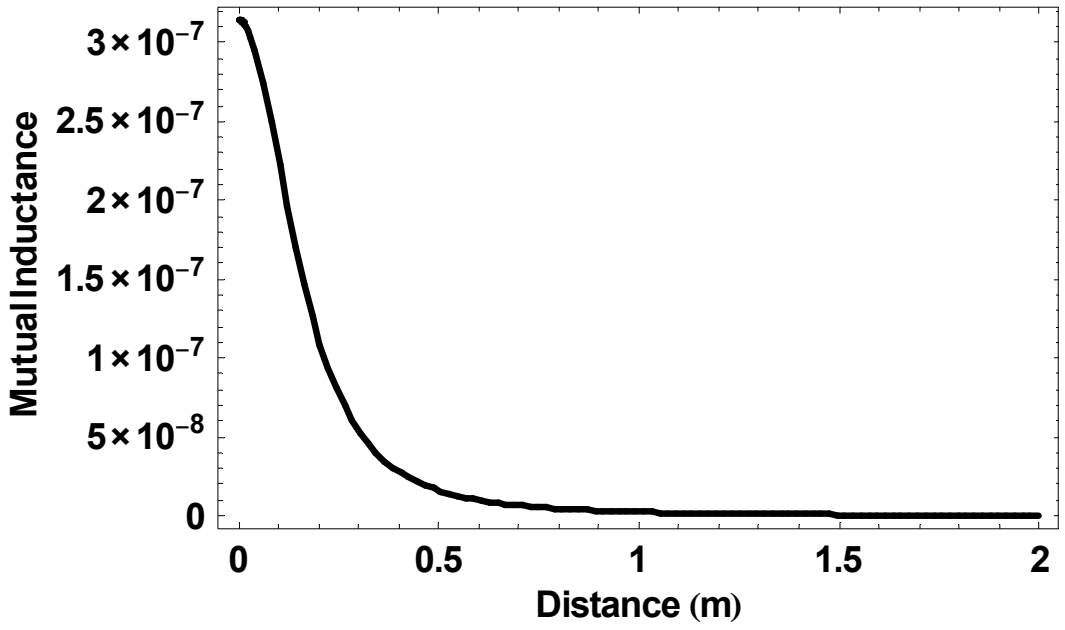

Figure 73. Sample plot of mutual inductance as a function of distance between a typical EAS tag and reader, with tag diameter = 2cm and reader coil diameter = 40cm.

5.1.2.4 Circuit Model

The fundamental performance specifications of a tag system (e.g. read range, orientation dependence, signal strength, etc.) are all related directly to the amount of electromagnetic coupling between the tag and reader. For a given RF-ID tag design, if good coupling is present, the other data-related performance factors (e.g. data rate, reading interval, etc.) are then mainly functions of the reader design and the data modulation scheme.

In a conventional inductively-coupled tag systems, the coupling is directly related to the mutual inductance between the reader and tag coils. A circuit model for this system can be made by treating the coupled coils as a transformer inductance with the appropriate turns ratios, and modeling the LC tag as a series resonant circuit. This circuit model is shown in Figure 74 below.

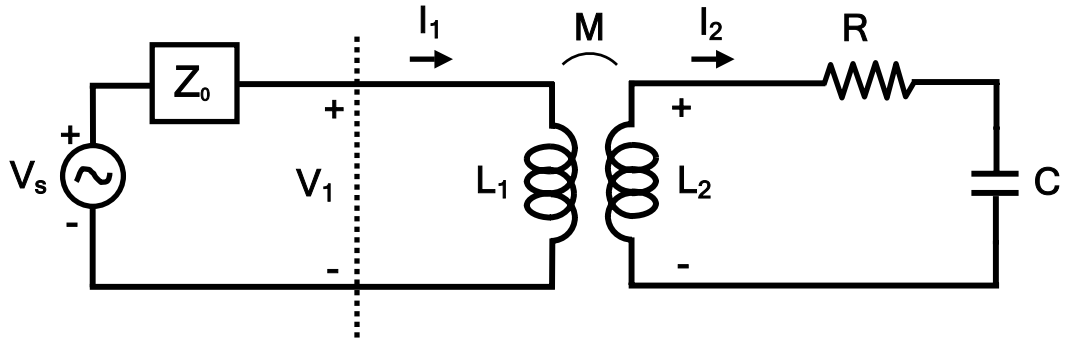

Figure 74. Circuit model for a resonator inductively coupled to a reader.

In order to solve for the reflected power, we want to solve for the impedance measured at the output terminals of the reader denoted by the vertical dotted line in Figure 74. To the right of the output terminals depicted in the schematic are the reader antenna and tag; and to the left of the output terminals is the reader signal generator and source impedance.

Given a mutual inductance ***M***, we can write the following equations that relate the voltages and currents in the reader antenna to the voltages and currents in the tag:

$$V_1 = j\omega L_1 I_1 + j\omega M I_2$$

$$V_2 = -j\omega L_2 I_2 - j\omega M I_1$$

$$V_2 = I_2\left(R + \frac{1}{j\omega C}\right) \qquad \text{(Eq. 42)}$$

where **M** is the mutual inductance between loop 1 and loop 2.

From the point-of-view of the reader, we can then solve for the impedance of the coupled circuit $Z_1 \equiv \frac{V_1}{I_1}$ yielding the following result:

$$Z_1 = j\omega L_1 + \frac{\omega^2 M^2}{j\omega L_2 + \frac{1}{j\omega C} + R} \qquad \text{(Eq. 47)}$$

Making use of the familiar relation $Q_0 = \frac{\omega_0 L_2}{R_2}$ for a series resonant circuit, the input impedance Z_1 can then be expressed in terms of the Q-factor:

$$Z_1 = j\omega L_1 + \frac{\omega^2 M^2 / R}{1 + jQ\left[1 - \left(\frac{\omega_0}{\omega}\right)^2\right]} \qquad \text{(Eq. 48)}$$

If we make the approximation that the losses are small, so that $\frac{\omega_0 - \omega}{\omega_0} << 1$, the input impedance Z_1 can be expressed more succinctly as

$$Z_1 \approx j\omega L_1 + \frac{(\omega_0 M)^2}{R\left[1 + jQ_0 \frac{2\Delta\omega}{\omega_0}\right]}$$

Although this expression does not seem familiar, it can be rearranged to yield a familiar result as follows:

$$Z_1 = j\omega L_1 + \left(\omega^2 M^2 / R\right)\frac{1}{1 + jQ\frac{2\Delta\omega}{\omega_0}}$$

$$Z_1 = j\omega L_1 + \frac{1}{j\omega\left(\frac{L_2}{\omega_0^2 M^2}\right) + \frac{1}{j\omega\left(C_2\omega_0^2 M^2\right)} + \frac{R}{\omega_0^2 M^2}}$$

$$Z_1 = j\omega L_1 + \frac{1}{j\omega C_{eff} + \frac{1}{j\omega L_{eff}} + G_0}$$

(Eq. 50)

where $C_{eff} = \frac{L_2}{\omega_0^2 M^2}$, $L_{eff} = C\omega_0^2 M^2$, and $G_0 = \frac{R}{\omega_0^2 M^2}$.

We can immediately recognize the second term as the impedance of a parallel-resonant circuit presented earlier:

$$Y_1 = G_{eff} + j\omega C_{eff} - \frac{1}{j\omega L_{eff}}$$

This is actually a general result, which shows that inductively-coupled electromagnetic resonators appear as a parallel LRC circuit in series with an inductor L_1 (the reader coil). The equivalent circuit for the reader-tag network is shown in Figure 75 below.

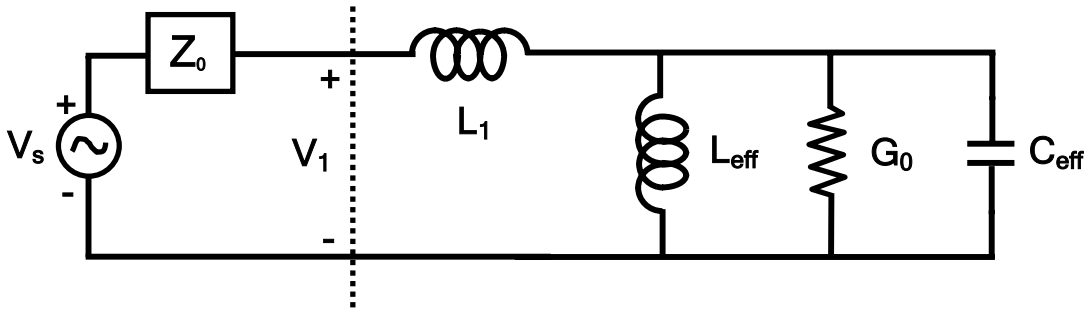

Figure 75. Equivalent parallel resonant circuit for a resonator inductively coupled to a tag reader.

Although the behavior of an isolated parallel LC circuit is well-known, we must now consider how the addition of series inductance L_1 and source impedance Z_0 will affect the resonator **Q** and resonant frequency ω. Assuming an ideal source model, we can simply work with the source impedance Z_0.

The clearest and most general way to describe the effect of the external coupling network on the LC resonator, is to combine the impedance of the source with the impedance of the reader antenna, and to express this external impedance into real and imaginary components (i.e. conductance G_0 and reactance B_{ex}) as shown in Figure 76 below.

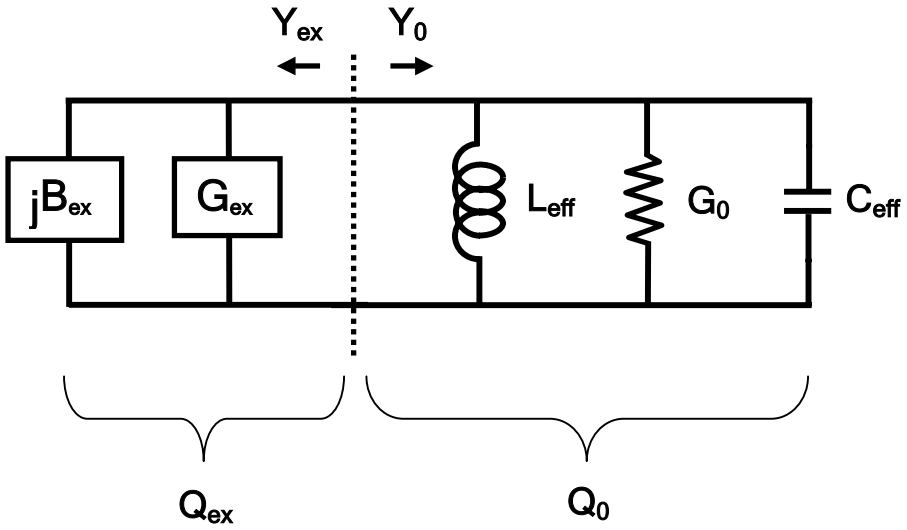

Figure 76. Equivalent parallel circuit for a resonator inductively-coupled to a tag reader showing internal and external contributions to the Q-factor.

The combined impedance for the LC resonator plus the external coupling network is thus given by

$$Y_{TOTAL} \approx G_{ex} + jB_{eff} + G_0\left[1 + j2Q_0\frac{\Delta\omega}{\omega}\right]$$

where $G_{ex} = \frac{Z_0}{Z_0^2 + \omega_0^2 L_1^2}$ and $B_{ex} = \frac{-\omega_0 L_1}{Z_0^2 + \omega_0^2 L_1^2}$

We know that at resonance, the imaginary components of the network must sum to zero, and we can use this fact to solve for the new resonant frequency of the coupled circuit.

Setting the imaginary part of Y_{TOTAL} to be zero, we can then solve for $\Delta\omega = \omega_L - \omega_0$, where ω_L is the new (loaded) resonant frequency:

$$\omega_L = \omega_0\left(1 + \frac{G_{ex}}{G_0}\frac{\omega_0 L_1}{2Q_0 Z_0}\right)$$

$$Y_{TOTAL} = (G_{ex} + G_0)\left[1 + j2G_0 Q_0\left(\frac{\omega - \omega_L}{\omega_0}\right)\right]$$

We can immediately recognize this as the standard admittance equation for a parallel resonant circuit with conductance $G_{ex} + G_0$, and with $Q = \frac{Q_0 G_0}{G_0 + G_{ex}}$. We call this new Q value the *loaded Q* or simply Q_L.

We can simplify these equations further. Although the external coupling network is not resonant, it is still valid to assign a Q-factor to this network in accordance with the original definition of Q (mentioned previously). Q-factors add like admittances, so we can speak of the loaded Q of any coupled resonator as the combination of the unloaded Q of the resonator plus the Q of the external coupling network as follows:

$$\frac{1}{Q_L} = \frac{1}{Q_{ex}} + \frac{1}{Q_0}$$

In order to compare the relative losses of the resonator with the losses of the external coupling network, it is also useful to define the *coupling factor* κ, which is the proportionality constant that measures the Q of the external coupling network relative to the intrinsic unloaded Q of the resonator.

$$\frac{1}{Q_L} = \frac{1}{Q_{ex}} + \frac{1}{Q_0} = \frac{\kappa}{Q_0} + \frac{1}{Q_0}$$

Using this definition for the resonant frequency and loaded Q-factor of the coupled circuit can be succinctly expressed as

$$Q_L = Q_0\left(\frac{1}{1+\kappa}\right)$$

$$\omega_L = \omega_0\left(1+\kappa\frac{\omega_0 L_1}{2Q_0 Z_0}\right)$$

$$\kappa \equiv \frac{G_{ex}}{G_0}$$

In order to calculate the reflected power and scattering parameters, it is necessary to solve for the reflection coefficient Γ, which is equivalent to the 1-port S-parameter, S_{11}.measured relative to the impedance of the source Z_0:

$$S_{11} = \Gamma \equiv \frac{Z_1 - Z_0}{Z_1 - Z_0}$$

Typically, Z_0 = 50Ω is the adopted standard for laboratory instruments and radio frequency circuits. However, for tag reader design, the value of can be chosen to be different from 50Ω (preferably higher) in order to provide a better match to the reader antenna. Using the known expressions for Z_1, the reflection coefficient can then be written as

$$\Gamma = \Gamma_d\left[1-\left(\frac{2k}{1+\kappa}\right)\cdot\left(\frac{1}{1+j2Q_L\left(\frac{\omega-\omega_L}{\omega_0}\right)}\right)\right] \quad \text{(Eq. 53)}$$

$$\text{where } \Gamma_d = \frac{j\omega_0 L_1 - Z_0}{j\omega_0 L_1 + Z_0}$$

For any transmission line having low loss and only inductance per unit length and capacitance per unit length, the characteristic impedance Z_0 will be purely real, so the quantity R_i/Z_0 will be real as well. From this, we can see that the magnitude of the reflection coefficient has a minimum at $\omega=\omega_0$, which matches observation.

On the complex plane, Γ sweeps out circles as a function of frequency. As is standard practice in the RF industry, these curves can be conveniently displayed on a normalized complex plane called a Smith Chart, whose origin corresponds to the point $Z= Z_0$ which indicates perfect matching and zero reflection (=0).

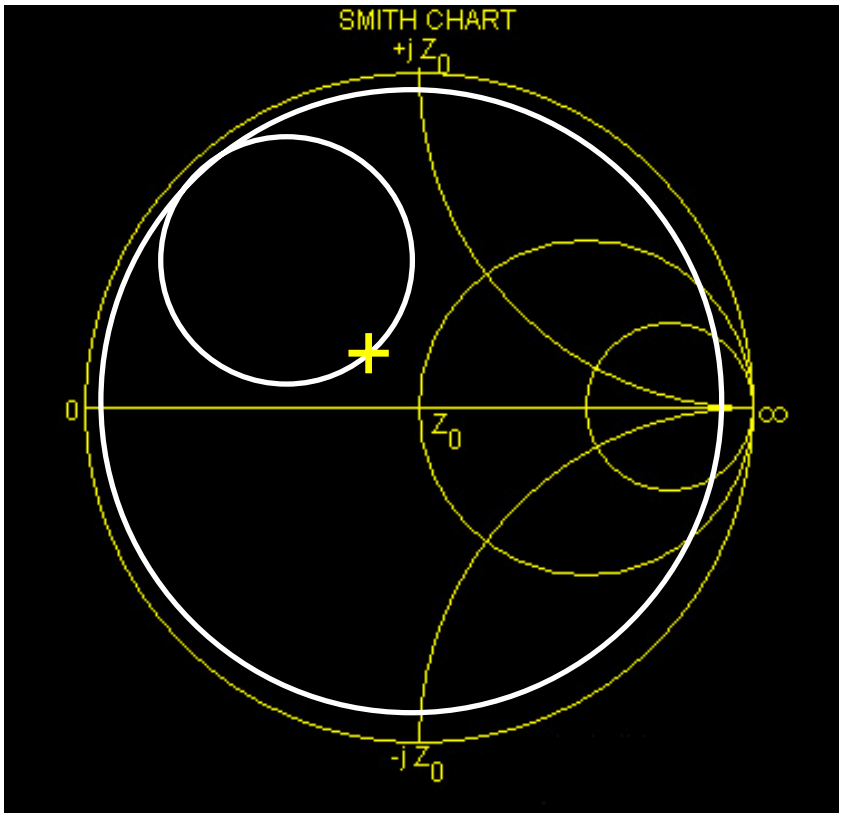

Figure 77. Simulated data of resonator reflection coefficient plotted on the Smith Chart, where lines of constant resistance appear as circles intercepted by lines of constant reactance. The point on the Q-circle closest to the origin corresponds to the frequency at resonance.

As illustrated in Figure 77 above, we can see that over a wide frequency sweep, Γ sweeps out a large circle which corresponds to the impedance of the reader coil. If the coupling has little loss, then the radius of this large circle will simply be diameter =1. In the vicinity of $\omega=\omega_0$, Γ will form an additional smaller circle which corresponds to the frequency response of the resonator itself. This

smaller circle is often referred to as the *Q-circle*. In terms of the resonator parameters, the center of the Q circle is located at $\Gamma_d\left(\frac{1}{1+\kappa}\right)$ and with radius $\frac{\kappa}{\kappa+1}$. The point at which the Q-circle meets the outer reactance circle is a function of the reader coil inductance as well as the length of the transmission line between the reader and the reader antenna coil.

By performing a measurement of the resonator and plotting the data on the Smith chart, many useful parameters can be measured directly from the data plot. Since the diameter of the Q-circle is directly related to the coupling factor, perhaps the most useful parameter to measure from the Smith chart is the coupling factor κ. If the coupling is strong enough to produce a Q-circle that passes through the origin ($Z= Z_0$), the resonator is said to be *critically-coupled*, which is the condition that provides optimum matching and power transfer to the resonator. One can see from the Smith Chart that critical coupling occurs at the point =1. If the Q-circle is small and does not cross the origin, the resonator is said to be under-coupled. If the Q-circle is large and extends beyond the origin, the resonator is said to be over-coupled.

5.1.2.5 Lumped Vs Distributed Capacitance

Using the coupling model and physical models derived above, several simulations were carried out in order to compare the performance differences between a lumped capacitance design and a distributed capacitance design.

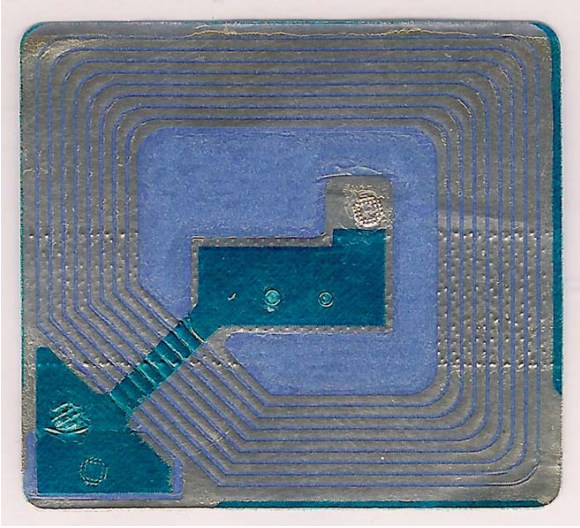

Figure 78. Photograph of planar LC tag showing lumped capacitance in center and outer corner.

The simulation parameters for the lumped-capacitance tag where chosen to match the geometry and materials properties of a common EAS tag, manufactured by CheckPoint system and Tyco-Sensormatic, shown in Figure 78 above. The parameters for the distributed-capacitance tag were chosen to be as similar as possible to those for the lumped-capacitance design; however, the thickness of the dielectric and the number of turns had to be altered in order to achieve approximately the same resonant frequency (~ 8 MHz).

The following are the parameters I used for my simulation:

Reader coil radius = 0.4m
Reader coil turns = 2

Tag width = 5cm
Tag height = 5cm
Width of tag metal trace = 1mm
Gap between traces on tag = 0.5mm
Thickness of metal on tag= 100um
Tag dielectric constant (polypropylene) = 2.4

Lumped	Distributed
Number of turns on tag = 9	Number of turns on tag = 5
Thickness of dielectric= 15um	Thickness of dielectric= 150um

The results are discussed briefly in the following sections, primarily as a means of comparing the lumped capacitance design with the distributed capacitance design. Comparison with measured data is done in section 5.3.4.

5.1.2.5.1 Mutual Inductance

Lumped

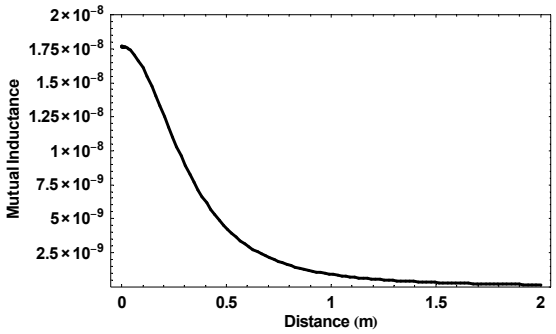

Distributed

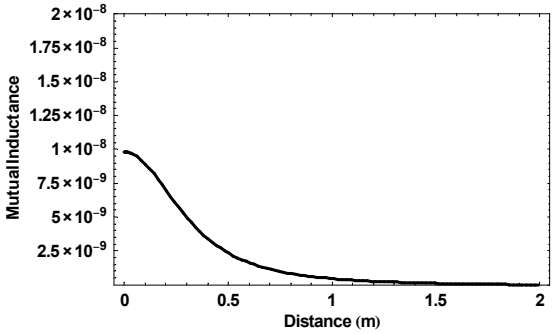

We can see that the lumped capacitance tag has greater mutual inductance, primarily due to the fact that it has a greater number of turns than the distributed capacitance tag.

5.1.2.5.2 Q-factor

Lumped

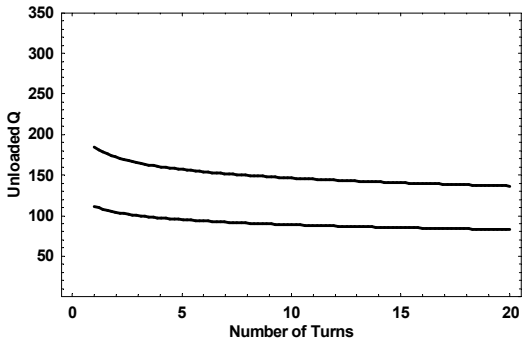

Distributed

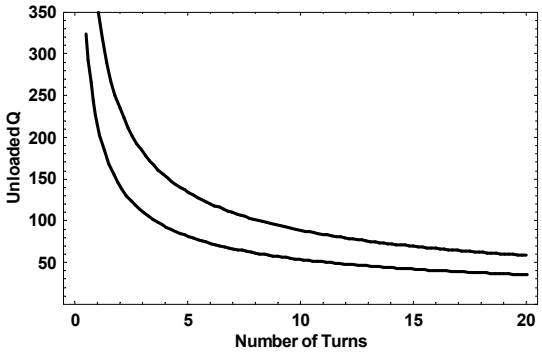

The simulation results above show the unloaded Q-factor for resonators made of copper and aluminum, respectively. The top trace is for copper, having the lower loss due to its higher conductivity. For the simulation, the bulk conductivity values were used; however, in practice, the conductivity will be somewhat lower depending on the metal deposition process used.

The lumped capacitance tag exhibits a Q-factor that is roughly constant as a function of frequency as expected using the simple series resonant circuit model. Although the resistance of the tag increases with the number of turns, the increase in inductance acts to preserve the Q-factor value. In the distributed-capacitance design, however, the Q-factor decreases sharply with the number of turns, due to the increasing capacitance.

5.1.2.5.3 Coupling Factor

Lumped

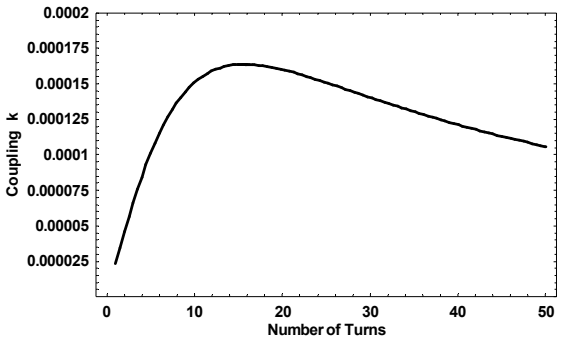

Distributed

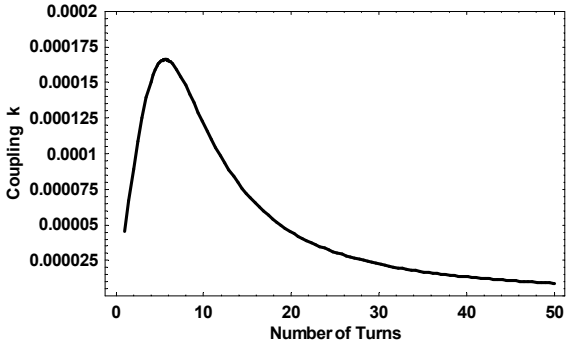

Both the lumped and distributed designs have an optimal number of turns, where the coupling is maximum. This value is dependent on the impedance of the source (tag reader). At low values of **N**, the coupling factor is limited by the amount of mutual inductance and flux capture. At high values of **N**, the coupling factor is limited by the increasing losses due to the resistance of the tag.

Lumped

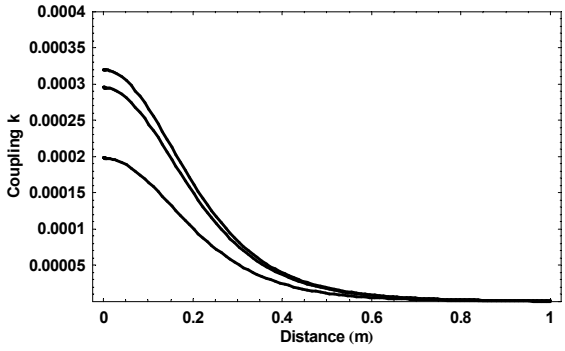

Distributed

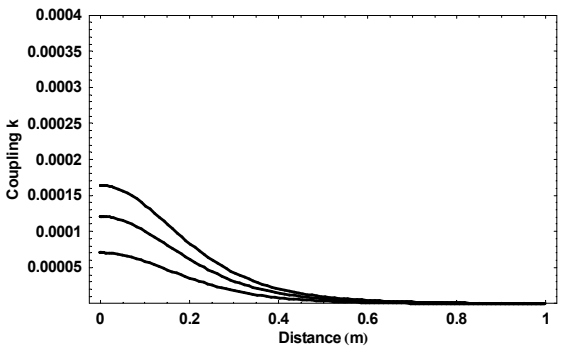

In the plot above, it is shown how the coupling coefficient varies as a function of distance for different values of ***N*** (***N***=5, ***N***=10, and ***N***=15). The coupling factor of the distributed-capacitance tag can be comparable to that of the lumped-capacitance design; however, due to the sharp dependence of the coupling factor on ***N*** for the distributed-capacitance design, the correct number of turns must be precisely calculated.

5.1.2.5.4 Reflection Coefficient and Scattering Parameter

Lumped

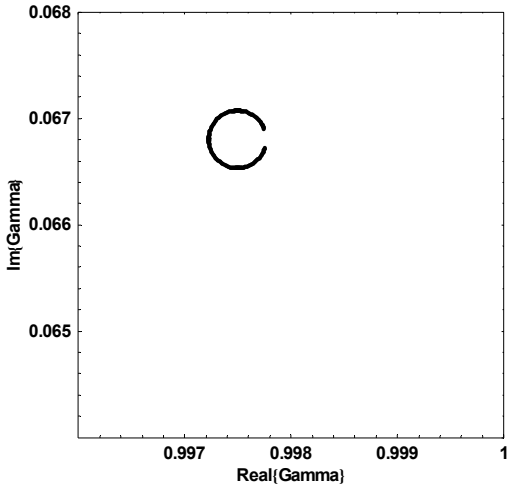

Distributed

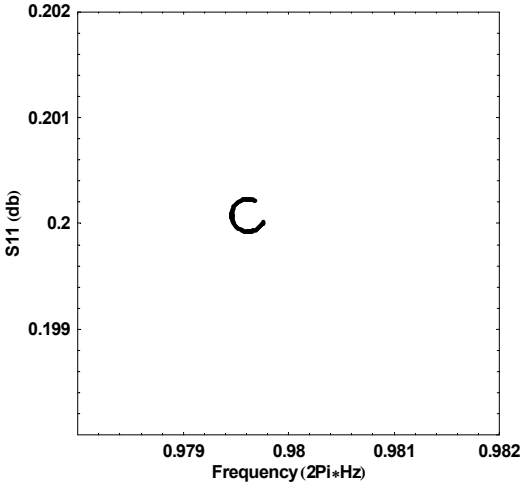

The Q-circles formed by the parametric plots of the reflection coefficient are shown above. Plotting the magnitude of the reflection coefficient as a function of frequency, the same data can be plotted in terms of the standard Scattering parameter $\mathbf{S_{11}}$ as shown below.

Lumped

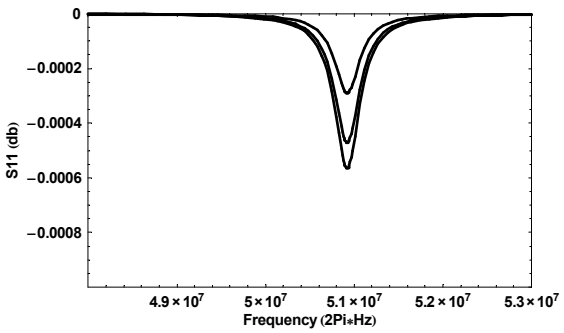

Distributed

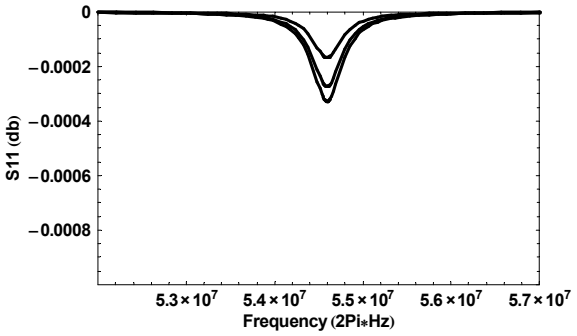

Each of the frequency-domain plots show $\mathbf{S_{11}}$ for three separate tag distances: 000 m, 0.1 m, and 0.2 m respectively. One can see that in general, the lumped capacitance design produces the largest signal in cases where the coupling is weak, such as in the EAS application. However, the relatively high Q-factor for the distributed tag at low values of ***N***, make the distributed-capacitance design attractive for short-distance applications where the coupling is strong.

5.2 Adding More Resonators: LC Arrays

With the motivation of using LC resonators to represent information, it is desirable to increase the number of resonances as a means if increasing the amount of information that can be represented. The simplest means of creating a multiple-resonance spectrum is simply to assemble an array of discrete LC resonators.

5.2.1 Information Capacity vs Number of Resonances

If we consider a frequency spectrum containing one or more resonant peaks, we can calculate the number of possible unique ID's that can be constructed, depending on the number of resonances present, as well as the position of the resonance peaks.

If we consider a single resonant peak that is *tunable* over a range of n possible values as shown below, it is possible to encode $Log_2(n)$ bits of information using that single peak alone:

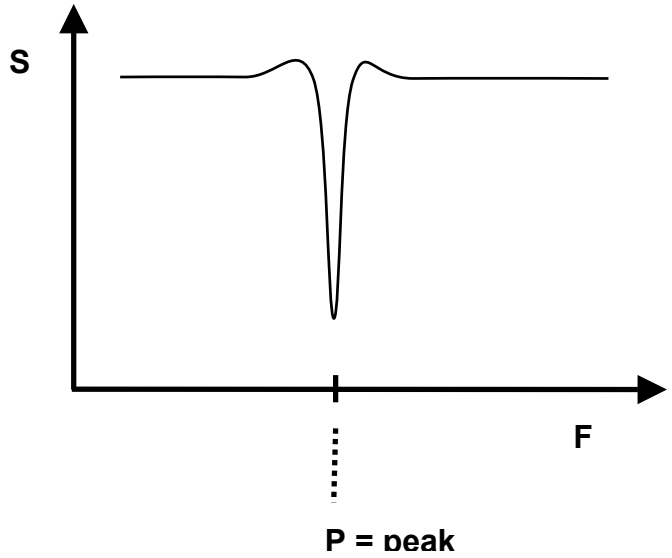

If, however, we consider several resonance peaks having *fixed* resonance frequencies as shown below, then it is possible to encode information simply through the presence or absence of specific resonance peaks. In this case, each resonance peak thus functions as a digital bit, and the number of bits of information that can be encoded is simply equal to the number of resonance peaks present.

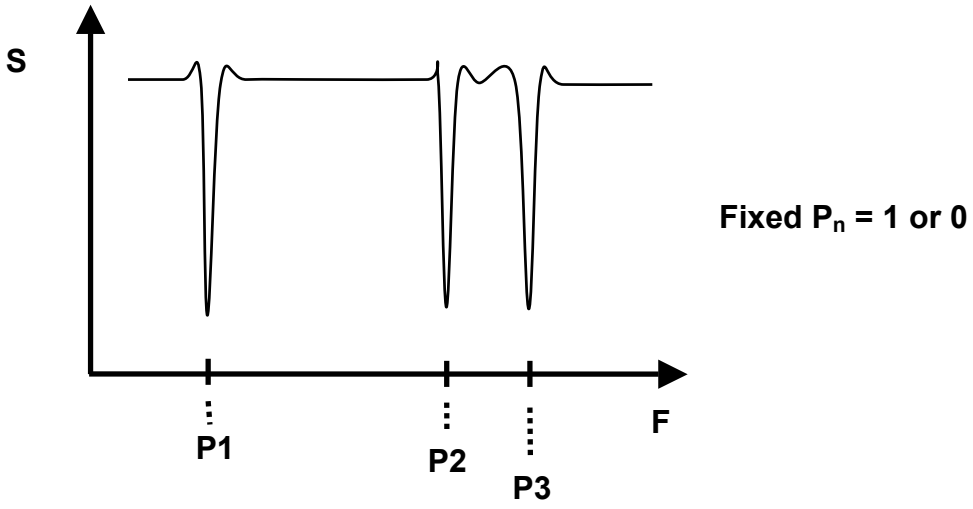

A third alternative is to employ multiple resonances that are also tunable, as shown below. In this case, the possible number of bits is given by the following:

$$\#\,bits = Log_2(n_1) + Log_2(n_2) + Log_2(n_3) + \ldots$$

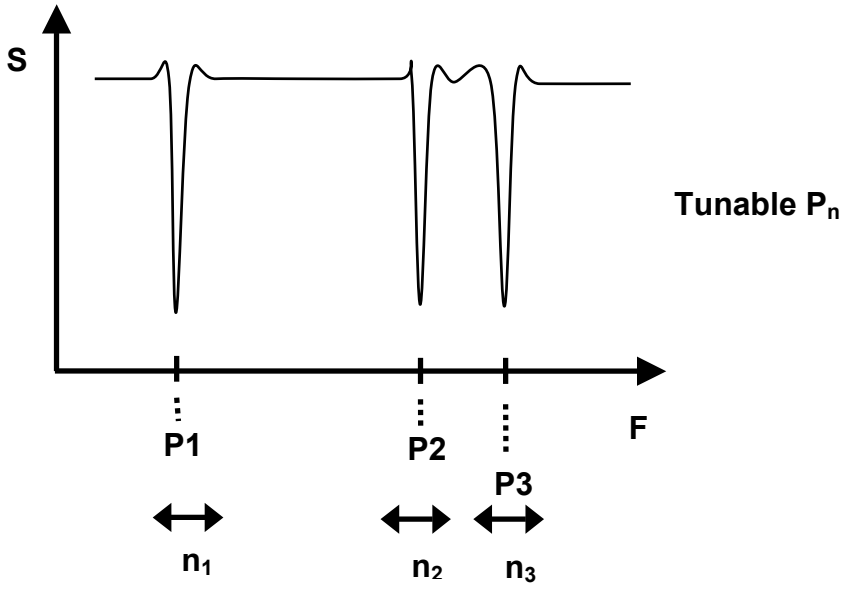

We see, therefore, that the number of resonance peaks has the greatest contribution to the number of information bits that can be represented. As a result, for the purpose of designing an ID tag, it I desirable to generate frequency spectra having as many resonances as possible.

5.2.2 Interaction between multiple resonators

As a first step to creating arrays of resonators, it is useful to consider any potential interactions that may exist among the resonators. If no interactions were present, then it would be possible to create a simple labeling system comprised of many discrete resonators tiled together.

5.2.2.1 Multiple-Resonator Circuit Model

In order to study electromagnetic interactions, we can employ a circuit model to represent the interaction between various tags and a reader. We can model the tag reader antenna as a coil, L_1, with voltage source V_1, and current I_1. This coil is magnetically coupled to resonant "tags" which are each modeled as LRC circuits. In the figure below, we illustrate the reader antenna coupled to 2 tags, LRC#1 and LRC#2, each with its own set of voltage and current.

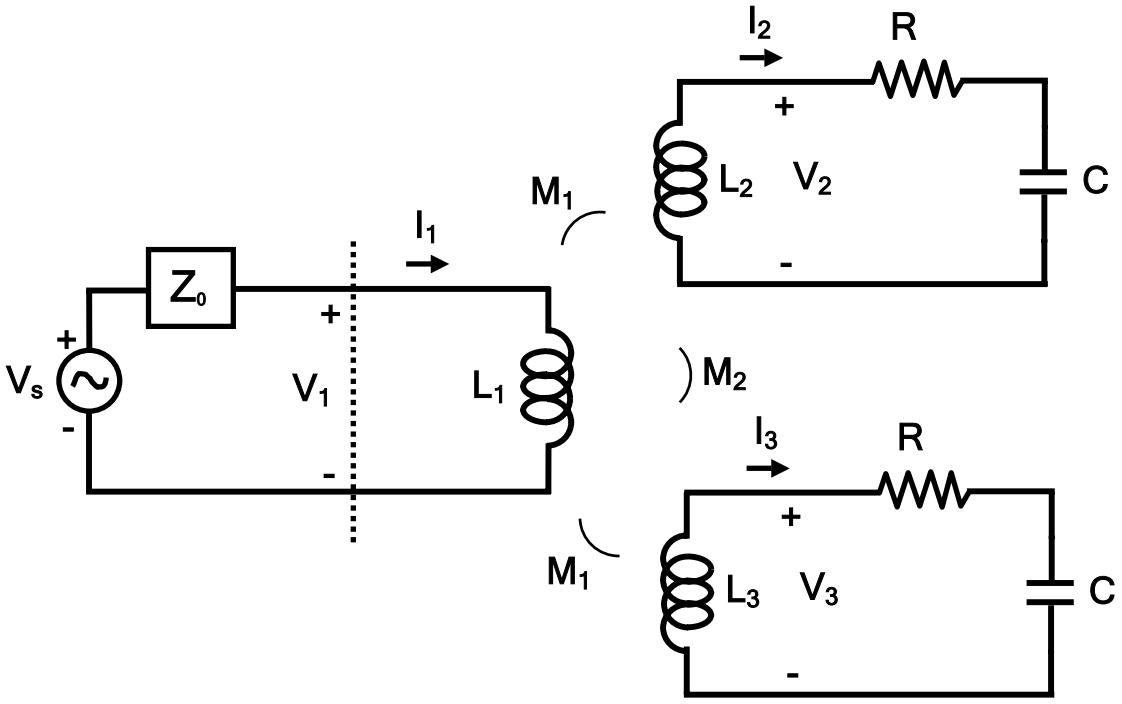

Fig. 79 Circuit model for tag reader inductively coupled to two separate resonators.

Since the reader antenna is assumed to be considerably larger than the resonant tags, such that the tags fit comfortably within the excitation field of the reader antenna, we can assume that the mutual inductance between the reader and each of the tags is the same for all tags. This is denoted as $\mathbf{M_1}$. (this assumption is not necessary, but useful for illustration) In addition, the mutual inductance between tag #1 and tag #2 is denoted as $\mathbf{M_2}$. We can then write the following system of equations:

$$V_1 = j\omega L_1 I_1 + j\omega M_1 I_2 + j\omega M_1 I_3$$

$$V_2 = -j\omega L_2 I_2 - j\omega M_1 I_1 - j\omega M_2 I_3$$

$$V_3 = -j\omega L_3 I_3 - j\omega M_1 I_1 - j\omega M_2 I_2$$

$$V_2 = I_2 \cdot \left(R + \frac{1}{j\omega C} \right)$$

$$V_3 = I_3 \cdot \left(R + \frac{1}{j\omega C} \right)$$

We can then solve the system of equations for $V_1/I_1=Z_1$, which is the relevant measurement performed by the tag reader:

$$Z_1 = j\omega L_1 + \frac{\omega^2 M_1^2 \left[Z_2 + Z_3 - 2j\omega M_2 \right]}{\omega^2 M_2^2 + Z_2 Z_3}$$

Here Z_2 and Z_3 are shorthand representations for the series impedances of each of the tags (represented by an LRC circuit). For example, $Z_2 = R + j\omega L_2 + 1/j\omega C_2$. By expanding the impedance terms, this formula can them be used to calculate the exact magnitude or phase of the measured signal.

In order to get a simplified formula for the frequency shift, however, we can assume the tags to be loss-less and identical, so that we can set R=0, and also drop all the enumerated subscripts for **R**, **L**, and **C**. Doing so leaves us with the following simplified formula:

$$Z_1 = j\omega L_1 + \frac{\frac{2\omega^4 M_1}{L^2} \left[\frac{1}{j\omega C} - M_2 j\omega + Lj\omega \right]}{\left[\omega^2 - \omega_0^2 \left(\frac{L^2}{L^2 - M_2^2} \right) + \omega_0^2 \left(\frac{LM_2}{L^2 - M_2^2} \right) j \right] \cdot \left[\omega^2 - \omega_0^2 \left(\frac{L^2}{L^2 - M_2^2} \right) - \omega_0^2 \left(\frac{LM_2}{L^2 - M_2^2} \right) j \right]}$$

$$\text{where} \quad \omega_0^2 \equiv \frac{1}{LC}$$

By looking at the “poles” of this expression (where Z_1 has local maxima), we can see that the resonant frequency occurs at:

$$\omega^2 = \omega_0^2 \left(\frac{L^2}{L^2 - M_2^2} \right)$$

As a check, the mutual inductance between tags can be "turned off" by setting $M_2 = 0$, and the resonant frequency formula then collapses to the familiar simple result of $\omega^2 = \omega_0^2 \equiv 1/LC$.

5.2.2.2 Energy Method Derivation

For larger number of resonators coupled to each other, it is perhaps more intuitive to use an energy calculation as an alternative method for describing the shift in the collective resonant frequency of the tags in the field of the antenna. We can still describe the reader and antenna with impedance $\mathbf{Z_1}$, voltage **V**, and current **I**, but we can work with the total *effective* inductance, capacitance, and resistance of the system as a whole, as given by the following relations:

$$C_e = \frac{I \cdot I^*}{4\omega_0^2 W_e} = \frac{|I|^2}{4\omega_0^2 W_e}$$

$$L_e = \frac{4W_m}{I \cdot I^*} = \frac{4W_m}{|I|^2}$$

$$R_e = \frac{2P_l}{I \cdot I^*} = \frac{2P_l}{|I|^2}$$

Where W_e and W_m are the electrical and magnetic stored energies of the system (and their sum equals the total stored energy), and $\mathbf{P_l}$ is the power loss.

At resonance, $W_e = W_m$ and we can relate the resonant frequency of the system to the effective inductance and capacitance of the system:

$$\omega_0 = \frac{1}{\sqrt{L_e C_e}}$$

For an inductively-coupled system, the number and relative position of the resonators (tags) changes the amount of magnetic energy of the system. As more tags (with coil antennas) are added to the system in potentially arbitrary orientations, we can then simply keep track of the increase or decrease of the magnetic energy of the system.

Thus each additional resonator contributes an amount of magnetic energy proportional to its current and the flux passing through it. The magnetic energy of *n* coupled circuits is given by:

$$W_m = \frac{1}{2}\sum_{i=1}^{n} I_i \varphi_i$$

Intuitively, it is thus possible to understand and qualitatively predict the resulting frequency shifts by simply knowing the relative orientations of the tags and the reader antenna. As we add or move a given tag in the reader antenna field, we simply need to note the direction of its induced field vector to see if its field will add or subtract from the total field of the system. Increasing the magnetic energy will reduce the resonant frequency, and decreasing the magnetic energy will increase the resonant frequency.

One can see that by changing the relative position/orientation of the tags and thus changing the magnitude and sign of the mutual inductance factors, that it is possible to shift the observed resonant frequency over a range of values. (even if all the tags have identical resonant frequencies)

It is worth noting that if the mutual inductance between the reader and each tag is *not* equal for all tags, then it is possible to produce an increase in the resonant frequency of some tags and a decrease in the resonant frequency of others. This can be shown using the derivation given above with distinct mutual inductances, $\mathbf{M_1}$, $\mathbf{M_2}$, and $\mathbf{M_3}$. Even if all tags have identical unloaded resonant frequencies, the mutual inductances can serve to shift individual peaks to produce multiple resonant peaks.

5.2.2.3 Implementation and Applications

As verification of the models derived above to understand and predict the resonant frequency shifts, several measurements were done using identical resonators. Data was recorded using the HP8753D Vector Network Analyzer and a single-loop antenna coil.

5.2.2.3.1 Tag Counting

For certain applications it is useful to know the number of tags present. In a retail environment, for example, labels containing planar LC resonators can be attached to various

objects such as, greeting cards in a display rack, or candy wrappers in a snack vending machine, in order to enable a variety of automated tasks such as real-time inventory.

In the case of identical resonant elements or "tags", it is possible to use the frequency shift measurement to determine the number of tags present within a certain zone. If it is possible to maintain a consistent spacing between the resonant elements, such as by stacking them on top of each other, then the additional mutual inductance presented by each tag is roughly constant, resulting in a relationship between resonant frequency and item count given by:

$$\omega^2 = \omega_0^2\left(\frac{L^2}{L^2 - [(n-1)M_2]^2}\right)$$ where n is the item count.

As the item count increases, the frequency shift dependence deviates from this curve due to conducting losses and AC loss, producing an increasingly smaller frequency shift as more resonant elements are added. In addition, to improve performance, errors in the frequency shift due to lateral misalignment of the tagged items (such as greeting cards or playing cards) can be reduced by increasing the size of the tag antenna (i.e. resonant element coil).

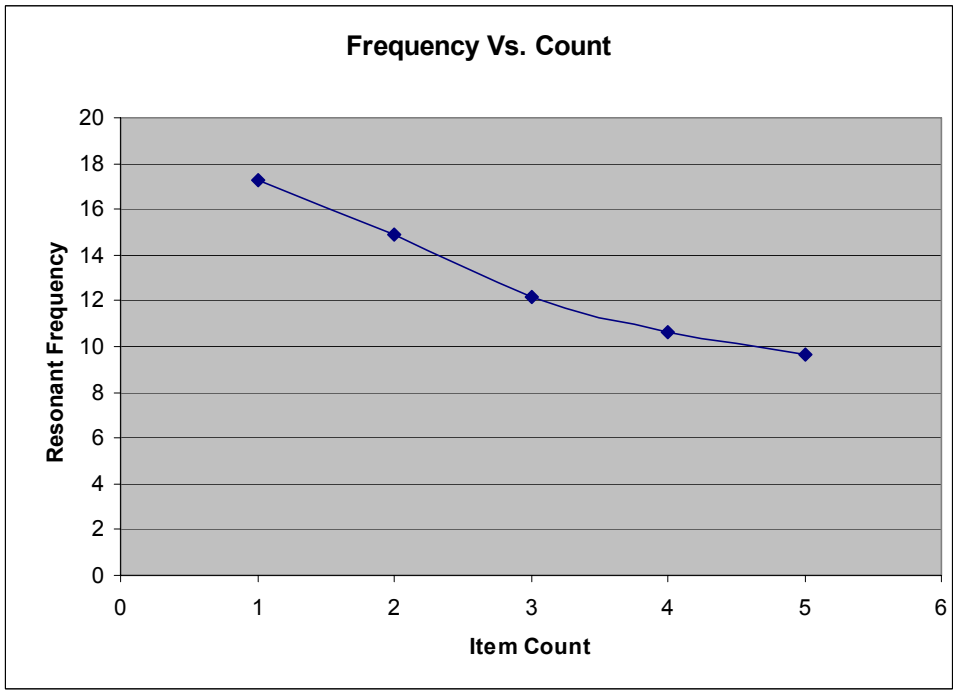

5.2.2.3.2 Vertical Positioning

Motivation. Instead of simply stacking multiple resonators (tags), it is also possible to use the frequency shift to ascertain the axial separation between two or more tags. (for example to know the separation between the faces of 2 toy building blocks) Since the mutual inductance M_2 is a (nonlinear) function of the axial separation between any two tags, the resonant frequency is also a function of this separation. This measurement is generally useful over a separation of distance roughly 3 diameters or less, where the magnetic field of each tag, and its resultant mutual inductance, are sufficiently high to produce a significant chance in the observed resonant frequency (of a few % or more). In most cases, the diameter of the reader antenna is considerably larger than the diameter of the tag antennas, so it is generally assumed that the mutual inductance M_1 (between the reader antenna and tags) remains roughly constant throughout the operating distance of the tags.

Sample frequency shift data for 2 tags as a function of axial separation is shown below:

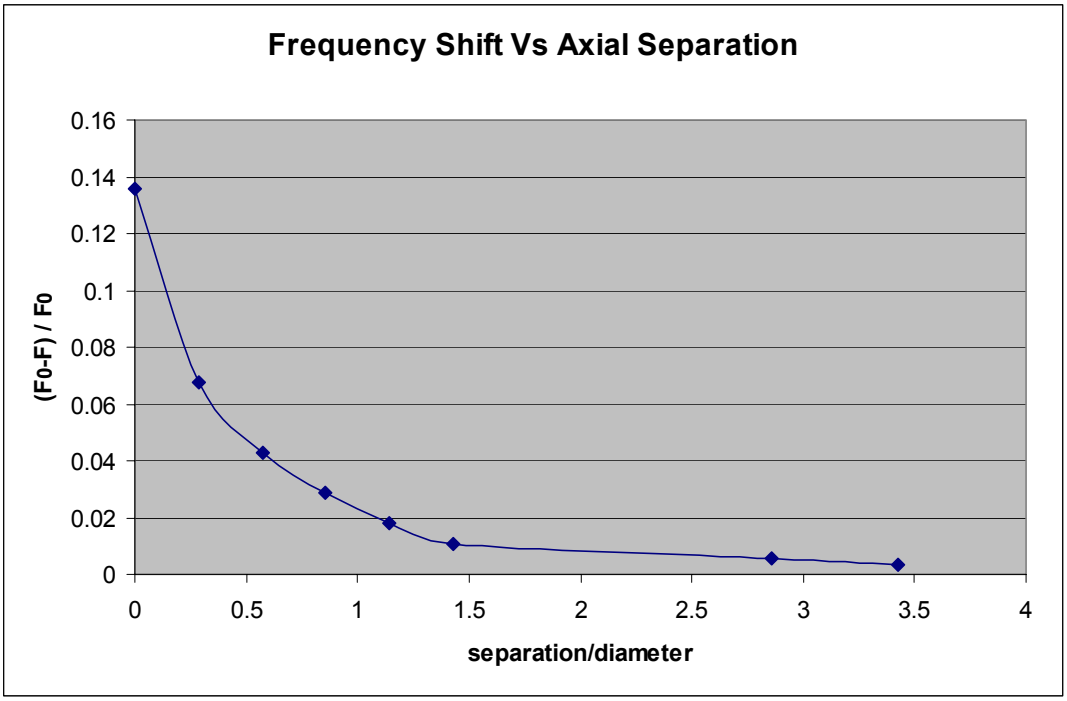

5.2.2.3.3 Lateral Positioning

The frequency shift can also be used to determine the lateral separation between two or more LC resonators (tags) that are in the excitation field of the tag reader. In this case, the mutual inductance M_2 between the tags produces a magnetic flux that *opposes* the flux due to the mutual inductance M_1 of the tag reader. The change of sign in the mutual inductance M_2 thus produces an *increase* in the observed resonance frequency. Another way to describe this is that the opposing magnetic fluxes partially cancel, which results in a smaller magnetic stored energy, hence a smaller effective inductance for the system, and thus a higher resonant frequency.

Sample frequency shift data as a function of lateral separation is shown below, for the case of two circular resonators lying side-by-side on a plane.

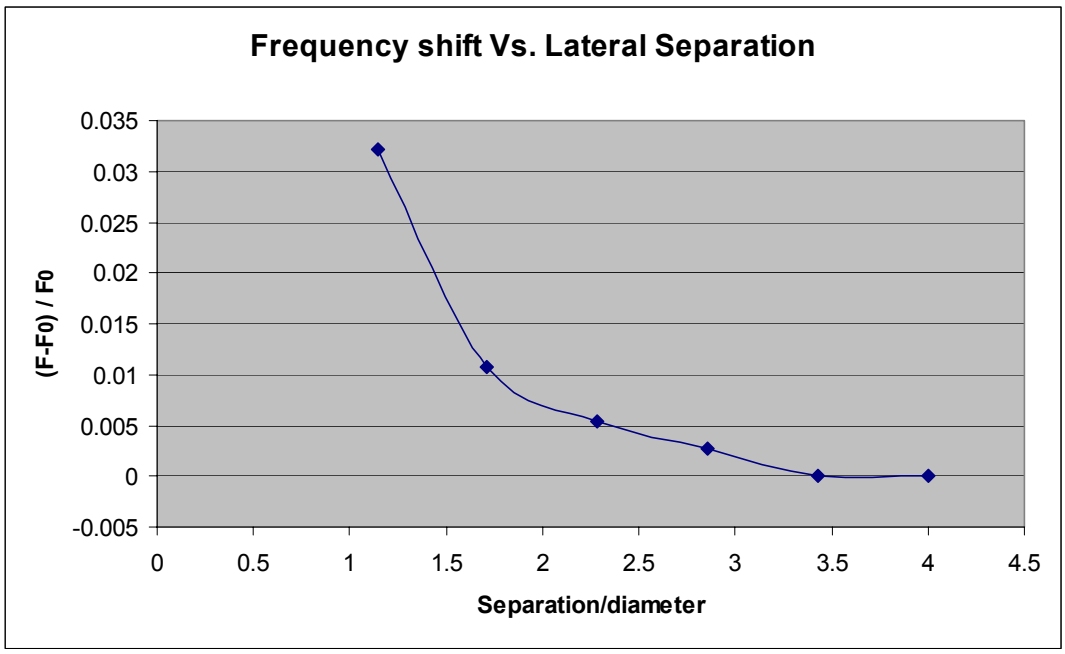

Given the fact that discrete resonators can be detuned by other resonators as well as external environmental parasitic coupling to dielectrics and metals, it is desirable to create a stable means of coupling resonances to each other.

5.3 Development of Multiply-Resonant LC Tags

An approach to creating structures that have a stable fixed coupling between resonances is to consider electronic labels that contain multiple resonances. In addition, we can begin to consider multiply-resonant structures that can be created from a single piece of metal.

5.3.1 Design Criteria

In trying to design a multiply-resonant tag label, it is useful to clearly define the criteria that this new label design should meet. In thinking about how this technology might be used commercially, my approach to designing a multiply-resonant ID tag was to create a single *common* tag design that can be mass produced very cheaply and then *individually tuned* by various means. This tuning can be a slight geometric alteration in the mechanical manufacture of the tag, or can be accomplished through some type of post-processing step, such as stamping, punching, printing, or annealing, for example.

As the basis for such an electronic ID label, I proposed the following criteria:

- **High-Q:** The resonances should be as strong as possible, with resonance peaks that are easily distinguishable.
- **Uniformity of resonances:** The resonance peaks should be of roughly equal amplitude.
- **Stable coupling between resonances:** The coupling between resonance peaks should be as stable as possible to avoid detuning.
- **Tuning Range:** It should be possible to produce resonance peaks over a wide range of frequencies, spanning roughly 5 - 100 MHz.
- **Tunability:** It should be possible to shift the position of the resonance peaks by a variety of simple and practical means.
- **Reasonable size:** for practical reasons, it is desirable to restrict the area of the tag to several square inches.
- **Reproducibility:** The electromagnetic design of the tag should be sufficiently stable so that identical tags can be produced in large quantities given reasonable manufacturing tolerances and process variations.

5.3.2 Existing Approaches and Prior Art

Over the past few decades, there have been several attempts to create a multi-resonant ID label. These designs are discussed briefly below.

5.3.2.1 Discrete LC Arrays (CWOS)

Perhaps the simples approach to creating a multi-resonant label is to place several discrete resonators on the same label side-by-side. CW Over Solutions has been producing such labels for a number of years, primarily as airline baggage labels. More recently, Checkpoint Systems has also begun to sell such labels for applications requiring a few bits of ID. Since each resonator itself can be as large as 2 in X 2 in, the resulting composite label can be impractically large. Thus, the main disadvantage of LC arrays is the large area of the labels.

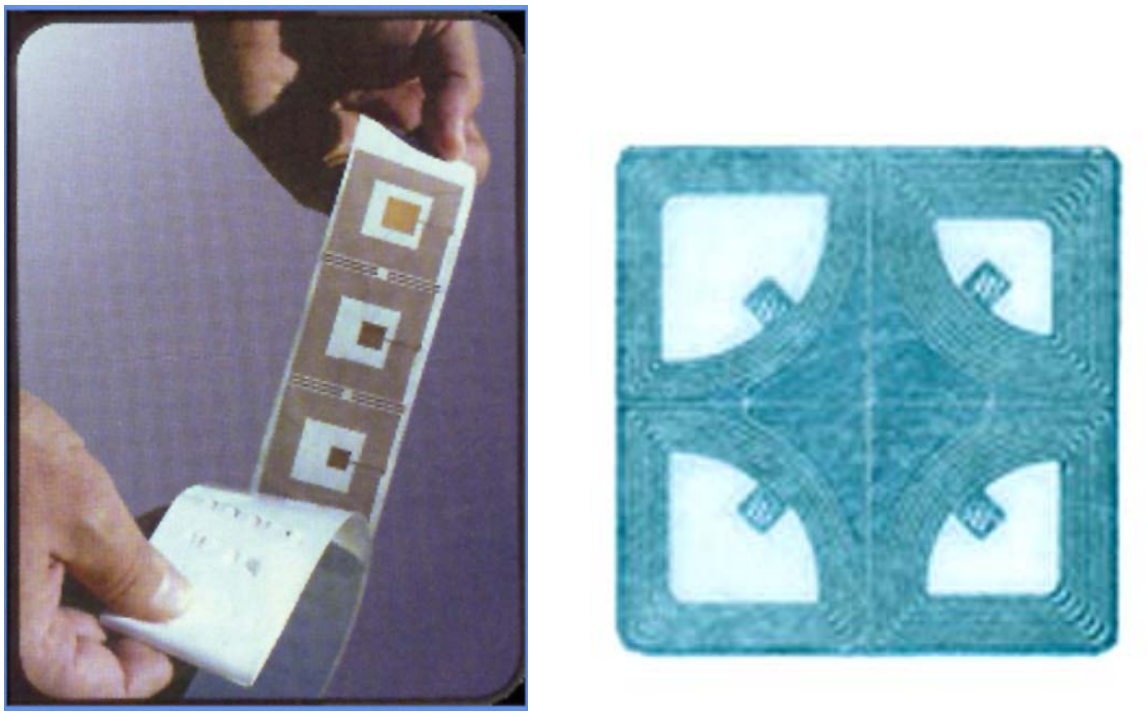

Figure 80. Examples of commercially-available LC array labels. (Left) Airline Luggage label by CW Over (Right) ExpressTrack Label made by CheckPoint Systems.

5.3.2.2 Overlapping LC Arrays (CheckPoint Systems)

As an attempt to reduce the total label area, one approach has been to overlap several discrete resonators. As mentioned in the previous sections, such overlap will produce significant detuning of the individual resonances; however, if the resonators are made to overlap such that the magnetic flux components intercepting each loop can cancel, then the detuning can be minimized. However, this “flux equilibrium point” is not a very stable means of coupling, since any inhomogenous interference from external objects will “unbalance” the flux equilibrium and detune the resonances. In addition, manufacturing costs and signal strength limits how many resonators can be stacked on top of one another.

5.3.2.3 Series Capacitor Design (Navitas)

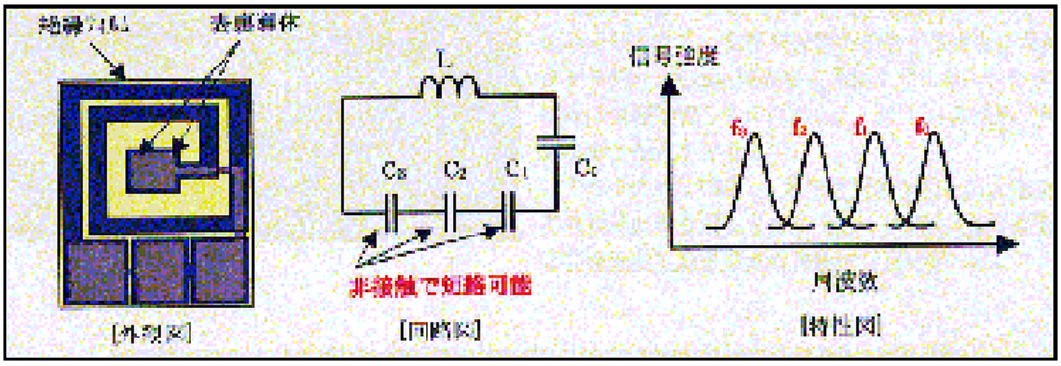

Figure 81. Sample figures from a 2002 Navitas brochure, showing their multiple capacitor tag design.

A useful method of producing multiple resonances from a single structure is to use a network of several lumped capacitors coupled to a single planar inductor coil. Variations of this technique using a printed circuit board were first commercialized by Schlage Lock and Westinghouse Security systems for use in access control cards that are still in use today. More recently, a Japanese label manufacturer Navitas has designed a planar metal foil label using this design.

I have not tested or analyzed this design and cannot comment on the relative merits of this approach; however, I can say that since all the capacitors share the same coil, the signal strength of each individual resonance is not as large as tat of discrete resonators. At present, these label are not widely available and are limited to four resonances.

5.3.2.4 Multi-Inductor Design (RF Code)

Instead of creating a network of lumped capacitors, it is also possible to create a network of inductors that serve to produce multiple resonances. These inductors can be coupled to lumped capacitances or can also be designed with distribute capacitance. One example of such a design is a multi-resonant tag known as the "Spider Tag" that was produced several years ago by a small start-up company called RF-Code. I have never seen one of these tags, but I have inferred the design from an old description of the technology on their web site, which no longer exists.

5.3.3 Proposed Design (MIT)

Given the design criteria as well as a knowledge of prior attempts at multiply-resonant structures, I decided to explore a new design family based on branching inductors having a distributed capacitance. The basic single-resonance design is shown in Figure 28 below. This structure can be cut from a single layer of metal to save cost and to provide a more direct means for coupling between the multiple resonances. In addition, I chose to use distributed capacitance instead of lumped capacitance in order to conserve area and provide additional area to add other resonant elements.

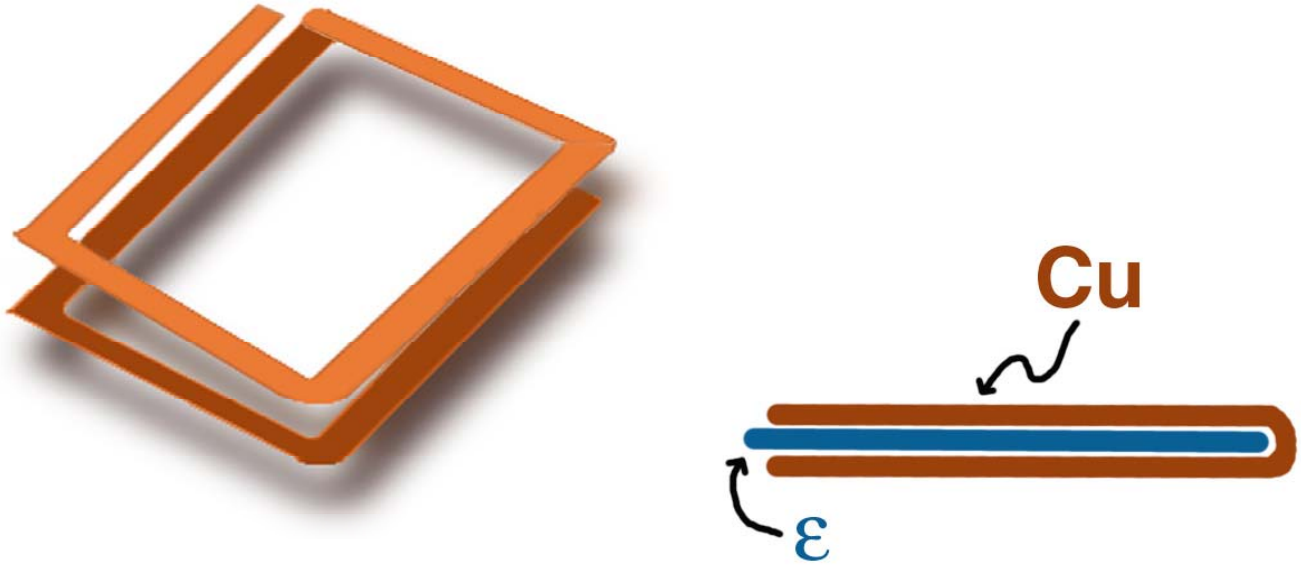

Figure 82. Basic elements of proposed design for multi-resonant tag.
(left) Perspective view (right) cross section view

Figure 83. Unfolded single-resonance distributed inductance tag.

One can see from an image of an unfolded single resonance tag (Figure 83) that the tag consists of a single metal trace, designed such that the rotation of each opposing face of the tag is anti-symmetric with respect to each other. The anti-symmetry ensures that the induced currents on the faces will add constructively. The capacitance required for resonance is thus formed in the gap between the two opposing halves of the tag.

Additional resonances are created by adding branches to the original metal trace as a means of creating multiple non-equivalent current pathways – each with its own inductance. An example of this type of tag is shown in Figure 84 along with a simplified graphical representation. The multiply-resonant tag can thus be represented as a branching tree structure, where each node of the tree proved an additional degree of freedom and contributes a resonance. By representing this design topology as a tree structure, such a description easily lends itself to parameterization and enumeration. As shown in Figure 85, the space savings afforded by the distributed capacitance design then enabled additional inductive branches to be added in order to create resonances.

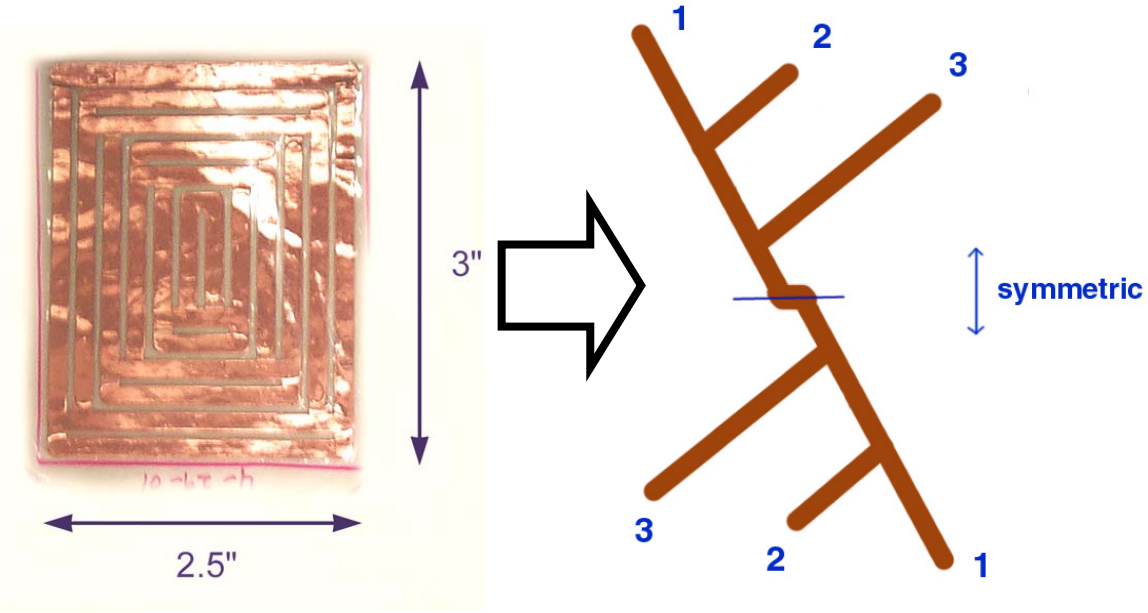

Figure 84. (left) Multiply-resonant planar LC tag and (right) equivalent graphical model.

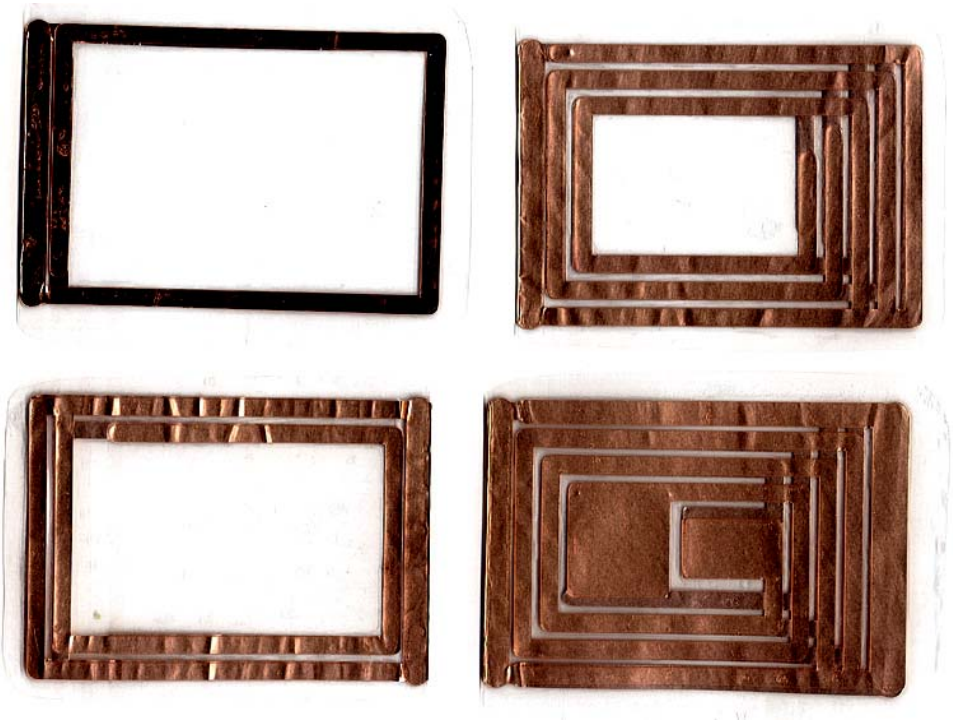

Figure 85. Example of design evolution, from a simple single-resonance structure (upper left) to a 5-resonance structure (lower right).

In summary, my proposed design offers the following advantages and disadvantages:

Advantages:

- **Compact area:** This design offers a greater number of resonances per unit area than any tag design I have seen.

- **Stable coupling:** Since the resonances are directly coupled through Ohmic contact with each other, this provides a more stable coupling between resonances.

- **High-Q:** Since each resonance is comprised of roughly a single turn of metal, there is very little loss in each resonance, enabling high Q-factors and relatively good signal-to-noise ratios at short read distances.

- **Low cost:** since the entire tag is cut from a single continuous layer of metal, this design can be manufactured at a relatively low cost.

Disadvantages:

- **Reduced signal at long read range:** Since this design employs a distributed capacitance with each inductor being only one turn or less, this tag design is not optimal for long-distance applications where flux capture is important to maximize mutual inductance. However, in my case, I was interested in creating a tag that could be used as a general-purpose electronic ID label with read ranges of several inches or less. Thus the trade-off between tag area and signal strength was justified.

5.3.4 ID Tag Implementation

Given the proposed tag design, it was possible to carry out an implementation of an electronic ID label using these multiply-resonant planar LC structures. In order to do so, several challenes had to be overcome, including tag manufacture and gaining, theoretical understanding, and information coding. Each of the main steps in the process is summarized and discussed briefly in the following sections.

5.3.4.1 Tag Fabrication and Testing

A reproducible process for manufacturing the tags was devised by repurposing a commercial vinyl sign cutting machine to cut copper sheet. For this, a Roland programmable knife plotter was employed. Once the tag was cut, the resulting structure was folded in half with a polypropylene dielectric (ordered from Goodfellow #PP301150/1) and laminated using a traditional heat-activated laminator machine. The tags were designed with a notch at the folding point in order to ensure proper and reproducible registration and alignment of the two halved of the tag when folded. Special care was also taken to ensure that the inserted edge of the dielectric was cut straight and fully inserted into the crease of the folded copper. The lamination process was standardized in order to maximize reproducibility. Each tag was run through the lamination machine twice at a fixed temperature setting.

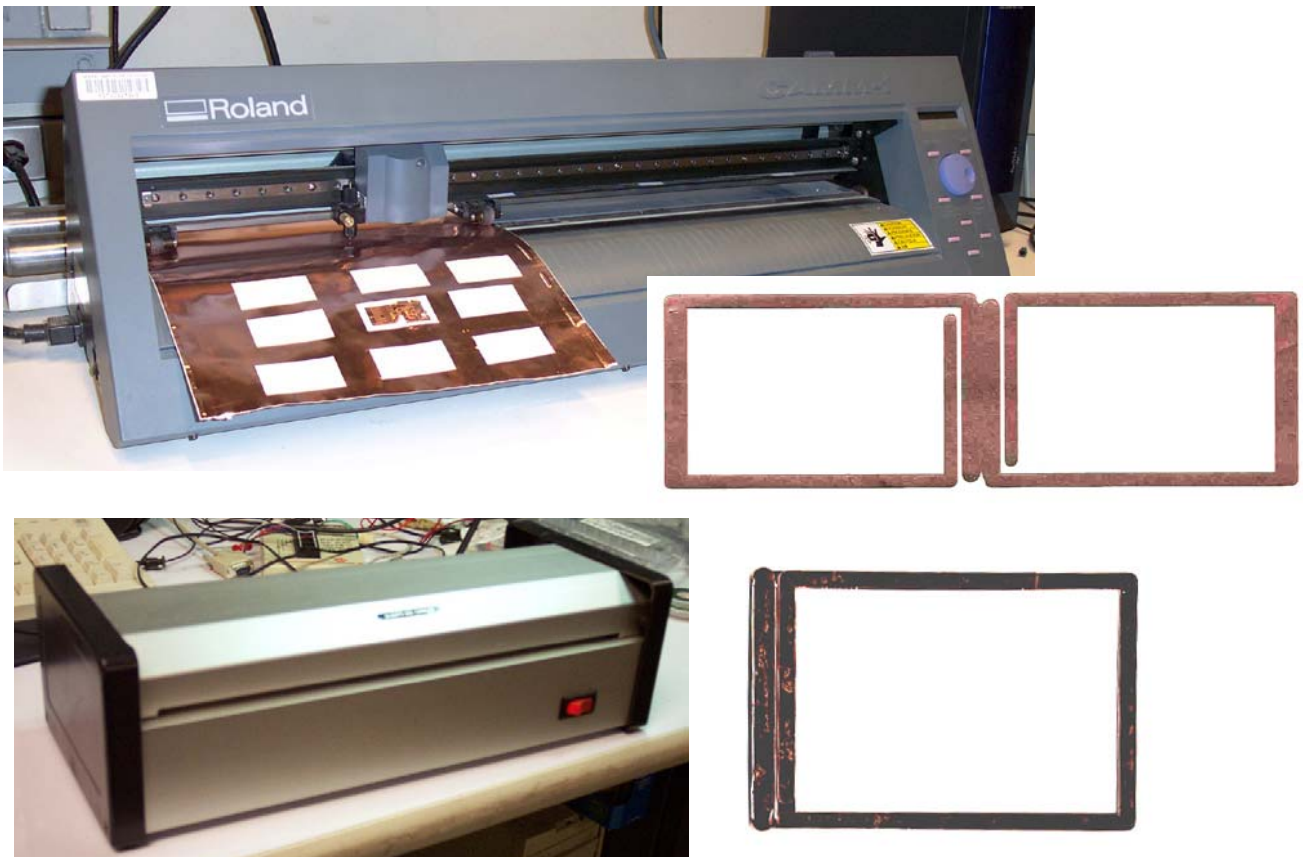

Figure 86. Equipment used to fabricate tags. (top) Roland programmable knife vinyl cutter machine and image of unfolded copper layer. (bottom) Lamination machine and image of completed tag after folding, dielectric insertion and lamination.

Figure 87. Photograph of loop antenna used as test probe. The photo on the left shows the standard measurement geometry. The photograph on the right depicts a misaligned tag which gives rise to additional parasitic resonances.

Following the lamination process, the tags were individually tested using the HP 8753D Vector Network Analyzer. From the reflected power magnitude spectrum, the individual resonant frequencies of each tag was recorded. For all testing, the loop antenna used to couple to the tag was made large enough to ensure uniform excitation of the tag, and the tag was placed safely within its perimeter (Figure 87). Unlike the case of a single resonance tag, the multiple current paths that exist in a multi-resonant design can enable several different current distributions, depending on the boundary conditions. This behavior is shown in Figure 66. In a commercial application, it is assumed that the reader antenna will be sufficiently larger than the tag in order to ensure uniform field excitation.

Figure 88. Sample measurement of a multiply resonant tag. Shown are a sample spectra (right) and a Q-measurement of the largest peak exhibiting a loaded Q>200 (left).

Figure 89. Frequency spectra from misaligned tag, showing additional resonances arising from non-uniform field excitation.

5.3.4.2 Early Multiply-Resonant Designs and Observations

Proof –of-concept of the proposed design was readily achieved using a simple rectangular geometry. Using this as a basis, over one hundred different designs were explored varying the shape, size, and linewidths of the tags. One goal of the early designs was to confine all the resonant frequencies to below 80 MHz, which was the practical upper limit of our custom-made tag reader at the time. The amount of branching was also explored as a means of optimizing the number of resonances per unit area. A sample of the different designs are shown in Figure 90. As many as eight resonances were achieved using a tag size of approximately 2.5 in X 3 in. A sample spectrum is shown in Figure 92.

Although the branching geometry proved to be fairly robust, it became apparent that several subtle aspects of this design were still unknown. In general, the resonant frequencies of each tag were found to be reproducible to within a few percent, but some tags designs were more reproducible than others. Perhaps the most challenging issue was the unequal amplitude of the resonant peaks, and considerable time was spent exploring this problem.

Although the tag fabrication process was very convenient, it was noticed that the lamination process was not ideal. Over a period of a couple months, the resonant frequencies of various tags were observed to shift due to delamination. However, the original spectrum of each tag could be recovered by passing it through the heated laminator several times. Therefore, when comparing various spectra from different tags manufactured over a period of many months, it was important to relaminate all the old tags in order to restore them to their original state. In commercial manufacturing, it is assumed that a different lamination process would be used in order to prevent such degradation over time.

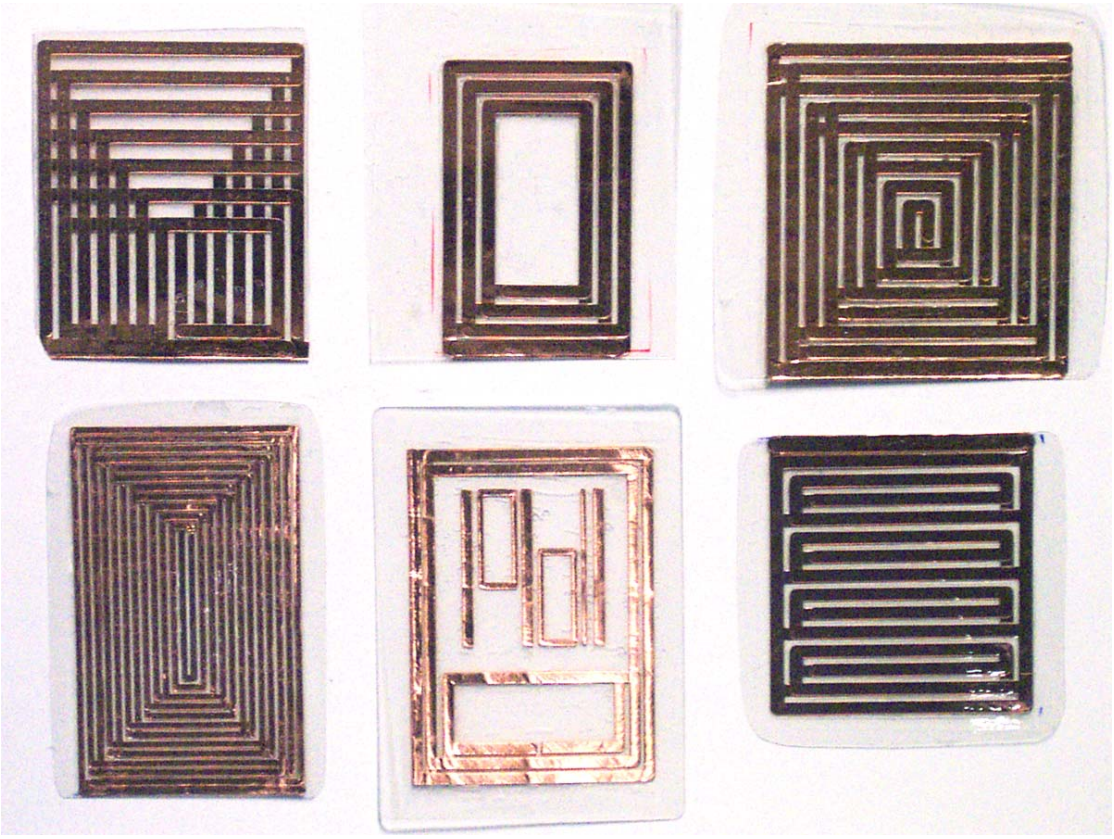

Figure 90. Frequency spectra from misaligned tag, showing additional resonances arising from non-uniform field excitation.

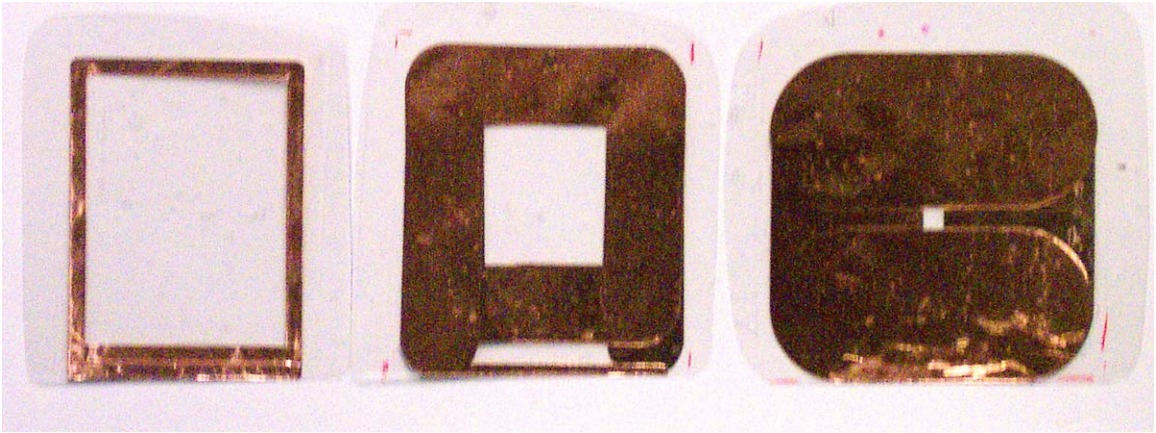

Figure 91. Photograph of three different single-resonant tags with line widths of 0.1 in, 1.0in and 2.0 in, respectively. Appreciable degradation in the Q-factor was observed only for widths <0.1in.

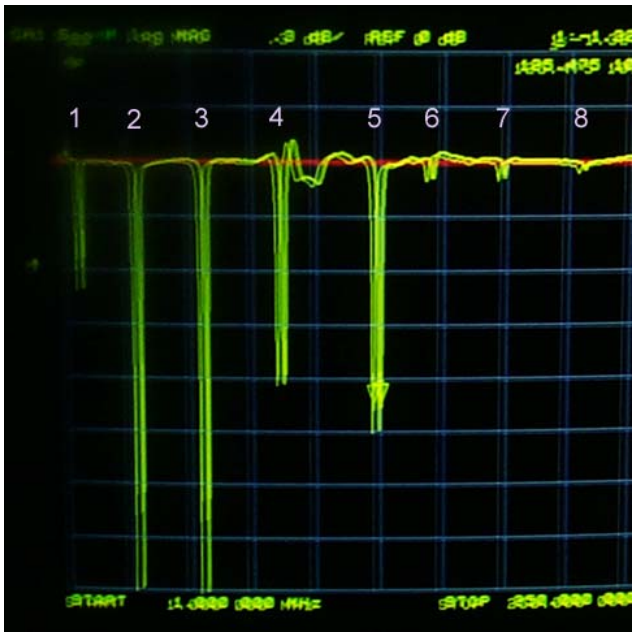

Figure 92. Sample frequency spectra from a multi-resonant LC tag exhibiting 8 resonances.

5.3.4.3 Single-Resonance Tag Design

Following the initial design exploration, I decided to simplify the problem as a means of understanding and addressing the subtle issues in my proposed design. As a first step, I made a series of single-resonance tags and compared the results to the results predicted from the electromagnetic coupling model derived earlier. In particular, I was interested in understanding the behavior of a distributed capacitance tag with a very low number of turns. A sample of one of the tags measured is shown in Figure 93 below.

Figure 93. Photograph of sample single resonance tag used in the parameter study. The tag shown has $\Theta = 420°$ with diameter = 2.5 inches.

For modeling the single-resonance tag, I used the following parameters:

Reader coil radius = 0.05m Reader coil turns = 1	Tag diameter = 2.5 inches = 6.35 cm Width of tag metal trace = 90 mils= 2.3 mm Gap between traces on tag = 2 mm Thickness of metal on tag= 250um Resistivity of copper = 1 X 10^{-7} Ω·m Tag dielectric constant (polypropylene) = 2.5 Thickness of dielectric = 15 um

The predicted and measured value of the loaded Q is shown in Figure 94. The measured values are in fairly good agreement with the predicted values. It should be noted that for the distributed capacitance tag, the value N=1 does not have any meaning since a single layer of metal does not have a capacitance (other than its own parasitic capacitance); therefore, it makes more sense to define N=1 as starting from the second turn of the coil, where the capacitance is non-zero.

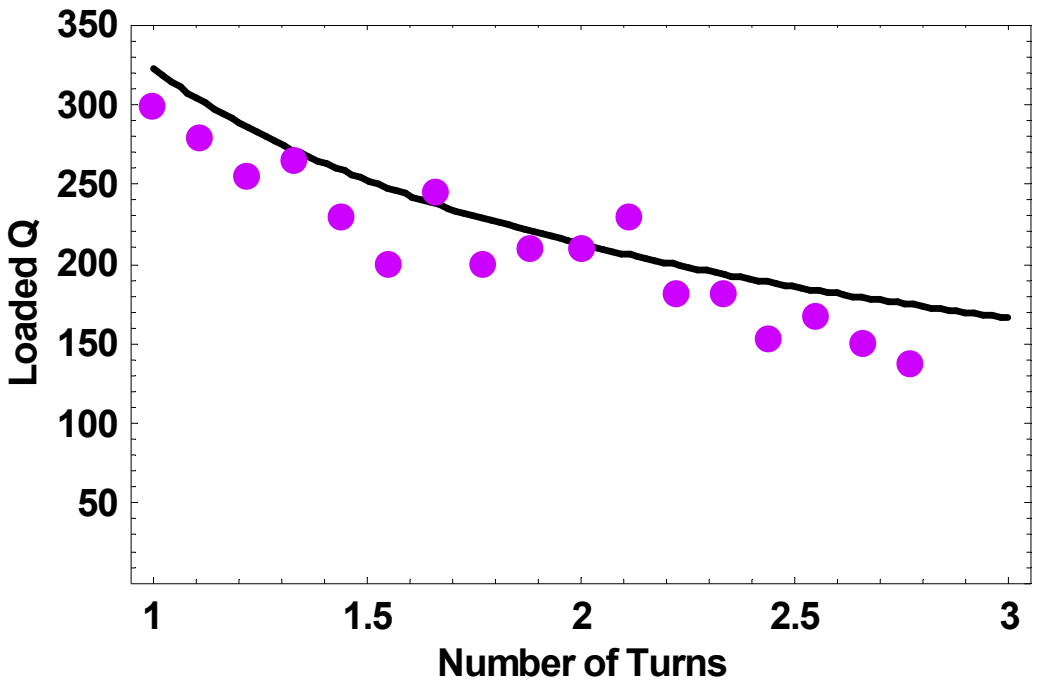

Figure 94. Plots of loaded Q as a function of frequency. The solid line indicated the predicted value and the circles represent measured data.

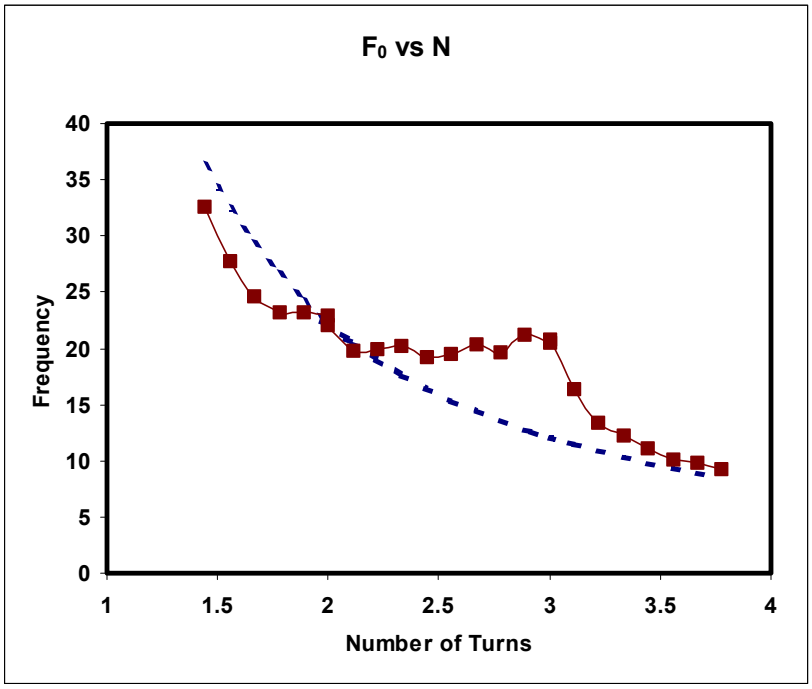

Figure 95. Plots of resonant frequency as a function of the number of turns. The dotted line represents the predicted values and the connected squares represent the measured data. The periodic undulations in the measured data is understood and expected from the geometrical constraints of the tag design.

The plot of resonant frequency as a function of the number of turns is shown in Figure 95. Although the measured data does not appear to match well with the predicted results, it actually does. Although the model assumes a uniformly increasing capacitance as the number of turns increases, this is actually not geometrically possible the way that the tag is constructed. As the length of the metal trace is increased to greater values of **N**, there are certain sections of the branch that will overlap with the opposing face of the tag and other sections that will not. Although even a single layer of metal trace does have capacitance, its value of capacitance (C << pF) is at least one order of magnitude smaller than the capacitance produced by opposing metal layers (C ~ 10 pF) If we take $R\Theta$ as the measure of the length of each branch, then we can see that as we grow the length of each branch from Θ=0, the two opposing branches will not begin to overlap until Θ=180°. During this time, the capacitance, and thus the resulting resonant frequency will remain relatively constant. As Θ increases to Θ=360, the distributed capacitance increases uniformly until Θ=540°. Beyond Θ=540°, the branches once again continue to grow without any opposing metal layer until the point Θ=720° is reached, and the cycle repeats. Therefore, every 180° (which corresponds to a full turn, since both branches are growing simultaneously) the resonant frequency will remain fairly constant, and in the second 180°, the distributed

capacitance will rapidly increase, acting to lower the resonant frequency. Thus, there are very few values of **N** where the opposing metal traces on both faces of the tag are completely overlapping. Agreement with the theoretical model is only expected at even values of **N**, where the metal traces have formed completely overlapping annular layers. Thus, we see that the measured data is actually in good agreement with what we expect.

Perhaps the most useful insight gained from studying the single-resonance tag is that the frequency response of the tag in this frequency range is largely dominated by the distributed capacitance. Apparent from the data is the fact that the reactance of the interlayer distributed capacitance is large compared to the inductance of a single branch and the reactance of any single-layer capacitance.

5.3.4.4 Double-Resonance Parameter Study

Having explored the single-resonance design, I proceeded to study the double-resonance design comprised of a simple 2-branch structure shown in Figure 96 (left) below.

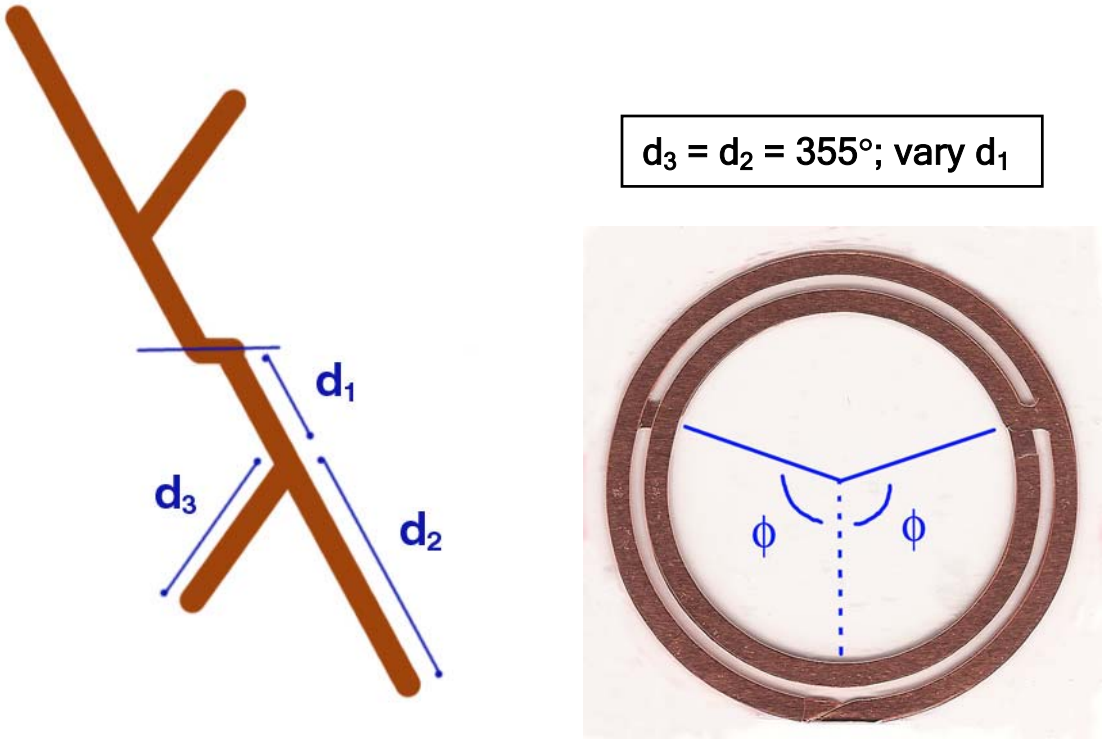

Figure 96. (left) Graphical representation of the double-resonance design used for the parameter study and (right) a photograph of the physical implementation showing variation of the length d_1.

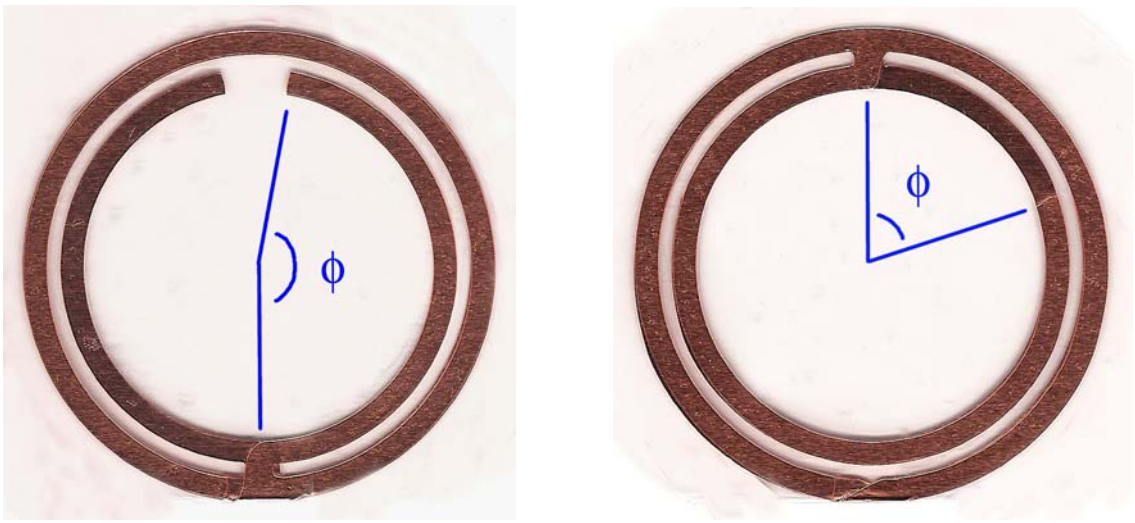

Figure 97. (left) Photograph of design used to study the effect of d_3 variation with d_1=0°, and (right) photograph of design used to study the effect of d_3 variation with d_1=180°.

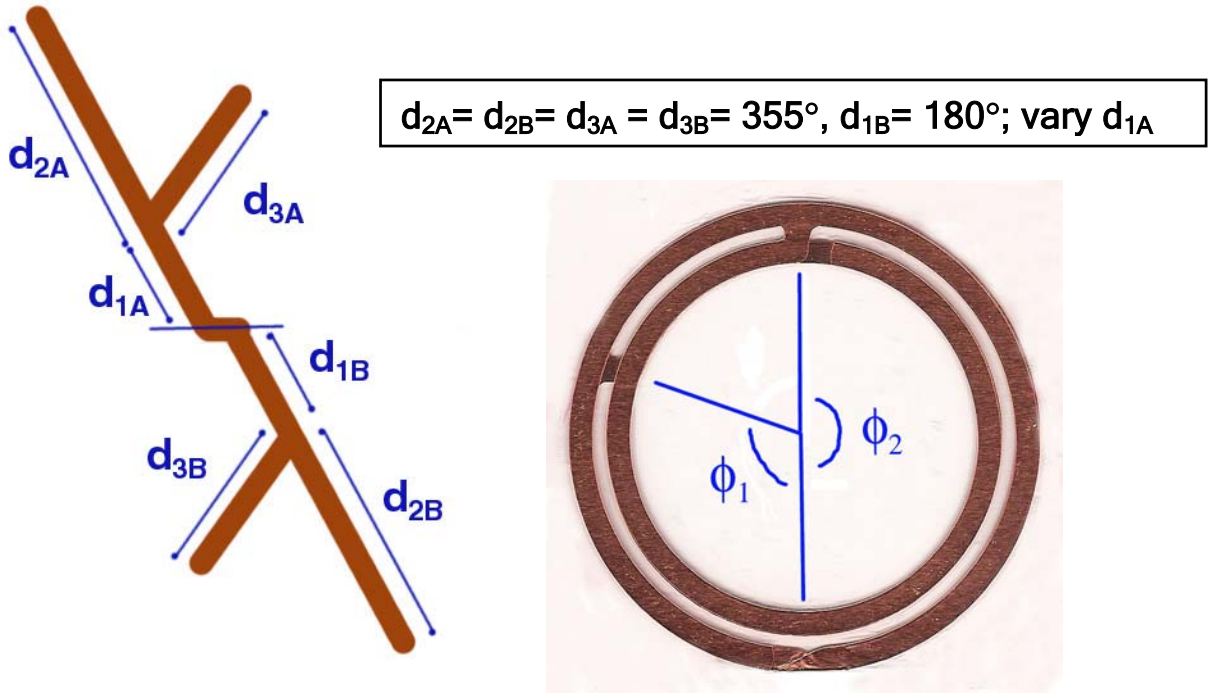

Figure 98. (left) Graphical model used to study asymmetric branch geometries, and (right) photograph of physical implementation used to study the effect of d_{1A} variation.

As shown in Figures 96-98, each of the dimensions of the 2-branch design was systematically varied while keeping the other parameters fixed. Each of the photographs in the Figures represents a set of 30 tags spanning a range of angles from 5° to 355° in equally-spaced intervals.

To my surprised, however, almost none of the tags fabricated for this parameter study exhibited a double resonance. Most tags exhibited a single strong resonance peak with a very weak second resonance. Having systematically varied all the basic dimensions of the 2-branch tag, it was unusual that there was not a single combination of parameters that could produce a strong double-resonance.

5.3.4.5 Inter-Branch Coupling

Given the unexpected result of the 2-branch design parameter study, I studied more carefully the multi-resonant design I had made previously in an effort to discover the basic principles and conditions that enable multiple resonance.

By performing design perturbations around a successful multi-resonant design, it was discovered that a key requirement for multiple-resonance is *inter-branch capacitance*. In addition to capacitive coupling to its "twin" branch on the opposing face of the tag, each branch in the tree structure also needed to be capacitively-coupled to at least one of its neighboring branches. This effect is shown in Figure 99 below for two similar tag designs.

Although it is not completely understood why the inter-branch capacitance is required, it is possible to offer a qualitative explanation. The inter-branch capacitance provides a means of distributing the energy in a tag to other branches and thus enable a richer set of initial conditions to produce resonances in other segments of the tag. As discussed in the previous section on the testing procedure for these tags, it is possible to excite other resonant modes within the tag by placing the tag inhomogeneously in the excitation field. As exhibited by other types of waveguide and resonant structures, it is possible to control and change the modes that get excited by simply changing the coupling parameters and initial conditions. Inter-branch coupling effectively adds greater degrees of freedom to the internal dynamics of the tag by introducing energy into the tag in new ways. Another important role of the inter-branch capacitance is simply to distribute and equalize the energy among the various resonant modes in the tag. This capacitive coupling between branches is thus a means of coupling together different resonant modes of the tag and enabling some of the energy of the stronger resonance peaks to get distributed to weaker modes.

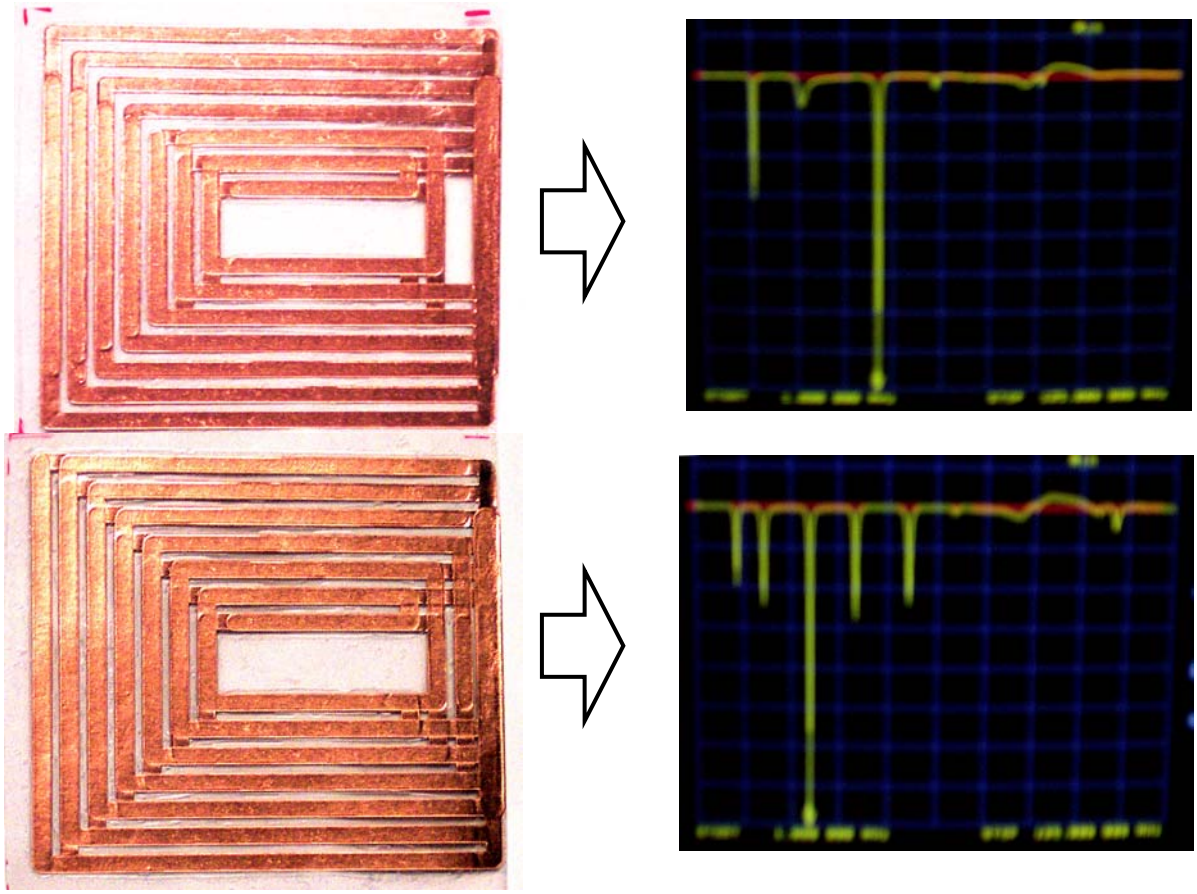

Figure 99. The effect of inter-branch coupling demonstrated for a given multi-resonant tag design. (top) photograph and spectra from tag with no inter-branch coupling (bottom) photograph and spectra from a nearly identical tag with the introduction of inter-branch coupling.

In order to validate the explanation and understanding of inter-branch capacitance, I created a circuit model of the tag itself and proceeded to simulate the response. The circuit model, shown in Figure 100, is a model of a 2-resonance 2-branch structure. The model includes the capacitance between the branches on opposing faces of the tag as well as a small inter-branch capacitance.

The circuit simulation was performed using a high frequency circuit simulation package called Serenade, created by Hewlett-Packard. The results of the simulation are shown in Figure 78. Although such a circuit simulation is insufficient to model the complex electromagnetic interactions within the tag, we can see from the simulation that the addition of inter-branch capacitance does serve to equalize the amplitude of the separate resonance peaks. It would be interesting to perform this simulation on an electromagnetic field simulation software package to better understand the dynamics and distribution of current within the tag.

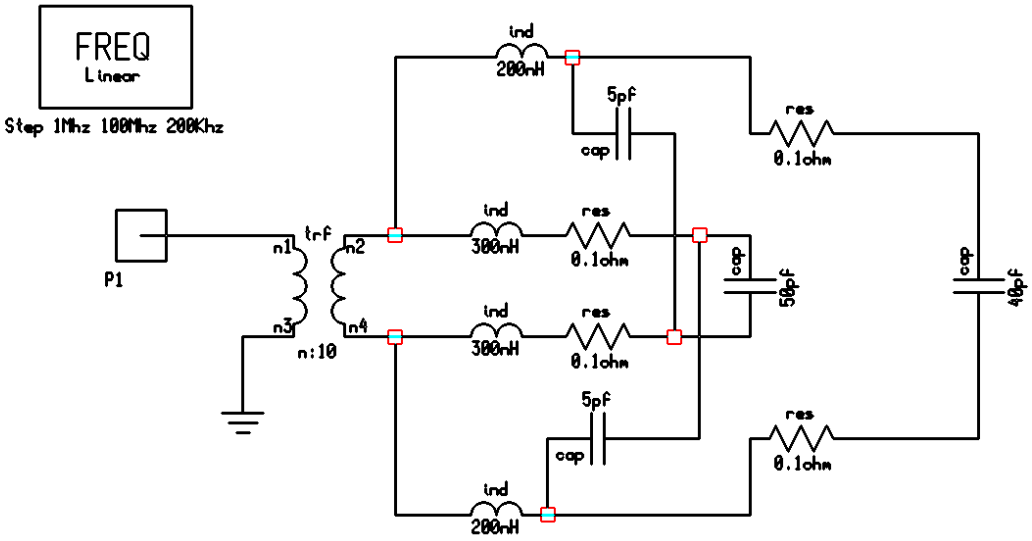

Figure 100. Tag circuit model used to study the effect of inter-branch coupling.

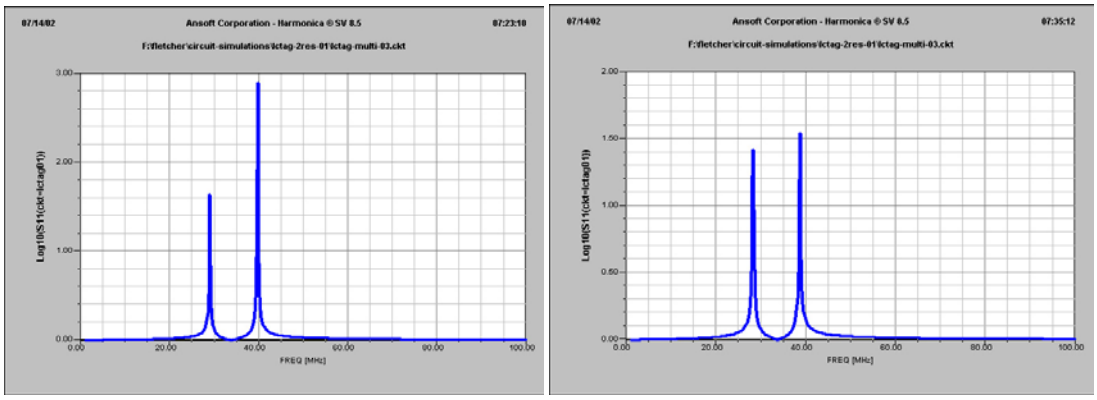

Figure 101. Simulation results for (left) tag with no inter-branch coupling and (right) tag with interbranch coupling.

5.3.4.6 Final Design

After gaining additional insight about inter-branch coupling, I converged on a final tag design that provided good reproducibility, simple design, and strong multiple resonances. In addition, I selected a design that could be easily adapted to other geometric aspect ratios, label sizes, and frequency ranges. The basic design is shown in Figure 102 below.

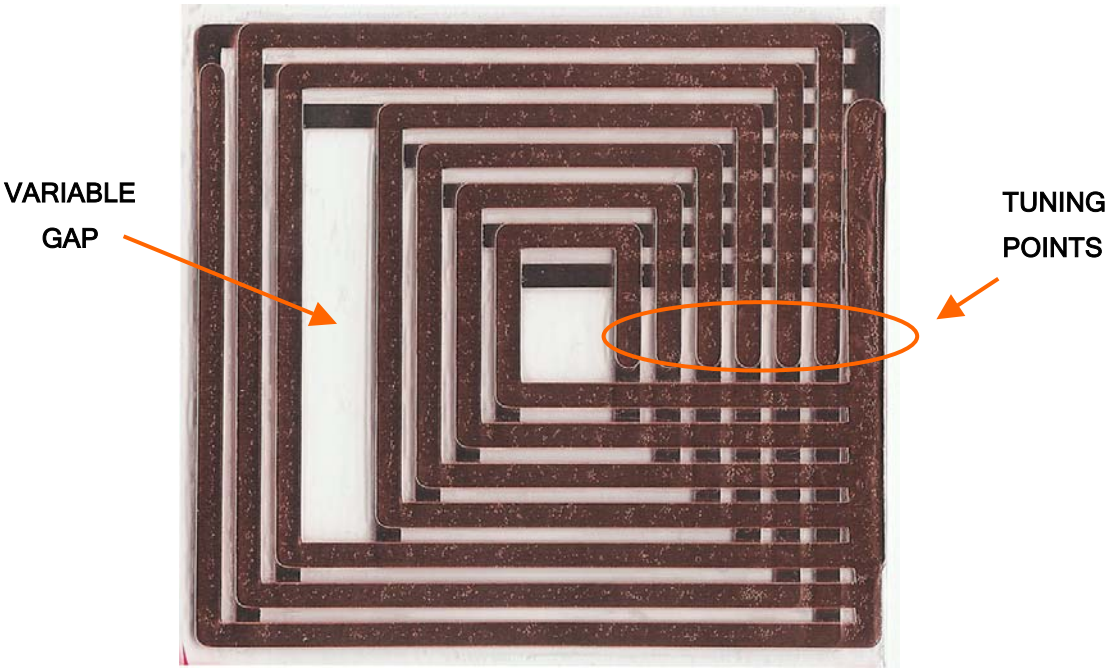

Figure 102. Basic final design for multi-resonant planar LC label.

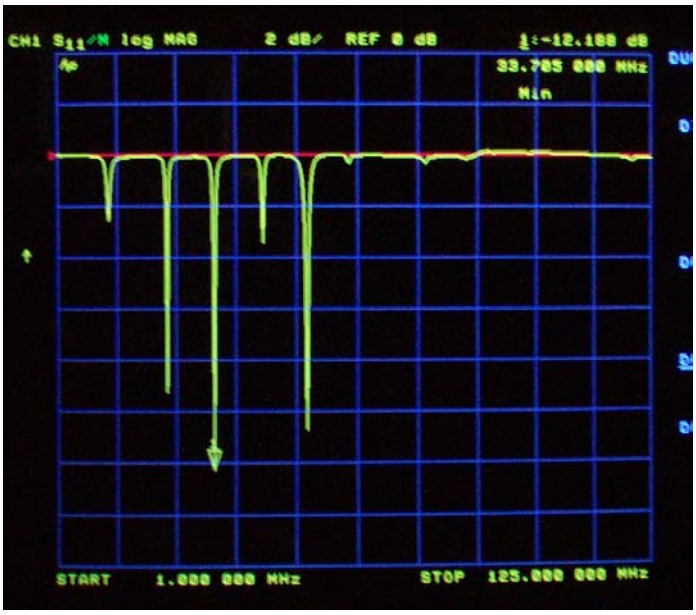

Peak positions:

P1 = 9.81 MHz
P2 = 20.7 MHz
P3 = 29.1 MHz
P4 = 38.7 MHz
P5 = 45.8 MHz

Figure 103. Baseline spectra for proposed design.

5.3.4.7 Peak Tuning

Given a baseline design for the multi-resonant tag, it was then necessary to explore various methods that could be used to tune the individual resonant peaks of the tag in order to enable the encoding of information.

I have separated the various tuning methods into two basic categories: metal layer alterations and dielectric layer alterations. Each of these methods is discussed briefly below.

5.3.4.7.1 Metal Layer

The metal layer comprising the tag can be modified during the time of tag manufacture as well as a means of post processing. As indicated in Figure 46 labeled “tuning points”, the proposed tag design shown contains several convenient locations on the tag where tuning can be implemented. Although there are numerous methods that can be used to alter or modify the individual resonant frequencies, I list below the most fundamental means of tuning the individual resonance peaks. For each method, I list in parenthesis the approximate tuning range of each meth given as a percentage of the resonant frequency.

- Ohmic Tuning (-) -- Each resonance peak can be individually deactivated by severing its connection to the rest of the structure or shorting opposing branches across the dielectric thickness.
- Inductive Tuning (8%) -- It is possible to increase the length of a given branch and adding more turns without overlapping with the metal layer of the opposing face of the tag. This increases the inductance of that particular branch, thus altering its resonant frequency.
- Capacitive Tuning (8%) -- It is possible to vary the amount of overlap between each branch and its corresponding branch on the opposing face of the tag. This overlap can be changed by altering the trace length as well as the trace width.
- Mutual Inductance Tuning (15%) -- Although the all the branches of the tag share the same sheet of metal, the distribution of flux among the different branches of the tag can be varied by shifting the relative position of the individual metal traces. This method can produce significant changes in the relative position of the individual resonance peaks.

5.3.4.7.2 Dielectric Layer

As an alternative to altering the metal layer, it is possible to alter the dielectric layer of the tag in order to tune the resonant frequencies. In general, modification of the dielectric layer is not preferred, since such modifications are less convenient for a high-volume label manufacturing process and thus ore expensive to implement.

- **Thickness (>50%)** -- The thickness of the dielectric has a very significant effect on the resonant frequency. Although it is not practical to controllably vary the dielectric thickness for separate sections of the tag, this method can be used as a means of retuning all the peaks of a given tag design into a different frequency range in order to meet the requirements of label dimensions and tag reader bandwidth limitations, for example.
- **Shorting (-)** -- It is possible to create holes in the dielectric that would produce electric shorts between metal traces on opposing faces of the tag.
- **Metal inter-layer (>25%)** -- Since it is known that the insertion of metal between the opposing plates of a parallel-plate capacitor serves to reduce its capacitance, this technique can also be adapted for use in tuning individual resonance peaks. It may be possible create, for example, a new type of dielectric that contains an embedded patterned metal layer, which effectively functions as a dielectric that has a spatially-varying dielectric constant.

As in any multi-resonant structure, there is a coupling between the individual resonances that limits the extent to which each resonance can be individually tuned. Although several of the tuning methods listed above can produce a significant shift in the resonant frequencies, it is challenging to tune a single resonance without affecting the others. Of the tuning methods listed above, capacitance tuning gave the best results, since the amount of overlap between corresponding branches in the tag cold be varied without changing the other geometric parameters or electrical properties of the tag.

5.3.4.8 Information Coding

Using the proposed multi-resonant tag design with capacitive tuning, the tuning range of the individual peaks was approximately 8%. However, given a manufacturing reproducibility of 2%, the number of tuning positions per resonance peak was limited to n=4. Using the following formula discussed previously, the number of ID bits can be calculated as follows:

$$\#\,\textit{bits} = \textit{Log}_2(4) + \textit{Log}_2(4) + \textit{Log}_2(4) + \textit{Log}_2(4) + \textit{Log}_2(4) = 10 - \textit{bits}$$

As discussed previously in Chapter 3, there are various ways to represent and translate the analog spectrum of a multi-resonant spectra into a usable digital ID code. Perhaps the most compact representation is simply to list the positions of the individual peaks. Using 256 frequency bins analyzed by the tag reader, we can thus assign 8 bits to each peak, resulting in a 40-bit ID bitcode for each label as follows:

$$\textit{Bitcode} = \textit{peakposition}\ \#1 + \textit{peakposition}\ \#2 + \textit{peakposition}\ \#3 + \ldots$$

Given the fact that each peak can only be tuned to 4 distinct positions, only two bits are necessary per tag. However, for the purpose of generality and ease of interpretation, I chose to assign the full eight bit address to each peak.

As a final step in creating a multi-bit electronic ID label, a custom designed tag reader and accompanying PC windows software was used to interrogate individual labels and convert their frequency spectra to an ID code. The tag reader I designed measures reflected power and is described in more detail in Chapter 7. The PC Windows software was initially implemented by Master's student Esa Masood, using the LabView software package created by National Instruments. The Windows interface was later implemented in Visual Basic, which I wrote from scratch and also enabled the PC to execute multiple control functions on the tag reader. Screen shots of these interfaces are shown below.

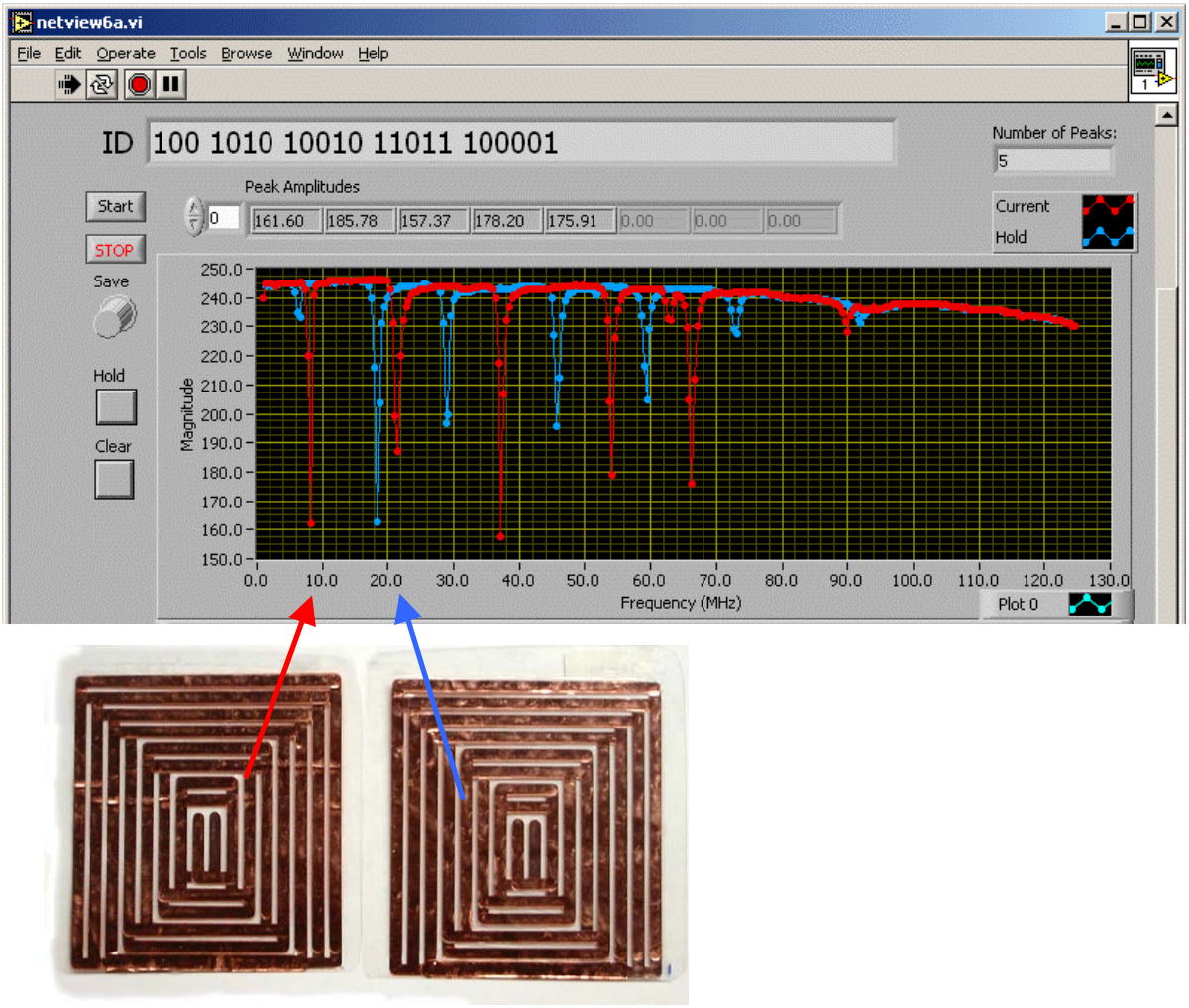

Figure 104. Initial PC windows interface showing spectra for two separate multi-resonant tags.

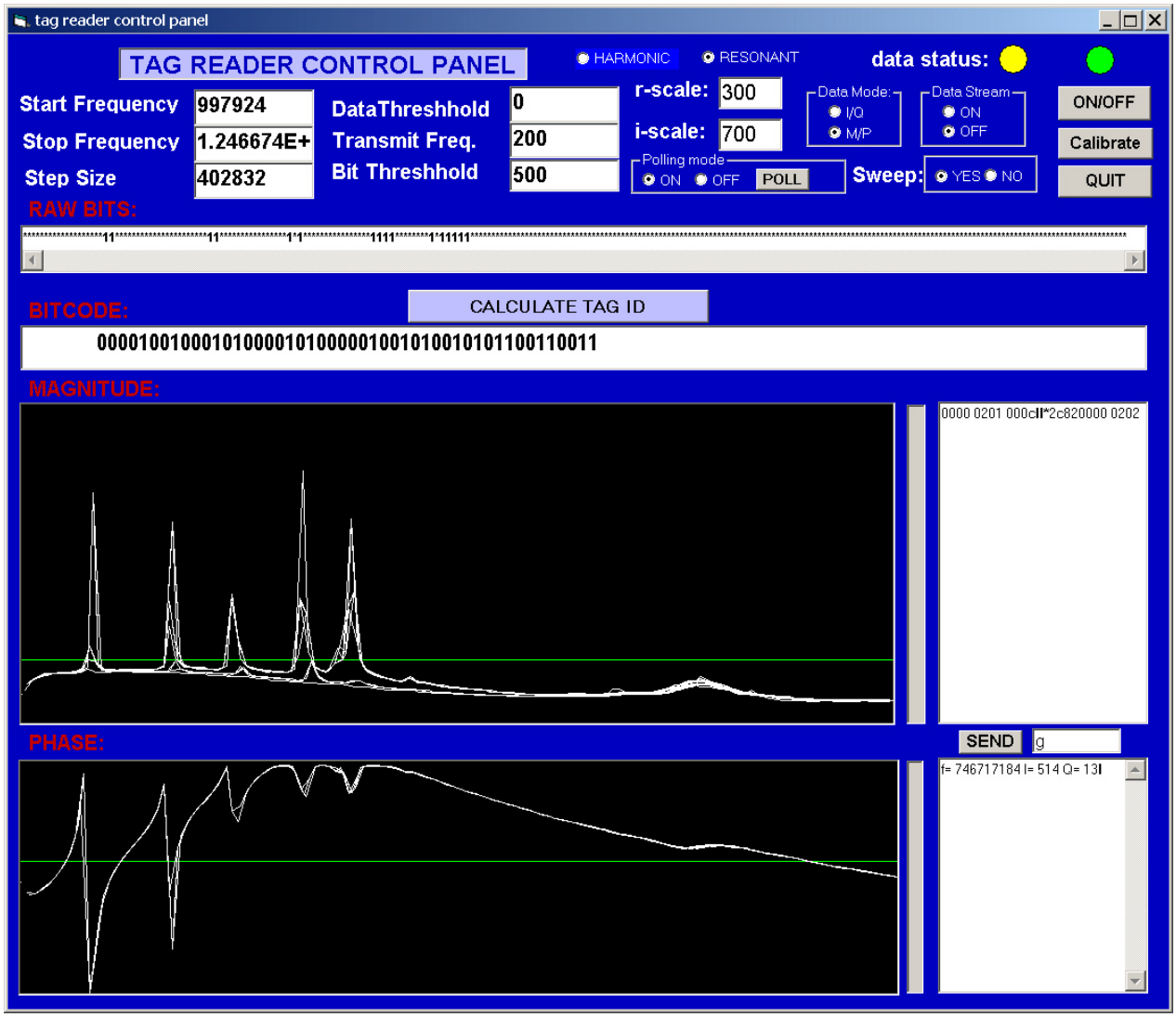

Figure 105. PC Windows interface implemented in Visual Basic showing spectra for a multi-resonant tags and also displaying the raw frequency bin data bits as well as a compact “bitcode” representation

5.3.5 Planar LC Tag Conclusions and Future Work

A 10-bit chipless ID tag has been demonstrated using a multi-resonant planar LC design. A few general observations and guidelines for useful for future designs are given below:

- **Line widths:** Using copper traces, a line width of 80 mils or so was adequate for most purposes. Although increasing the linewidth does increase the Q-factor, above 120 mils or so, there are diminishing returns. Below 80 mils, the effect of linewidth on the Q factor becomes appreciable.
- **Number of resonances:** The is a practical limit to how many resonance can be nested into the same branching structure due to the limited area, flux capture, and shielding effects. The inner branches of the multi-resonant design are necessarily smaller diameter, and thus capture less flux resulting in a smaller amplitude resonant peak. In addition, there is a smaller effect due to the shielding of the outer turns on the inner ones. For a tag the size of a business card (2.5" X 3"), the practical limit of the number of resonances using this design is approximately 5-8, depending on the line width chosen.
- **Distributed capacitance:** The distributed capacitance enables a more efficient use of the tag area; however excessive capacitance limits the Q-factor and limits the number of coil turns that are possible for a desired resonant frequency. A promising solution to this problem is to limit the amount of distributed capacitance by employing *partial* overlap between coil layers. This preserves the useful features of a distributed capacitance tag while increasing performance to that of a traditional lumped capacitance tag design.
- **Read range:** For the multi-branch tag design employed here, it is important to keep in mind that there is a crucial trade-off between the number of resonances and the read range of the tag. At short read ranges, the tag signal is most limited by the Q-factor, and thus this mode of operation is well-suited for this design (which has relatively high Q). At long read ranges, however, the tag signal is more limited by the coupling factor (derived from the mutual unductance). Increasing the coupling factor required a greater number of coil turns, which in turn limits the number of branches that can fit within a given tag area.

It is clear that many more bits of ID are theoretically possible, given the amount of intrinsic tuning range for the resonances produced as well as the operating frequency range of the tag reader. The primary challenge in achieving the full information capacity for this tag design is the ability to predict the resulting resonant frequencies as a function of tag geometry. Although such calculations are not possible analytically, it may be possible to create a mode chart for such structures similar to those used for designing microwave cavity resonators and dielectric resonators, as shown in Figure 106 below. This chart can be generated numerically through the use of electromagnetic field solvers or may be derived empirically by recording the data for a

large number of tags and plotting it on appropriate axes. In general, better design tools for chipless RFID tags can be a great aid to further development of this research field.

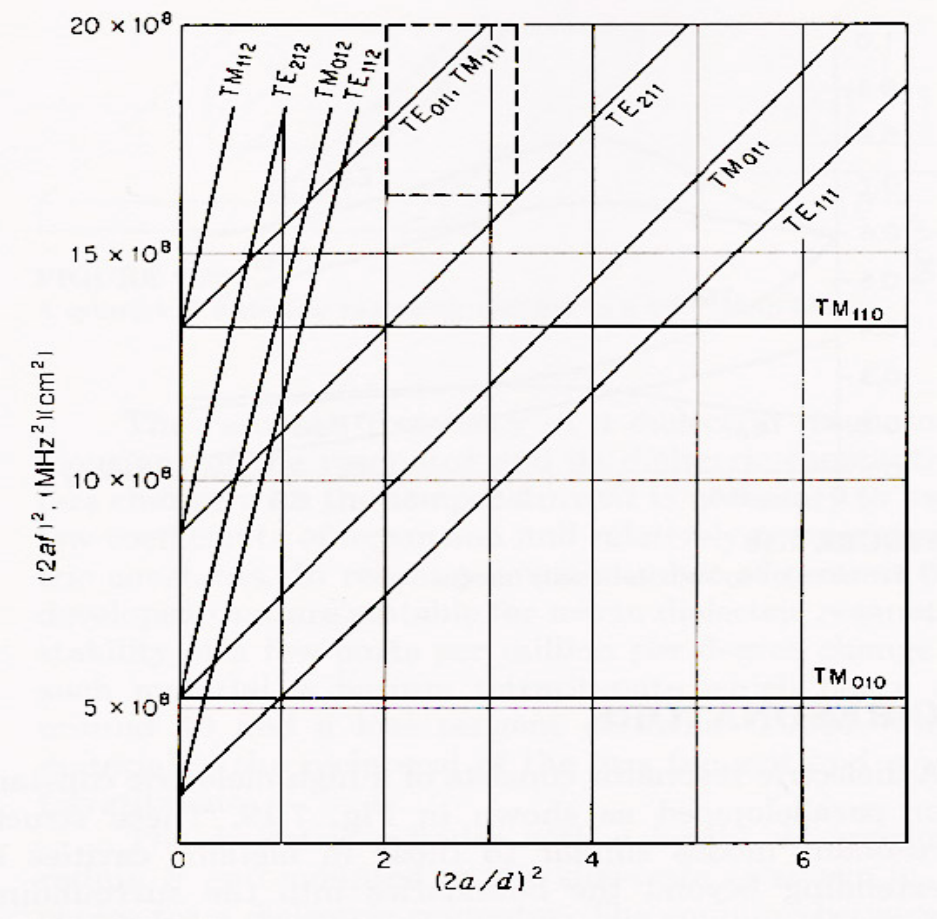

Figure 106. Mode chart for a cylindrical cavity with height **a** and diameter **d**.

CHAPTER VI.

Chipless Tags as Sensors

6.1 Introduction

In many modern technological applications, ranging from manufacturing to smart homes to medical devices, there is an increasing need for sensors. Furthermore, large-scale deployment of sensors for the consumer and industrial markets requires that the sensors be cheap – perhaps even disposable. Chipless sensors make this possible.

Although RFID tags with integrated sensors have existed for some time for military intelligence applications as well as for wildlife radio tagging, it was not until the 1990's that RFID tags with integrated sensors have become commercially available, primarily as a result of tire and automotive applications. By creating new classes of sensors based on chipless RFID technology, sensing capability can now be integrated into new high-volume low-cost products such as smart packaging materials.

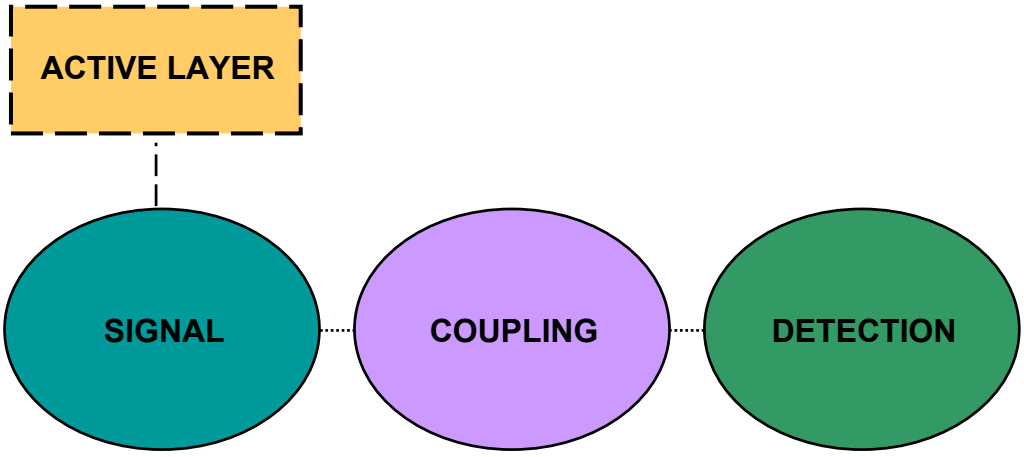

Figure 107. Sample response from a tag containing five resonators of different frequencies and frequency bins illustrating simple spectral encoding scheme.

6.2 Basic Design Principles

The operation of a chipless electromagnetic sensor can be described by the basic tag model with the addition of an active layer that serves to modulate the tag signal in response to a local stimulus (e.g. heat, light, pressure, etc.). The modulation provided by the active layer can be in the form of a frequency shift, amplitude change, phase shift, or time delay, for example, that is a function of the external stimulus. This modulation is then interpreted and translated by the tag reader into meaningful sensor data.

The following are basic considerations in the design of a chipless RFID sensor:

- **Choice of sensor material:** Materials whose electromagnetic properties are strongly coupled to other physical properties are informally known as *smart materials*. In choosing a smart material for use as the active layer, it is important to consider the efficiency of the electromagnetic and mechanical coupling between the active layer and the signal layer of the tag in order to optimize the response and prevent attenuation of the tag signal. In addition, it is very important to consider the operating conditions of the tag and other environmental factors that may affect the tag response. If the goal is to detect a particular stimulus, a sensor is not very useful if it also responds to everything else; this criterion is known as *specificity*, and is controlled by proper materials engineering and also packaging of the tag (mentioned below).

- **Geometry:** The electromagnetic response of the tag and sensor material is affected by the geometric design of the tag. An understanding of the physical mechanisms and electromagnetic fields of the tag helps to guide the optimum placement and size of the sensor material. In some cases, a small amount of sensor material placed in a region of high field concentration can produce better results than using larger amounts of sensor material across a larger section of the tag.

- **Packaging:** In the process of packaging or label conversion, it is important to know both the electromagnetic and mechanical properties of the materials used. At the very least, the substrate or packaging materials must not attenuate the tag signal. However, the packaging material can also be used to enhance tag performance. The design of the sensor tag packaging can be used to concentrate the electric or magnetic field, and it can also be used to shield or isolate unwanted external stimuli that can interfere with the performance of the sensor material for its intended purpose, such as mechanical stress of thermal heating.

6.3 Data Coding for Chipless Sensors

Chipless sensors have been successfully implemented using each of the major chipless technologies, including SAW tags, harmonic magnetic materials, and resonant structures. Of these, the LC resonator is perhaps the easiest to adapt for sensor applications, and can be measured with relatively high precision.

For a resonant sensor implementation, it is generally best to encode the sensor data in the resonant frequency. The primary reason for this is that the resonant frequency is independent of energy losses in the tag and independent of coupling losses. Therefore the resonant frequency shifts can be directly attributed to the sensor element in the tag and is not affected as the tag is moved relative to the reader antenna. In addition, the measurement of frequency is relatively easy to implement in hardware with the use of frequency counters or a digital synthesis.

Sensor data can also be encoded in the Q-factor of a resonator by providing a means of degrading the Q via an external parameter. However,the reciprocal of Q is proportional to the existing dissipative loss mechanisms in the resonator; therefore the maximum Q is limited by the minimum loss in the system. Since the *measured* Q also depends on losses external to the resonator, including the effect of antenna coupling, Q is an unreliable parameter for encoding information unless all external losses, coupling, and geometry are known; in addition, a lower Q will also reduce the tag signal and affect the read range of the tag. Certain *wired* sensor devices, such as accelerometers, contain mechanical resonators and may use Q as a sensor parameter; however, for wireless sensors, the measurement of Q is less reliable.

6.4 Temperature Sensors Based On Magnetic Materials

One common category of sensors is temperature sensors. These sensors are commonly in demand for many types of automated processes such as manufacturing, control, or inspection. For many applications it is not convenient or not possible to attach wires to the desired measuring point; furthermore, it is often not economically feasible to employ radio circuitry. In other applications, such as the shipment of refrigerated food or medication, it is desirable to have an embedded temperature sensor that can detect and record if the item was exposed to high temperature during shipping. For this need, I have developed a family of chipless temperature sensors for a variety of such applications that can be interrogated wirelessly and are sufficiently low-cost to be disposable.

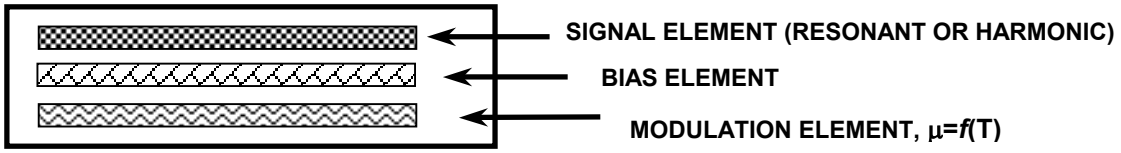

Figure 108. **Structure of temperature sensor**

6.4.1 Basic Elements

As pictured in Figure 1, the temperature sensors investigated are comprised of three basic elements: the signal element, a bias element, and a modulation element, stacked in a 1cm X 3cm X .5cm package. The signal element consists of either a square-loop soft magnetic material which produces detectable harmonics, or a magnetoelastic material [1] which has a detectable resonance frequency. The bias element is a thin strip semi-permanent magnet material (such as Arnokrome 3, made by Arnold Engineering), and the modulation element is a magnetic material with a Curie temperature near the operating temperature for a given application. The magnetization spectrum of these sensors can be detected over a distance of several inches or more through the use of an interrogation coil and active electronics similar to those used for anti-theft tags in libraries and retail shops.

The modulation element implemented for this study was a 29.5/70.5% Ni-Fe alloy in the form of a 30mm X 10mm X 1mm thin strip. Using a DMS vibrating sample magnetometer, the Curie temperature for this material was measured to be approximately 70°C. By varying the nickel content over the range 28-80%, it is possible to achieve other Curie temperatures in the range of 30°C - 540°C.

6.4.2 Type 1: Non-Reversible Temperature Threshold Sensor

A temperature threshold sensor was constructed using a harmonic signal element (FeNiCoBSi amorphous wire) and a weak bias element producing a bias field of 40 Oe at room temperature (21°C). The amplitude of the applied AC interrogation field was approximately 25 Oe and less, depending on the distance between the sensor and the interrogation coil. Since the amplitude of the interrogation field was less than the local sensor bias field, the amorphous wire could not be driven to reverse its magnetization, and no harmonics were observed. As the temperature was increased near and beyond the Curie temperature of the bias element, the vanishing local bias field enabled harmonics to be observed. Upon cooling the sensor to room temperature, the harmonics remained. Since this mechanism is non-reversible with temperature, a sensor of this type, with the appropriate bias element, would be useful for identifying food or medicine containers that have been exposed to high temperature during shipping.

6.4.3 Type 2: Reversible Temperature Threshold Sensor

By combining a harmonic element (FeNiCoBSi amorphous wire) with a modulation element (Ni-Fe strip), it was possible to create a temperature threshold sensor that is reversible. At low temperatures (20°C), the Ni-Fe strip has a measured initial permeability μ=43, which served to shunt the magnetization of the amorphous wire and attenuate the harmonics. In raising the temperature to 80°C, strong harmonics emerged, as explained by the low (μ<5) permeability of the Ni-Fe strip at this temperature. Upon cooling the sensor, the harmonics diminished once again as the permeability of the Ni-Fe increased (see Figure 2). This process was repeatable. Such a sensor could find potential use in applications that employ repeated temperature cycling.

6.4.4 Type 3: Continuous Readout Temperature Sensor

If a magnetoeleastic strip ($Fe_{35}Ni_{33}Co_{19}B_8Si_5$ amorphous ribbon) is used as the signal element, its resonant frequency is a function of the local DC bias field. By employing a bias element with a Ni-Fe shunt, it was possible to generate a temperature-dependent local bias field on the magnetoelastic strip. Thus, the temperature of the sensor could be continuously monitored by tracking the resonant frequency signal of the sensor. The measured curve is shown in Figure 3. Over the temperature range 20°C-70°C, a significant frequency shift of 4% was observed. Given the sharp resonance peak of the magnetoelastic resonator (Q>100), through proper mounting of the magnetoeleastic strip and a simple frequency measurement (+/- 100 Hz), a temperature accuracy of 2°C could be readily achieved. It is possible to make sensors which operate at other temperature ranges by choosing a Ni-Fe composition with the appropriate Curie temperature.

[1] Kim, C.K., O'Handley R.C.; Metallurgical & Materials Transactions A – Physical Metallurgy and Materials Science, vol. 27A, No.10, Oct. 1996, pp. 3203-13.

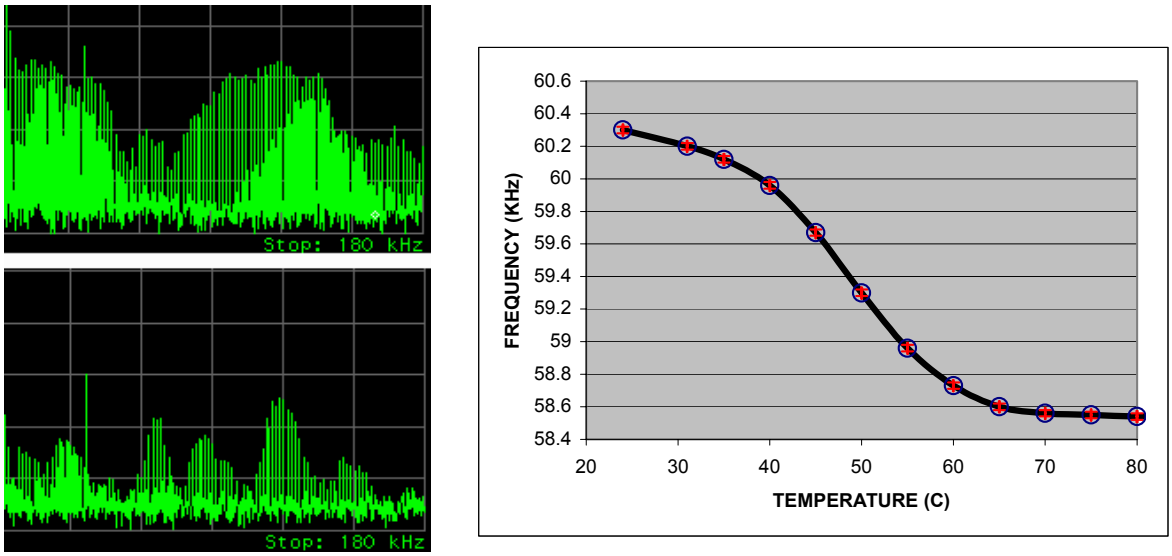

Figure 109. Results for temperature sensor Type 2 (data for Type 1 is similar). (top) harmonic spectra at 80°C. (bottom) harmonic spectra at 20°C

6.5 Force Sensor

Most force sensors on the market today function as variable resistors, whose electrical resistance is a function of the applied force or pressure. Unfortunately, the response of these devices is relatively noisy and hysteretic. Much of this is due to the fact that these devices do not rely on an intrinsic microscopic property of the sensor material, but instead rely on an average macroscopic response of the sensor structure. A typical resistive force sensor makes use of the effective resistance of the sensor structure, which can be comprised of conducting particles in a semi-insulating matrix, or layers of conducting cilia-like structures (see Figure 110). As these structures are compressed, their resistance decreases due to decreased percolation threshold (in the particle case) or increased connectivity (in the cilia case). Because the effective resistance of these structures is an average of a finite number of discrete distributed conducting pathways, their resistance is not a smooth function of the applied force. This is particularly noticeable when trying to resolve small changes (e.g. $\leq$ 5%)in the applied force. As one might expect, it is also difficult to make a very thin (< 1mm) force sensor of this type which has good resolution as well as a high dynamic range (e.g. .01-10 Newtons).

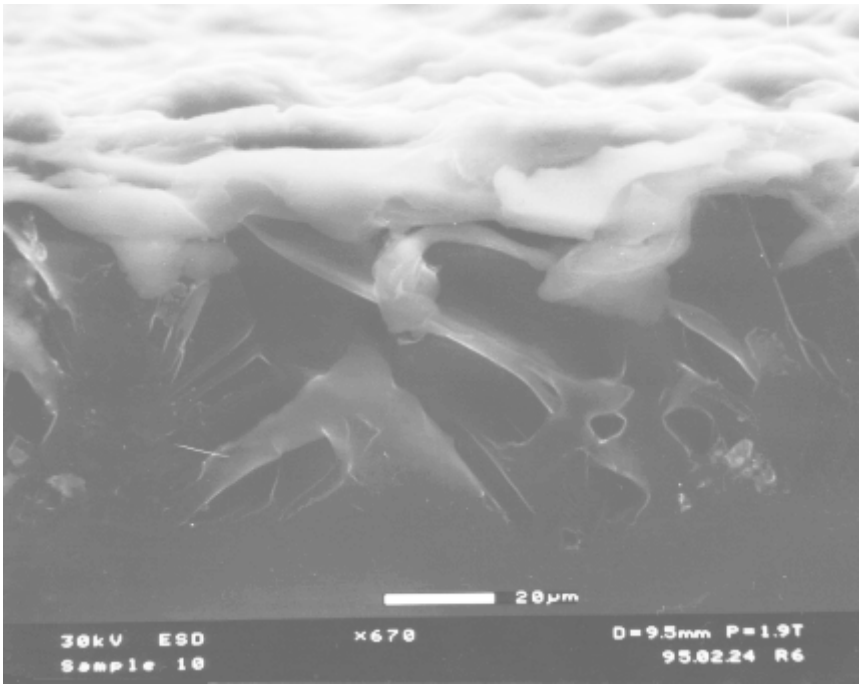

Figure 110. SEM cross section of an force sensor made by Interlink, Inc. showing a metallized layer over a bed of conductive elastomer cilia-like structures. As the material is compressed, the increased interconnection within the material structure increases the number of conduction paths and reduces the electrical resistance of the structure. On this microscopic scale, it is easy to see why the electrical resistance is not a smooth continuous function of the applied force.

In order to demonstrate the use of a electromagnetic resonator as a wireless force sensor, a planar LC resonator was fabricated, using a force-sensitive dielectric. Although the obvious approach might be to insert a compressible elastomeric foam between the capacitor places, we wanted to make the sensor as thin as possible, so a piezoelectric polymer was used as the dielectric. The two-coil planar resonator was designed and etched from copper clad 1000K120 Kapton made by Rogers. The two coils were then folded upon each other, with a 25mm dielectric placed between the two layers. The dielectric region was comprised of either teflon sheet or the piezoelectric polymer polyvinyldifluoride (PVDF), supplied by AMP, Inc. The structure was then epoxied under vacuum or laminated to seal the dielectric between the layers.

The performance of the sensor tag was evaluated using an Instron 4411 mechanical tester and the HP network analyzer (see Figure 111). The sensor tag was placed over a 2" diameter sapphire base containing a loop antenna. The whole assembly was placed onto the lower anvil of an Instron machine. On top of the coil assembly, a 3" x 3" x 3" cube of non-conducting foam was placed between the sensor tag and the top anvil. Both the network analyzer and Instron press were connected to a PC via a GPIB interface. The Instron was programmed to apply a load in increments and output both the applied load and displacement from the origin. The resonant frequency and Q-factor for of the sensor tag was simultaneously recorded. These numbers form

the basis for the data. The specific force sensor demonstrated in this paper is designed to have a sensing range similar to a human finger, so an applied load range of 0-5 Newtons was chosen

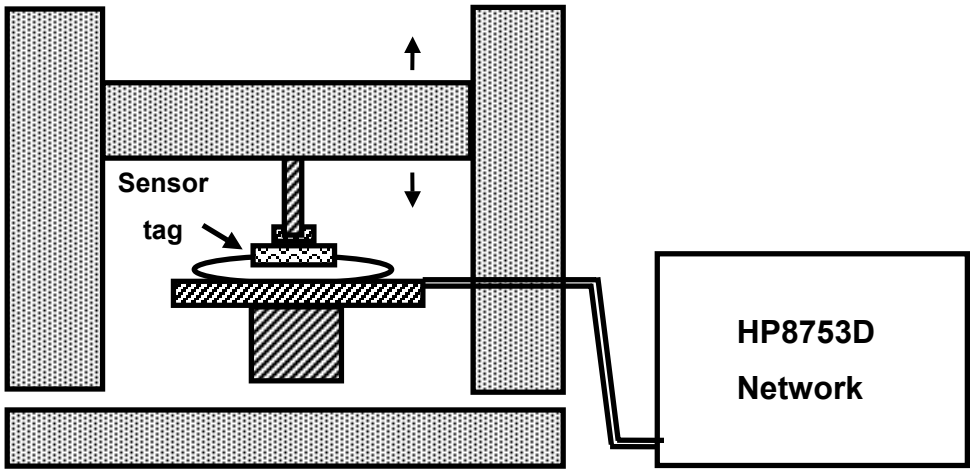

Figure 111. Schematic diagram of the test apparatus for testing the force sensor.

The resonant frequency response of the planar tank circuits with PVDF dielectric was compared to that of tags containing Teflon, a conventional high-frequency dielectric. Results are plotted in Fig 26.

For the resonator containing the normal dielectric, its response can be modeled as a simple LRC-circuit composed of an inductor, resistor, and plate capacitor with a dielectric material. By applying an elastic model to the deformation of the dielectric material under applied stress, the resonant frequency of the tag can be derived as a function of applied stress:

$$\omega_n = \omega_{n_0} \cdot \sqrt{\frac{E-\sigma}{E}} \quad \text{(Eq. 63)}$$

where ω_{n_0} is the resonant frequency of the tag absent any applied stress, E is the Young's Modulus of the dielectric material, and σ is the applied stress. Rearranging Eq. 63 yields an expression relating the ratio of the change of resonant frequency versus initial resonant frequency and the induced strain, ε, in the dielectric material:

$$\frac{\Delta\omega}{\omega_{n_0}} = 1 - \sqrt{1-\varepsilon} \qquad \text{(Eq. 64)}$$

The measured data and the curve predicted by this model is included in Figure 26 and very closely matched the measured data to within 0.1%.

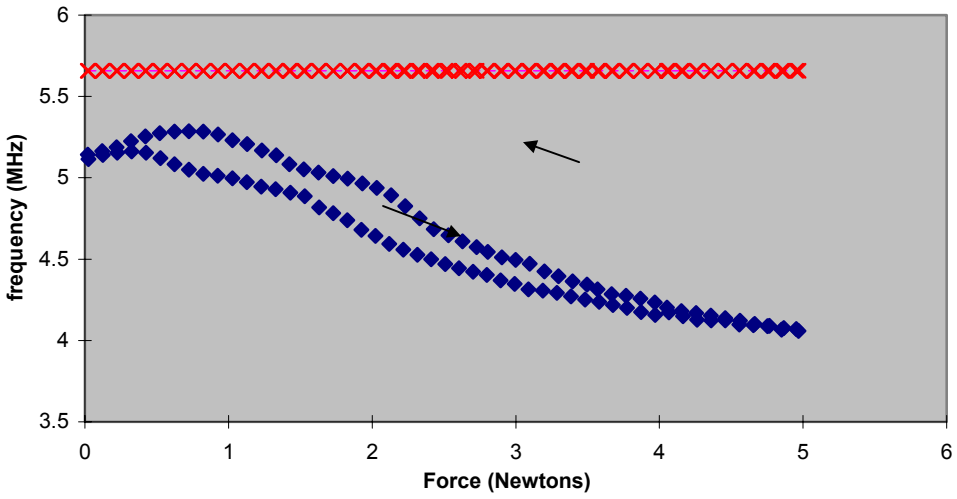

Figure 112. Data for wireless force sensor incorporating a piezoelectric polymer dielectric (lower curve). The upper curve is the response of an identical resonant structure incorporating a normal dielectric material (teflon), which appears nearly flat when plotted on this scale.

In comparing the teflon response to the response produced using PVDF, this model indicates that in a typical dielectric material with Young's Modulus of about 3 GPa (comparable to PVDF and clear teflon sheet), a 10% change in frequency would occur when there is a strain of 19%. Further manipulation of equation (2) shows that in order to produce in a 10% change in the resonant frequency of the tag, a force of 60000 Newtons would need to be applied to the tag. On the other hand, the tag incorporating the piezoelectric material shows a significant response with an applied force of as little as 0.1 Newtons. A theoretical curve (not including hysteresis) could be derived for the piezoelectric response by solving the coupled tensor equations:

$$\begin{aligned} \varepsilon E &= \varepsilon_T E + dT \\ S &= dE + s^E T \end{aligned} \qquad \text{(Eq.65)}$$

where, E is the electric field, T is the mechanical stress, d is the piezoelectric coefficient, ε is the complex permittivity at zero stress, and s^E is the mechanical compliance at zero field.

The primary advantages of the PVDF force sensor tag are its small thickness (< 0.5 mm) and good sensitivity to small forces. The main apparent disadvantage of this sensor is hysteresis. Piezoelectric materials are intrinsically hysteretic, but their response is repeatable. Some hysteresis, however, can be partially attributed to the packaging of the PVDF and thus can be improved with better packaging design. This type of sensor has also proven to be quite

robust, and continued to perform with no noticeable degradation in sensitivity even after subjecting this force sensor to abuse, such as stepping on it or striking it with a hammer. We also estimate that the manufacturing cost of such a sensor could be less than $0.05.

6.6 Humidity Sensor

Another interesting structure that can be made from a planar LC resonator and piezoelectric polymer is a humidity sensor. The test design for this structure consisted of a single planar coil with connection to an opposing electrode forming the opposite plate of the capacitor. The piezoelectric polymer between the capacitor plates was sized to protrude slightly from the edges of the capacitor and exposed to the ambient environment. A rigid substrate was used for the sensor to avoid piezoelectric effects due to flexure. A simple sketch of the structure is shown in Figure 113.

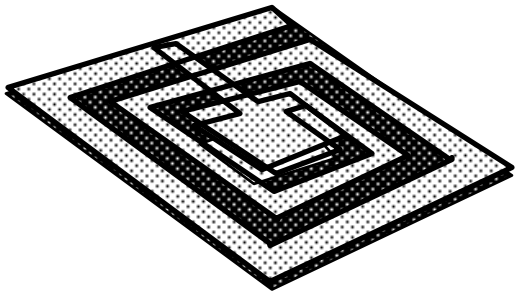

Figure 113. Sketch of the humidity sensor, showing planar LC resonator with piezoelectric polymer dielectric.

Quantitative evaluation of this sensor has yet not been completed, but the empirical results look very promising. Breathing on the sensor produces a positive frequency shift on the order of 10% and the sensor response appears smooth and repeatable. If a hand is held over the sensor, the sensor exhibits a frequency shift of several percent simply from the humidity emanating from the palm of the hand. It was originally thought that the sensor response was thermally activated, but upon further evaluation using a variable temperature chamber, hot plate, and application of different gas environments (dry helium vs. humid air), the sensor exhibited no thermally-induced frequency shift greater than the expected shift from thermal expansion. It is currently suspected that the humidity induced frequency shift is due to a surface charge effect at the edge of the capacitor which produces a humidity-dependent leakage across the plates thus reducing the effective capacitance. The observed 10% frequency shift corresponds to a 20% change in the capacitance and is consistent with this explanation given the dimension of the capacitor plates and the theoretical contribution of the edges to the capacitance

$$C = \frac{\varepsilon A}{d}\left[1 + \frac{\ln(\pi a / d)}{\pi a / d} + \frac{\ln(\pi b / d)}{\pi b / d}\right] \qquad \text{(Eq.66)}$$

where a and b are the transverse dimensions of the plates, and d is the spacing between the plates. From this equation, we see that the edge effects become increasingly important to the disctibuted capacitance as the dimensions of the plate and the linewidths decrease.

6.7 Linear Position Sensor

It is currently a challenge to wirelessly measure the linear position of a piston within a cylinder. In manufacturing applications, currently technology consisting of a magnet and hall-effect sensor cannot measure continuous position but only detects when the piston has reached a certain position range. As a possible solution to this problem, we designed a simple displacement sensor using a magneto-mechanical resonator for the purpose of measuring the linear position of a piston in a small cylinder (10cm long). A strip of amorphous metal ribbon packaged in a plastic cavity was attached to the body of the cylinder. Additionally, a weak flat bias magnet made of Arnochrome 3 ™ of ~ .5 Oe or so can be included with the ribbon to provide a small constant bias field; however, for simplicity this additional magnet was not used for this study. The magnetoelastic ribbons used were amorphous alloys manufactured by Allied Signal and prepared in a width of 1.2cm and length of 3.55 cm. A properly oriented permanent magnet was attached to the end of the piston, thus providing a bias field to the ribbon which varied with linear position of the piston but did not vary with azimuthal rotation of the piston shaft (Figure 114).

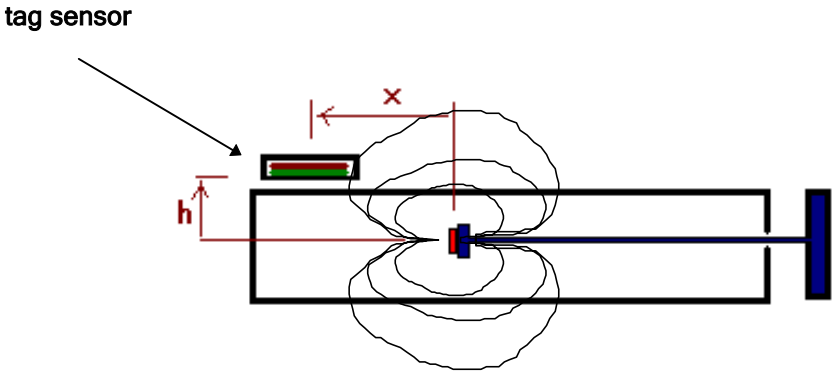

Figure 114. Schematic view of cylinder with position sensor, showing the magnetic field lines emanating from the permanent magnet mounted on the end of the moveable piston.

Since the resonant behavior or the ribbon depends on the bias field as well as its material properties, the linear position of the piston could then be deduced by tracking the resonant frequency of the ribbon. The basic conceptual approach is illustrated in Figure 115. The dependence of the local bias magnetic field presented to tag as a function of piston position could be varied by changing the mounting position of the tag on the cylinder; and the resulting resonant frequency shift resulting from this field could be also be tuned independently through annealing treatments of the amorphous metal ribbon.

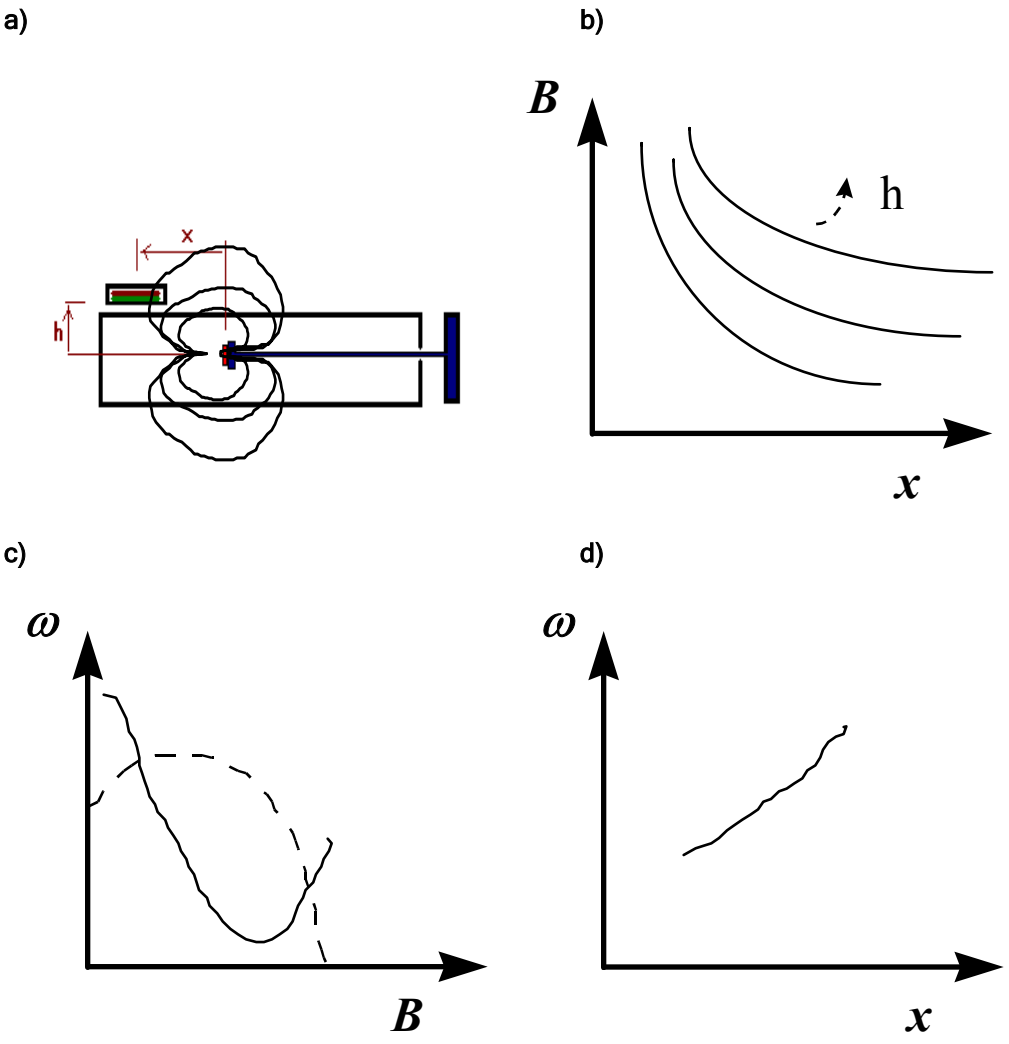

Figure 115. Illustration showing the basic concept of the position sensor. a) illustration of cylinder configuration (same as Figure 114) b) the magnet field measured at the position of the sensor as a function of the linear position of the piston. c) data showing how the sensor frequency (solid line) and amplitude (dotted line) vary as a function of the applied magnetic field. d) sample data showing how the resonant frequency of the sensor varies as a function of the piston position.

In order to increase the linear distance over which the sensor could operate, a preliminary annealing study was carried out to investigate the optimum processing parameters for the ribbons that were tailored to this application. Since it was desirable to increase the usable range of bias fields, a slightly sheared M-H loop is desirable, so a transverse-field anneal was used. Samples of composition $Fe_{38}Ni_{39}Mo_{2.4}B_1Si_{0.2}$ were annealed at a temperature near 400 degrees Celsius using several different annealing fields. A second alloy used for this study was $Fe_{35}Ni_{33}Co_{19}B_8Si_5$, which was annealed by Sensormatic using another recipe.

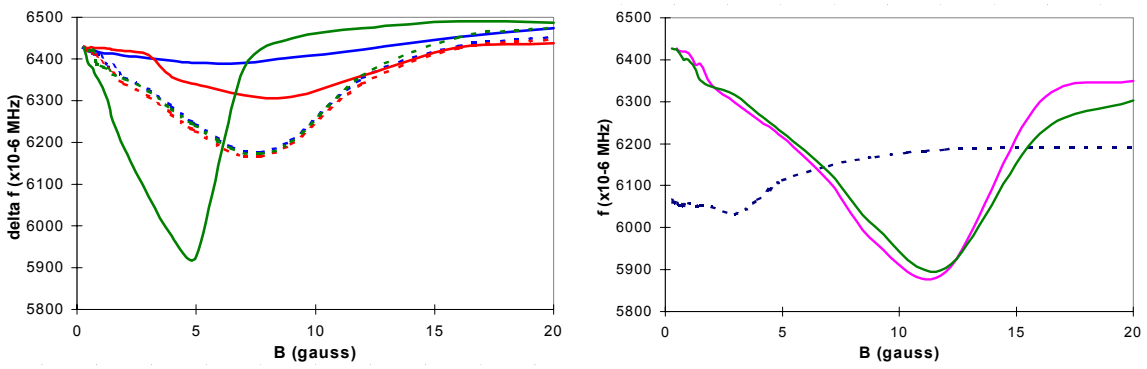

Figure 116. Bias-field dependence of the resonant frequency as a function of annealing treatment. On the left is data for $Fe_{38}Ni_{39}Mo_{2.4}B_1Si_{0.2}$ for transverse annealing fields of 0, 200, 300 Oe. (curves for higher fields are flatter) On the right, is the result for $Fe_{35}Ni_{33}Co_{19}B_8Si_5$ after the Sensormatic annealing treatment. Dotted lines denote pre-annealed as-cast result.

The resonant frequency shift as a function of an applied DC bias field was then measured using an Hewlett-Packard 8753D Network Analyzer. A representative sample of the measured data is shown in Figure 30. For $Fe_{38}Ni_{39}Mo_{2.4}B_1Si_{0.2}$, we suspect the annealing temperature was slightly higher than optimum, as exhibited by the extra degree of flattening in the curves likely due to partial recrystallization of the amorphous metal.

One sample of each type of amorphous metal sample was selected for use as the sensor tag and mounted on the cylinder. The resonant frequency of each tag was then recorded as a function of the piston position. The results are shown in Figure 31.

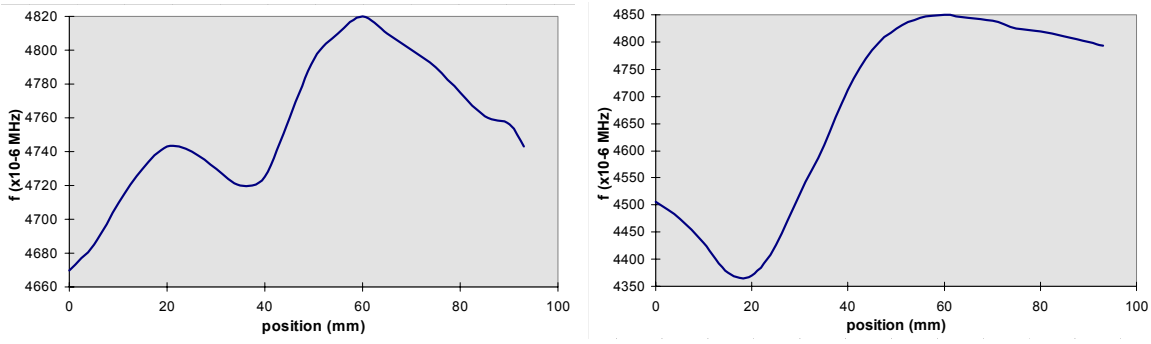

Figure 117. Plot of tag frequency vs. piston position for $Fe_{38}Ni_{39}Mo_{2.4}B_1Si_{0.2}$ (left) and $Fe_{35}Ni_{33}Co_{19}B_8Si_5$ (right).

As evident from the Figure, the usable sensing range was approximately 2 cm (from x = 40 mm to x = 60 mm) for $Fe_{38}Ni_{39}Mo_{2.4}B_1Si_{0.2}$, and was approximately 4 cm (from x = 20 mm to x = 60 mm) for $Fe_{35}Ni_{33}Co_{19}B_8Si_5$. By further optimizing the placement of the sensor tag as well as the strength of the permanent magnet used, it should be possible to extend the usable range of operation to 8 cm or more for a cylinder of this size (10 cm long). For a larger size cylinder, the design can be scaled up using a larger size magnetoelastic ribbon; or for very long cylinders, separate tags can be used along the length of the cylinder to track the piston position along the entire length of its stroke.

6.8 pH sensor

Emily Cooper

CHAPTER VII.

Tag Reader Instrumentation

Figure 118. Photograph of a variety of electromagnetic tags, photographed to scale, including both EAS and RFID labels.

7.1 Introduction

The preceding chapters described the operation of various types of electromagnetic tags, many of which are pictured in Figure 38 above. The increasing need for object-based information has made electromagnetic identification attractive for many uses, and new varieties of this ID technology appear every year. But although Radio-Frequency Identification (RFID) technology has existed for almost 20 years, there is yet no single data standard for either retail or industrial applications. In addition to the cost per label, the lack of a clear data standard has also been a factor limiting the widespread use of RFID.

For the most part, Electronic Article Surveillance (EAS) labels have existed independently of RFID. However, the benefits of increased automation and real-time inventory data have been incentives for manufacturers to integrate electromagnetic tags with RFID and EAS capabilities into product packaging in the same way that barcode UPC codes are created today. Such a uniform approach to electromagnetic tagging is an attractive concept, but will require significant development in the identification information infrastructure.

While the tag industry is still evolving with many competing technologies, it is prudent to consider the evolution of the detector (tag reader) as well as the label (tag). While retailers and manufacturers struggle to integrate bar code, EAS, and RFID systems in a comprehensively useful manner, much of the burden and risk in committing to a particular form of technology can be alleviated by developing an infrastructure that is flexible and can seamlessly support multiple tagging technologies. This is the basic concept of an open architecture for electromagnetic tagging.

7.2 Basic Requirements

The fundamental function of a tag reader is to transmit energy to a tag, to detect the response of the tag, and to translate the resulting analog signal into meaningful digital data. Although the broad definition of tag reader can include energy propagation in the form of ultrasonics or light, we restrict ourselves here to the case of near-field electromagnetic energy, using either inductive or capacitive coupling.

If we do not include far-field microwave backscatter tags, the standard operating frequency for RFID tags is 125 KHz and 13.56 MHz. A switching network inside the tag produces an amplitude modulation of the excitation signal which can be detected as loading on a single antenna or as a pick-up voltage on a separate receive antenna. To encode information, most RFID systems employ simple AM modulation, but others employ an additional layer of modulation on a subcarrier frequency in the form of FSK or BPSK.

Commercial EAS tagging systems do not encode data and simply detect the presence of a tag. Tags that employ a harmonic means of detection require the tag reader to transmit energy at a low frequency (e.g. 77 Hz) and subsequently scan a higher frequency range (few KHz) to collect a harmonic spectrum. In the resonant mode of detection, the tag reader transmits a RF excitation pulse (at 58 KHz or 8 MHz) then listens for ringing oscillations produced by the tag.

In addition to the tags and frequencies mentioned above, other varieties of tags and sensors have been developed which operate in the frequency range 50 Hz - 50 MHz. For example, access control badges originally developed by Westinghouse require the tag reader to detect embedded resonant structures in the range 5-30 MHz. At MIT, we have developed various forms

of electromagnetic material structures to function as ID tags or as a new class of disposable wireless sensors.[i]

In this context, it is possible to outline some ideal fundamental requirements for a general-purpose tag reader:

- The ability to transmit power at a digitally specified frequency over the range of a few Hz to 50 MHz.
- The ability to modulate the transmitted power
- The ability to detect signals at specified frequencies, which may differ from the transmitted frequency.
- Detection frequency resolution of at least 0.1%
- The ability to analyze the detected signals and relay the information to an external network or computer.

Naturally, the specific implementation of these requirements will depend on the specific application, the read range requirement and the targeted cost.

Since it is not practical to build a tuned antenna that could operate over many decades of frequency range, we have assumed that all tag reader antennas would be untuned, with an optimally flat frequency response. For some cases, it is desirable to permit easy substitution of antennas.

7.3 Design Examples and Analysis

Using the basic set of requirements outlined above we set out to explore several design approaches with respect to different cost targets and varying degrees of complexity.

7.3.1 Implementation of A Wide-Band Harmonic And Resonant Tag Reader

For approximately $500 parts cost, we built a tag reader with an operating frequency range of DC-300 KHz that is capable of detecting resonant as well as harmonic signals.

The bock diagram of this reader is shown in Figure 1. The nickname for this reader is “Sweeper.”

Initial versions of this board employed digitally controlled phase-locked loop (PLL) synthesizers, but the PLL had limited frequency range and had an inherent settling time when changing frequencies. For these reasons, we converted to direct digital synthesis (DDS) for generating our signals.

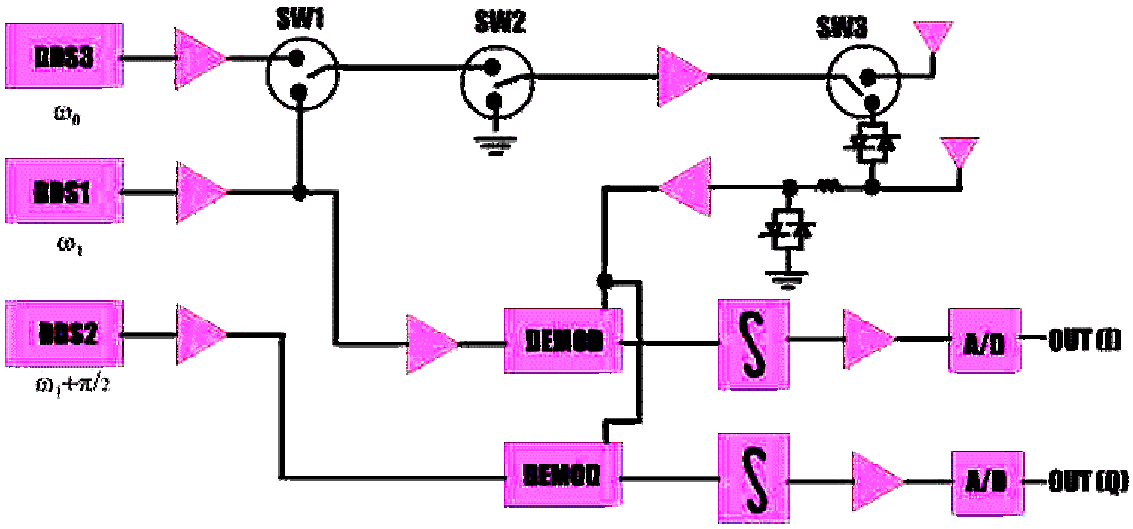

Fig. 119 Block Diagram and photograph of the wide-band harmonic and resonant tag reader, nicknamed “Sweeper.”

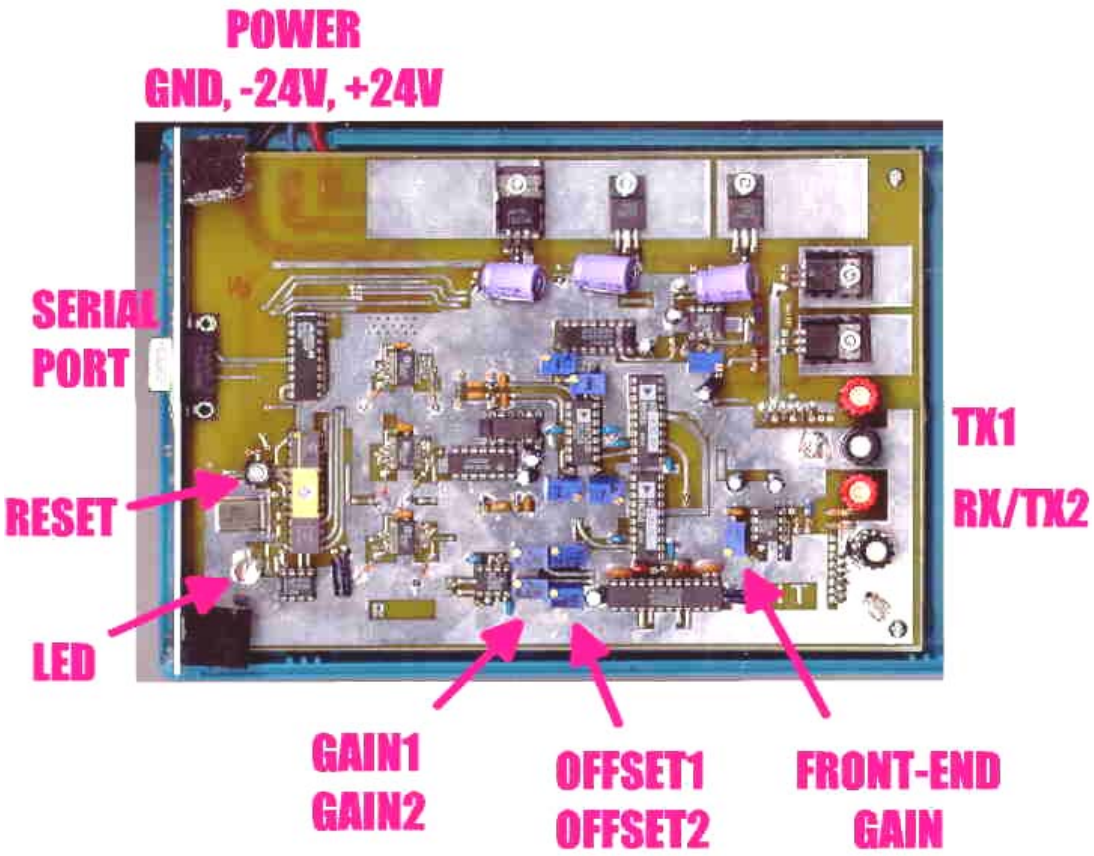

Fig. 120 Block Diagram and photograph of the wide-band harmonic and resonant tag reader, nicknamed “Sweeper.”

Three AD9850 DDS chips having a frequency resolution of .0251 Hz were employed on the Sweeper board, one for generating the transmitted signal and two for generating the frequencies required for demodulation. The two receiving DDS chips can be set to arbitrary relative phase, but are generally set to a phase difference of 90° apart to generate I- and Q- components of the received signal. Amplitude modulation of the output waveform is accomplished with a solid state switch for simple ON/OFF keying, and frequency and phase modulation can be accomplished in software via the DDS.

Two modes of detection were possible on the Sweeper board: harmonic mode and resonant mode. In harmonic mode, the reader would transmit at a fixed frequency and sweep the frequency of the receiver to collect a spectrum. In resonant mode, the board would sweep both the transmitter and receiver over a range of discrete frequencies, stopping at each frequency to output an RF pulse and listen for the ringing oscillations of any existing resonant structure. The integration times for the detection were software-programmable, so that a variety of both high and low Q structures could be interrogated.

The frequency range of the board was limited by the AD630 synchronous demodulator which is rated to 300 KHz. The solid state switches and push-pull power amplifier stage were limited to approximately 1 MHz.

The received signals were digitized using an LTC1298 12-bit dual-channel serial ADC interfaced to a 20 MHz PIC16C76 microcontroller with 8K of program memory. There was sufficient program memory to implement Taylor series approximation functions in assembly code to translate the I/Q values of the data to magnitude and phase values. The data could then be sent serially to an external host using a variety of user-definable formats. For RFID tags, the output frequency would be held constant and the data demodulation done in software.

This tag reader was designed to operate using either a one or two antenna configuration, settable in software through the use of a solid state switch. Using a supply voltage of +/- 24 V at 800 mA, the Sweeper board could easily power an untuned 15-inch diameter coil and detect resonant EAS tags at a range of 12 inches and harmonic tags at a range of 4 inches. It is expected that read range performance could be improved beyond these values, since we made little effort to optimize the gain and sensitivity of the receiver.

7.3.2 Implementation of a Mid-Range DDS Tag Reader

Using a target cost of $50, we set out to build a scaled-down battery-powered version of the previous design to operate in the frequency range 5-40 MHz. This operating range was chosen since the tags at this frequency are relatively cheap, and the transmit antenna at this frequency can be implemented as a single-turn coil integrated onto the printed circuit board.

The functional blocks of this tag reader are shown in Figure 2. Frequency generation in this reader is done by a single DDS chip (from which the name “Mini-DDS reader” follows). The output of the DDS is passed through a 4-pole low-pass filter to remove the higher-order alias frequency harmonics. The filtered signal is then amplified using a fast op-amp.

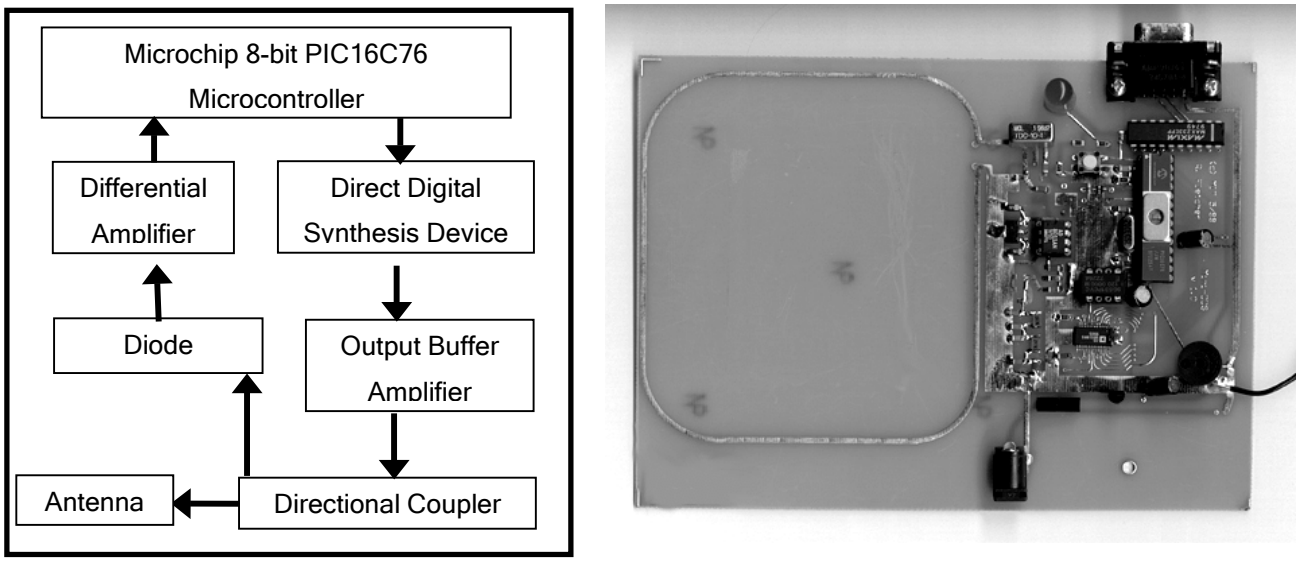

Fig. 121 Block Diagram and photo of the Mini-DDS reader

Detection of a resonant tag is accomplished through the use of a 50 Ω directional coupler configured to measure antenna loading. In this configuration, the untuned single-turn antenna presents an optimally unmatched load and the reflected power is channeled through the directional coupler output. However, when a resonant structure is placed within range of the antenna, the impedance of the resonator dominates the response, and the resulting matched impedance at resonance produces a dip in the reflected power. This method of detection eliminates the need for a broad-band tuned antenna. Also, since the antenna is untuned, the tag reader is quite immune to spurious responses caused by any stray reactance in the environment.

The reflected power output of the directional coupler is fed to a diode detector and the resulting voltage is amplified by an instrumentation amplifier and digitized using a built-in 8-bit A/D module on the microcontroller.

Using a 4-inch diameter reader antenna and a 2-inch diameter EAS tag, a read range of 6 inches was achieved. Reading a 13.56 MHz RFID tag was not attempted, but software demodulation should be possible if the data rate of the tag can be set sufficiently slow.

The tag reader can be powered from a 9-Volt battery, drawing less than 100 mA. If the tag reader needs to communicate with an external device, such as an RS-232 serial port, the additional power needed to drive the interface cable will shorten the battery life accordingly.

7.3.3 Implementation of a Minimal Tag Reader

In the interest of minimizing cost and complexity, we explored a scaled-down version of the previous design with a target cost of $5 in parts. We refer to this design as the "Zen tag reader."

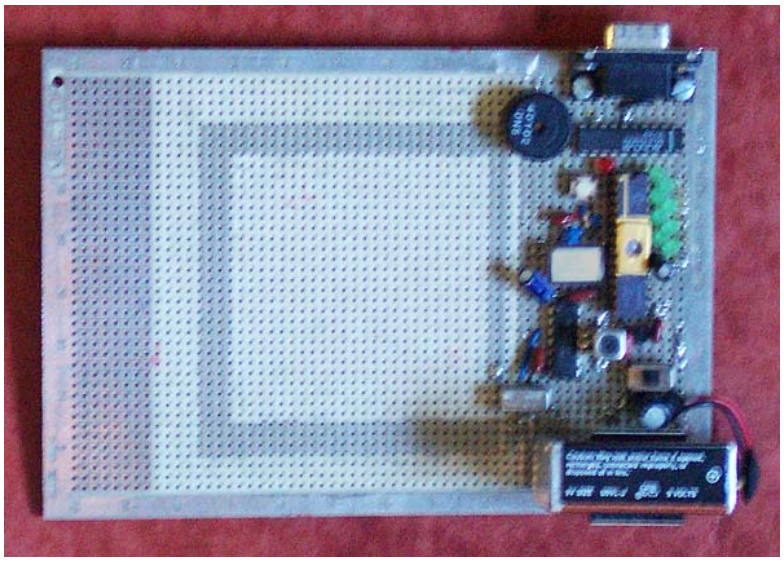

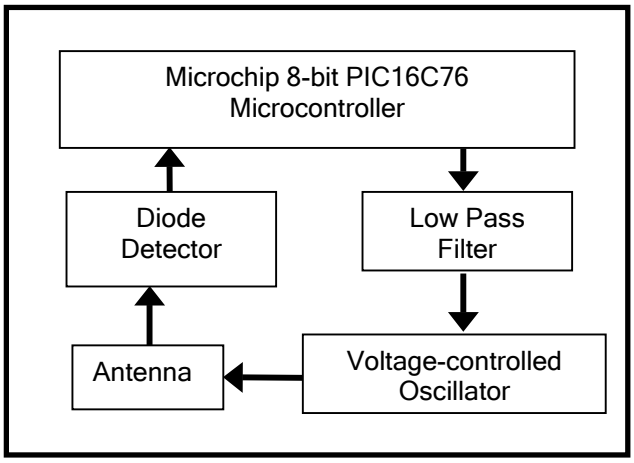

Fig. 122 Photograph and block Diagram of minimal "Zen" tag reader

Using a design very similar to the Min-DDS reader, it was possible to dramatically reduce the parts cost by simply eliminating the directional coupler, the instrumentation amplifier, and the DDS chip. Considering various approaches to generate a variable frequency, we decided to implement a voltage-controlled oscillator (VCO) using a varactor diode as the tuning element. The control voltage for the VCO was generated in software using a variable duty-cycle square wave which was then fed to a low-pass filter to produce a DC voltage level. The finite control

resolution of the duty-cycle and the fundamentally logarithmic response of the low-pass filter limited the frequency resolution to steps of 500 KHz spanning the frequency range 5-15 MHz.

The detection of a resonant tag structure was accomplished by simply sensing a dip in antenna voltage produced by loading at resonance. This approach is reminiscent of the "grid-dip meters" employed in the early 20th century. A benefit of using the VCO is the fact that the VCO employs a resonant tank circuit. Therefore, it was possible to integrate the sensing coil as part of the VCO resonator, which resulted in greater sensitivity, thus compensating for the lack of an instrumentation amplifier in the receive path.

Without using a directional coupler, any change in reactance can also produce a frequency-independent change in the antenna voltage. Therefore, the baseline voltage is also a function of the stray capacitance or inductance near the antenna. This was an important consideration when mounting the reader for a given application.

For battery-powered applications, control over the output frequency was challenging, since a drooping battery voltage would cause some shift in the VCO frequency despite an onboard voltage regulator. Instead of attempting a more complex frequency-control algorithm, we eliminated the need for calibration by implementing a frequency counter using the built-in hardware counter on the PIC microcontroller. By directly measuring the frequency generated by the VCO, closed-loop control of the frequency was then possible.

At a fixed frequency, the performance of the Zen reader was comparable to that of the Mini-DDS reader. However, its limited frequency resolution is insufficient for finding very narrow resonance peaks within a 10 MHz frequency range. Nonetheless, such a reader could be used at a fixed frequency for RFID tags and also as a very coarse swept-frequency reader for detecting a dozen or so tags tuned to specific resonant frequencies. Such a reader would be appropriate for simple applications, such as toys.

7.3.4 A Versatile Software Radio Implementation of a Tag Reader

Software radio architectures offer great versatility, due to their modular functional decomposition. The basic software radio, whether it is a spectrometer, a monitor for extraterrestrial communication, or a simple tag reader, has three parts: a synthesis stage which converts a digital output signal to analog form, an all-digital stage for performing some computation, and an analog stage for capturing and digitizing an input signal.

The versatility comes from the second, all-digital stage. Progress in digital design can now put an enormous amount of high-speed computing power into a small, cheap package, allowing implementation of complex operations - such as spectral analysis, adaptable filtering, optimizing control, and pattern recognition, often at rates sufficient for real-time processing. Furthermore, several digital designs can be used at varying stages of product development - for example, a complicated FPGA (field programmable gate array) can be used for prototyping a device, a

microcontroller can be used for simple testbeds, and an ASIC - perhaps synthesized from the FPGA design itself - can be used for the final product. Because of the abstraction layer between the analog stages and the digital one, computations can even be done remotely - say, on a powerful computer connected to the radio via the Internet.

Physically, a field programmable array (FPGA) is a chip with reconfigurable combinatorial logic, lookup tables, wires, and flipflops in a 2-dimensional array. Elements within the FPGA can be designated as local RAM, others can be treated as input pins, and still others can be combined into registers, accumulators, multiplexers, and other elements. FPGAs can be programmed in many different hardware description languages (HDLs), including the industry-standard ones for specifying digital circuitry, Verilog and VHDL. These hardware description languages allow the same logic (down to the register, wire, and gate level) to be represented independently of the underlying FPGA hardware (with its combinatorial logic blocks, ratsnests, longlines, pinwires, and other odd constructs). For a tag reader, we can replace a standard DDS chip - which generates a sinusoidal waveform at a specified frequency - with a Verilog description of the DDS, implemented on an FPGA. The Verilog DDS is versatile, allowing one to create a modulation scheme, a shaping function, or a special sweep mode, with just a few lines of code. Adding this functionality to an exisiting DDS chip can be difficult.

We designed a swept tag reader using a mid-range 950-logic cell, 10,000-gate Xilinx XC4010XL-PC84 FPGA and a 12-MHz clock (as part of an XESS Xilinx Evaluation Board). Eight pins of the FPGA were linked to the digital inputs of an AD7228 8-bit parallel DAC, and 12 pins of the FPGA were linked to the digital outputs of an AD1671 12-bit ADC. The unipolar DAC output was filtered, AC-coupled and fed to a 0.5 Watt push-pull power amplifier stage to power the transmit coil. A receiver coil was placed just under the transmitter coil, and the output of this coil was amplified to fit the 0-5Volt range of the AD1671 ADC.

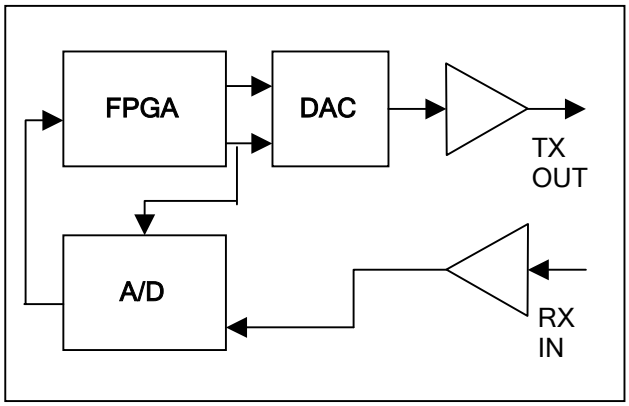

Fig. 123 Initial implementation of an FPGA-based software- radio tag reader.

Verilog code for a direct-digital synthesis (DDS) module was written and implemented for the Xilinx FPGA on the XESS board. A DDS contains four simple digital constructs: a clock, a

frequency word, a phase accumulator, and an output amplitude. At each clock tick, the phase accumulator is incremented by the value of the frequency word, and the top few bits of the phase accumulator are then converted to a sinusoidal output amplitude via a lookup table. The result is a sinusoidal output with a precisely tunable output frequency, appropriate for performing a network analyzer task such as sweeping through frequencies, or for performing a communication task like FSK modulation. The fundamental block diagram for the FPGA reader is shown in Figure 4.

The FPGA tag reader was able to detect loading from a 58 kHz EAS tag placed inside its small antenna coil, but there was insufficient room on the FPGA to perform the synchronous demodulation needed to extend the read range. Rather than switch to a larger FPGA, we are currently exploring simple ways to make more efficient use of our existing FPGA chip. Some of these options include:

- placing the phase-to-amplitude lookup table in external DRAM, SRAM, or ROM/EEPROM
- storing only one quadrant of the sinewave, from q = 0 to p/2, and using a little bit of logic to compute amplitudes in the other three quadrants doing some of the computation in a general purpose microcontroller, DSP, or computer attached to the FPGA
- relegating the FPGA mainly to the realms of fast digital control, interfacing, and reactive performance.

7.4 Tag reader control Interface

Coming out of the work we described in Section III above, we discovered that certain functionality was common to all the tag readers. For example, in all the tag readers described, there is the ability to sweep over a part of the tag reader's excitation frequency range with variable resolution; as a result there exist commands to set the start frequency, the stop frequency, and the frequency step size. Defaults are set during the power-up cycle of the microcontroller; however, in the course of the tag reader's use there is almost always a need to change them. In a similar fashion, there is other functionality that requires external control, and thus we were drawn to the idea of a standard tag reader interface. We developed a standard set of possible control commands and associated byte sequences that an external agent controlling the tag reader would need to be able to control and communicate with a given tag reader.

A standard software interface simplifies the development of subsequent tag readers by providing a common command set, a subset of which could be implemented in any particular tag reader, depending on the capabilities of its hardware. Separating the design of the tag reader's control structure from the hardware implementation allows us to develop a single robust control program (for a workstation) that would be able to control any tag reader and monitor its data

visually. This approach has proved useful as we have developed applications that require multiple tag readers connected to a network.

Command	Sweeper	Mini-DDS	Zen
Set Start Frequency	X	X	X
Set Stop Frequency	X	X	X
Set Step Frequency	X	X	X
Set Single Frequency	X	X	X
Set Detection Threshold	X	X	X
Output data stream	X	X	X
Run calibration routines	X	X	X
Retrieves internal state	X	X	X
Restart sweep	X	X	X
Enable onboard output channel			X
Harmonic Detection	X		
Disable Transmit Stage	X	X	
CW Frequency detection	X		
Accept External Frequency Commands	X	X	X

Table 1 A brief list of some of the common control commands implemented for various tag readers.

7.5 Infrastructure issues and opportunities

As tag readers become cheaper and more ubiquitous, there is an increasing need to pay attention to the infrastructure necessary to transfer, interpret, and store all the generated information. If we consider a future home, office, retail, or manufacturing environment, it is necessary to find a convenient and efficient way to form networks of such devices and perhaps even to connect them to the Internet.

Fig. 124 Block Diagram of minimal “Zen” tag reader

For most tagging applications, a local area network is desirable. Instead of developing our own proprietary protocol to link tag readers together, we decided to make our tagreaders compatible with standard Ethernet networks employing the TCP/IP protocol. To do so, we used a small 2 in. X 3 in. Ethernet adapter developed in our laboratory. This plug-in adapter converts RS-232 serial data at 110 Kbs to TCP/IP data packets. For a prototype installation used at the Museum of Modern Art in New York City during the summer of 1999, we installed eight tag readers embedded beneath a table and connected to the local area network. On the Ethernet network, a particular data port number identifies each tag reader, and the tag readers constantly output their data on this port. Any interested listener on the network could select a given port and access all

the data output by one or more of the tag readers. This allowed multiple workstations connected to the network to monitor any tag reader data in real-time.

For simple Internet access, we have implemented a dial-up modem protocol as a subroutine in our tag reader firmware. This enables the use of an inexpensive external modem as a means of connecting to the Internet. As an example, we have demonstrated a tag reader that can periodically dial the local ISP, establish a connection, and transmit its data files via e-mail to a subscriber.

For portable applications and remote wireless connectivity, we are developing the use of two-way pager technology for tag readers. In regions where pager networks are not accessible, our group has also developed a small satellite transmitter interface for communicating directly with a low-earth orbiting satellite system such as Argos or Orbcom.

7.6 Future Developments

We have presented the concept of an open architecture for electromagnetic tagging. The hardware architecture is open in the sense that its functionality can be reconfigured in software via a network to meet the specific needs of a particular application and tag technology. Implementation of such a general purpose reader requires frequency agility and fast logic capable of performing real-time frequency control, transmit modulation, and receiver software demodulation. In addition to standardizing the interface to the tag, it is also important to develop a common software interface, which enables computers on a network to control and communicate with multiple tag readers over the network.

CHAPTER VIII.

Conclusions and Future Work

The work presented in this thesis has demonstrated and proven the use of low-cost chipless material structures as ID tags and wireless sensors. Nevertheless, a significant amount of work remains to commercialize these technologies and integrate them into existing commercial applications.

The field of electromagnetic tagging has been slowly evolving over the past 30 years and new technologies will continue to emerge. However, it is clear that material science and physics will continue be a vital part of future development in this field. Many of these can build on the concepts and topics presented in this thesis.

8.1 Hybrids: RFID + Materials

As the RFID industry struggles to lower the cost of chip-based RFID tags, it is clear that chipless technologies will play an important role in establishing a practical migration path from present-day technologies to the future low-cost RFID vision that is the goal of many companies.

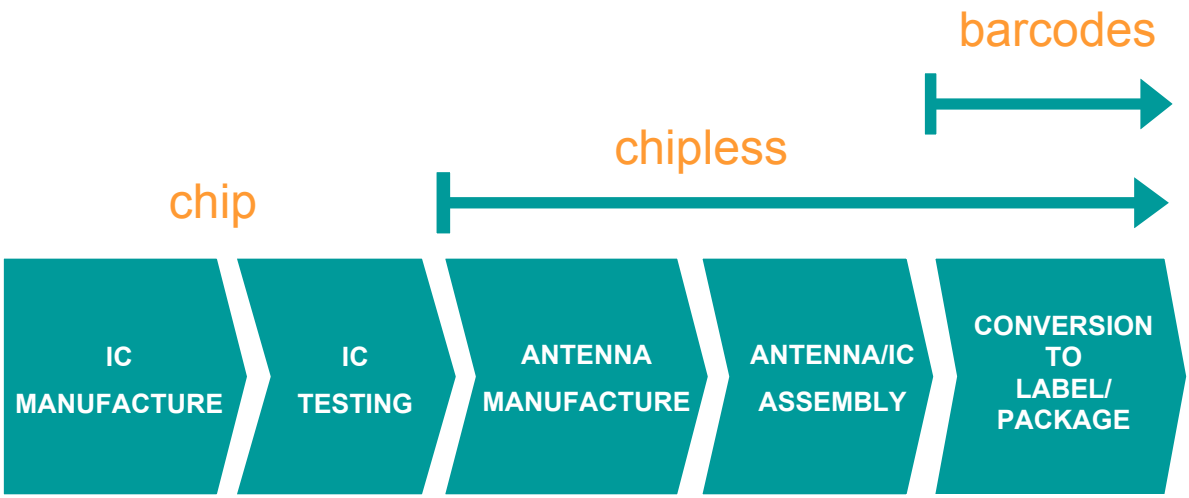

Figure 125. Illustration of separate elements and processing steps comprising an electronic label, showing the connection between chip labels, chipless, and barcode labels.

Although we have been presenting chipless and chip-based technologies as two separate things, they need not be. There are obviously many opportunities to create hybrid tags that combine parts of chip circuits and parts of chipless elements. Slowly, over time various parts of the RFID IC (e.g. memory, rectifier, modulator, etc) can be migrated to other lower-cost technologies. Naturally, sensor tags are already an example of a hybrid tag, which incorporate both chip and chipless components.

While many RFID chip manufacturers promise a sub-10-cent tag, this is only possible with tag volumes of 1 billion units or more, which is several times larger than the entire world market for RFID tags. Incompatible tag designs and tag standards leads to market fragmentation, which prevents very large volumes. In addition to agile readers, the market can really benefit from an *agile tag* --one that can operate at multiple frequencies and with multiple label configurations. Only then can the industry converge to more universal tag designs that can be sold in high volumes. Chipless technologies can play an important role in driving this convergence and gaining a more universal approach to fabricating smart labels.

8.2 Information Persistence and Write-ability

The work presented in this thesis demonstrates various ways to interrogate the information stored in material structures. However, for some applications, there is a need to remotely write information to a tag, and in the case of a sensor, there is also a need to record and store information in the tag. These needs, which I call *information persistence and write-ability*, are the subject of ongoing research.

If it were possible to induce a stable change in a material's state over some distance, then it would be possible to reversibly change the information contained in a material tag. The ability to reprogram the information in a tag is a powerful feature that would enable objects to have memory and would allow us to know the history of an object. This would allow us to store information on a package or a book binding in a manner very analogous to the way information is written on credit cards or ATM cards now. Of course, the advantage of an electromagnetic tag is that the information could be written and read from a distance.

8.2.1 Present Technology

For the problem of remote writeability, at present, there exist 1-bit writeable tags, which means the tag has only two states, ON or OFF. This class of tags is commonly used as anti-theft tags in the EAS (Electronic Article Surveillance) market. In the EAS industry, changing the state of a tag from the armed state to the unarmed state is known as *tag deactivation*.

For a harmonic type of tag (described previously), tag deactivation is done by adding to the tag a strip of semi-hard magnetic material, such as Arnokrome-3, which adds a bias field which

serves to shift the M vs. H curve of the harmonic material outside of the range of the excitation field. Assuming, for example, that the non-linear "step-portion" of the magnetization curve occurs exactly at the origin, then if the added bias field is larger than the maximum amplitude of the externally applied excitation field, then the excitation field will never be able to flip the magnetization of the harmonic material. As a result, the tag will remain in one of its saturated magnetic states and thus produce no flux jumps and no harmonics. However, if the bias magnet is demagnetized, then the magnetization curve will once again be centered at the origin and the tag is once again operational (i.e. ON).

In the case of a resonator type of tag, deactivation in LC resonator tags is generally carried out by applying a strong magnetic field pulse which shorts out either the capacitor or shorts out the turns in the inductor. In both these cases, these "weak links" are purposely designed into the tag and are not a general characteristic of LC resonators. For a magnetomechanical resonator, the tag can be deactivated by demagnetizing the bias magnet packaged with the tag, thus disabling the magneto-mechanical coupling which allows the tag to vibrate. Unlike the case of the LC resonator, deactivation of a magnetoelastic tag is not destructive, so the process is reversible.

It should be noted that all the reversible mechanisms mentioned here rely on magnetizing or demagnetizing a strip of material. Due to practical considerations (available power, safety issues, etc.), these approaches are limited to a distance of 10 centimeters or so.

8.2.2 Possible Solutions for Remote Write-ability

A desirable goal for writeable electromagnetic tags is to be able to individually address bits within a tag over a fair distance (.1m or more). Approaches we are investigating include frequency-addressed and field-addressed bistable mechanisms. Bistable material mechanisms is needed in order to maintain a stable change in state, and frequency- and field- addressing schemes can be used to provide bit selectivity. Certainly, energy considerations are perhaps the greatest constraint in trying to achieve operation over distance. To this aim, resonators could be useful, since they not only provide frequency selectivity, but they also serve as a means of storing and effectively amplifying available energy.

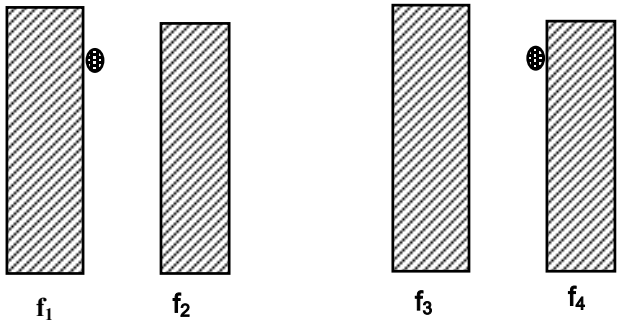

Figure 126. Sketch outlining the principle of a bistable frequency addressed read-write tag. Shown are two separate frequency resonators with a small magnetic exchange particle.

Work in this area is ongoing at MIT as well as in industry (see for example, Navitas in Japan); however, for the purpose of illustration, it is useful to mention a frequency addressed concept I devised back in 1996, using using a mechanical analogy. Consider the tag in Figure 126, which contains two magnetoelastic ribbons, each cut to a different length thus having different resonant frequencies. It is assumed that a sufficient bias field is present so the strips can function as magnetomechanical resonators. In addition there is a small magnetized particle which can attach itself to either strip. When the particle attaches itself to a strip, it increases the total resonator mass, thus lowering its resonant frequency; this means that there are four distinct frequencies which can exist on this tag. If a strip containing the magnetic particle is excited, then the resulting vibration can be enough to cause the particle to detach itself from that strip and attach itself to the other strip. Given this information, it is theoretically possible to fabricate a multi-bit writeable tag that could operate over a reasonable distance (> .1m), with each bit consisting of two resonators and four operating frequencies (2 for reading, 2 for writing), for example. An actual implementation of this concept was attempted in the lab, but did not prove sufficiently robust for practical application. Nevertheless, the concept of frequency-addressing can serve as a model for other non-mechanical bistable tag mechanisms.

8.2.3 Possible Solutions for Information Persistence

The ability to continuously record or log the information in a chipless sensor remains a longer-term research problem, but we can find inspiration for such mechanisms in the natural world. The rings in the truck of a tree, for example, are a physical representation of the history of the tree and its external conditions. Another example is the process of crystal growth. By analogy, if it were possible to design a chemical or biological reaction that lives on a chipless tag, then the local stimuli at any given time, can potentially have an affect on the end-products of this reaction. The physical products of this reaction can then potentially be interrogated remotely via electromagnetic means.

8.3 Polymer Electronics

In order to achieve lower-cost, there is continuing interest in exploring alternative materials and processes for fabricating electronic circuits. Although plastic materials and polymer compounds are very common today, these materials are relatively new, and until recently their electronic properties were not very interesting. It was discovered in 1977, however, that polymer materials containing a backbone chain of alternating single and double bonds can exhibit relatively high electrical conductivities when properly doped. These materials, containing a "π-conjugated" network of bonds are now simply known as *conjugated polymers*. As the interest in these materials has grown, several families of conjugated polymers have achieved prominence, most

notably the polyaniline and polypyrrole families. Some of the more common varieties of conjugated polymers are shown in Figure 110 below.

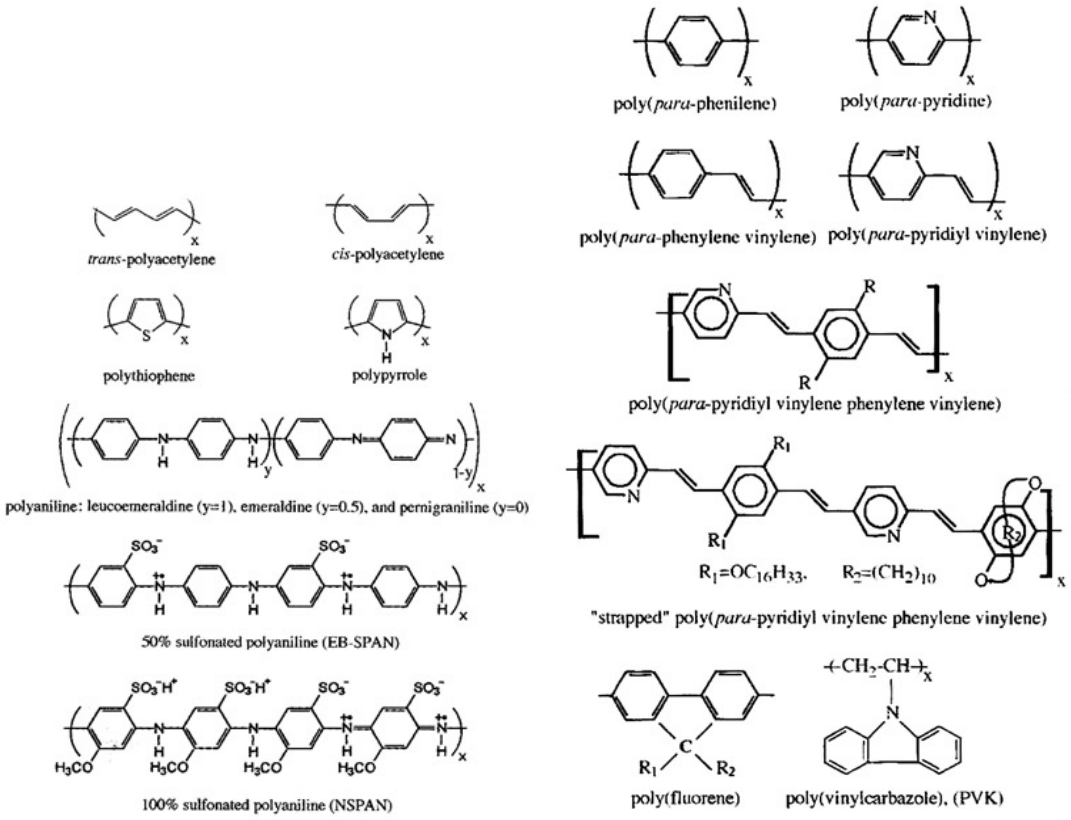

Figure 126. Some of the major classed of electronic polymers used today.

Electronic polymer materials have traditionally been unstable in air and difficult to manufacture in volume. However, over the past twenty years, major advances have occurred in the synthesis and processing of these materials for applications in optics, tribology and electromagnetic coatings. Although the best conductivities achieved by these materials to date is ~10^5 S/m, which is still a couple orders of magnitude worse than common metals, these materials have nevertheless become a viable substitute for certain types of electronic devices and components.

The primary trend over the past decade has been to imitate traditional semiconductor devices and build electronic polymer analogs of transistor circuits. In addition to conducting varieties of conjugated polymers, a great deal of work has been devoted to producing semiconducting polymer materials for use in these structures. Over the past several years, companies such as Philips Research, Lucent, Seiko Epson, and Plastic Logic has successfully created working field-effect transistors manufactured by solution methods or ink-jets. A typical geometry for these devices, comprised of the source, drain, and gate electrodes with intervening dielectric and

semiconducting layers, is shown in Figure 120. Although there are many variations, of this geometry, most are very similar.

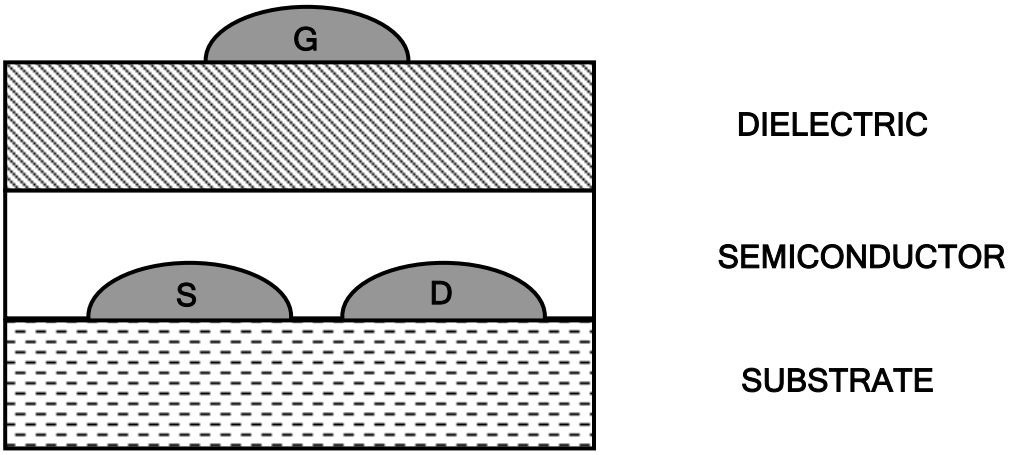

Figure 127. Sample geometry of an all-polymer field-effect transistor with high-conductivity source (S), drain (D), and gate (G) electrodes.

Although arrays of polymer transistors have been constructed, particularly for display applications, the complexity of polymer transistor circuits has been limited. For RFID tagging applications, major challenge has been electron mobility, which limits the operating frequency and switching time of the fabricated circuits. In addition, the long-term stability and shelf-life of these materials is still not sufficiently mature for commercialization. All of these challenges are still active areas of research.

Perhaps a more interesting development is that researchers have begun to invent new type of electrochemical devices that are very unlike traditional semiconductor transistors. It seems to me that instead of trying to copy and emulate silicon circuitry, it is prudent to explore other types of electronic devices that can be fabricated with these materials. There is a very good chance that there are numerous yet undiscovered families of useful electrochemical devices that are lurking in these materials systems.

It is also worth noting that electronic polymer materials also have a great potential impact on antenna structures for RFID tags and readers. One of the conducting polymers, polyethylenedioxythiophene (otherwise known as PEDOT) also happens to be optically transparent, which is a very attractive property for certain tag and reader applications (such as blood specimen tubes and reader antennas on windshields, etc). One of the patents I filed with Motorola in 1997 is on the use of transparent reader and tag antennas using such materials.

8.4 Analog Electronics

At present, one of the main challenges to low-cost chip-based RFID is that many transistors (on the order of several thousand at minimum) are required in order to create the functionality of an RFID chip. Digital electronics makes it convenient to implement memory cells as well as complex data protocols. However, this is not the only way to do it.

Since the days before digital electronics, there has been a great deal of work in analog systems as a means of processing and storing information. The rich dynamics of analog systems provide for complex functionality. Although analog signals are not as convenient to decode as digital signals, the great advantage is that they can be implemented using far fewer transistors, often also with far less power. As well as several other research institutions, the MIT Center for Bits and Atoms is actively pursuing this research field (see for example the graduate work of Ben Vigoda). For examples of some of the basic building blocks that can be created from using just a few transistors, I refer the reader to articles by Barrie Gilbert, one of the masters of this field.

8.5 NMR/NQR

Even though the cost of a polymer IC can potentially be very low, it will never be as cheap as printing with ink. In addition, for certain applications, there will always be a need to hide information in the raw materials themselves, instead of attaching a visible label.

Within this context, perhaps the most intellectually appealing form of electromagnetic signal is the type that occurs naturally in the electrons and nuclei of most materials. These phenomena are commonly known as ESR (Electron Spin Resonance) or EPR (Electron Paramagnetic Resonance) and NMR (Nuclear Magnetic Resonance), respectively. The frequency of these resonances are a function of the local magnetic field; at a bias field of 1 Tesla, for example, the resonant frequencies occur in the range of several GHz and 50 MHz, respectively. For the purpose of low-cost electromagnetic tagging, NMR is more attractive than EPR, because the frequencies below 100 MHz are more easily accessible by consumer electronics, and also because it is already widely used in medical applications to image human tissue. However, if long read-range is needed, the high-frequency of ESR enabled far-field excitation and detection.

The physical source of NMR is the magnetic moment arising from the charge, Z, and quantum mechanical spin, I, of nuclei: $\mu = ZeI/2M_nc$, where e is the charge on the electron and c is the speed of light. The application of a static magnetic field, H_0, causes a discrete splitting of the spin energy levels and also defines a direction in space against which projections of the spin angular momentum can be taken. In a macroscopic sample of material, the Boltzmann distribution among

these spin energy levels gives rise to a net macroscopic magnetization which can be detected using a coil which applies a sinusoidal magnetic field, H_1, that is transverse to the static field.

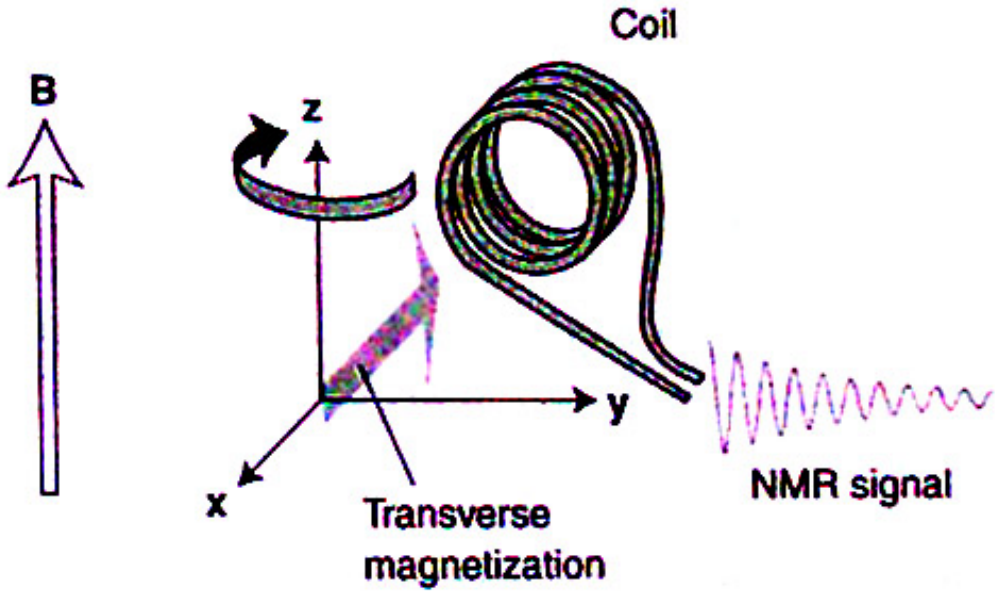

Figure 127. illustration of basic elements of Nuclear Magnetic Resonance.

If we view the individual spins as magnetic dipoles in an external magnetic field, we see that these spins will precess about the H_0 axis at a rate proportional to the local magnitude of H_0, just as the precession rate of a mechanical toy top is determined by the strength of the local gravitational field. This frequency is given by $\omega = \gamma H$, where γ is defined as the gyromagnetic ratio and depends on the type of nuclei (e.g. $\gamma = 5.586$ for water). When the frequency of the applied transverse field is equal to this precession frequency, the transverse field will apply a net torque on the magnetic dipole that will tip the dipole towards and away from the H_0 axis. Because this signal only appears at a specific frequency, it behaves as a resonance, and it is this time-varying magnetization that is sensed by the magnetic coil as the NMR signal.

It is important to note that the measured resonant frequency is not only dependent on the type of nuclei, but also on the local microscopic magnetic environment. This magnetic environment is dependent on the molecular electronic structure exhibited by the chemical bonding. As a result, materials will generally exhibit a spectrum of resonance peaks indicating not only composition but also bonding geometries. It is this property of NMR which can find potential application in electromagnetic sensing as a means of identifying objects and ascertaining something about its chemical state.

For modeling the signal produced by a coil filled with an NMR material, it is useful to know the complex impedance of the coil, which is given by

$$Z = jL_0\omega(1+4\pi\chi') + L_0\omega 4\pi\chi'' + R_0$$

where L_0 is the inductance of the empty coil, and the real and imaginary components of the magnetic susceptibility derived from the Bloch equation for magnetization are given by

$$\chi' = -\chi_0'\omega_0 T_2 \frac{(\omega_0-\omega)^2 T_2}{1+(\omega_0-\omega)^2 {T_2}^2 + \gamma^2 {H_1}^2 T_1 T_2}$$

$$\chi'' = -\chi_0''\omega_0 T_2 \frac{1}{1+(\omega_0-\omega)^2 {T_2}^2 + \gamma^2 {H_1}^2 T_1 T_2}$$

where χ_0 is the value of the static susceptibility. T_1 is the relaxation time associated with the component of magnetization in the direction of H_0, and T_2 is the relaxation time associated with the transverse component of the magnetization due to the phase coherence of the individual spins. The complex impedance of the coil allows one to design circuits containing NMR coils.

Implementation of NMR need not be expensive. In Spring 1997, I implemented a small table-top NMR system for approximately $200 using a permanent magnet (see Figure 108). This was our laboratory's first NMR signal, motivated by the interest in employing NMR as a platform for quantum computing led and pioneered by Neil Gershenfeld. The challenge and cost here was not in designing the electronics but rather in designing the magnet in order to produce a sufficiently uniform field. After several unsuccessful attempts, the first NMR signal was achieved on June 17, 1997 using 5-inch diameter pole pieces made from Hyperm-49 Iron Nickel alloy with precisely machined acrylic spacers. The flux-return between the NdFeB permanent magnets was far less critical and I was able to implement it just using a simple U-shape iron vise clamp.

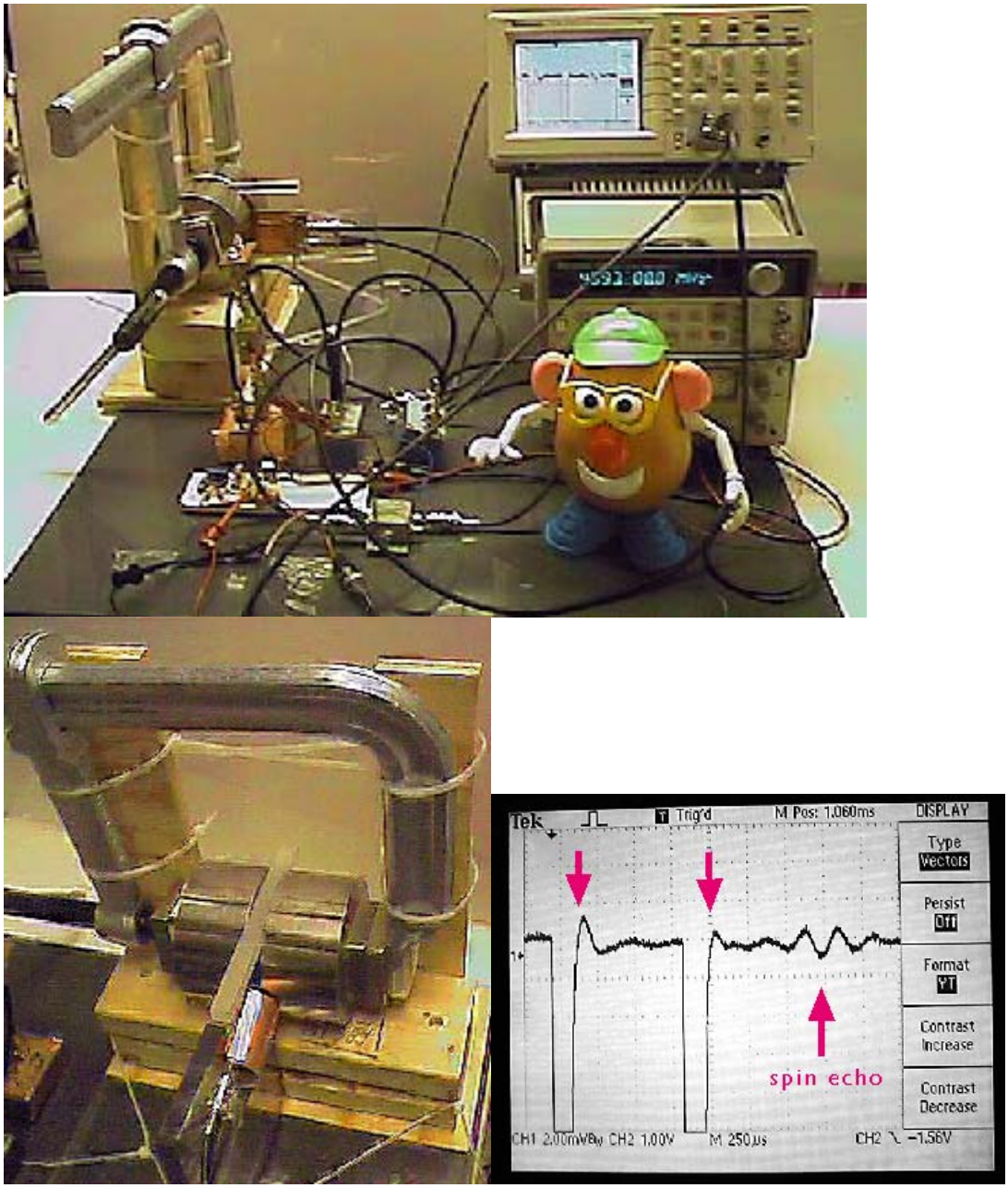

Figure 128. Photographs of table-top NMR instrumentation as well as oscilloscope signal.

Figure 128. The QR-500 Nuclear Quadrupole Resonance scanner sold by InVision Technologies and used at several airports around the world.

Given the encumbrance of the required DC magnetic field in NMR systems, another magnetic resonance phenomenon has recently gained greater attention for tagging applications, despite a lower signal-to-noise ratio. Known as Nuclear Quadrupole Resonance (NQR), this probing technique has been developed for commercial and military use over the past 20 years. NQR is functionally similar to NMR with a (10X) smaller signal to noise ratio, but does not require the DC magnetic field generally created by a large and expensive permanent magnet or electromagnet. Instead of relying on the DC magnetic field to break symmetry and define the magnetic z-axis, Quadrupole Resonance is enabled by the nuclear quadrupole moment that arises from nuclear and electronic interactions. While only certain materials exhibit a Quadrupole Resonance, many important compounds that contain nitrogen, such as landmines, explosives, or cocaine, and chlorine compounds can be detected. Although this effect was first discovered and developed in the early 1950's by Bob Pound at Harvard, its value for security and military applications has driven commercial applications by companies such as Quantum Magnetics (now part of InVision Technologies). At MIT, the Quanta group at the MIT Center for Bits and Atoms as well as members of the Physics and Media Group (Yael MacGuire, Matt Reynolds, Jason Taylor, and Ben Recht) have been leading the effort to develop low-cost NQR instrumentation and techniques.

For the purpose of low-cost electromagnetic tagging, magnetic resonance phenomena is very attractive, since the "tag" can simply exist in the form of an ink or material strip with an identifiable frequency spectra. However, due to the low signal strengths and significant RF transmitter power

required compared to other tagging technologies, magnetic resonance readers are relatively expensive and not yet practical for portable use.

Finally, given all the possible tagging technologies that will continue to emerge in the near future, it may be valid to ask the questions:

What is the ideal tag?

and

What is the ideal reader?

Naturally, the answer to these questions will depend on the particular application, however, it is fair to say that perhaps the ideal tag is no tag: where the information is seamlessly and invisibly integrated into the materials used to make an object. Correspondingly, we can say that the ideal reader is a wireless device that could electromagnetically write information to any material and read it back. ESR, NMR, and NQR come very close to that.

References

[Bao] Z. Bao, H. Schon, H. Meng and J. Slusky, *Organic Transistors with Self-Assembled Materials and Nano-Scale Channels,* Proceedings of Material Research Society Fall Meeting 2001, Session BB: Organic Optoelectronic Materials, Processing, and Devices.

[Brown] A.R. Brown, A. Pomp, C.M. Hart and D.M. de Leeuw , *Logic Gates Made From Polymer Transistors and Their Use in Ring Oscillators,* Science, vol. 270, no. 5238, pp. 972-974, 1995.

[Butterworth] S. Butterworth and F. Smith, Proc. Phys. Soc., vol. 43, p. 166.

[Callaway] J. Callaway, *Quantum Theory of the Solid State, Part A,* Academic Press, 1974.

[Chui] C.K. Chui (ed), *Wavelets: A Tutorial in Theory and Applications*, Academic Press, 1992.

[Collin] R. E. Collin, *Foundations for Microwave Engineering*, McGraw-Hill, 2nd edition, 2001.

[Drury] C. J. Drury, C.M.J. Mutsaers, C. M. Hart, M. Matters and D.M. de Leeuw, *Low-Cost All-Polymer Integrated Circuits,* Appl. Phys. Let., vol. 73, no. 1, ppp. 108-110, 6 July 1998.

[Ebbing] D.D. Ebbing, *General Chemistry,* 1984.

[Elliott] R.S. Elliott, *Electromagnetics: History, Theory, and Applications,* IEEE Press, 1993.

[Farchioni] R. Farchioni and G. Grosso (eds.), *Organic Electronic Materials: Conjugated Polymers and Low Molecular Weight Organic Solids,* Springer, 2001.

[Fletcher] R. Fletcher and J. Cook, *Measurement of Surface Impedance vs. Temperature Using a Generalized Sapphire Resonator Technique,*. Rev. of Scientific Instruments, vol. 65, no. 8, pp. 2658-2666.

[Ginzton] E. Ginzton, *Microwave Measurements*, McGraw-Hill, 1957.

[Grimes] C.A. Grimes, K.G. Ong, K. Loiselle, P.G. Stoyanov, D. Kouzoudis, Y. Liu, C. Tong and F. Tefiku, *Magnetoelastic sensors for remote query environmental monitoring,* Smart Mater. Struct. vol. 8, pp. 639-646, 1999.

[Hanson] D.F. Hanson, *Microwave Resonators*, Dielectric Resonators, D. Kajfez and P. Guillon (eds), Vector Fields, 1990.

[Haus] H. Haus, J. Melcher, *Electromagnetic Fields and Energy*, Prentice Hall, 1989.

[Kajfez1] D. Kajfez, *Correction for Measured Resonant Frequency of Unloaded Cavity*, Electronic Letters, vol. 20, no. 2, 19 January 1984.

[Kajfez2] D. Kajfez, P. Guillon (eds), *Dielectric Resonators*, Vector Fields, 1990.

[Kajfez3] D. Kajfez, *Correction for Measured Unloaded Frequency of Cavity,* Electronics Letters, vol. 20, no. 2, p. 81, 1992.

[Kajfez4] D. Kajfez, *Q-Factor Measurement with Network Analyzer,* IEEE Trans. On Microwave Theory and Techniques, vol. MTT-32, no. 7, July 1984.

[Kajfez5] D. Kajfez and E. Hwan, *Q-Factor Measurement with Network Analyzer*, IEEE Trans. Microwave Theory and Techniques Electronics, vol. MTT-32, No. 7, July 1984.

[Kajfez6] D. Kajfez, *Q Factor,* Vector Fields, 1994.

[Kawase] T. Kawase and C. Newsome, *Late-New Paper: Actice-Matrix Operation of Electrophoretic Devices with Inkjet-Printed Polymer Thin Film Transistors,* Proceedings of Society for Information Display, 2002 International Symposium, Digest of Technical Papers, p. 1017.

[Kraus] J.D. Kraus, *Electromagnetics,* 4th edition, McGraw-Hill, Inc. 1992.

[Levitt] M.H. Levitt, *Spin Dynamics: Basics of Nuclear Magnetic Resonance,* John Wiley & Sons, Ltd., 2001.

[Mermerlstein1] M. Mermelstein, *IEEE Trans. Mag.*, vol. 22, p. 442, 1986.

[Mermerlstein2] M. Mermelstein, *IEEE Trans. Mag.*, vol. 28, p. 36, 1992.

[Mills] J.P. Mills, *Electromagnetic Interference,* Prentice Hall, 1993.

[O'Handley1] R. O'Handley, *Magnetic Materials: Principles and Applications*, John Wiley and Sons, 1998.

[O'Handley2] R. O'Handley, *Magnetic Materials for EAS Sensors*, Journal of Materials Engineering and Performance, vol. 2, no. 2, p. 211, April 1993.

[O'Handley3] R.C. O'Handley, *Modern Magnetic Materials: Principles and Applications,* John Wiley & Sons, Inc., 2000.

[Plonsey1] R. Plonsey and R.E. Collin, *Principles and Apllications of Electromagnetic Fields,* McGraw-Hill Book Co., Inc., 1961.

[Plonsey2] R. Plonsey, R. E. Collin, Principles and Applications of Electromagnetic Fields, p. 336-341, 1961.

[Popovic] B.D. Popovic, *Introductory Engineering Electromagnetics*, Addison-Wesley, 1971.

[Pozar] D.M. Pozar, *Microwave Engineering,* Addison-Wesley, 1990.

[Rado] G.T. Rado and H. Suhl (eds.), *Magneticsm,* Academic Press, 1963.

[Ramo] S. Ramo, J.R. Whinnery and T. van Duzer, *Fields and Waves in Communication Electronics,* 3rd edition, John Wiley & Sons, Inc.., 1994.

[Reitz] J. Reitz, F. Milford and R. Christy; *Foundations of Electromagnetic Theory*, 4th Edition, Addison-Wesley, 1993.

[Rogers] J.A. Rogers, K. Baldwin, Z. Bao, J. Hsu and L. Loo, *Printed Organic Electronics and Molded Polymers for Integrated Optics,* Proceedings of Material Research Society Fall Meeting 2001, Session DD: Polymer Interfaces and Thin Films.

[Sirringhaus] H. Sirringhaus and R. Friend, *Polymer Transistor Circuits Fabricated by Solution Self-Assembly and Direct Inkjet Printing,* Proceedings of Material Research Society Fall Meeting 2001, Session BB: Organic Optoelectronic Materials, Processing, and Devices.

[Staelin] D. Staelin, A. Morgenthaler and J. A. Kong; *Electromagnetic Waves*, Prentice-Hall, 1994.

[Stearns] T.H. Stearns, *Flexible Printed Circuitry,* McGraw-Hill, 1996.

[Sucher] M. Sucher, *Measurement of Q,* Handbook of Microwave Measurements, 3rd Edition, M. Sucher and J. Fox (eds), Interscience Publishers, 1963.